

FULL WAVEFORM INVERSION (FWI) IN FREQUENCY DOMAIN FOR THE WAVE PROPAGATION FOR VISCO ACOUSTIC MEDIUM APPLIED IN SYNTHETIC DATA

SHERYL KARINA AVENDAÑO PÉREZ
Instituto de Física
Universidad de Antioquia

**A Thesis submitted to the Institute of Physics
in partial fulfillment of the requirements
for the degree of Master of Physics**

Advisor

HEBERT MONTEGRANARIO
Instituto de Matemáticas
Universidad de Antioquia

Co-Advisor

JUAN CARLOS MUÑOZ CUARTAS
Instituto de Física
Universidad de Antioquia



November 2017

ABSTRACT

Seismic modeling is an important step in the process used for imaging earth subsurface. In this work the principal objective is to implement the technique Full Waveform Inversion in seismic synthetic data for obtain an estimate of the velocity profile with the that were generated. Current applications require accurate models associated with solutions of the equation of wave propagation in realistic medium. In this work, we propose a modeling for 2D wave propagation in a visco-acoustic medium with variable velocity and density, handled in the frequency domain under conditions that describe dissipation depending on the quality factor Q . We use mixed-grid finite-difference method and optimize it for the case of the visco-acoustic medium with the aim to minimize numerical dispersion. We present solutions for test cases in homogeneous media and compare the analytic solutions. Further, we compare the solution using conventional grid (5-point scheme) and our mixed grid implementation (9-point scheme), finding a better response with the mixed grid 9-point scheme. We also studied the characteristics of the numerical solution, wave fields P-waves are discussed for different velocity profiles, damping functions and Q values finding that the method performs very well with very much potential in applications of FWI.

ACKNOWLEDGMENTS

I want to thank to my parents, my brothers and friends who gave me their unconditional support. To my advisers for their patience and effort to get the best possible result. To the Seismic Tomography Group, in the Universidad de Antioquia, for their confidence and constant help in the research process. And also ECOPETROL, who believed in me and my work gave me the opportunity to consolidate my education with a postgraduate degree.

This thesis work is supported by the Colombian Oil Company ECOPETROL and COLCIENCIAS as a part of the research project grant No. 0266-2013.

TABLE OF CONTENTS

List of Figures	v
1 INTRODUCTION	1
2 MODELING VISCO-ACOUSTIC WAVE EQUATION	6
2.1 Wave propagation in viscous medium	6
2.2 Damping Functions	8
2.3 Equation of propagation in a viscoacoustic medium	10
2.4 Equation of propagation in other media	13
3 NUMERICAL SOLUTION AND TECHNIQUE	15
3.1 Conventional Grid	16
3.2 Rotated Grid	18
3.3 Mixed grid and Lumped Mass term	21
3.4 Dispersion Analysis	24
3.5 The Source	27
3.6 Perfectly-matched layer (PML) absorbing boundary conditions	31
3.7 Numeric solution in visco-acoustic medium and other mediums	36
4 PHYSICAL ANALYSIS OF THE PROPOSE SOLUTION	38
4.1 Numerical solution vs Analytic solution	39
4.1.1 9-point scheme and 5-point scheme	40
4.1.2 The Scale factor of the source	43
4.2 Media with variable velocity, density and attenuation	49
4.2.1 Three Layers velocity profile	50
4.2.2 Complex velocity profile	50
4.2.3 Marmousi velocity profile	51
4.3 Wave propagation in other mediums	52
4.3.1 Shot comparison for density	53
4.3.2 Shot comparison for viscosity	66
4.3.3 Spectrum comparison for density	77
4.3.4 Spectrum comparison for viscosity	78
5 FULL WAVEFORM INVERSION IN FREQUENCY DOMAIN	83
5.1 Inversion Method: Numerical considerations	84
5.1.1 A brief summary of non-linear minimization methods	85
5.1.2 Cycle skipping and phase difference	86

5.2	An Inversion Scheme in frequency domain	87
5.2.1	Gradient of the objective function	87
5.2.2	Virtual Source Matrix	89
5.2.3	Hessian of the objective function	92
5.2.4	The Optimal Step Length	92
5.2.5	Other considerations	93
5.3	First results	93
5.3.1	Gradients for single source by frequency	97
5.3.2	Gradients for single source for an interval of frequencies	99
5.3.3	Gradients for multiples source by frequency	100
5.3.4	Gradients for multiple sources by a interval of frequencies	105
5.3.5	Filtering gradients with Hessian	110
5.4	FWI applying in three layers velocity profile	111
6	CONCLUSIONS	114
	Bibliography	116

LIST OF FIGURES

2.1	The attenuation and the phase velocity in the Cole-Cole model	11
2.2	The attenuation and the phase velocity in the General model	12
2.3	Plane-wave propagation with Kolsky Model	13
2.4	Plane-wave propagation with Cole-Cole Model difference with Kolsky model	13
2.5	Plane-wave propagation with General Model, difference with Kolsky model	13
3.1	Illustration of the mixed grid used in the numerical solution	16
3.2	Workspace \mathcal{U} and boundary workspace $\partial\mathcal{U}$ for the numerical solution	17
3.3	Ratio between the imaginary part of the theoretical and numerical wave number for several cases of $1/G_r$	26
3.4	Ratio between the imaginary part of the theoretical and numerical wave number for several cases of G_i	26
3.5	Integral values for discrete dirac delta calculate for ec.3.66 for different frequency values, assuming the position of the source is $x_s = 1[\text{Km}]$ and $z_s = 1[\text{Km}]$	29
3.6	Integral values for discrete Dirac delta calculate for Eq. 3.66 for different frequency values, assuming the position of the source is $x_s = 1[\text{Km}]$ and $z_s = 0.015[\text{Km}]$	29
3.7	Integral values for discrete Dirac delta calculate for Eq. 3.66 for different scale factor, assuming the position of the source is $x_s = 1[\text{Km}]$ and $z_s = 1[\text{Km}]$	30
3.8	Integral values for discrete Dirac delta calculate for Eq. 3.66 for different scale factor, assuming the position of the source is $x_s = 1[\text{Km}]$ and $z_s = 0.015[\text{Km}]$	30
3.9	PML in \mathcal{U} and boundary workspace $\partial\mathcal{U}$ for the numerical solution, in x coordinate . . .	32
3.10	PML in \mathcal{U} and boundary workspace $\partial\mathcal{U}$ for the numerical solution, in z coordinate . . .	32
3.11	Field P-wave with $m_0 = f$	34
3.12	Field P-wave with $m_0 = 0$	34
3.13	Modulus P-wave with $m_0 = 3.0$ and $f = 3[\text{Hz}]$. The first figure show the modulus P-wave for all (x, z) and the following figures show the modulus P-wave for a fixed z	35
3.14	Modulus P-wave with $m_0 = 3.0$ and $f = 10[\text{Hz}]$. The first figure show the modulus P-wave for all (x, z) and the following figures show the modulus P-wave for a fixed z . . .	35
3.15	Field P-wave with $m_0 = f, \omega$ for $f = 3, 5, 10, 30 [\text{Hz}]$	36
4.1	Shots (Real part) propagating in medium with constant velocity, density and attenuation for $f = 10, 40, 70 [\text{Hz}]$ and receivers in $z = 1100 [\text{m}]$ deep (close to the source in $z = 1000 [\text{m}]$)	41
4.2	Shots (Real part) propagating in medium with constant velocity, density and attenuation for $f = 10, 40, 70 [\text{Hz}]$ and receivers in $z = 100 [\text{m}]$ deep (away from the source in $z = 1000 [\text{m}]$)	41

4.3	Shots (Imaginary part) propagating in medium with constant velocity, density and attenuation for $f = 10, 40, 70$ [Hz] and receivers in $z = 1100$ [m] deep (close to the source in $z = 1000$ [m])	42
4.4	Shots (Imaginary part) propagating in medium with constant velocity, density and attenuation for $f = 10, 40, 70$ [Hz] and receivers in $z = 100$ [m] deep (away from the source in $z = 1000$ [m])	42
4.5	Modulus P-Wave propagating in medium with constant velocity, density and attenuation for $f = 1, 2, \dots, 50$ [Hz] in point $z = 1100$ [m] and $x = 1000$ [m](near the source), with different σ , the position of the source is $x_s = 1$ [Km] and $z_s = 1$ [Km]	43
4.6	Modulus P-Wave propagating in medium with constant velocity, density and attenuation for $f = 1, 2, \dots, 50$ [Hz] in point $z = 100$ [m] and $x = 1000$ [m](away from the source), with different σ , the position of the source is $x_s = 1$ [Km] and $z_s = 1$ [Km]	44
4.7	Modulus P-Wave propagating in medium with constant velocity, density and attenuation for $f = 1, 2, \dots, 50$ [Hz] in point $z = 100$ [m] and $x = 1000$ [m](near the source), with different σ , the position of the source is $x_s = 1$ [Km] and $z_s = 0.015$ [Km]	45
4.8	Modulus P-Wave propagating in medium with constant velocity, density and attenuation for $f = 1, 2, \dots, 50$ [Hz] in point $z = 1100$ [m] and $x = 1000$ [m](near the source), with different σ , the position of the source is $x_s = 1$ [Km] and $z_s = 0.15$ [Km]	46
4.9	Modulus P-Wave propagating in medium with constant velocity, density and attenuation for $f = 1, 1.5, 2, \dots, 20$ [Hz][Hz] in point $z = 100$ [m] and $x = 1000$ [m](away from the source), with different σ , the position of the source is $x_s = 1$ [Km] and $z_s = 1$ [Km]	47
4.10	Modulus P-Wave propagating in medium with constant velocity, density and attenuation for $f = 1, 1.5, 2, \dots, 20$ [Hz] in point $z = 1100$ [m] and $x = 1000$ [m](near the source), with different σ , the position of the source is $x_s = 1$ [Km] and $z_s = 1$ [Km]	47
4.11	Modulus P-Wave propagating in medium with constant velocity, density and attenuation for $f = 1, 1.5, 2, \dots, 20$ [Hz][Hz] in point $z = 100$ [m] and $x = 1000$ [m](near the source), with different σ , the position of the source is $x_s = 1$ [Km] and $z_s = 0.015$ [Km]	48
4.12	Modulus P-Wave propagating in medium with constant velocity, density and attenuation for $f = 1, 1.5, 2, \dots, 20$ [Hz] in point $z = 1100$ [m] and $x = 1000$ [m](away from the source), with different σ , the position of the source is $x_s = 1$ [Km] and $z_s = 0.015$ [Km]	48
4.13	P-wave 5 [Hz]. Three Layers	49
4.14	P-wave 25 Hz. Three Layers	49
4.15	P-wave 50 Hz. Three Layers	49
4.16	Geometric configuration of the velocity profile	50
4.17	P-wave 5 [Hz]. Complex velocity profile	51
4.18	P-wave 25 Hz. Complex velocity profile	51
4.19	P-wave 50 Hz. Complex velocity profile	51
4.20	Marmousi velocity profile	52
4.21	P-wave 5 [Hz]. Marmousi velocity profile	53
4.22	P-wave 25 Hz. Marmousi velocity profile	53
4.23	P-wave 50 Hz. Marmousi velocity profile	53
4.24	P-wave in the $z = 10$ [m] for three layers velocity profile with ρ constant and variable for 5 [Hz]	55
4.25	P-wave in the $x = 1000$ [m] for three layers velocity profile with ρ constant and variable for $f = 5$ [Hz]	55

4.26 P-wave in the $z = 10$ [m] for three layers velocity profile with ρ constant and variable for 25 [Hz]	56
4.27 P-wave in the $x = 1000$ [m] for three layers velocity profile with ρ constant and variable for $f = 25$ [Hz]	56
4.28 P-wave in the $z = 10$ [m] for three layers velocity profile with ρ constant and variable for 50 [Hz]	57
4.29 P-wave in the $x = 1000$ [m] for three layers velocity profile with ρ constant and variable for $f = 50$ [Hz]	57
4.30 P-wave in the $z = 10$ [m] for complex velocity profile with ρ constant and variable for 5 [Hz]	59
4.31 P-wave in the $x = 1000$ [m] for complex velocity profile with ρ constant and variable for $f = 5$ [Hz]	59
4.32 P-wave in the $z = 10$ [m] for complex velocity profile with ρ constant and variable for 25 [Hz]	60
4.33 P-wave in the $x = 1000$ [m] for complex velocity profile with ρ constant and variable for $f = 25$ [Hz]	60
4.34 P-wave in the $z = 10$ [m] for complex velocity profile with ρ constant and variable for 50 [Hz]	61
4.35 P-wave in the $x = 1000$ [m] for complex velocity profile with ρ constant and variable for $f = 50$ [Hz]	61
4.36 P-wave in the $z = 1900$ [m] for three layers velocity profile with ρ constant and variable for 5 [Hz]	63
4.37 P-wave in the $z = 1900$ [m] for complex velocity profile with ρ constant and variable for $f = 5$ [Hz]	63
4.38 P-wave in the $z = 1900$ [m] for three layers velocity profile with ρ constant and variable for 25 [Hz]	64
4.39 P-wave in the $z = 1900$ [m] for complex velocity profile with ρ constant and variable for $f = 25$ [Hz]	64
4.40 P-wave in the $z = 1900$ [m] for three layers velocity profile with ρ constant and variable for 50 [Hz]	65
4.41 P-wave in the $z = 1900$ [m] for complex velocity profile with ρ constant and variable for $f = 50$ [Hz]	65
4.42 P-wave in the $z = 10$ [m] for three layers velocity profile with ρ constant and variable for 5 [Hz]	67
4.43 P-wave in the $x = 1000$ [m] for three layers velocity profile in acoustic and visco-acoustic medium for $f = 5$ [Hz]	67
4.44 P-wave in the $z = 10$ [m] for three layers velocity profile in acoustic and visco-acoustic medium for 25 [Hz]	68
4.45 P-wave in the $x = 1000$ [m] for three layers velocity profile in acoustic and visco-acoustic medium for $f = 25$ [Hz]	68
4.46 P-wave in the $z = 10$ [m] for three layers velocity profile in acoustic and visco-acoustic medium for 50 [Hz]	69
4.47 P-wave in the $x = 1000$ [m] for three layers velocity profile in acoustic and visco-acoustic medium for $f = 50$ [Hz]	69
4.48 P-wave in the $z = 10$ [m] for complex velocity profile in acoustic and visco-acoustic medium for 5 [Hz]	71

4.49 P-wave in the $x = 1000$ [m] for complex velocity profile in acoustic and visco-acoustic medium for $f = 5$ [Hz]	71
4.50 P-wave in the $z = 10$ [m] for complex velocity profile in acoustic and visco-acoustic medium for 25 [Hz]	72
4.51 P-wave in the $x = 1000$ [m] for complex velocity profile in acoustic and visco-acoustic medium for $f = 25$ [Hz]	72
4.52 P-wave in the $z = 10$ [m] for complex velocity profile in acoustic and visco-acoustic medium for 50 [Hz]	73
4.53 P-wave in the $x = 1000$ [m] for complex velocity profile in acoustic and visco-acoustic medium for $f = 50$ [Hz]	73
4.54 P-wave in the $z = 1900$ [m] for three layers velocity profile with ρ constant and variable for 5 [Hz]	74
4.55 P-wave in the $z = 1900$ [m] for complex velocity profile with ρ constant and variable for $f = 5$ [Hz]	74
4.56 P-wave in the $z = 1900$ [m] for three layers velocity profile with ρ constant and variable for 25 [Hz]	75
4.57 P-wave in the $z = 1900$ [m] for complex velocity profile with ρ constant and variable for $f = 25$ [Hz]	75
4.58 P-wave in the $z = 1900$ [m] for three layers velocity profile with ρ constant and variable for 50 [Hz]	76
4.59 P-wave in the $z = 1900$ [m] for complex velocity profile with ρ constant and variable for $f = 50$ [Hz]	76
4.60 P-wave in the $z = 10$ [m] for three layers velocity profile with ρ constant and variable for $x = [10, 1000, 1990]$ [m] and source frequency $f_s = 30$ [Hz]	79
4.61 P-wave in the $z = 1900$ [m] for three layers velocity profile with ρ constant and variable for $x = [10, 1000, 1990]$ [m] and source frequency $f_s = 30$ [Hz]	79
4.62 P-wave in the $z = 10$ [m] for complex velocity profile with ρ constant and variable for $x = [10, 1000, 1990]$ [m] and source frequency $f_s = 30$ [Hz]	80
4.63 P-wave in the $z = 1900$ [m] for complex velocity profile with ρ constant and variable for $x = [10, 1000, 1990]$ [m] and source frequency $f_s = 30$ [Hz]	80
4.64 P-wave in the $z = 10$ [m] for three layers velocity profile in acoustic and visco-acoustic medium for $x = [10, 1000, 1990]$ [m] and source frequency $f_s = 30$ [Hz]	81
4.65 P-wave in the $z = 1900$ [m] for three layers velocity profile with in acoustic and visco-acoustic medium for $x = [10, 1000, 1990]$ [m] and source frequency $f_s = 30$ [Hz]	81
4.66 P-wave in the $z = 10$ [m] for complex velocity profile with in acoustic and visco-acoustic medium for $x = [10, 1000, 1990]$ [m] and source frequency $f_s = 30$ [Hz]	82
4.67 P-wave in the $z = 1900$ [m] for complex velocity profile in acoustic and visco-acoustic medium for $x = [10, 1000, 1990]$ [m] and source frequency $f_s = 30$ [Hz]	82
5.1 Geometric configuration of the velocity profile	94
5.2 Gradient for acoustic modeling and acoustic inversion for receivers line in $z = 15$ [m]	95
5.3 Gradient for visco-acoustic modeling and visco-acoustic inversion for receivers line in $z = 15$ [m]	95
5.4 Gradient for visco-acoustic modeling and acoustic inversion for receivers line in $z = 15$ [m]	95
5.5 Gradient for acoustic modeling and acoustic inversion for receivers line in $z = 1990$ [m]	96
5.6 Gradient for visco-acoustic modeling and visco-acoustic inversion for receivers line in $z = 1990$ [m]	96

5.7	Gradient for visco-acoustic modeling and acoustic inversion for receivers line in $z = 1990[\text{m}]$	96
5.8	Gradient for acoustic modeling and acoustic inversion for receivers line in $z = 15[\text{m}]$	98
5.9	Gradient for visco-acoustic modeling and visco-acoustic inversion for receivers line in $z = 15[\text{m}]$	98
5.10	Gradient for visco-acoustic modeling and acoustic inversion for receivers line in $z = 15[\text{m}]$	98
5.11	Gradient for acoustic modeling and acoustic inversion for receivers line in $z = 1990[\text{m}]$	99
5.12	Gradient for visco-acoustic modeling and visco-acoustic inversion for receivers line in $z = 1990[\text{m}]$	99
5.13	Gradient for visco-acoustic modeling and acoustic inversion for receivers line in $z = 1990[\text{m}]$	99
5.14	Gradient for acoustic modeling and acoustic inversion for receivers line in $z = 15[\text{m}]$	101
5.15	Gradient for visco-acoustic modeling and visco-acoustic inversion for receivers line in $z = 15[\text{m}]$	101
5.16	Gradient for visco-acoustic modeling and acoustic inversion for receivers line in $z = 15[\text{m}]$	101
5.17	Gradient for acoustic modeling and acoustic inversion for receivers line in $z = 1990[\text{m}]$	102
5.18	Gradient for visco-acoustic modeling and visco-acoustic inversion for receivers line in $z = 1990[\text{m}]$	102
5.19	Gradient for visco-acoustic modeling and acoustic inversion for receivers line in $z = 1990[\text{m}]$	102
5.20	Phase difference for acoustic modeling and acoustic inversion for receivers line in $z = 15[\text{m}]$	103
5.21	Phase difference for visco-acoustic modeling and visco-acoustic inversion for receivers line in $z = 15[\text{m}]$	103
5.22	Phase difference for visco-acoustic modeling and acoustic inversion for receivers line in $z = 15[\text{m}]$	103
5.23	Phase difference for acoustic modeling and acoustic inversion for receivers line in $z = 1990[\text{m}]$	104
5.24	Phase difference for visco-acoustic modeling and visco-acoustic inversion for receivers line in $z = 1990[\text{m}]$	104
5.25	Phase difference for visco-acoustic modeling and acoustic inversion for receivers line in $z = 1990[\text{m}]$	104
5.26	Gradient for acoustic modeling and acoustic inversion for receivers line in $z = 15[\text{m}]$	106
5.27	Gradient for visco-acoustic modeling and visco-acoustic inversion for receivers line in $z = 15[\text{m}]$	106
5.28	Gradient for visco-acoustic modeling and acoustic inversion for receivers line in $z = 15[\text{m}]$	106
5.29	Gradient for acoustic modeling and acoustic inversion for receivers line in $z = 1990[\text{m}]$	107
5.30	Gradient for visco-acoustic modeling and visco-acoustic inversion for receivers line in $z = 1990[\text{m}]$	107
5.31	Gradient for visco-acoustic modeling and acoustic inversion for receivers line in $z = 1990[\text{m}]$	107
5.32	Phase difference for acoustic modeling and acoustic inversion for receivers line in $z = 1990[\text{m}]$	108
5.33	Phase difference for visco-acoustic modeling and visco-acoustic inversion for receivers line in $z = 1990[\text{m}]$	108
5.34	Phase difference for visco-acoustic modeling and acoustic inversion for receivers line in $z = 1990[\text{m}]$	108
5.35	Phase difference for acoustic modeling and acoustic inversion for receivers line in $z = 1990[\text{m}]$	109
5.36	Phase difference for visco-acoustic modeling and visco-acoustic inversion for receivers line in $z = 1990[\text{m}]$	109
5.37	Phase difference for visco-acoustic modeling and acoustic inversion for receivers line in $z = 1990[\text{m}]$	109
5.38	Gradient for acoustic modeling and acoustic inversion	110
5.39	Gradient for visco-acoustic modeling and visco-acoustic inversion	110
5.40	Final velocity for visco-acoustic modeling and visco-acoustic inversion.	112
5.41	Final velocity for visco-acoustic modeling and visco-acoustic inversion.	112
5.42	Phase difference for visco-acoustic modeling and visco-acoustic inversion	113
5.43	Phase difference for visco-acoustic modeling and visco-acoustic inversion	113

INTRODUCTION

Seismic exploration consists in the generation of mechanical waves using an artificial source such that waves propagate through the subsurface. With this the responses (reflections and refractions) are detected and recorded by a number of receiving stations for posterior processing. From the study of recorded data, one can obtain subsurface images, which are then related to the geological layers, seismic sections, velocity fields, and other physical properties that are important parameters for seismic exploration (Florez, 2004).

Since 1845 different theories, methods and techniques have been developed to improve the acquisition and processing of the data obtained in the seismic exploration, whose objective is to characterize an area of interest using these final data to deduce parameters the medium through which the waves have propagated, such as velocity, density, permittivity, etc. Seismic tomography is one of the main reconstruction techniques of these physical properties that affect the propagation of the seismic waves and mathematically raises an **inverse problem** (Angeles and Coss, 2005).

The wave propagation in the sub-surface, can be carried out solving a **direct problem**, where we assume to know the structure and properties of the subsoil and we propose equations using the physics of wave propagation to be able to model, in that medium, with the hope of reproducing our observations. In seismic tomography, however, the observed data are used to infer the structure of the subsurface, again using propagation physics of the wave, but now in combination with an **inverse problem** (Thurber and Ritsema, 2007). That is, the inverse problem is solved by comparing the data predicted by the direct problem solved with initial values for the parameters of the model, with the data observed. This comparison allows to update the proposed parameters and the process is repeated until the estimated parameters produce predicted data are close to the observed data. So, the first step to solve the **inverse problem** is to define the **direct problem**.

To be clear in terminology, we define **the model** as a mathematical abstraction that tries to reconstruct a process observed in nature, which is our direct problem. These mathematical relationships depend on a number of **model parameters**, which are identified by the so-called "physical constants", as well as one or several physical variables independent of the model. When

applying the model to these parameters generates a **model response** that corresponds to the solution found by a specific configuration of the model. According to this terminology, we will call the *function* G the operator that represents **the model** and relates the data or **response of the model \mathbf{d}** with the **parameters \mathbf{m}**

$$\mathbf{d} = G(\mathbf{m}) \rightarrow \tilde{G}(\mathbf{d}) = \hat{\mathbf{m}}. \quad (1.1)$$

The relation $\mathbf{d} = G(\mathbf{m})$ is known as **direct problem**, while $\tilde{G}(\mathbf{d}) = \hat{\mathbf{m}}$ would represent the **inverse problem**, with \tilde{G} being the inverse transformation of G . Unfortunately finding an inverse model, \tilde{G} , is not easy and possible in most cases. For this, an inversion scheme is used, where a synthetic data or calculated data \mathbf{d}_{calc} is generated through a model and initial values for the parameters, then compared with the observed data \mathbf{d}_{obs} in search for a model that minimizes the difference between \mathbf{d}_{obs} and \mathbf{d}_{calc} . Seismic tomography consists in obtaining the model parameters of the sub-surface $\hat{\mathbf{m}}$ through an inversion process that relates comparison between models $\mathbf{d}_{calc}(\mathbf{m})$ and observed data \mathbf{d}_{obs} , minimizing the misfit function

$$\begin{aligned} \chi(\mathbf{m}) &= \frac{1}{2} \|\delta \mathbf{d}\|_2^2 = \frac{1}{2} \delta \mathbf{d}^T \delta \mathbf{d} = \frac{1}{2} \left[\sum_{i=1}^M \delta d_i^2 \right] \\ &= \frac{1}{2} [\mathbf{d}_{obs} - G(\mathbf{m})]^T [\mathbf{d}_{obs} - G(\mathbf{m})]. \end{aligned} \quad (1.2)$$

The objective is minimize $\chi(\mathbf{m})$ through variations in the parameters \mathbf{m} of the model, variations defined by minimization methods that may be linear, slightly non-linear, quasi-linear or non-linear, depending on the direct problem.

But the modeling of wave propagation in real sub-surface is a complex task, physics is complicated and several simplifying approximations have to be made, however a closer model to the real propagation of the seismic wave model, means a more appropriate method to use when nonlinearity in the relationship between the model parameters and data, and the parameters vary markedly with the coordinates. (Fichtner, 2011a)

In particular, the realistic modeling of wave propagation is an important step in the process used for imaging earth subsurface. Currently, one of the most powerful and novel techniques of seismic tomography that uses solutions of the wave equation is the so called Full Waveform Inversion (FWI) (Fichtner, 2011a). The seismic tomography is called **Full Waveform Inversion** when the model is a full numerical solution of the equation of wave motion.

However, the estimation of these parameters is not easy. There is an extensive list of authors dealing with the study of inverse methods to solve inverse problems, all agree on their difficulty because the information received may be imprecise, insufficient or inconsistent (Jackson, 1979). The direct problem, using wave propagation equations, **is nonlinear**, because of the problem becomes more difficult to invert and certain restrictive methods have to be applied in order to obtain solutions that do not require an exaggerated use of computing resources.

So, the first step is to understand and emulate the complex wave phenomena in a realistic heterogeneous medium. For this, it is necessary a seismic modeling where the result is a wavefield obtained through the numerical solution of the wave equation. Acoustic wave propagation is the simplest modeling approximation, followed by the second simplifying approximation, isotropy. However in order to get precise information about the physical properties of the sub-surface, the better we model the propagation of waves, the better the result of the understanding of the properties of the medium. Although the acoustic approach has been very successful so far in the modeling of wave propagation in the sub-surface, the Earth is not totally elastic, neither totally viscous and a combination of both extreme behaviours should fit the properties of wave propagation.

The visco-acoustic media can be defined as a medium without cross propagation but exhibits attenuation in the amplitude of the longitudinal wave, this media presents two phenomena, dissipation, produced by energy absorption such that wave amplitude is reduce especially at high frequency and dispersion, by the change in the density, where the wave velocity depends the frequency (Wang, 2009).

To describe the attenuation of seismic wave front energy (Carcione et al., 2002) proposed a model based in linear solid material rheology and memory variables. They show how the use of memory variables describes the propagation of waves in the medium and accounts for attenuation of the energy of the propagating waves at large distances from the source. Latter, (Dutta et al., 2013) have used the same modeling approach, however, using only one relaxation mechanism, they show how the method works to compensate for attenuation in least-squares reverse time migration.

In (Huazhong and Libin, 2003) they used a visco-acoustic wave equation to compensate for the energy decrease of wave propagation in a realistic media using an extrapolator based in the propagator of the wave equation in the forward and backward direction. They show that using a Q-based attenuation model it is possible to fully describe the propagation of waves in the visco-acoustic media. In (Suh et al., 2012) have used visco-acoustic modeling into an anisotropic medium to compensate for attenuation in RTM migration. While (Yang and Liu, 2014) present a detailed comparison of different visco-acoustic wave equations and studied their dissipation and dispersion properties, providing a rough idea about how the most commonly used visco-acoustic wave equations perform.

Visco-acoustic modeling have been implemented also in 3D high computing demand simulations (Brossier et al., 2010), (Operto et al., 2007a) and has also been used in the development of specific geometrical configurations (TTI) (Operto et al., 2007b) exhibiting accurate descriptions of the wave propagation in the media.

As it can be seen, it is still important to study this kind of problems. Commonly the size of the computational problem is one of the principal drawbacks. Since high accuracy is required and therefore, large matrix systems are involved, which introduces expensive constraints from the technical point of view. The goal then is to look for methods that at the same level of adjust provide high quality solutions that offer the opportunity to explode the computational power available to

date. Not to mention the necessity to introduce multi-source modeling in more realistic media.

Now, seismic waveform inversion has been studied during the last decade in both the time and frequency domain. In (Lailly, 1983) and (Tarantola, 1984) they propose for waveform inversion the use of the acoustic wave, gradient of the misfit function (see Ec. 1.2) as a correlation between forward and backward propagation, as done in some migration algorithms, (Pratt and Worthington, 1990) and (Pratt, 1990) which applied the same idea but in the frequency domain. Since then, several inversion strategies have been worked out to determine the appropriate step and to minimize the misfit function.

In (Pratt and Hicks, 1998) and (Fichtner, 2011a), the most commonly used methods are compiled for working with low linearity inverse problems: Gauss-Newton and Full Newton, which propose to define the descent step by means of the gradient and the Hessian of the misfit function and suggest the use of the adjoint method as an alternative to find the variations of the calculated data with respect to the parameters of the model, as described in (Plessix, 2006).

In 2001, (Hicks and Pratt, 2001) propose a two-step inversion procedure using local descent methods, applying this approach to shallow seismic data from the North Sea collected over a gas-sand deposit. In this work they propose to work the attenuation using the quality factor Q . Other works for waveform inversion in frequency domain are for instance (Shin and Cha, 2008), where they explode the wavefield in the Laplace domain, that is equivalent to the zero frequency component of the damped wavefield. In (Kim et al., 2009) they recover P-wave and S-wave velocity and density models using coupled Acoustic-Elastic equation and in the work present in (Tao and Sen, 2013), they propose a scattering-integral approach, where a gradient is calculated with data-weighted Frechet kernel which involves calculation of Green's functions.

This work focuses on the propagation of mechanical waves in a medium with explicit attenuation modelled through the damping functions and quality Q factor. Frequency domain is adopted in this work since it involves the study of effects of the modeling (attenuation, dispersion) on individual wave frequencies. We pay especial attention to the quality of the solution and provide results of the implementation of optimal mixed-grid scheme looking for minimization of the numerical dispersion in the implementation. Instead of modeling explicitly the elastic and viscous excitation modes (Carcione et al., 2002), we model the dissipative effect of the medium explicitly through damping functions that attenuate the wave amplitude according to the quality factor of the media for different frequencies. We also tested a simple inversion scheme, finding the gradient of the mismatch function using the attached method and virtual sources, optimizing the descent step (Pratt and Hicks, 1998), (Plessix, 2006) to find the velocity model related to the observed data, in this case, from an initial model.

In the second chapter of this work we present all the physical and mathematical formalism, we present the formulation of our visco-acoustic wave equation and attenuation modeling. In chapter 3 we present the numerical techniques, the implementation of the mixed grid technique and the optimization performed to minimize dispersion in the visco-acoustic case. In chapter 4 we present the results, the analysis of numerical dispersion, and the performance of the attenuation models for different velocity profiles. In chapter 5 we present the mathematical formalism for inversion

problem, adjoint method, virtual source and optimization by the descent step. Finally, in chapter 6 we present the results, analysis of the application the FWI in the synthetic data, followed by our concluding remarks and conclusions.

MODELING VISCO-ACOUSTIC WAVE EQUATION

So, as mentioned in the previous chapter, the first part for the inversion is the definition of the direct problem. The model is an important part of the problem that allows the calculation of the synthetic data $\mathbf{d}_{calc}(\mathbf{m})$ to be compared with the observed data \mathbf{d}_{obs} and allow us to estimate model parameters $\hat{\mathbf{m}}$ by minimizing an objective function, $\chi(\mathbf{m}) \rightarrow \|\mathbf{d}_{obs} - \mathbf{d}_{calc}(\mathbf{m})\|^2$ (see Ec. 1.2), such that $\forall \mathbf{m} \neq \hat{\mathbf{m}} \quad \chi(\hat{\mathbf{m}}) < \chi(\mathbf{m})$.

Since, our problem is related with a Full Waveform Inversion for wave propagation in the visco-acoustic medium, then the direct problem should describe wave propagation in a continuous medium, in our case a dissipative one. Once we have the differential equations that describe the situation, we will use the method of finite differences to solve this equations. In this chapter we present a summary of the physical formulation of the problem, definitions and modeling for the damping function and we arrive to the equation of motion we solve with finite difference scheme.

2.1 Wave propagation in viscous medium

To describe the physical phenomenon, it is necessary to take into account the basic principles of propagation of waves in a continuous medium and must define a governing equation, in order to define the system response to disturbances for a given material. The wave propagation rests on its foundations in mechanics of the continuum medium and in order to formulate the problem we need to state a set of basic equations that describe the motion of the medium and the perturbations propagating inside it. Let consider a medium with density $\rho(\mathbf{x}, t)$ and volume V . In such a medium particles can move (displace) by it from their equilibrium configuration with velocity $\mathbf{v}(\mathbf{x}, t)$, such that the principle of mass conservation is described by

$$\left(\frac{\partial}{\partial t} + \mathbf{v}(\mathbf{x}, t) \cdot \nabla \right) \rho(\mathbf{x}, t) + \rho(\mathbf{x}, t) \nabla \cdot \mathbf{v}(\mathbf{x}, t) = 0. \quad (2.1)$$

Equation (2.1) states the conservation of mass, so we are assuming no flow in the fluid medium. Now, to describe the motion of particles, we use linear and angular momentum. The

linear momentum, $\mathbf{P}_{\text{lin}}(t)$, of the body is gives by

$$\mathbf{P}_{\text{lin}}(t) = \int_V \rho(\mathbf{x}, t) \mathbf{v}(\mathbf{x}, t) dV. \quad (2.2)$$

And angular momentum, $\mathbf{L}(t)$, is gives by

$$\mathbf{P}_{\text{ang}}(t) = \int_V \mathbf{x} \times \rho(\mathbf{x}, t) \mathbf{v}(\mathbf{x}, t) dV. \quad (2.3)$$

The principle of conservation of linear momentum states that the rate of change of the linear momentum is equal to the resultant force acting on the body and the principle of angular momentum states that the rate of change of momentum of a body with respect to a given point is equal to the moment of the surface and body forces with respect to that point (Mase and Mase, 1999). With this, we have:

$$\rho(\mathbf{x}, t) \left(\frac{\partial}{\partial t} + \mathbf{v}(\mathbf{x}, t) \cdot \nabla \right) \mathbf{v}(\mathbf{x}, t) = \nabla \cdot \boldsymbol{\sigma}(\mathbf{x}, t) + \mathbf{f}(\mathbf{x}, t), \quad (2.4)$$

$$\int_V \epsilon_{ijk} \sigma_{jk}(\mathbf{x}, t) dV = 0. \quad (2.5)$$

Eqs. (2.2) and (2.3) area an statement of linear and angular momentum conservation. Where $\boldsymbol{\sigma}$ is the stress tensor, \mathbf{f} represents the body forces, ϵ_{ijk} is the Lev-Civita tensor.

The principles described above are applicable to any medium and under a body force. To complete our system we need a relationship that defines the internal behavior of the medium, for closure one requires an equation of state, eq. (2.6), or governing equation that relates the intrinsic properties of the medium with its dynamical variables. In the case of linear solids it is written as

$$\sigma_{ij} = \varepsilon_{kl}(\mathbf{x}, t) \otimes \frac{\partial}{\partial t} C_{ijkl}(\mathbf{x}, t). \quad (2.6)$$

Where C is the elastic tensor, ε is the strain tensor and \otimes is the convolution operator. Eq. (2.6) indicates that we assume that $\boldsymbol{\sigma}$ depends linearly on the history of the strain tensor $\varepsilon(\mathbf{x}, t) = \frac{1}{2} (\nabla \mathbf{u}(\mathbf{x}, t) + \nabla \mathbf{u}^T(\mathbf{x}, t))$, where $\mathbf{u}(\mathbf{x}, t)$ is the particle displacement (Mase and Mase, 1999). The linear elasticity in the solids, indicates that the deformation and internal stresses of the body are linearly related, which is an approximation commonly used and which is restricted to the case that the material deforms infinitesimally. The strain tensor $\varepsilon(\mathbf{x}, t)$ represent the infinitesimal strain, a linear approximation to the Lagrangian strain tensor \mathbf{E} and is related with the strain tensor (internal forces) $\boldsymbol{\sigma}$ linearly, by means of the elastic tensor (Mase and Mase, 1999).

Now, for the simpler situation of an acoustic medium the wave propagation is longitudinal, such that oscillation of the particles is parallel to the direction of wave propagation then, there is no shear waves. If we assume that the medium have the following properties:

- Irrotational: $\nabla \times \mathbf{v} = 0$
- Compressible: $\nabla \cdot \mathbf{v} \neq 0$

- The flow is approximately constant $\nabla \cdot (\mathbf{v}\rho) \approx 0$
- And $\frac{\partial u_i}{\partial x_j} = 0$ if $i \neq j$

We can reduce the governing equation (2.6) to

$$\sigma_{ij}(\mathbf{x}, t) = \nabla \cdot \mathbf{u}(\mathbf{x}, t) \otimes M(\mathbf{x}, t) \delta_{ij}. \quad (2.7)$$

Where δ_{ij} is a kronecker delta and $M(\mathbf{x}, t)$ is the time derivative of the elastic tensor $\mathbf{C}(\mathbf{x}, t)$ often named complex bulk module (Fichtner, 2011a). $M(\mathbf{x}, t)$ accounts for the elastic and dissipative properties of the medium.

On the other hand, for a visco-acoustic medium one can arrive to a relation between the stress tensor $\sigma(\mathbf{x}, t)$ and the pressure field of a perturbation $p(\mathbf{x}, t)$ (pressure wave):

$$\sigma_{ij}(\mathbf{x}, t) = -p(\mathbf{x}, t) \delta_{ij}. \quad (2.8)$$

2.2 Damping Functions

Using equations (2.7) and (2.8) one can arrive to Hooke's law

$$p(\mathbf{x}, t) = -\nabla \cdot \mathbf{u}(\mathbf{x}, t) \otimes M(\mathbf{x}, t). \quad (2.9)$$

Where \otimes is convolution operator. And combining (2.4), (2.5) one can get second Newton's law.

$$\left(\frac{\partial}{\partial t} + \gamma(\mathbf{x}) \right) \mathbf{v}(\mathbf{x}, t) = \frac{1}{\rho(\mathbf{x})} (\nabla \cdot \sigma(\mathbf{x}, t) + \mathbf{f}(\mathbf{x}, t)). \quad (2.10)$$

Where $\gamma(\mathbf{x})$ is called the rate deformation function, such that it represents the temporal variation of the strain tensor and is related to the viscosity of the medium. It is noticeable that this balance of forces in the equation (2.8) is similar to the balance of forces for a damped harmonic oscillator, where $\gamma(\mathbf{x})$ it is an important term in the relation of energy stored and energy lost per cycle (Wang, 2009).

Applying a Fourier transform in the temporal variables to eqs. (2.7) and (2.8) and making some arrangements we have

$$-i\omega P(\omega, \mathbf{x}) = M(\omega, \mathbf{x}) \nabla \cdot \mathbf{V}(\omega, \mathbf{x}), \quad (2.11)$$

$$i\omega \mathbf{V}(\omega, \mathbf{x}) = -\frac{b(\mathbf{x})}{\xi(\omega, \mathbf{x})} \nabla P(\omega, \mathbf{x}) + \frac{b(\mathbf{x})}{\xi(\omega, \mathbf{x})} \mathbf{F}(\omega, \mathbf{x}). \quad (2.12)$$

Where $P(\omega, \mathbf{x})$, $M(\omega, \mathbf{x})$, $\mathbf{V}(\omega, \mathbf{x})$, $\mathbf{F}(\omega, \mathbf{x})$ are the Fourier transform the $p(\mathbf{x}, t)$, $M(\mathbf{x}, t)$, $\mathbf{v}(\mathbf{x}, t)$, $\mathbf{f}(\mathbf{x}, t)$ respectively. The Fourier transform used in this work have the following definition:

$$\tilde{f}(\omega) = \int_{-\infty}^{\infty} f(t)e^{-i\omega t} dt.$$

In eq. (2.12) $\xi(\omega, \mathbf{x}) = 1 - i\frac{\gamma(\mathbf{x})}{\omega}$, is the damping function and $b(\mathbf{x}) = \frac{1}{\rho(\mathbf{x})}$, is the bouyancy of the medium.

The propagation of waves in a visco-acoustic medium presents both dissipation and dispersion. These effects are modeled using the damping functions, $\xi(\omega, \mathbf{x})$ so that the attenuation occurs, and since the realistic situation implies dispersion in the medium, this damping must be modeled as a frequency dependent process.

The complex bulk modulus $M(\omega, \mathbf{x})$ must be related to $\xi(\omega, \mathbf{x})$ subject to the constraint that when no dissipation $M(\omega, \mathbf{x}) \rightarrow K(\mathbf{x})$, where $K(\mathbf{x})$ is an acoustic bulk modulus (Carcione et al., 2002). The complex bulk modulus, in time domain, accounts for the acoustic and dissipative properties of the medium and is the time derivative of the elastic tensor $C(t, \mathbf{x})$.

If the medium is acoustic but no viscous, $C(t, \mathbf{x}) \rightarrow C(\mathbf{x})$, such that the equations 2.9 and 2.10 reduce to the equation for acoustic medium, where the governing equation 2.7 is $\sigma_{ij}(\mathbf{x}, t) = \nabla \cdot \mathbf{u}(\mathbf{x}, t)K(\mathbf{x})\delta_{ij}$, where $K(\mathbf{x}) = \frac{1}{c(\mathbf{x})^2\rho(\mathbf{x})}$, with $c(\mathbf{x})$ as velocity wave propagation.

Now we define

$$M(\omega, \mathbf{x}) = K(\mathbf{x})\alpha(\omega, \mathbf{x}), \quad (2.13)$$

where $\alpha(\omega, \mathbf{x}) = \alpha_r(\omega, \mathbf{x}) + i\alpha_i(\omega, \mathbf{x})$, with α complex, α_r and α_i real and imaginary part, α represent the viscosity in the media, such that is related with $\gamma(\omega, \mathbf{x})$ and $\xi(\omega, \mathbf{x})$. To establish a relation between α and ξ we combine the equations (2.9) and (2.10) in the homogeneous case, with $\rho = cte$, $c = cte$ and $\gamma = cte$ and obtain:

$$\left(\frac{\xi}{\alpha} k^2 + \nabla^2 \right) P = \nabla \cdot \mathbf{F}. \quad (2.14)$$

Where $k = \frac{\omega}{c}$ is the wave-number, P is the pressure field in the frequency domain, and F is the external body force. Now Equation (2.12) reduces to the acoustic wave equation in frequency domain, if $\gamma = 0$, which is equivalent, $\xi = 1$, such that α must be $\alpha = 1$.

But, if we assume that $\alpha \sim \xi$, Equation (2.12) reduces to the familiar acoustic wave equation if the proportion is a real number, which would physically mean that the pressure field is not attenuated, but change its wave-number, as if the viscosity changes the velocity of the wave but the propagation is acoustic. This does not make much sense, the attenuation of the pressure field can be represented as propagation in an acoustic medium with a lower wave velocity but not the dispersion, which is the change of velocity with frequency.

Another possible relation between α and ξ , is that they are inversely proportional, $\alpha \sim \frac{1}{\xi}$. Since $\alpha = \frac{1}{\xi}$ then the equation is recast as

$$(\tilde{k}^2 + \nabla^2)P = \nabla \cdot \mathbf{F}. \quad (2.15)$$

Equation (2.13) is the Helmholtz equation with complex coefficients, where \tilde{k} is called complex wave number. The real part of \tilde{k} is $\frac{\omega}{c}$, the conventional wave number, and the imaginary part $\frac{\gamma}{c}$ is the pseudo wave number. This concept is applied in attenuation-dispersion models related to the quality factor Q . In other words, we can relate our damping function $M(\omega, \mathbf{x})$ with the models of attenuation and dispersion, in this way it allows us to propose damping functions that have an actual relationship with the properties of the medium we want to model.

According to this, we can define

$$M(\omega, \mathbf{x}) = \frac{K(\mathbf{x})}{\xi(\omega, \mathbf{x})}. \quad (2.16)$$

2.3 Equation of propagation in a viscoacoustic medium

Then, the equation for wave propagation in our visco-acoustic medium can be obtained combining equations (2.9), (2.10) and (2.12) as

$$\frac{\omega^2 P(\omega, \mathbf{x})}{K(\mathbf{x})} + \frac{1}{\xi(\omega, \mathbf{x})} \nabla \cdot \left(\frac{b(\mathbf{x})}{\xi(\omega, \mathbf{x})} \nabla P(\omega, \mathbf{x}) \right) = \frac{1}{\xi(\omega, \mathbf{x})} \nabla \cdot \left(\frac{b(\mathbf{x})}{\xi(\omega, \mathbf{x})} \mathbf{F}(\omega, \mathbf{x}) \right). \quad (2.17)$$

In this situation we have the freedom to choose the way we model the attenuation. For example, using the models described in (Wang, 2009), where they define the wavenumber as $k(\omega) = \frac{\omega}{c(\omega)} = \frac{\omega}{\nu(\omega)} - i\kappa(\omega)$ (in the book called $\alpha(\omega)$), where $c(\omega)$ is the complex velocity, $\nu(\omega)$ the phase velocity and $\kappa(\omega)$ the attenuation wavenumber, rewriting in terms of ξ , it looks like

$$\xi(\omega, \mathbf{x}) \cong \frac{c}{\nu(\omega)} + i \frac{\kappa(\omega)c}{\omega} \approx 1 - i \frac{\kappa(\omega)c}{\omega}.$$

Where $\nu(\omega) \sim c$. According to this we decided to study three different attenuation-dispersion models:

1. Kolsky's (Modified):

$$\kappa(\omega, \mathbf{x}) = \frac{|\omega|}{2Q(\mathbf{x})c(\mathbf{x})}, \quad (2.18)$$

$$\frac{1}{\nu(\omega, \mathbf{x})} = \frac{1}{c(\mathbf{x})} \left(1 - \frac{1}{\pi Q(\mathbf{x})} \ln \left| \frac{\omega}{\omega_h} \right| \right). \quad (2.19)$$

Where ω_h is the highest possible seismic frequency, about 1000π Hz. From Eq. 2.19 we can say that $\frac{c}{\nu(\omega, \mathbf{x})} = 1 - f_1(\omega)$, now for $\omega = [2\pi, 1000\pi]$ Hz and $Q = [30, 650]$, $f_1(\omega) \sim [-0.06, 0]$, the term $\frac{c}{\nu(\omega, \mathbf{x})} \sim [1.06, 1.0]$ So, the damping function can be written as:

$$\xi(\omega, \mathbf{x}) = 1 - f_1(\omega) - i \frac{1}{2Q(\mathbf{x})} \approx 1 - i \frac{1}{2Q(\mathbf{x})}. \quad (2.20)$$

2. Cole-Cole attenuation model

$$\kappa(\omega, \mathbf{x}) = \frac{\omega\beta(\tau)^{1+\beta} \sin\left(\frac{\pi\beta}{2}\right)}{\tau v_0 Q_c \left[1 + (2\tau)^\beta \cos\left(\frac{\beta\pi}{2}\right) + (\tau)^{2\beta}\right]}, \quad (2.21)$$

$$\frac{1}{\nu(\omega, \mathbf{x})} = \frac{1}{v_0} \left(1 - \frac{\beta(\tau)^{1+\beta} \left[\cos\left(\frac{\pi\beta}{2}\right) + (\tau)^{1+\beta}\right]}{Q_c \left[1 + (2\tau)^\beta \cos\left(\frac{\beta\pi}{2}\right) + (\tau)^{2\beta}\right]}\right), \quad (2.22)$$

$$\tau = \left|\frac{\omega}{\omega_h}\right|; \quad \mu(\mathbf{x}) = \frac{1}{\pi Q(\mathbf{x})};$$

$$\frac{1}{v_0} = \frac{1}{c(\mathbf{x})} \left(\frac{\tau}{2Q(\mathbf{x})} + \tau^{-\mu(\mathbf{x})}\right); \quad Q_c = \frac{1 + 2Q(\mathbf{x})\tau^{-(1+\mu(\mathbf{x}))}}{1 + \tau^{-2}}.$$

Where β is a constant in the range $[0, 1]$, in (Wang, 2009), to compare the Cole-Cole model with the Kolsky model they use the approach $Q_c \sim \frac{\beta^2}{4} \pi Q(\mathbf{x})$ and $\frac{1}{v_0} \sim \frac{1}{c(\mathbf{x})} \left(1 + \frac{\mu(\mathbf{x})}{\beta}\right)$ such that they obtain the figure:

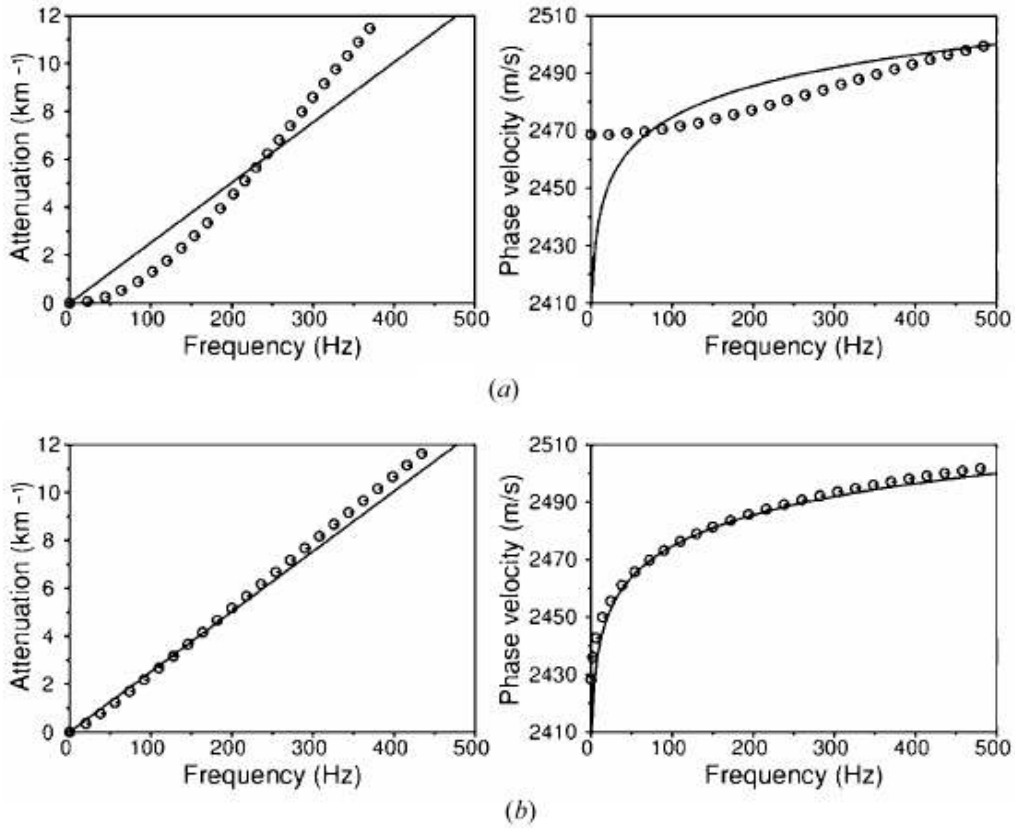


Figure 2.1: The attenuation and the phase velocity in the Cole-Cole model (circled lines) with a) $\beta = 1.0$ and b) $\beta = 0.4$, compared with those in the Kolsky model (solid lines). Modified figure of (Wang, 2009)

So, with this approach the damping function is:

$$\xi(\omega, \mathbf{x}) \approx 1 - i\beta \frac{4 \left[1 + \frac{1}{\pi\beta} Q(\mathbf{x}) \right] (\tau)^{1+\beta} \sin\left(\frac{\pi\beta}{2}\right)}{\tau\beta^2\pi Q(\mathbf{x}) \left[1 + (2\tau)^\beta \cos\left(\frac{\beta\pi}{2}\right) + (\tau)^{2\beta} \right]}. \quad (2.23)$$

3. General linear model

$$\kappa(\omega, \mathbf{x}) = \frac{1}{c_\infty} \left[\frac{a}{2} \left(1 + \frac{\omega^2\tau^2}{2} \right) + b \right] \frac{\omega^2\tau^2}{(1 + \omega^2\tau^2)}, \quad (2.24)$$

$$\frac{1}{\nu(\omega, \mathbf{x})} = \frac{1}{c_\infty} \left\{ 1 + \left[a \left(1 + \frac{5\omega^2\tau^2}{8} \right) + b \right] \frac{1}{(1 + \omega^2\tau^2)} \right\}. \quad (2.25)$$

Where τ is a constant denoting the relaxation time, $v_\infty = \mu(\omega \rightarrow \infty)$, a and b are coefficients that depend on the quality factor $Q(\mathbf{x})$. To compare the General linear model with the Kolsky model use the approach $v_\infty = c(\mathbf{x})$, $\tau = \omega_h^{-1}$ and $a = -\frac{8}{7Q(\mathbf{x})}$ and $b = \frac{13}{7Q(\mathbf{x})}$ such that we obtain the following figures:

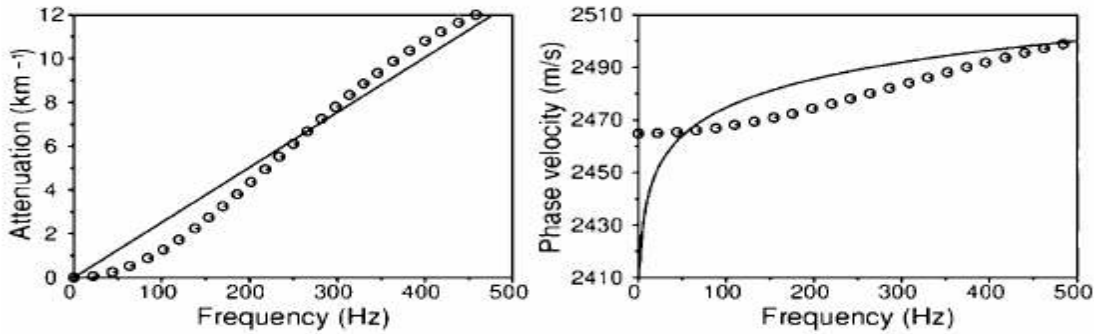


Figure 2.2: The attenuation and the phase velocity in the General model (circled lines) compared with those in the Kolsky model (solid lines). Modified figure of (Wang, 2009)

So, with this approach the damping function is:

$$\xi(\omega, \mathbf{x}) \approx 1 - i \left[\frac{13}{7Q(\mathbf{x})} - \frac{4}{7Q(\mathbf{x})} \left(1 + \frac{\omega^2\tau^2}{2} \right) \right] \frac{\omega\tau^2}{(1 + \omega^2\tau^2)}. \quad (2.26)$$

Now, in (B. and T., 2002), they present results of the comparison of the difference into plane-wave propagation with Kolsky, Cole-Cole and the General Model for the same set of parameters. The difference is more remarkable with Cole-Cole model, in this case, they use $\beta = 0.1$, the attenuation is much smaller than the one produced with Kolsky model.

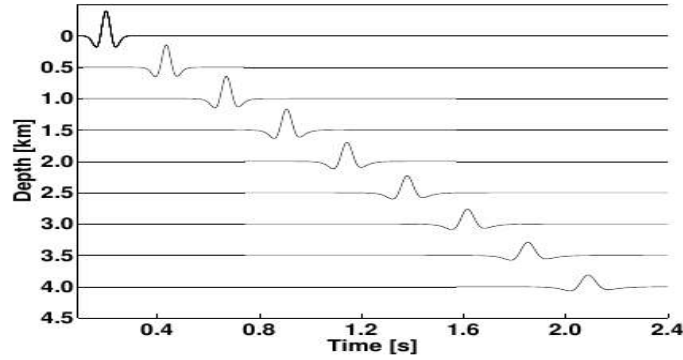


Figure 2.3: Plane-wave propagation with Kolsky Model. Modified figure of (B. and T., 2002)

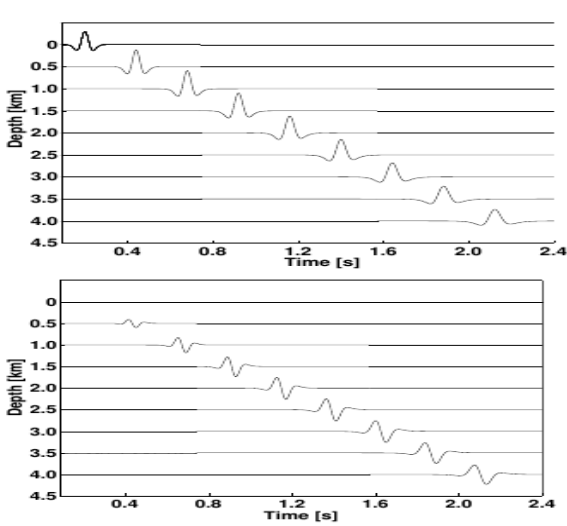


Figure 2.4: Plane-wave propagation with Cole-Cole Model (top), difference with Kolsky model (bottom). Modified figure of (B. and T., 2002)

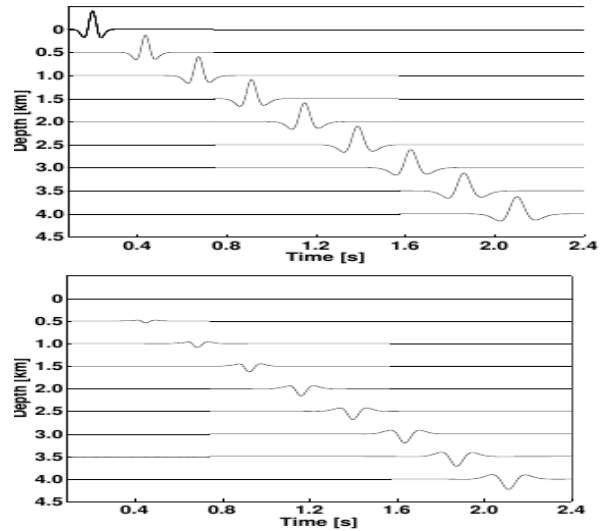


Figure 2.5: Plane-wave propagation with General Model (top), difference with Kolsky model (bottom). Modified figure of (B. and T., 2002)

2.4 Equation of propagation in other media

In order to make a complete analysis, consider the cases where $\rho = \text{cte}$ or $\gamma = 0$ in the eq. 2.14 and obtain the equations for the propagation of a wave in the following media:

- An Acoustic medium with constant density ($\rho = \text{cte}$ and $\gamma = 0$). In the acoustic case σ is zero, a the medium is no viscous. If the density is also constant in space, we have the acoustic equation:

$$\frac{\omega^2 P(\omega, \mathbf{x})}{c^2(\mathbf{x})} + \nabla^2 P(\omega, \mathbf{x}) = \nabla \cdot \mathbf{F}(\omega, \mathbf{x}). \quad (2.27)$$

This equation represents the wave propagation in the most ideal medium possible.

- Acoustic medium with variable density ($\rho = \rho(\mathbf{x})$ and $\gamma=0$). In the acoustic case σ is zero, the medium is not viscous. If the density is variable in space, we have the acoustic equation with variable density:

$$\frac{\omega^2 P(\omega, \mathbf{x})}{K(\mathbf{x})} + \nabla \cdot (b(\mathbf{x}) \nabla P(\omega, \mathbf{x})) = \nabla \cdot (b(\mathbf{x}) \mathbf{F}(\omega, \mathbf{x})). \quad (2.28)$$

- Visco-acoustic medium with constant density ($\rho = \text{cte}$ and $\gamma \neq 0$). In the visco-acoustic case σ is no zero, the medium is viscous. If the density is constant in space, we have the acoustic equation with constant density:

$$\frac{\omega^2 P(\omega, \mathbf{x})}{c^2(\mathbf{x})} + \frac{1}{\xi(\omega, \mathbf{x})} \nabla \cdot \left(\frac{1}{\xi(\omega, \mathbf{x})} \nabla P(\omega, \mathbf{x}) \right) = \frac{1}{\xi(\omega, \mathbf{x})} \nabla \cdot \left(\frac{1}{\xi(\omega, \mathbf{x})} \mathbf{F}(\omega, \mathbf{x}) \right). \quad (2.29)$$

Comparing the solutions of our modeling with simpler media we can get an image of the contribution of the presence of a variable density ρ or attenuation γ in the medium. By noting how the pressure field $P(\omega, \mathbf{x})$ changes when one of these conditions is present or not, we make sure that our approach and numerical solution match the expected conditions for the presence of these variables, decrease in the amplitude of the field or dispersion.

NUMERICAL SOLUTION AND TECHNIQUE

In general, obtaining a solution of equation (2.17) is not possible for arbitrary medium properties and boundaries. A natural approach is then to look for numerical solutions using e.g. finite differences. Assuming a 2D problem with coordinates $\mathbf{x} = (x, z)$ the problem in eq. (2.17) can be re-written as

$$-i\omega P(\omega, \mathbf{x}) = K(\mathbf{x}) \frac{1}{\xi(\omega, \mathbf{x})} \left(\frac{\partial V_x(\omega, \mathbf{x})}{\partial x} + \frac{\partial V_z(\omega, \mathbf{x})}{\partial z} \right) \quad (3.1)$$

$$i\omega V_x(\omega, \mathbf{x}) = -\frac{b(\mathbf{x})}{\xi(\omega, \mathbf{x})} \frac{\partial P(\omega, \mathbf{x})}{\partial x} + S_x(\omega, \mathbf{x}) \quad (3.2)$$

$$i\omega V_z(\omega, \mathbf{x}) = -\frac{b(\mathbf{x})}{\xi(\omega, \mathbf{x})} \frac{\partial P(\omega, \mathbf{x})}{\partial z} + S_z(\omega, \mathbf{x}) \quad (3.3)$$

Where $S_x(\omega, \mathbf{x}) = \nabla \cdot \left(\frac{b(\mathbf{x})}{\xi(\omega, \mathbf{x})} F_x(\omega, \mathbf{x}) \right)$ and $S_z(\omega, \mathbf{x}) = \nabla \cdot \left(\frac{b(\mathbf{x})}{\xi(\omega, \mathbf{x})} F_z(\omega, \mathbf{x}) \right)$

Although the finite difference method is widely used for solving differential equations, it has very well known problems of numerical dispersion that are related to the discretization of the media. To avoid these numerical problems (Jo, 1996) propose a scheme of two overlapping grids to solve the PDE. One of the grids has a conventional cartesian grid, and the second one is a rotated cartesian grid (see Fig. 3.1). In this kind of setup, the solution is obtained evaluating the fields in a total of 9 grid points, thus reducing the numerical dispersion and trying to cover all directions of propagation.

Another problem for the numerical solution are the boundary conditions. It is important to control the calculation in the workspace limit to prevent erroneous data within it, since at the border, if no correction is made, the value of the pressure field is taken as null, making the boundary a reflector. Let us name our workspace as $(\mathcal{U} = \forall(x, z) \in [x_{pml}, L_x + x_{pml}] \times [z_{pml}, L_z + z_{pml}])$ and we extend the workspace with $(\partial\mathcal{U} = \forall(x, z) \in [0, L_x + 2x_{pml}] \times [0, L_z + 2z_{pml}] \mid (x, z) \notin \mathcal{U})$ and used Perfectly-Matched-Absorbing (PML) boundary conditions (Berenger, 1994)(see Fig. 3.2). This

boundary conditions in frequency domain uses two damping function ξ_x and ξ_z which are related with ξ .

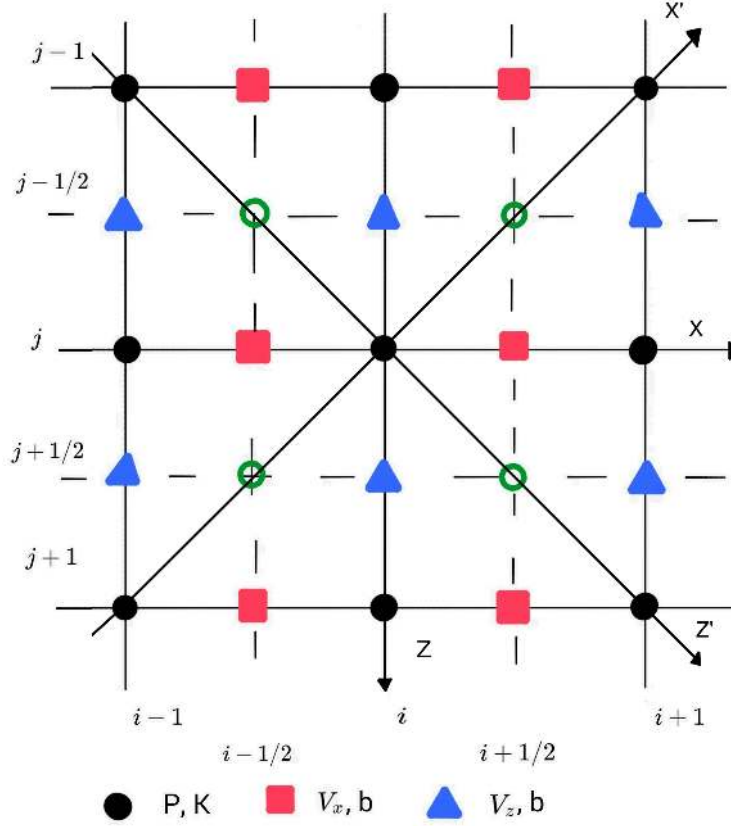


Figure 3.1: Illustration of the mixed grid used in the numerical solution. The black points represent the field pressure in the conventional grid, the triangular and square points represent the field particle velocity in the intercalated grid and the diagonals represent the axes for the rotated grid. The partial derivatives are computed for points in conventional grid and rotated grid, in total 9 points.

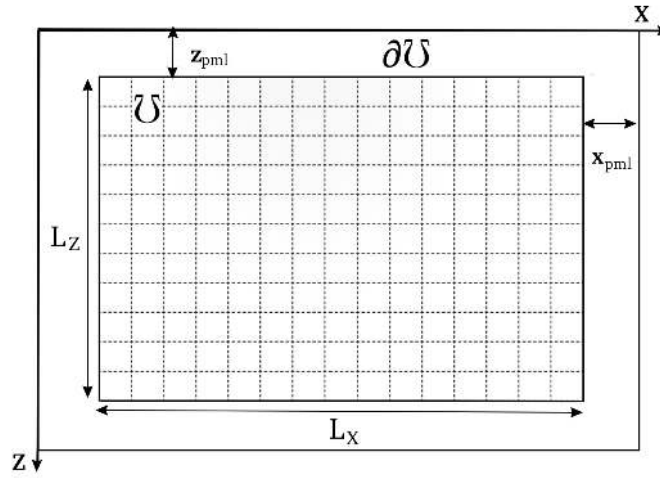
3.1 Conventional Grid

Then, using centered finite-difference for partial derivatives, in conventional grid, Eq. (3.1) is:

$$-i\omega P_{(i,j)}(\omega) = K_{(i,j)} \frac{1}{\xi_{(i,j)}(\omega)} \left(\left. \frac{\partial V_x(\omega, \mathbf{x})}{\partial x} \right|_{(i,j)} + \left. \frac{\partial V_z(\omega, \mathbf{x})}{\partial z} \right|_{(i,j)} \right). \quad (3.4)$$

And the derivatives of the function $\mathbf{V}(\mathbf{x}, \omega)$ are expressed as

$$\left. \frac{\partial V_x}{\partial x} \right|_{(i,j)} \approx \frac{1}{\Delta} (V_{x(i+1/2,j)} - V_{x(i-1/2,j)}), \quad (3.5)$$


 Figure 3.2: Workspace \mathcal{U} and boundary workspace $\partial\mathcal{U}$ for the numerical solution

$$\left. \frac{\partial V_z}{\partial z} \right|_{(i,j)} \approx \frac{1}{\Delta} (V_{z(i,j+1/2)} - V_{z(i,j-1/2)}). \quad (3.6)$$

Where Δ is the grid spacing and (i, j) refer to the index of the grid, $i = 1, 2, \dots, nx$ and $j = 1, 2, \dots, nz$. Now, for the eq. (3.2) and (3.3) we obtain

$$i\omega V_{x(m,n)}(\omega) = -\frac{b_{(m,n)}}{\xi_{(m,n)}(\omega)} \left. \frac{\partial P(\omega, \mathbf{x})}{\partial x} \right|_{(m,n)} + S_{x(m,n)}(\omega), \quad (3.7)$$

$$i\omega V_{z(m,n)}(\omega) = -\frac{b_{(m,n)}}{\xi_{(m,n)}(\omega)} \left. \frac{\partial P(\omega, \mathbf{x})}{\partial z} \right|_{(m,n)} + S_{z(m,n)}(\omega). \quad (3.8)$$

To solve eq. (3.5) using eq. (3.7) with $m = i + 1/2$ and $n = j$ for the first term and $m = i - 1/2$ and $n = j$ for the second term. In the same way, we solve eq. (3.6) using eq. (3.8) with $m = i$ and $n = j + 1/2$ for the first term and $m = i$ and $n = j - 1/2$ for the second term. While the derivatives of $P(\mathbf{x}, \omega)$ are given by

$$\left. \frac{\partial P}{\partial x} \right|_{(i+1/2,j)} \approx \frac{1}{\Delta} (P_{(i+1,j)} - P_{(i,j)}), \quad (3.9)$$

$$\left. \frac{\partial P}{\partial x} \right|_{(i-1/2,j)} \approx \frac{1}{\Delta} (P_{(i,j)} - P_{(i-1,j)}), \quad (3.10)$$

$$\left. \frac{\partial P}{\partial z} \right|_{(i,j+1/2)} \approx \frac{1}{\Delta} (P_{(i,j+1)} - P_{(i,j)}), \quad (3.11)$$

$$\left. \frac{\partial P}{\partial z} \right|_{(i,j-1/2)} \approx \frac{1}{\Delta} (P_{(i,j)} - P_{(i,j-1)}). \quad (3.12)$$

Using the above equations, we obtain:

$$i\omega \frac{\partial V_x}{\partial x} \Big|_{(i,j)} \approx \frac{1}{\Delta} \left(-\frac{b_{(i+1/2,j)}}{\xi_{(i+1/2,j)}(\omega)} \frac{\partial P(\omega, \mathbf{x})}{\partial x} \Big|_{(i+1/2,j)} + \frac{b_{(i-1/2,j)}}{\xi_{(i-1/2,j)}(\omega)} \frac{\partial P(\omega, \mathbf{x})}{\partial x} \Big|_{(i-1/2,j)} \right) + (S_{x(i+1/2,j)}(\omega) - S_{x(i-1/2,j)}(\omega)), \quad (3.13)$$

$$i\omega \frac{\partial V_z}{\partial z} \Big|_{(i,j)} \approx \frac{1}{\Delta} \left(-\frac{b_{(i,j+1/2)}}{\xi_{(i,j+1/2)}(\omega)} \frac{\partial P(\omega, \mathbf{x})}{\partial z} \Big|_{(i,j+1/2)} + \frac{b_{(i,j-1/2)}}{\xi_{(i,j-1/2)}(\omega)} \frac{\partial P(\omega, \mathbf{x})}{\partial z} \Big|_{(i,j-1/2)} \right) + (S_{z(i,j+1/2)}(\omega) - S_{z(i,j-1/2)}(\omega)). \quad (3.14)$$

Where $b_{(i\pm 1/2,j)} = \frac{b_{(i\pm 1,j)} + b_{(i,j)}}{2}$ and $b_{(i,j\pm 1/2)} = \frac{b_{(i,j\pm 1)} + b_{(i,j)}}{2}$, in the same way for $\xi_{(i\pm 1/2,j)}$, $\xi_{(i,j\pm 1/2)}$, $S_{x(i\pm 1/2,j)}$, $S_{x(i,j\pm 1/2)}$, $S_{z(i\pm 1/2,j)}$ and $S_{z(i,j\pm 1/2)}$. So, the solution in conventional grid is:

$$\frac{\omega^2 P_{(i,j)}}{K_{(i,j)}} + \frac{1}{\Delta \xi_{(i,j)}} \left(\frac{b_{(i+1/2,j)}}{\xi_{(i+1/2,j)}(\omega)} \frac{\partial P(\omega, \mathbf{x})}{\partial x} \Big|_{(i+1/2,j)} - \frac{b_{(i-1/2,j)}}{\xi_{(i-1/2,j)}(\omega)} \frac{\partial P(\omega, \mathbf{x})}{\partial x} \Big|_{(i-1/2,j)} \right) + \frac{1}{\Delta \xi_{(i,j)}} \left(\frac{b_{(i,j+1/2)}}{\xi_{(i,j+1/2)}(\omega)} \frac{\partial P(\omega, \mathbf{x})}{\partial z} \Big|_{(i,j+1/2)} - \frac{b_{(i,j-1/2)}}{\xi_{(i,j-1/2)}(\omega)} \frac{\partial P(\omega, \mathbf{x})}{\partial z} \Big|_{(i,j-1/2)} \right) = (S_{x(i+1/2,j)}(\omega) - S_{x(i-1/2,j)}(\omega) + S_{z(i,j+1/2)}(\omega) - S_{z(i,j-1/2)}(\omega)). \quad (3.15)$$

Now the source term $(S_{x(i+1/2,j)} - S_{x(i-1/2,j)} + S_{z(i,j+1/2)} - S_{z(i,j-1/2)})$ represents $S_{(i,j)}$. This is done for simplicity because we have a point source, normally a Ricker wavelet.

3.2 Rotated Grid

Now, for the rotated grid, using a rotation of 45° , we obtain the transformation rule for the derivatives in such system, then in the rotated system

$$\frac{\partial}{\partial x} = \frac{\sqrt{2}}{2} \left(\frac{\partial}{\partial x'} + \frac{\partial}{\partial z'} \right) \quad \frac{\partial}{\partial z} = \frac{\sqrt{2}}{2} \left(-\frac{\partial}{\partial x'} + \frac{\partial}{\partial z'} \right). \quad (3.16)$$

Such that the eq. (3.4) for the rotated grid is:

$$-i\omega P_{(i,j)}(\omega) = \frac{\sqrt{2}}{2} \frac{K_{(i,j)}}{\xi_{(i,j)}(\omega)} \left(\frac{\partial V_x(\omega, \mathbf{x})}{\partial x'} + \frac{\partial V_x(\omega, \mathbf{x})}{\partial z'} - \frac{\partial V_z(\omega, \mathbf{x})}{\partial x'} + \frac{\partial V_z(\omega, \mathbf{x})}{\partial z'} \right) \Big|_{(i,j)}. \quad (3.17)$$

And the centered finite-difference of partial derivatives, in the rotated grid of $\mathbf{V}(\mathbf{x}, \omega)$ are

$$\frac{\partial V_x}{\partial x'} \Big|_{(i,j)} \approx \frac{(V_{x(i+1/2,j-1/2)} - V_{x(i-1/2,j+1/2)})}{\sqrt{2}\Delta}; \quad \frac{\partial V_z}{\partial x'} \Big|_{(i,j)} \approx \frac{(V_{z(i+1/2,j-1/2)} - V_{z(i-1/2,j+1/2)})}{\sqrt{2}\Delta}; \quad (3.18)$$

$$\left. \frac{\partial V_z}{\partial z'} \right|_{(i,j)} \approx \frac{(V_{z(i+1/2,j+1/2)} - V_{z(i-1/2,j-1/2)})}{\sqrt{2}\Delta}, \quad \left. \frac{\partial V_x}{\partial z'} \right|_{(i,j)} \approx \frac{(V_{x(i+1/2,j+1/2)} - V_{x(i-1/2,j-1/2)})}{\sqrt{2}\Delta}. \quad (3.19)$$

Now, for the eq. (3.2) and (3.3) we obtain

$$i\omega V_{x(m,n)}(\omega) = -\frac{\sqrt{2}}{2} \frac{b_{(m,n)}}{\xi_{x(m,n)}(\omega)} \left[\left. \frac{\partial P(\omega, \mathbf{x})}{\partial x'} \right|_{(m,n)} - \left. \frac{\partial P(\omega, \mathbf{x})}{\partial z'} \right|_{(m,n)} \right] + S_{x(m,n)}(\omega), \quad (3.20)$$

$$i\omega V_{z(m,n)}(\omega) = \frac{\sqrt{2}}{2} \frac{b_{(m,n)}}{\xi_{z(m,n)}(\omega)} \left[\left. \frac{\partial P(\omega, \mathbf{x})}{\partial x'} \right|_{(m,n)} - \left. \frac{\partial P(\omega, \mathbf{x})}{\partial z'} \right|_{(m,n)} \right] + S_{z(m,n)}(\omega). \quad (3.21)$$

We redefine ξ to ξ_x for V_x and ξ_z for V_z such that we can apply an efficient absorbing boundary conditions PML, according to this $\xi_{x(m,n)} = \xi_{x(m,n+1)}$ and $\xi_{z(m,n)} = \xi_{z(m+1,n)}$. This aspect will be discussed later in section 3.6.

So, to solve eq. (3.18) using eq. (3.20) we set $m = i + 1/2$ and $n = j - 1/2$ for the first term and $m = i - 1/2$ and $n = j + 1/2$ for the second term. In the same way, to solve eq. (3.19) using eq. (3.21) we set $m = i + 1/2$ and $n = j + 1/2$ for the first term and $m = i - 1/2$ and $n = j - 1/2$ for the second term. While the derivatives of $P(\mathbf{x}, \omega)$ are

$$\left. \frac{\partial P}{\partial x'} \right|_{(i+1/2,j-1/2)} \approx \frac{1}{\sqrt{2}\Delta} (P_{(i+1,j-1)} - P_{(i,j)}); \quad \left. \frac{\partial P}{\partial z'} \right|_{(i+1/2,j-1/2)} \approx \frac{1}{\sqrt{2}\Delta} (P_{(i+1,j)} - P_{(i,j-1)}); \quad (3.22)$$

$$\left. \frac{\partial P}{\partial x'} \right|_{(i+1/2,j+1/2)} \approx \frac{1}{\sqrt{2}\Delta} (P_{(i+1,j)} - P_{(i,j+1)}); \quad \left. \frac{\partial P}{\partial z'} \right|_{(i+1/2,j+1/2)} \approx \frac{1}{\sqrt{2}\Delta} (P_{(i+1,j+1)} - P_{(i,j)}); \quad (3.23)$$

$$\left. \frac{\partial P}{\partial x'} \right|_{(i-1/2,j+1/2)} \approx \frac{1}{\sqrt{2}\Delta} (P_{(i,j)} - P_{(i-1,j+1)}); \quad \left. \frac{\partial P}{\partial z'} \right|_{(i-1/2,j+1/2)} \approx \frac{1}{\sqrt{2}\Delta} (P_{(i,j+1)} - P_{(i-1,j)}); \quad (3.24)$$

$$\left. \frac{\partial P}{\partial x'} \right|_{(i-1/2,j-1/2)} \approx \frac{1}{\sqrt{2}\Delta} (P_{(i,j-1)} - P_{(i-1,j)}); \quad \left. \frac{\partial P}{\partial z'} \right|_{(i-1/2,j-1/2)} \approx \frac{1}{\sqrt{2}\Delta} (P_{(i,j)} - P_{(i-1,j-1)}). \quad (3.25)$$

Using the above equations, we obtain:

$$\begin{aligned} i\omega \left. \frac{\partial V_x}{\partial x'} \right|_{(i,j)} &\approx -\frac{1}{2\Delta} \frac{b_{(i+1/2,j-1/2)}}{\xi_{x(i+1/2,j-1/2)}(\omega)} \left[\left. \frac{\partial P(\omega, \mathbf{x})}{\partial x'} \right|_{(i+1/2,j-1/2)} + \left. \frac{\partial P(\omega, \mathbf{x})}{\partial z'} \right|_{(i+1/2,j-1/2)} \right] \\ &+ \frac{1}{2\Delta} \frac{b_{(i-1/2,j+1/2)}}{\xi_{x(i-1/2,j+1/2)}(\omega)} \left[\left. \frac{\partial P(\omega, \mathbf{x})}{\partial x'} \right|_{(i-1/2,j+1/2)} + \left. \frac{\partial P(\omega, \mathbf{x})}{\partial z'} \right|_{(i-1/2,j+1/2)} \right] \\ &+ (S_{x(i+1/2,j-1/2)}(\omega) - S_{x(i-1/2,j+1/2)}(\omega)), \end{aligned} \quad (3.26)$$

$$\begin{aligned}
 i\omega \frac{\partial V_z}{\partial x'} \Big|_{(i,j)} &\approx -\frac{1}{2\Delta} \frac{b_{(i+1/2,j-1/2)}}{\xi_{z(i+1/2,j-1/2)}(\omega)} \left[\frac{\partial P(\omega, \mathbf{x})}{\partial x'} \Big|_{(i+1/2,j-1/2)} + \frac{\partial P(\omega, \mathbf{x})}{\partial z'} \Big|_{(i+1/2,j-1/2)} \right] \\
 &+ \frac{1}{2\Delta} \frac{b_{(i-1/2,j+1/2)}}{\xi_{z(i-1/2,j+1/2)}(\omega)} \left[\frac{\partial P(\omega, \mathbf{x})}{\partial x'} \Big|_{(i-1/2,j+1/2)} + \frac{\partial P(\omega, \mathbf{x})}{\partial z'} \Big|_{(i-1/2,j+1/2)} \right] \\
 &+ (S_{z(i+1/2,j-1/2)}(\omega) - S_{z(i-1/2,j+1/2)}(\omega)), \tag{3.27}
 \end{aligned}$$

$$\begin{aligned}
 i\omega \frac{\partial V_x}{\partial z'} \Big|_{(i,j)} &\approx \frac{1}{2\Delta} \frac{b_{(i+1/2,j+1/2)}}{\xi_{x(i+1/2,j+1/2)}(\omega)} \left[\frac{\partial P(\omega, \mathbf{x})}{\partial x'} \Big|_{(i+1/2,j+1/2)} - \frac{\partial P(\omega, \mathbf{x})}{\partial z'} \Big|_{(i+1/2,j+1/2)} \right] \\
 &- \frac{1}{2\Delta} \frac{b_{(i-1/2,j-1/2)}}{\xi_{x(i-1/2,j-1/2)}(\omega)} \left[\frac{\partial P(\omega, \mathbf{x})}{\partial x'} \Big|_{(i-1/2,j-1/2)} - \frac{\partial P(\omega, \mathbf{x})}{\partial z'} \Big|_{(i-1/2,j-1/2)} \right] \\
 &+ (S_{x(i+1/2,j+1/2)}(\omega) - S_{x(i-1/2,j-1/2)}(\omega)), \tag{3.28}
 \end{aligned}$$

$$\begin{aligned}
 i\omega \frac{\partial V_z}{\partial z'} \Big|_{(i,j)} &\approx \frac{1}{2\Delta} \frac{b_{(i+1/2,j+1/2)}}{\xi_{z(i+1/2,j+1/2)}(\omega)} \left[\frac{\partial P(\omega, \mathbf{x})}{\partial x'} \Big|_{(i+1/2,j+1/2)} - \frac{\partial P(\omega, \mathbf{x})}{\partial z'} \Big|_{(i+1/2,j+1/2)} \right] \\
 &- \frac{1}{2\Delta} \frac{b_{(i-1/2,j-1/2)}}{\xi_{z(i-1/2,j-1/2)}(\omega)} \left[\frac{\partial P(\omega, \mathbf{x})}{\partial x'} \Big|_{(i-1/2,j-1/2)} - \frac{\partial P(\omega, \mathbf{x})}{\partial z'} \Big|_{(i-1/2,j-1/2)} \right] \\
 &+ (S_{z(i+1/2,j+1/2)}(\omega) - S_{z(i-1/2,j-1/2)}(\omega)). \tag{3.29}
 \end{aligned}$$

Where $b_{(i\pm 1/2,j\pm 1/2)} = \frac{b_{(i\pm 1,j\pm 1)} + b_{(i\pm 1,j)} + b_{(i,j\pm 1)} + b_{(i,j)}}{4}$, in the same way for $S_{x(i\pm 1/2,j\pm 1/2)}$ and $S_{z(i\pm 1/2,j\pm 1/2)}$.

For $\xi_{x(i\pm 1/2,j\pm 1/2)} = \frac{\xi_{x(i\pm 1,j)} + \xi_{x(i\pm 1,j)} + \xi_{x(i,j)} + \xi_{x(i,j)}}{4} = \xi_{x(i\pm 1/2,j)} \approx \xi_{(i\pm 1/2,j)}$.

And for $\xi_{z(i\pm 1/2,j\pm 1/2)} = \frac{\xi_{z(i\pm 1,j)} + \xi_{z(i\pm 1,j)} + \xi_{z(i,j)} + \xi_{z(i,j)}}{4} = \xi_{z(i,j\pm 1/2)} \approx \xi_{(i,j\pm 1/2)}$

So, the solution in the rotated grid is:

$$\begin{aligned}
 & \frac{\omega^2 P_{(i,j)}}{K_{(i,j)}} + \frac{\sqrt{2}}{4\Delta\xi_{(i,j)}} \frac{b_{(i+1/2,j-1/2)}}{\xi_{(i+1/2,j)}(\omega)} \left[\frac{\partial P(\omega, \mathbf{x})}{\partial x'} \Big|_{(i+1/2,j-1/2)} + \frac{\partial P(\omega, \mathbf{x})}{\partial z'} \Big|_{(i+1/2,j-1/2)} \right] \\
 & - \frac{\sqrt{2}}{4\Delta\xi_{(i,j)}} \frac{b_{(i-1/2,j+1/2)}}{\xi_{(i-1/2,j)}(\omega)} \left[\frac{\partial P(\omega, \mathbf{x})}{\partial x'} \Big|_{(i-1/2,j+1/2)} + \frac{\partial P(\omega, \mathbf{x})}{\partial z'} \Big|_{(i-1/2,j+1/2)} \right] \\
 & - \frac{\sqrt{2}}{4\Delta\xi_{(i,j)}} \frac{b_{(i+1/2,j+1/2)}}{\xi_{(i+1/2,j)}(\omega)} \left[\frac{\partial P(\omega, \mathbf{x})}{\partial x'} \Big|_{(i+1/2,j+1/2)} - \frac{\partial P(\omega, \mathbf{x})}{\partial z'} \Big|_{(i+1/2,j+1/2)} \right] \\
 & + \frac{\sqrt{2}}{4\Delta\xi_{(i,j)}} \frac{b_{(i-1/2,j-1/2)}}{\xi_{(i-1/2,j)}(\omega)} \left[\frac{\partial P(\omega, \mathbf{x})}{\partial x'} \Big|_{(i-1/2,j-1/2)} - \frac{\partial P(\omega, \mathbf{x})}{\partial z'} \Big|_{(i-1/2,j-1/2)} \right] \\
 & - \frac{\sqrt{2}}{4\Delta\xi_{(i,j)}} \frac{b_{(i+1/2,j-1/2)}}{\xi_{(i,j-1/2)}(\omega)} \left[\frac{\partial P(\omega, \mathbf{x})}{\partial x'} \Big|_{(i+1/2,j-1/2)} + \frac{\partial P(\omega, \mathbf{x})}{\partial z'} \Big|_{(i+1/2,j-1/2)} \right] \\
 & - \frac{\sqrt{2}}{4\Delta\xi_{(i,j)}} \frac{b_{(i-1/2,j+1/2)}}{\xi_{(i,j+1/2)}(\omega)} \left[\frac{\partial P(\omega, \mathbf{x})}{\partial x'} \Big|_{(i-1/2,j+1/2)} + \frac{\partial P(\omega, \mathbf{x})}{\partial z'} \Big|_{(i-1/2,j+1/2)} \right] \\
 & - \frac{\sqrt{2}}{4\Delta\xi_{(i,j)}} \frac{b_{(i+1/2,j+1/2)}}{\xi_{(i,j+1/2)}(\omega)} \left[\frac{\partial P(\omega, \mathbf{x})}{\partial x'} \Big|_{(i+1/2,j+1/2)} - \frac{\partial P(\omega, \mathbf{x})}{\partial z'} \Big|_{(i+1/2,j+1/2)} \right] \\
 & + \frac{\sqrt{2}}{4\Delta\xi_{(i,j)}} \frac{b_{(i-1/2,j-1/2)}}{\xi_{(i,j-1/2)}(\omega)} \left[\frac{\partial P(\omega, \mathbf{x})}{\partial x'} \Big|_{(i-1/2,j-1/2)} - \frac{\partial P(\omega, \mathbf{x})}{\partial z'} \Big|_{(i-1/2,j-1/2)} \right] \\
 & = S_{(i,j)}. \tag{3.30}
 \end{aligned}$$

For simplicity and because the source is punctual, normally Ricker wavelet, the sum of term $S_{i\pm 1/2, j\pm 1/2}$ is reduced the $S_{(i,j)}$

3.3 Mixed grid and Lumped Mass term

Then, the terms in the conventional grid are represented by

$$\frac{1}{\xi(\omega, \mathbf{x})} \nabla \cdot \left(\frac{b(\mathbf{x})}{\xi(\omega, \mathbf{x})} \nabla P(\omega, \mathbf{x}) \right) \Big|_{(i,j)} = \Gamma_{(i,j)} P. \tag{3.31}$$

While in the rotated grid are

$$\frac{1}{\xi(\omega, \mathbf{x})} \nabla' \cdot \left(\frac{b(\mathbf{x})}{\xi(\omega, \mathbf{x})} \nabla' P(\omega, \mathbf{x}) \right) \Big|_{(i,j)} = \Theta_{(i,j)} P. \tag{3.32}$$

Where the notation ∇' stands for derivatives on the rotated system. And the solution of eq. (2.17) can be written in the mixed-grid superposition as

$$m_1 \Gamma_{(i,j)} P + (1 - m_1) \Theta_{(i,j)} P + \frac{\omega^2}{K_{(i,j)}} P_{(i,j)} = S(\omega, \mathbf{x})|_{(i,j)}. \tag{3.33}$$

Where m_1 is a coefficient that regulates the relation between the contribution of the terms by the conventional and rotated grid for the derivatives terms in eq. (2.17).

Now, to improve the accuracy of the mixed-grid stencil the pressure acceleration term $\frac{\omega^2}{K(\mathbf{x})}P(\omega, \mathbf{x})$ in eq. (2.17), may not be taken as a term implying only the collocation point (the so-called lumped approximation), the implementation of the mixed grid aims to reduce the numerical dispersion, taking 9 points to find the values of the derivatives, if the free term $\frac{\omega^2}{K(\mathbf{x})}P(\omega, \mathbf{x})$ takes only the point value $P_{i,j}$ the contribution of rotated grid $\Theta_{(i,j)}$ will be diminished and the homogeneity of the solution will be lost to some degree (Operto and Virieux, 2006).

In order to solve this issue we may approximate this term by using a weighted average over the mixed operator stencil nodes, as it is done in finite-element modelling ((Marfurt, 1984), (Strikwerda, 2007)). Then in this situation the lumped mass term shall take the form:

$$\frac{\omega^2 P(\omega, \mathbf{x})}{K(\mathbf{x})} \Big|_{(i,j)} = \frac{\omega^2}{K_{(i,j)}} \left(m_2 P_{(i,j)} + m_3 \Sigma_{1(i,j)} P + \frac{m_4}{4} \Sigma_{2(i,j)} P \right). \quad (3.34)$$

With $\Sigma_{1(i,j)} P = \frac{1}{4}(P_{i+1,j} + P_{i-1,j} + P_{i,j+1} + P_{i,j-1})$, $\Sigma_{2(i,j)} P = \frac{1}{4}(P_{i+1,j-1} + P_{i-1,j-1} + P_{i-1,j+1} + P_{i+1,j+1})$ and $m_4 = 1 - m_2 - 4m_3$, where m_2 and m_3 are coefficients regulating the relation between the contribution of the terms by the conventional and rotated grid in the lumped mass term. Then, the final version of the discretized equation (2.17) is:

$$m_1 \Gamma_{(i,j)} P + (1 - m_1) \Theta_{(i,j)} P + \frac{\omega^2}{K_{(i,j)}} \left(m_2 P_{(i,j)} + m_3 \Sigma_{1(i,j)} P + \frac{m_4}{4} \Sigma_{2(i,j)} P \right) = S(\omega, \mathbf{x})|_{(i,j)}. \quad (3.35)$$

After simplifications it can be finally written as

$$D_{(i,j)} P_{(i,j)} + D1_{(i,j)} P_{(i+1,j)} + D2_{(i,j)} P_{(i-1,j)} + D3_{(i,j)} P_{(i,j+1)} + D4_{(i,j)} P_{(i,j-1)} + D5_{(i,j)} P_{(i+1,j-1)} + D6_{(i,j)} P_{(i-1,j+1)} + D7_{(i,j)} P_{(i+1,j+1)} + D8_{(i,j)} P_{(i-1,j-1)} = S_{(i,j)}. \quad (3.36)$$

Each D -term is given by

$$D_{(i,j)} = \frac{\omega^2}{K_{i,j}} m_2 - (\eta_{x1(i,j)} + \eta_{x2(i,j)} + \eta_{z1(i,j)} + \eta_{z2(i,j)}) m_1 - (\eta_{rx1(i,j)}^+ + \eta_{rx2(i,j)}^+ + \eta_{rz1(i,j)}^+ + \eta_{rz2(i,j)}^+) (1 - m_1). \quad (3.37)$$

$$D1_{(i,j)} = \frac{\omega^2}{K_{i,j}} m_3 + \eta_{x1(i,j)} m_1 + (\eta_{rx1(i,j)}^- + \eta_{rz1(i,j)}^-) (1 - m_1), \quad (3.38)$$

$$D2_{(i,j)} = \frac{\omega^2}{K_{i,j}} m_3 + \eta_{x2(i,j)} m_1 + (\eta_{rx2(i,j)}^- + \eta_{rz2(i,j)}^-) (1 - m_1), \quad (3.39)$$

$$D3_{(i,j)} = \frac{\omega^2}{K_{i,j}} m_3 + \eta_{z1(i,j)} m_1 + (\eta_{rx2(i,j)}^- + \eta_{rz1(i,j)}^-) (1 - m_1), \quad (3.40)$$

$$D4_{(i,j)} = \frac{\omega^2}{K_{i,j}} m_3 + \eta_{z2(i,j)} m_1 + \left(\eta_{rx1(i,j)}^- + \eta_{rz2(i,j)}^- \right) (1 - m_1), \quad (3.41)$$

$$D5_{(i,j)} = \frac{\omega^2}{K_{i,j}} (1/4 - m_2/4 - m_3) + \eta_{rx1(i,j)}^+ (1 - m_1), \quad (3.42)$$

$$D6_{(i,j)} = \frac{\omega^2}{K_{i,j}} (1/4 - m_2/4 - m_3) + \eta_{rx2(i,j)}^+ (1 - m_1), \quad (3.43)$$

$$D7_{(i,j)} = \frac{\omega^2}{K_{i,j}} (1/4 - m_2/4 - m_3) + \eta_{rz1(i,j)}^+ (1 - m_1), \quad (3.44)$$

$$D8_{(i,j)} = \frac{\omega^2}{K_{i,j}} (1/4 - m_2/4 - m_3) + \eta_{rz2(i,j)}^+ (1 - m_1). \quad (3.45)$$

Where the terms η have the form:

$$\eta_{x1(i,j)} = \frac{1}{\xi_{(i,j)}} \frac{1}{\Delta^2} \frac{b_{(i+1/2,j)}}{\xi_{(i+1/2,j)}}; \quad \eta_{x2(i,j)} = \frac{1}{\xi_{(i,j)}} \frac{1}{\Delta^2} \frac{b_{(i-1/2,j)}}{\xi_{(i-1/2,j)}}; \quad (3.46)$$

$$\eta_{z1(i,j)} = \frac{1}{\xi_{(i,j)}} \frac{1}{\Delta^2} \frac{b_{(i,j+1/2)}}{\xi_{(i,j+1/2)}}; \quad \eta_{z2(i,j)} = \frac{1}{\xi_{(i,j)}} \frac{1}{\Delta^2} \frac{b_{(i,j-1/2)}}{\xi_{(i,j-1/2)}}; \quad (3.47)$$

$$\eta_{rx1(i,j)}^\pm = \frac{b_{(i+1/2,j-1/2)}}{4\Delta^2 \xi_{(i,j)}} \left(\frac{1}{\xi_{(i+1/2,j)}} \pm \frac{1}{\xi_{(i,j-1/2)}} \right); \quad \eta_{rx2(i,j)}^\pm = \frac{b_{(i-1/2,j+1/2)}}{4\Delta^2 \xi_{(i,j)}} \left(\frac{1}{\xi_{(i-1/2,j)}} \pm \frac{1}{\xi_{(i,j+1/2)}} \right); \quad (3.48)$$

$$\eta_{rz1(i,j)}^\pm = \frac{b_{(i+1/2,j+1/2)}}{4\Delta^2 \xi_{(i,j)}} \left(\frac{1}{\xi_{(i+1/2,j)}} \pm \frac{1}{\xi_{(i,j+1/2)}} \right); \quad \eta_{rz2(i,j)}^\pm = \frac{b_{(i-1/2,j-1/2)}}{4\Delta^2 \xi_{(i,j)}} \left(\frac{1}{\xi_{(i-1/2,j)}} \pm \frac{1}{\xi_{(i,j-1/2)}} \right). \quad (3.49)$$

As it is well known, one of the advantages of the solution of the problem of wave propagation in frequency domain is that at the end, the problem can be formulated as a linear problem for each single frequency ω . In our case, that linear problem shall have the form $\mathbf{A}\mathbf{p} = \mathbf{s}$, where the matrix \mathbf{A} is made of the coefficients $D_{(i,j)}$, $m = iN_z + j$, $i = 0, 1, 2, \dots, N_x - 1$ and $j = 0, 1, 2, \dots, N_z - 1$.

$$A_{(m,n)} = D_{(m)} \delta_{m,n} + D1_{(m)} \delta_{m,n+N_z} + D2_{(m)} \delta_{m,n-N_z} + D3_{(m)} \delta_{m,n+1} + D4_{(m)} \delta_{m,n-1} + D5_{(m)} \delta_{m,n+N_z-1} + D6_{(m)} \delta_{m,n-N_z+1} + D7_{(m)} \delta_{m,n+N_z+1} + D8_{(m)} \delta_{m,n-N_z-1}. \quad (3.50)$$

This matrix is sparse, indefinite, complex and square. The vector \mathbf{s} is the source vector discretized around the coordinates (x_0, z_0) . Finding \mathbf{p} as the solution to the problem stated in $\mathbf{A}\mathbf{p} = \mathbf{s}$ is equivalent to solve the system of equations (2.17).

3.4 Dispersion Analysis

As it is clear from the use of finite differences, the numerical solution requires a discretization to represent the physical domain that in our case is implemented in a regular mesh which has both a finite physical extent and finite number of mesh points. However, the number of points per wavelength of the approximate field is not the same in every direction, and this artificial artifact due to the discreteness adds to the numerical dispersion of the solution. Clearly, this is not a problem that can be ignored.

Since the solution is not exact there is already an error on the approach, if we add this pollutive effect to the solution, we will have, specially at long wavelengths, an inappropriate estimate of the solution due to the undersampling where long wavelengths are not sampled at high enough spatial frequencies to provide a trustable solution at those wavelengths (Deraemaeker et al., 1999). The pollution effect is a problem present in the numerical solution of Helmholtz equation when the accuracy of the numerical solution deteriorates with increasing wave number (Ihlenburg and Babuška, 1995), (Ihlenburg and I.Babuška, 1997) and (Ospina, 2016).

In this part we will make use of the know behaviour of the problem of wave propagation in a homogeneous media (eq.2.12) (Jo, 1996). In this case for constant velocity, density and attenuation in a media without source we have that the wave equation (eq.2.12) may be written as

$$\begin{aligned} (\Delta + \tilde{k}^2)P(x_i, z_j) &\approx m_1 \Gamma_{(i,j)} P + \\ (1 - m_1) \Theta_{(i,j)} P + \Phi(m_2, m_3)_{(i,j)} P &= 0. \end{aligned} \quad (3.51)$$

Where m_1, m_2, m_3 are parameters that we will find subject to the condition of minimization the dispersion of the solution. To do so, remember that in this case ρ and c have a constant value, therefore the problem has an analytic solution, given by:

$$P(r) = P_0 e^{-i(\tilde{\mathbf{k}} \cdot \mathbf{r})}. \quad (3.52)$$

Where $\tilde{\mathbf{k}}$ is a complex wave vector and \mathbf{r} is the position vector. Now, If we introduce the solution (3.52) into the numerical scheme in equation (3.51), we see that the numeric complex wavenumber can be written as the ratio of two arbitrary functions A and B as

$$\tilde{k}^2 = \frac{1}{\Delta^2} \frac{A(\tau_r, \tau_i, \theta)}{B(\tau_r, \tau_i, \theta)}. \quad (3.53)$$

Where if G_r is the number of grid points per wavelength, then $\tau_r = \frac{1}{G_r}$ is the number of wavelengths per grid point. The same relation holds for the pseudo grid number for pseudowavelength G_i and $\tau_i = \frac{1}{G_i}$ and where θ is the propagation angle. With this notation, the relation between the complex wave number, complex wave length and complex grid number is

$$\begin{aligned}
 \tilde{k} &= \frac{\omega}{c} - i\frac{\gamma}{c} \\
 \tilde{\lambda} &= \Delta G_r - i\Delta G_i \\
 \tilde{k}^T &= \frac{2\pi}{\Delta G_r} - i\frac{2\pi}{\Delta G_i}.
 \end{aligned} \tag{3.54}$$

Taking the square root of eq. (3.54), dividing by the theoretical estimate of \tilde{k} , \tilde{k}^T and separating in real and imaginary parts one gets

$$N(\tau_r, \tau_i, \theta) = \frac{k_r^N}{k_r^T} = \frac{G_r}{2\pi} \Re \left(\sqrt{\frac{A}{B}} \right) = \frac{1}{2\pi\tau_r} \Re \left(\sqrt{\frac{A}{B}} \right), \tag{3.55}$$

$$M(\tau_r, \tau_i, \theta) = \frac{k_i^N}{k_i^T} = \frac{G_i}{2\pi} \Im \left(\sqrt{\frac{A}{B}} \right) = \frac{1}{2\pi\tau_i} \Im \left(\sqrt{\frac{A}{B}} \right). \tag{3.56}$$

Then our objective function is:

$$\begin{aligned}
 \chi(m_1, m_2, m_3) &= \int \int \int [(1 - N(\tau_r, \tau_i, \theta))^2 \\
 &+ (1 - M(\tau_r, \tau_i, \theta))^2] d\theta d\tau_r d\tau_i.
 \end{aligned} \tag{3.57}$$

Which we try to minimize for $\theta \in [0, \pi/2]$ and $\tau_r, \tau_i \in [0.001, 0.15]$ (Chen, 2004). The result of the minimization gives the values of m_1 , m_2 and m_3 that minimize the dispersion we find that $m_1 = 0.6667$, $m_2 = 0.6556$, $m_3 = 0.0889$. It is important to mention that when there is no attenuation, we get the same result that (Jo, 1996) $m_1 = 0.5461$, $m_2 = 0.6248$, $m_3 = 0.09381$. Also using the values $m_1 = 1.0$, $m_2 = 1.0$, $m_3 = 0.0$ we can recover the usual 5-point scheme.

Now, to study the difference between the numerical dispersion produced by the scheme of 9-points and the scheme of 5-points, we plot in figures (3.3) and (3.4) the relation between the theoretical and numeric wave numbers for the real and imaginary parts, $\frac{k_r^N}{k_r^T}$ and $\frac{k_i^N}{k_i^T}$. We use the optimum values found in the minimization, and plot the behaviour for different propagation angles, $\theta = 0, \frac{\pi}{12}, \frac{\pi}{6}, \frac{\pi}{4}$ in the eq. (3.55) and (3.56). We compute $M(\tau_r, \tau_i, \theta)$ for $\tau_r = 0.1, 0.044, 0.001$, and $\tau_i = [0.001, 0.15]$, and compute $N(\tau_r, \tau_i, \theta)$ for $\tau_i = 0.1, 0.044, 0.001$ and $\tau_r = [0.001, 0.15]$

To understand this figure keep in mind that according, to the discussion of this section, the closer these ratios are to 1, the lower the numerical dispersion and the better the quality of the solution. Solid lines show the ratio computed for the scheme of 9-points while dashed lines show the ratio estimated for the 5-point scheme. The different lines for each scheme (different colour lines) show the result for different propagation angles θ .

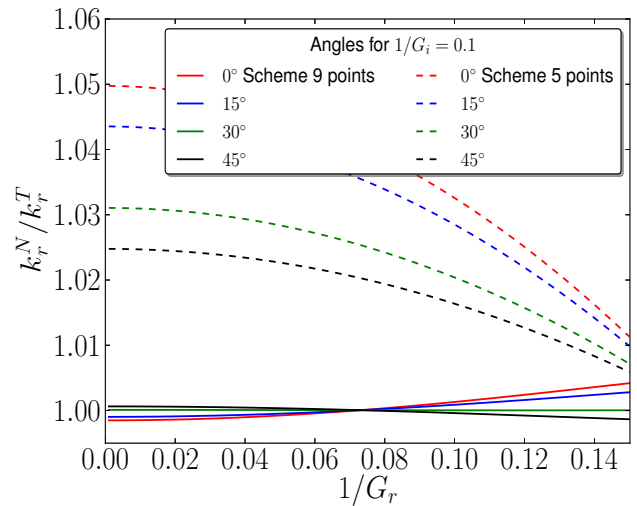
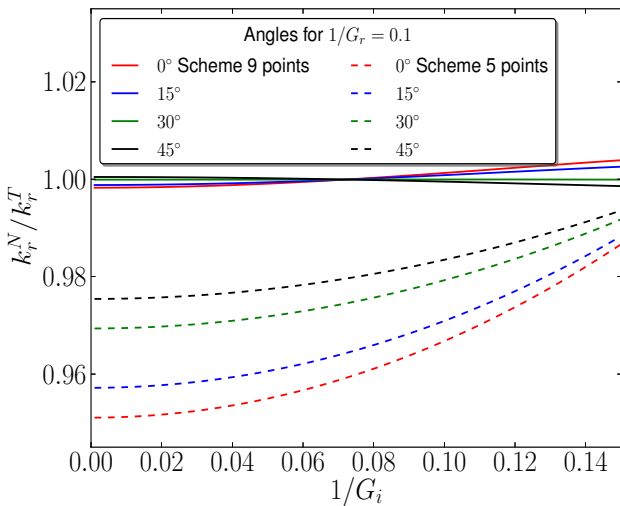
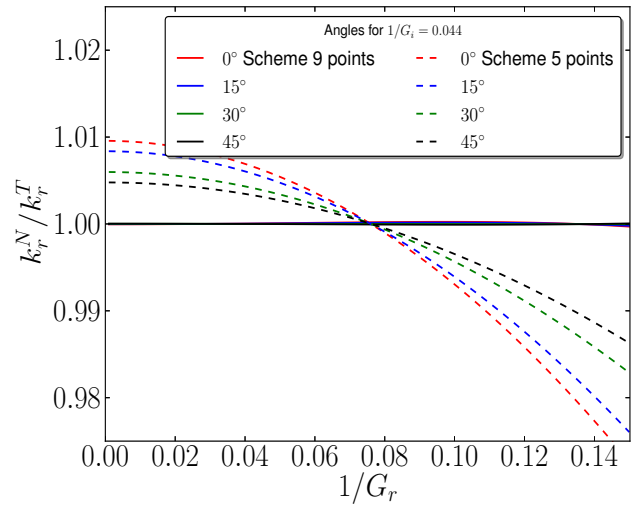
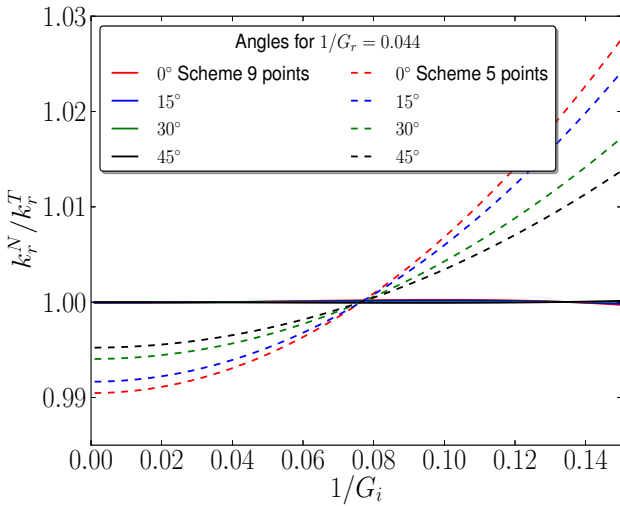
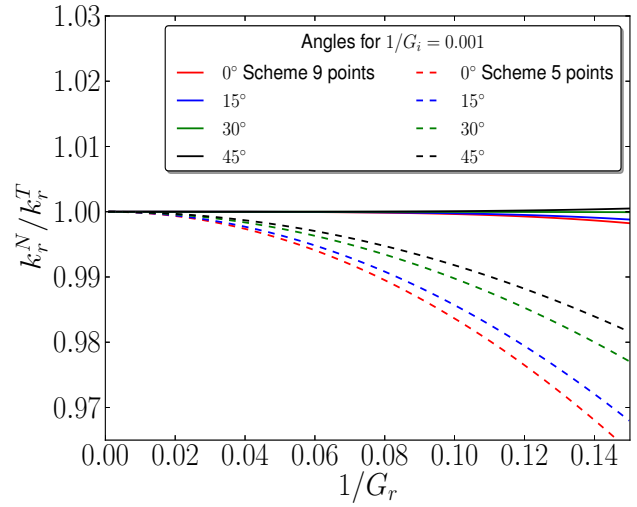
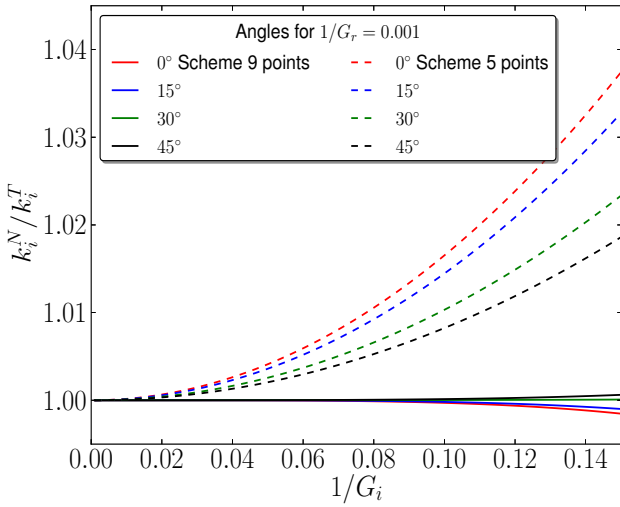


Figure 3.3: Ratio between the imaginary part of the theoretical and numerical wave number for several cases, from left to right: a) Ratio k_i^N to k_i^T for $1/G_r = 0.001$ b) k_i^N and k_i^T for $1/G_r = 0.044$ c) k_i^N and k_i^T for $1/G_r = 0.1$

Figure 3.4: Ratio between the real part of theoretical and numerical wave number for several cases, from left to right: a) Ratio k_r^N and k_r^T for $1/G_i = 0.001$ b) k_r^N and k_r^T for $G_i = 0.044$ c) k_r^N and k_r^T for $G_i = 0.1$

Notice that for a fixed value of τ_r or τ_i the dispersion is smaller for the 9-point scheme. The same behaviour can be observed for different values of τ_r and τ_i . In general, independent of the scheme (9-point or 5-points) for large propagation angles the dispersion is smaller, but still is the smallest for the 9-point scheme and the scatter between different propagation angles for this scheme is also very small.

Figures (3.3) and (3.4) clearly show that the implementation of the mixed grid and optimization presented in this section provides a high accuracy solution to the problem of wave propagation in a complex visco-acoustic medium at a relatively low computational cost.

Now, according to the above, we define the cell size Δ

$$\Delta = \frac{\lambda}{G_r} = \frac{c_{min}}{fG_r}. \quad (3.58)$$

Where $G_r = 7$, c_{min} is minimal wave velocity, f is the frequency. Therefore, $\tau_r \approx 0.14$, which is within our range of values for τ_r , $[0.001, 0.15]$. Looking at the attenuation models discussed in eqs. (2.20), (2.23), (2.26) one can show that for the value of the parameters used in this work and the physical conditions we explore, it will always be the case that $\lambda_i > \lambda_r$, then we always choose the approach to make Δ as a function of the wavelength and not of pseudo wavelength.

3.5 The Source

In eq (2.17) the source is $S(\omega, \mathbf{x}) = \frac{1}{\xi(\omega, \mathbf{x})} \nabla \cdot \left(\frac{b(\mathbf{x})}{\xi(\omega, \mathbf{x})} \mathbf{F}(\omega, \mathbf{x}) \right)$ such that $\mathbf{F}(\omega, \mathbf{x})$ is a body force. The source in these models is generally an impulse at point $\mathbf{x}_s = (x_s, z_s)$ commonly the term $\nabla \cdot \mathbf{F}(\omega, \mathbf{x}) = R(\omega)\delta(\mathbf{x} - \mathbf{x}_s)$ where $R(\omega)$ is the Ricker wavelet:

$$R(\omega) = R_0 \frac{2}{\sqrt{\pi}} \frac{f^2}{f_s^3} e^{-\frac{f^2}{f_s^2}}. \quad (3.59)$$

Where $\delta(\mathbf{x} - \mathbf{x}_s)$ is a dirac delta function, but in the discretization can be represented with the Kronecker delta. The R_0 is maximum amplitude of the ricker wavelet. Now, if we assume that the divergence of the force is $\nabla \cdot \mathbf{F}(\omega, \mathbf{x}) = R(\omega)\delta(\mathbf{x} - \mathbf{x}_s)$, the force could be written:

$$\mathbf{F}(\omega, \mathbf{x}) = R(\omega) \frac{(\mathbf{x} - \mathbf{x}_s)}{|\mathbf{x} - \mathbf{x}_s|^3}. \quad (3.60)$$

With this source applied Eq (2.17) it can written as:

$$S(\omega, \mathbf{x}) = R(\omega) \frac{b(\mathbf{x})}{\xi(\omega, \mathbf{x})^2} \left(\delta(\mathbf{x} - \mathbf{x}_s) + \frac{[\nabla b(\mathbf{x}) - \nabla \xi(\omega, \mathbf{x})] \cdot (\mathbf{x} - \mathbf{x}_s)}{|\mathbf{x} - \mathbf{x}_s|^3} \right). \quad (3.61)$$

The second term has considerable value close to the source but almost nothing away from it because of the higher order term. However, the dot product between variations of the inverse of the density and variation of attenuation with distance between them is very close to zero for values

close of the source, such that we can consider that the second term may be discarded close to the source.

So, in a medium with constant velocity, density and attenuation, the source is approximately

$$S_{(i,j)} = \frac{R_0}{\xi^2 \rho} \frac{2}{\sqrt{\pi}} \frac{f^2}{f_s^3} e^{-\frac{f^2}{f_s^2}} \delta_{i,i_s} \delta_{j,j_s}. \quad (3.62)$$

Where (i_s, j_s) is a point in the grid where the source is placed. For case when the velocity, density and attenuation are not constant we propose that the source should have the form

$$S_{(i,j)} = \frac{b_{(i,j)}}{\xi_{(i,j)}^2} R_0 \frac{2}{\sqrt{\pi}} \frac{f^2}{f_s^3} e^{-\frac{f^2}{f_s^2}} \delta_{i,i_s} \delta_{j,j_s}. \quad (3.63)$$

Where $\delta_{i,i_s} \delta_{j,j_s}$ can be approximated a:

$$\delta_{i,i_s} \delta_{j,j_s} \approx \frac{1}{\pi \sigma_x \sigma_z} e^{-\left(\frac{x_i - x_s}{\sigma_x}\right)^2} e^{-\left(\frac{z_j - z_s}{\sigma_z}\right)^2}. \quad (3.64)$$

This definition comes from the Dirac delta function as the limit (in the sense of distributions) of the sequence of zero-centered normal distributions $\delta_\sigma(x) = \frac{1}{\sqrt{\pi}\sigma} \exp\left(-\frac{x^2}{\sigma^2}\right)$ as $\sigma \rightarrow 0$. The factor σ must have a relationship with the grid spacing Δ , i.e. $\sigma_x = \sigma_z \sim \Delta$.

The discretization of the Dirac delta is used because of the changes in grid spacing, that according with Eq. 3.58 depends on the frequency. Is important to ensure that the source energy is evenly distributed within our space to avoid losses by locating the entire amplitude at a point which can not be located unequivocally in all grids. That is, comply with the property of the Dirac Delta:

$$\int_{-\infty}^{\infty} \delta(\mathbf{x}) d\mathbf{x} = 1 \quad \Rightarrow \quad \sum_{i=0}^{N_x} \sum_{j=0}^{N_z} \delta_{i,i_s} \delta_{j,j_s} dh^2 \approx 1 \quad \text{in the discrete case.} \quad (3.65)$$

With this we can ensure that the solution, in the discrete domain is well defined (Mayo, 1984), (Tornberg and Engquist, 2004). With this, we can define $\sigma = \sigma_x = \sigma_z$ as $\sigma = s\Delta$, using Eq. 3.64:

$$I(s, f) = \sum_{i=0}^{N_x} \sum_{j=0}^{N_z} \frac{1}{\pi s^2 \Delta^2} e^{-\left(\frac{i\Delta - x_s}{s\Delta}\right)^2} e^{-\left(\frac{j\Delta - z_s}{s\Delta}\right)^2} \Delta^2 \approx 1. \quad (3.66)$$

To get a correct value for s , we calculate Eq. 3.66 for different frequency values, assuming the position of the source is $x_s = 1$ [Km] and $z_s = 1$ [Km] in an area of 2 [Km] \times 2 [Km], with $c = 2100$ [m/s]. The frequencies are $f = 1, 5, 15, 30, 50$ [Hz], we do not compute it for higher frequencies since the Δ in these cases is smaller approaching the continuous form of the Dirac delta, for scale factor $s = [0.5, 2.0]$. With these values we obtain the figure 3.5.

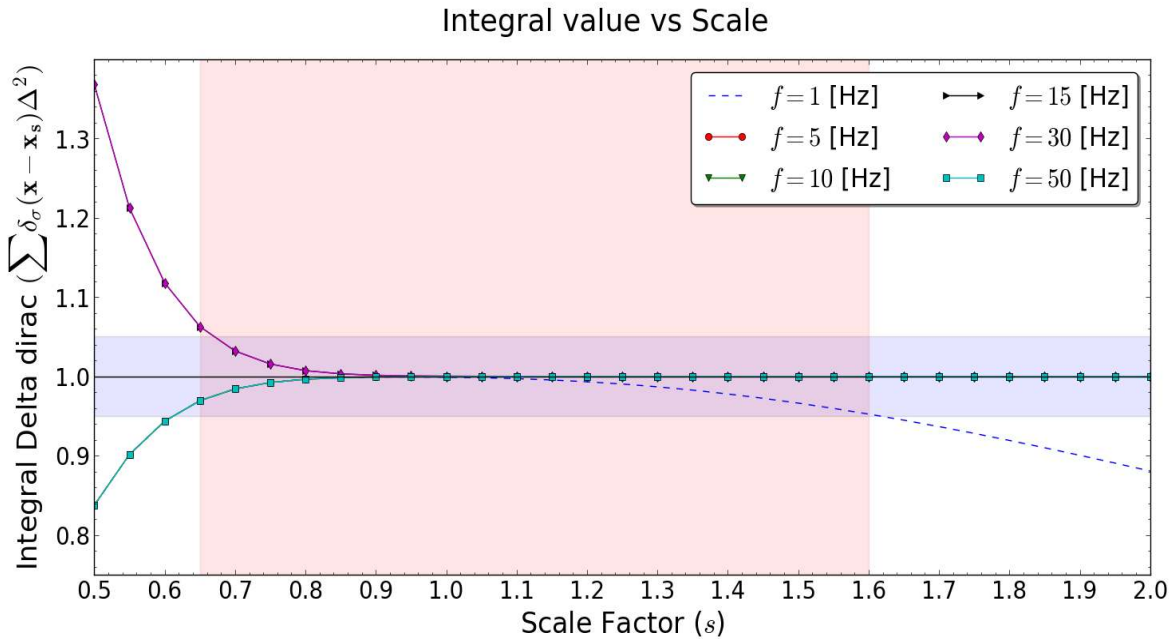


Figure 3.5: Integral values for discrete dirac delta calculate for ec.3.66 for different frequency values, assuming the position of the source is $x_s = 1[\text{Km}]$ and $z_s = 1[\text{Km}]$

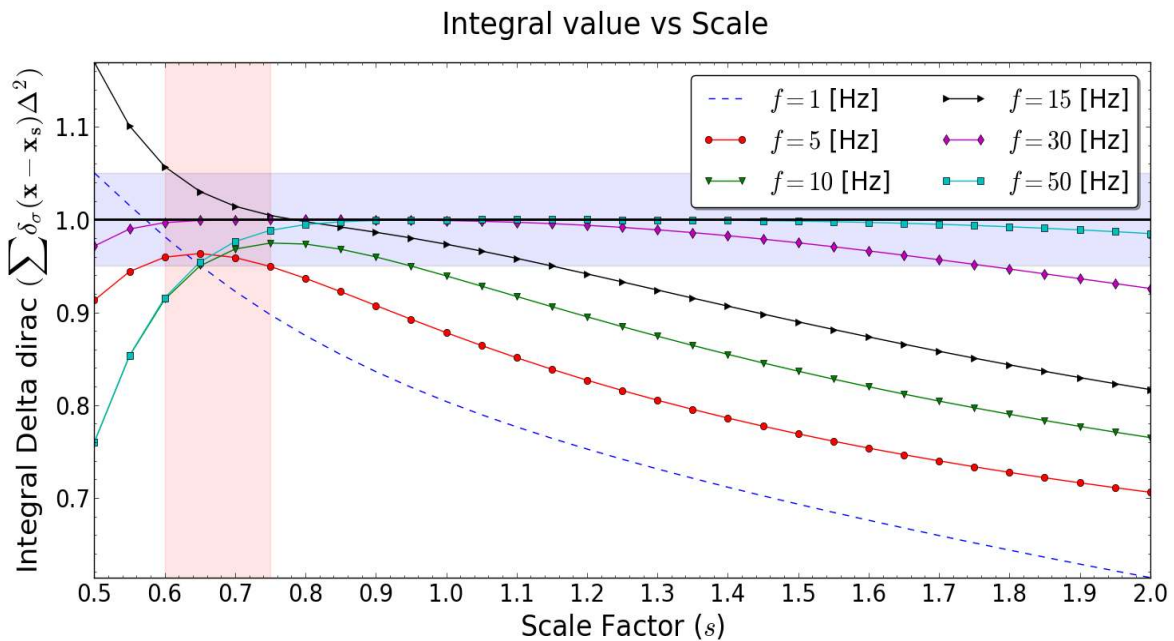


Figure 3.6: Integral values for discrete Dirac delta calculate for Eq. 3.66 for different frequency values, assuming the position of the source is $x_s = 1[\text{Km}]$ and $z_s = 0.015[\text{Km}]$

We can see in the figure, that the values of $I(s, f)$ remain close to 1 $I(s, f) = [0.95, 1.05]$ for the different frequencies, the scale factor s get values $s = [0.65, 1.6]$. In Figure 3.6, we do the same calculation but with the source at $x_s = 1[\text{Km}]$ and $z_s = 15[\text{m}]$. We can see in the figure as the

allowed values for the scale factor are reduced to $s = [0.6, 0.75]$ for $I(s, f) = [0.95, 1.05]$, the more the scale factor is increased, for low frequencies, the integral takes values that are farthest from 1.

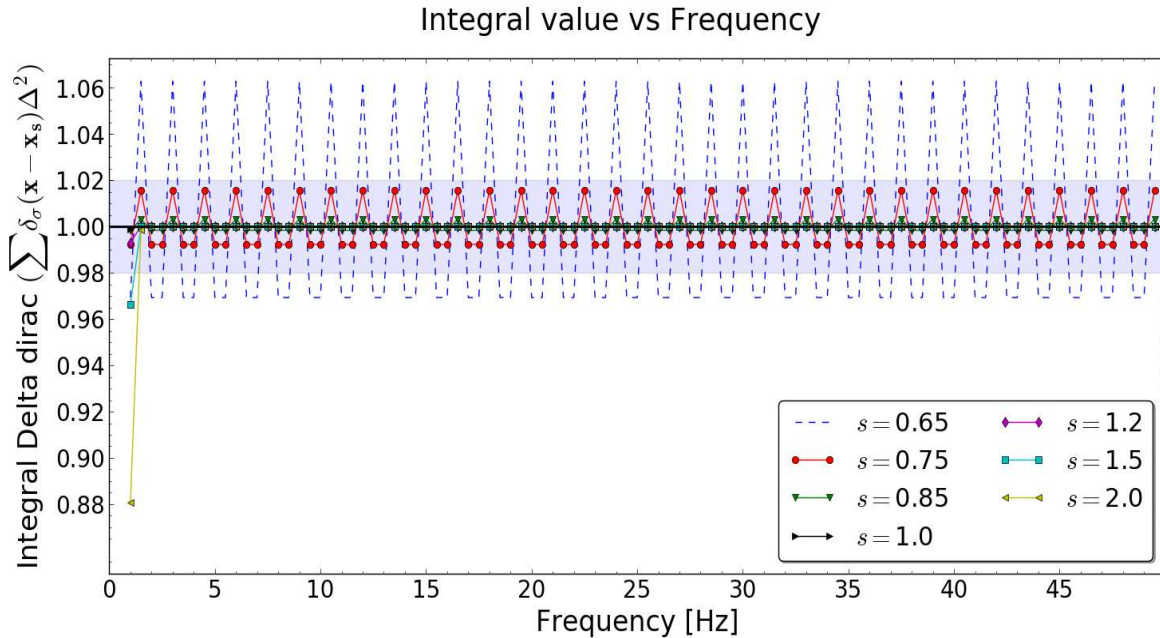


Figure 3.7: Integral values for discrete Dirac delta calculate for Eq. 3.66 for different scale factor, assuming the position of the source is $x_s = 1[\text{Km}]$ and $z_s = 1[\text{Km}]$

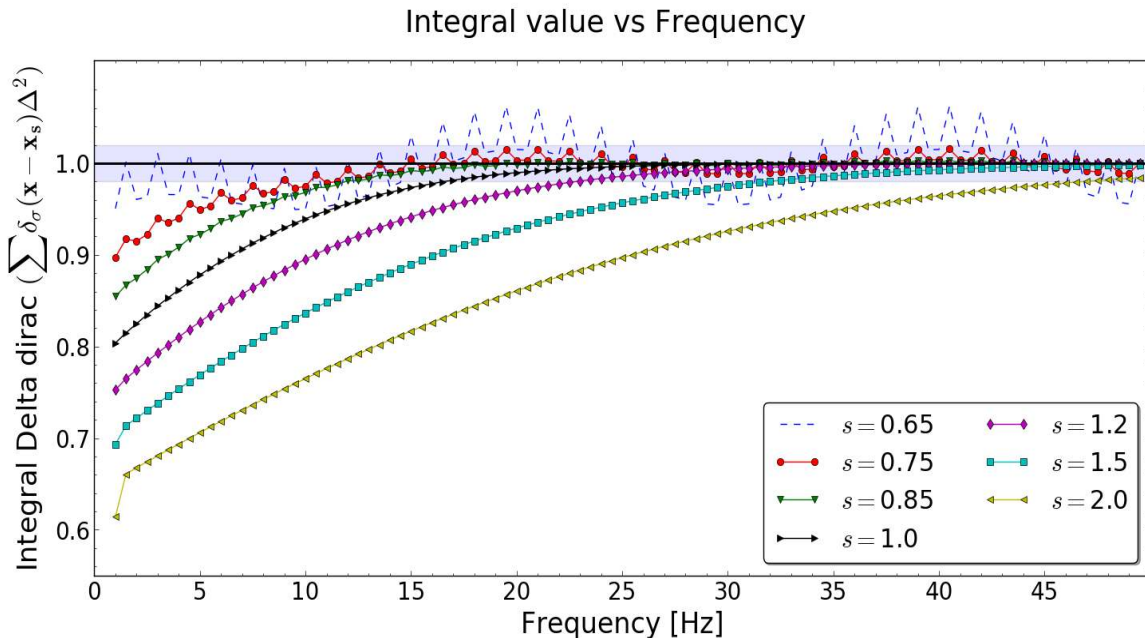


Figure 3.8: Integral values for discrete Dirac delta calculate for Eq. 3.66 for different scale factor, assuming the position of the source is $x_s = 1[\text{Km}]$ and $z_s = 0.015[\text{Km}]$

Now, to ensure the right choice for s , we compute Eq. 3.66 for different scale factors, assuming the position of the source is $x_s = 1[\text{Km}]$ and $z_s = 1[\text{Km}]$ in an area of $2[\text{Km}] \times 2[\text{Km}]$, with $c = 2100[\text{m/s}]$. The scale factors are $s = 0.65, 0.75, 0.85, 1.0, 1.5, 2.0$ for frequencies $f = [1.0, 50.0][\text{Hz}]$. With these values we obtain the figure 3.7. In the figure 3.8, we do the same calculation but with the source in $x_s = 1[\text{Km}]$ and $z_s = 15[\text{m}]$.

We can see in the figures 3.7 and 3.8, that the values of $I(s, f)$ remain close to 1 in the scale factor previously found, we can also note that for low frequencies, the integral has a value close to 1 for scale factors $s < 1$, for scaling factors $s = [1, 2]$ the integral has values distant to 1. But, for scale factor $s = [0.65, 0.75]$, our range defined above, there is a discontinuity in the calculation of the values of the integral, these oscillations could affect the form of amplitude of our model.

According to this we can assume that the correct value for the scale factor s , for our tests with sources located in the center of the domain or at the top, should be $s = [0.75, 1.0]$

3.6 Perfectly-matched layer (PML) absorbing boundary conditions

An important ingredient for the solution of Equation (2.17) is the boundary conditions. In this work we will assume a simplistic approximation and will use perfectly-matched absorbing boundary conditions. The absorbing boundary condition is a virtual boundary very simple to use, since our media is in principle dissipative.

The PML method consists on using two damping functions to suppress the value of the pressure field in the boundaries at the edges of the square computational domain, $\gamma_x(x)$ and $\gamma_z(z)$ and an nonphysical pressure wavefield P_x and P_z such that $P = P_x + P_z$. This technique is similar to a sponge-like absorbing boundary condition (C. et al., 1985), but attenuation occurs at each dimension independently.

In our case, we simply expanded the computational domain \mathcal{U} from $N_x \times N_z$ to $\partial\mathcal{U}$ from $N_{xe} \times N_{ze}$ where $N_{xe} = N_x + 2n_{xpml}$ and $N_{ze} = N_z + 2n_{zpml}$, where n_{xpml} and n_{zpml} are the number of extra points from the boundary condition (see figure 3.9 and 3.10). In the expanded region the damping functions have the form (Operto and Virieux, 2006) as can be seen in Eq. 3.69 and 3.70.

$$\xi_z(\omega, \mathbf{x}) = \begin{cases} 1 + i \left[\frac{m_0 \gamma_{zpml}}{\omega} \right] & z < z_{pml} \\ \xi(\omega, \mathbf{x}) & z_{pml} < z < L_z + z_{pml} \\ 1 + i \left[\frac{m_0 \gamma_{zpml}}{\omega} \right] & z > z_{pml} + L_z \end{cases}, \quad (3.67)$$

$$\xi_x(\omega, \mathbf{x}) = \begin{cases} 1 + i \left[\frac{m_0 \gamma_{xpml}}{\omega} \right] & x < x_{pml} \\ \xi(\omega, \mathbf{x}) & x_{pml} < x < L_x + x_{pml} \\ 1 + i \left[\frac{m_0 \gamma_{xpml}}{\omega} \right] & x > x_{pml} + L_x \end{cases}, \quad (3.68)$$

$$\gamma_{xpml}(\omega, \mathbf{x}) = \begin{cases} \cos\left(\frac{x - x_{pml}}{x_{pml}} \frac{\pi}{2}\right) + \gamma(\omega, x_{pml}, z) & x < x_{pml} \\ 1 - \cos\left(\frac{x - L_x - x_{pml}}{x_{pml}} \frac{\pi}{2}\right) + \gamma(\omega, L_x, z) & x > x_{pml} + L_x \end{cases}, \quad (3.69)$$

$$\gamma_{zpml}(\omega, \mathbf{x}) = \begin{cases} \cos\left(\frac{z - z_{pml}}{z_{pml}} \frac{\pi}{2}\right) + \gamma(\omega, x, z_{pml}) & z < z_{pml} \\ 1 - \cos\left(\frac{z - L_z - z_{pml}}{z_{pml}} \frac{\pi}{2}\right) + \gamma(\omega, x, L_z) & z > z_{pml} + L_z \end{cases}. \quad (3.70)$$

Where m_0 is a parameter that changes with frequency and takes a value that makes the amplitude of the wave at the boundary of the domain to fall below a given threshold. The PML for z is defined the same way.

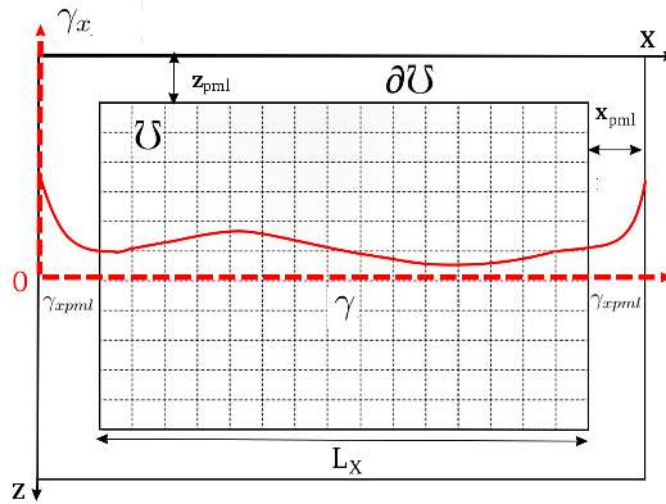


Figure 3.9: PML in \mathcal{U} and boundary workspace $\partial\mathcal{U}$ for the numerical solution, in x coordinate

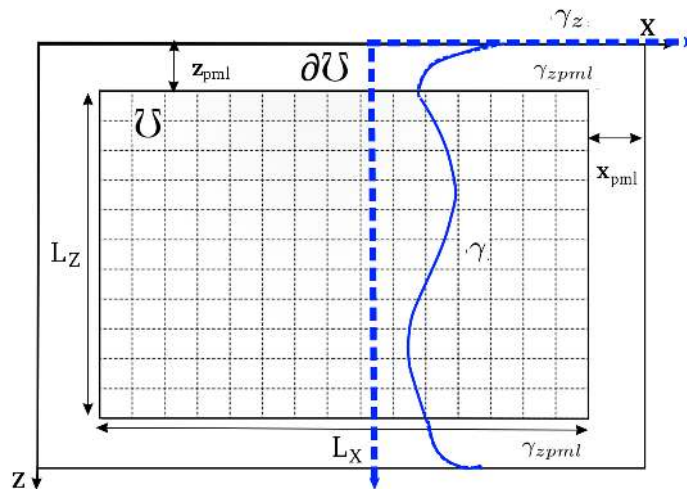


Figure 3.10: PML in \mathcal{U} and boundary workspace $\partial\mathcal{U}$ for the numerical solution, in z coordinate

Now, we compute the value of the P-wave amplitude in an area of $2[\text{Km}] \times 2[\text{Km}]$, with constant velocity of the media is $2100 [\text{m/s}]$, the Ricker frequency is $30 [\text{Hz}]$, the constant quality factor is $Q = 50$, using the damping function eq. (2.15), the cell size Δ is $\frac{\lambda}{G_r}$, where $G_r = 7$, scale factor $s = 0.75$. The position of the source is $x_0 = 1[\text{Km}]$ and $z_0 = 1[\text{Km}]$.

Fig. (3.11) shows the real, imaginary part and modulus of field P-wave with PML ($m_0 = f$) and (3.12) shows the real, imaginary part and modulus of field P-wave without PML ($m_0 = 0$) in a medium with constant velocity, attenuation and density for $15 [\text{Hz}]$.

The expected result is a symmetrical and spherical field but in the image of P-Wave without PML presents a perturbation that is not in agreement with the physical setup if the problem. In this figure we can see the importance of the PML so that the results are consistent with the physics of the medium.

In (Operto and Virieux, 2006), m_0 is chosen on trial and error, in this work we propose to define m_0 , n_{xpml} and n_{zpml} as a function of frequency. In fig. (3.13) shows the modulus of field P-wave ($m_0 = 3.0$) for $3 [\text{Hz}]$ for all (x, z) , $z = 500 [\text{m}]$ and $z = 1000 [\text{m}]$. (3.14) shows modulus of field P-wave ($m_0 = 3.0$) for $10 [\text{Hz}]$ for all (x, z) , $z = 500 [\text{m}]$ and $z = 1000 [\text{m}]$, in a medium with constant velocity, attenuation and density.

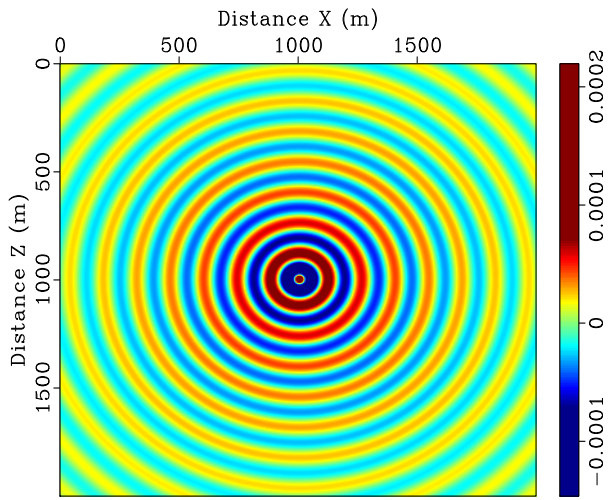
In this case we have used the same $m_0 = 3.0$ at different frequency. At first it seemed that it was adequate but after several experiments, we noticed that the more we increase the frequency the PML starts to loss effectiveness. This is because the term m_0 controls the way in which the functions γ_{pml} attenuate the amplitude of the wave, the larger the frequency the faster the attenuating term falls, so m_0 must counteract this drop in high frequencies. Therefore m_0 is frequency dependent.

We have noticed for low frequencies $m_0 = f$ is not enough to achieve a good response. Fig. (3.15) shows the modulus of field P-wave in $z = 100 [\text{m}]$ for numerical solution using $m_0 = f$ (solid line) and $m_0 = \omega = 2\pi f$ (dash line) obtained with the 9-point schemes for $f = 3, 5, 10, 30 [\text{Hz}]$. We can see that a better choice for m_0 is $m_0 = 2\pi f$, especially for low frequencies.

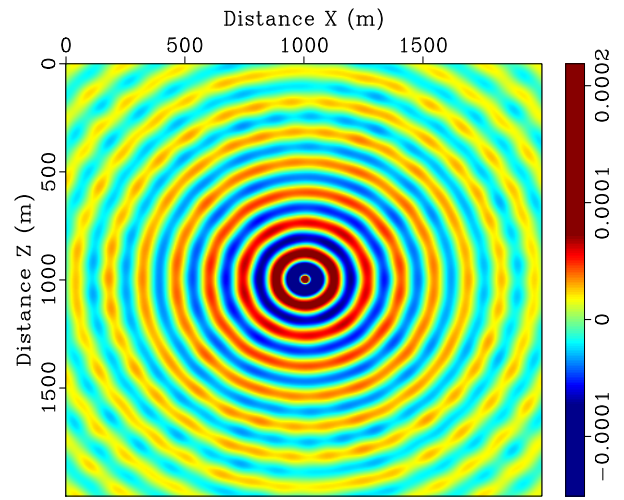
In addition n_{xpml} and n_{zpml} are also frequency dependent, which for low frequencies (long wavelengths) should have a good percentage of the values N_x and N_z such that the amplitude of the pressure field is attenuated correctly, while for high frequencies (long wavelengths) are just a few points more to make it, such that n_{xpml} and n_{zpml} is calculated for:

$$\begin{aligned} n_{xpml} &= e_{pml}(f)N_x & n_{zpml} &= e_{pml}(f)N_z \\ e_{pml}(f) &= c_1f^3 + c_2f^2 + c_3f + c_4. \end{aligned} \quad (3.71)$$

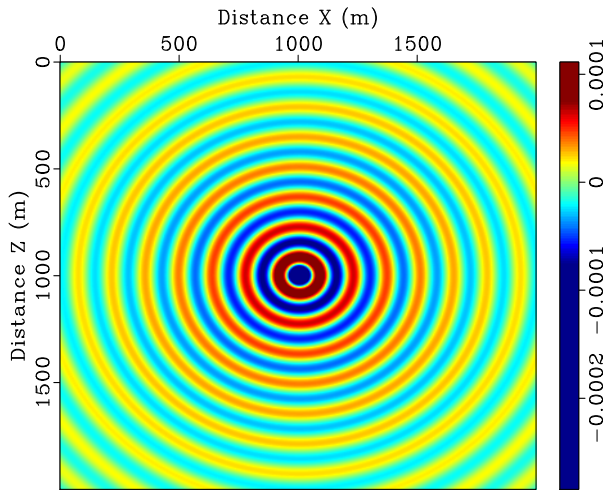
With $c_1 = -1.241890 \times 10^{-6}$, $c_2 = 3.37128949 \times 10^{-4}$, $c_3 = -3.0697652929 \times 10^{-2}$ and $c_4 = 1.068192783161$.



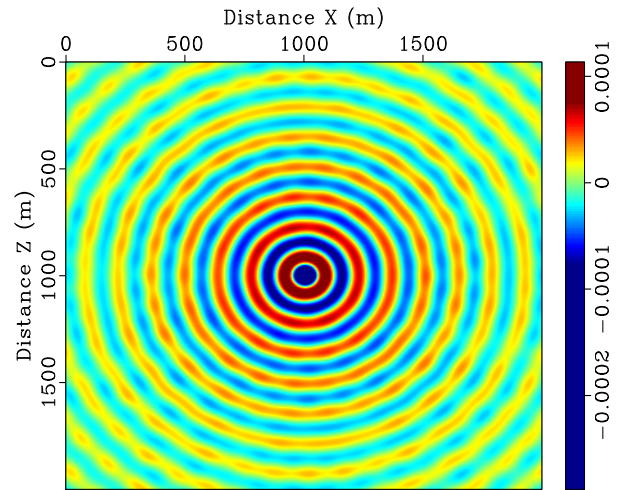
Real P-Wave a 15 Hz



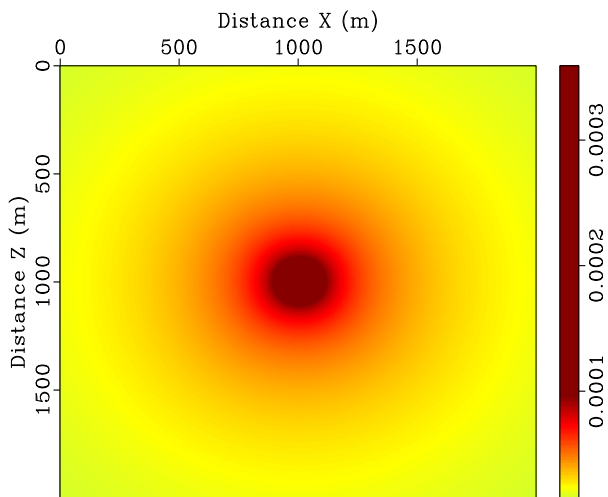
Real P-Wave a Hz



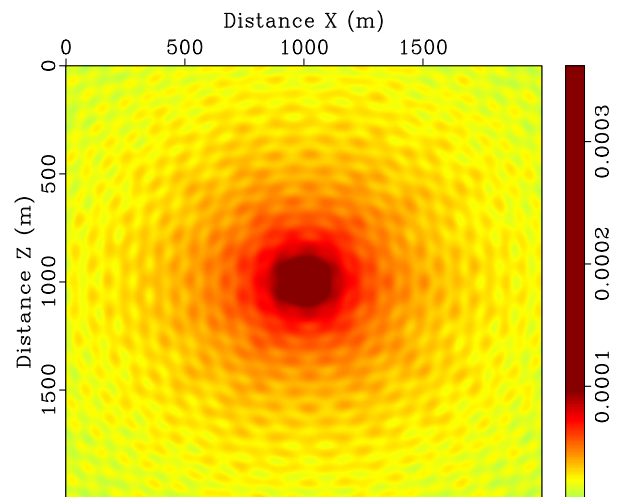
Imag P-Wave a 15 Hz



Imag P-Wave a 15 Hz



Mod P-Wave a 15 Hz



Mod P-Wave a 15 Hz

Figure 3.11: Field P-wave with $m_0 = f$

Figure 3.12: Field P-wave with $m_0 = 0$

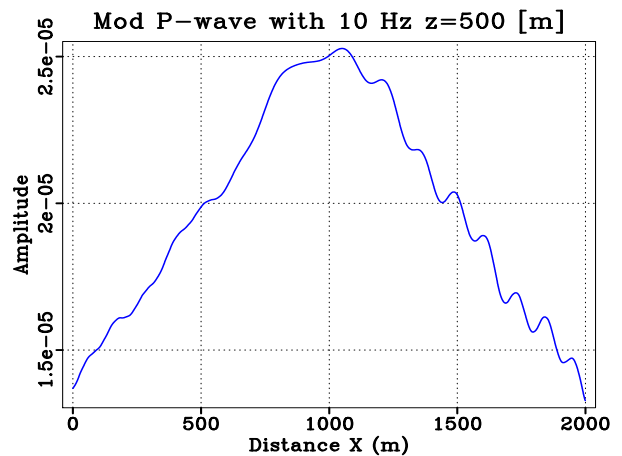
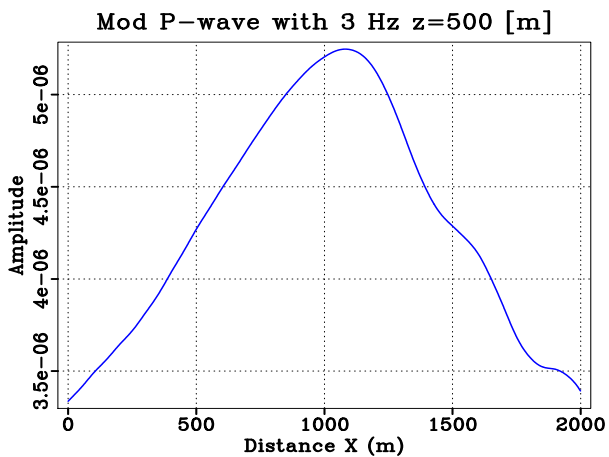
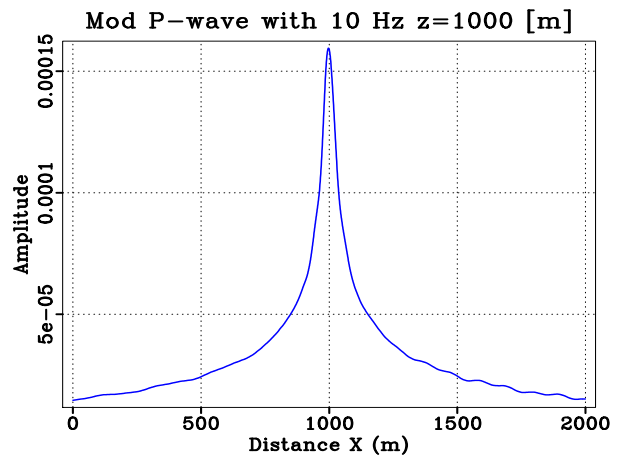
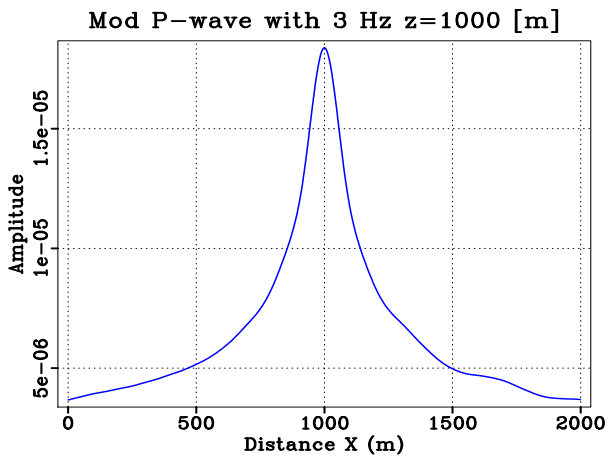
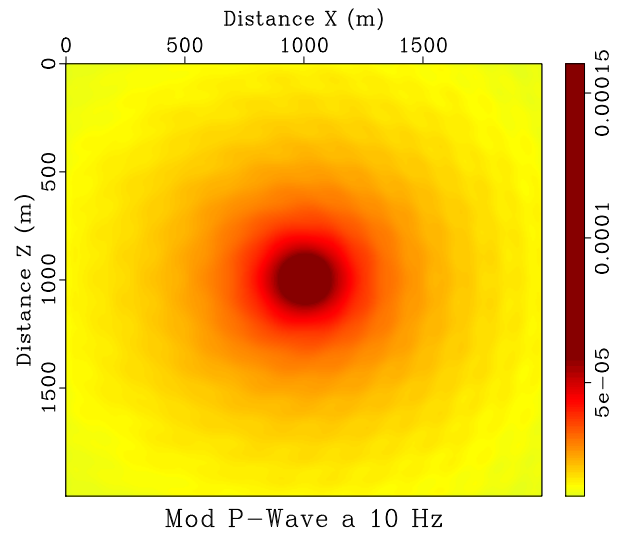
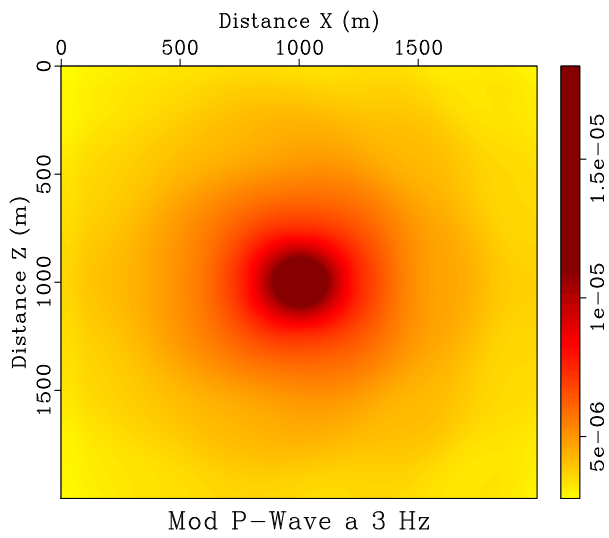


Figure 3.13: Modulus P-wave with $m_0 = 3.0$ and $f = 3$ [Hz]. The first figure show the modulus P-wave for all (x, z) and the following figures show the modulus P-wave for a fixed z .

Figure 3.14: Modulus P-wave with $m_0 = 3.0$ and $f = 10$ [Hz]. The first figure show the modulus P-wave for all (x, z) and the following figures show the modulus P-wave for a fixed z .

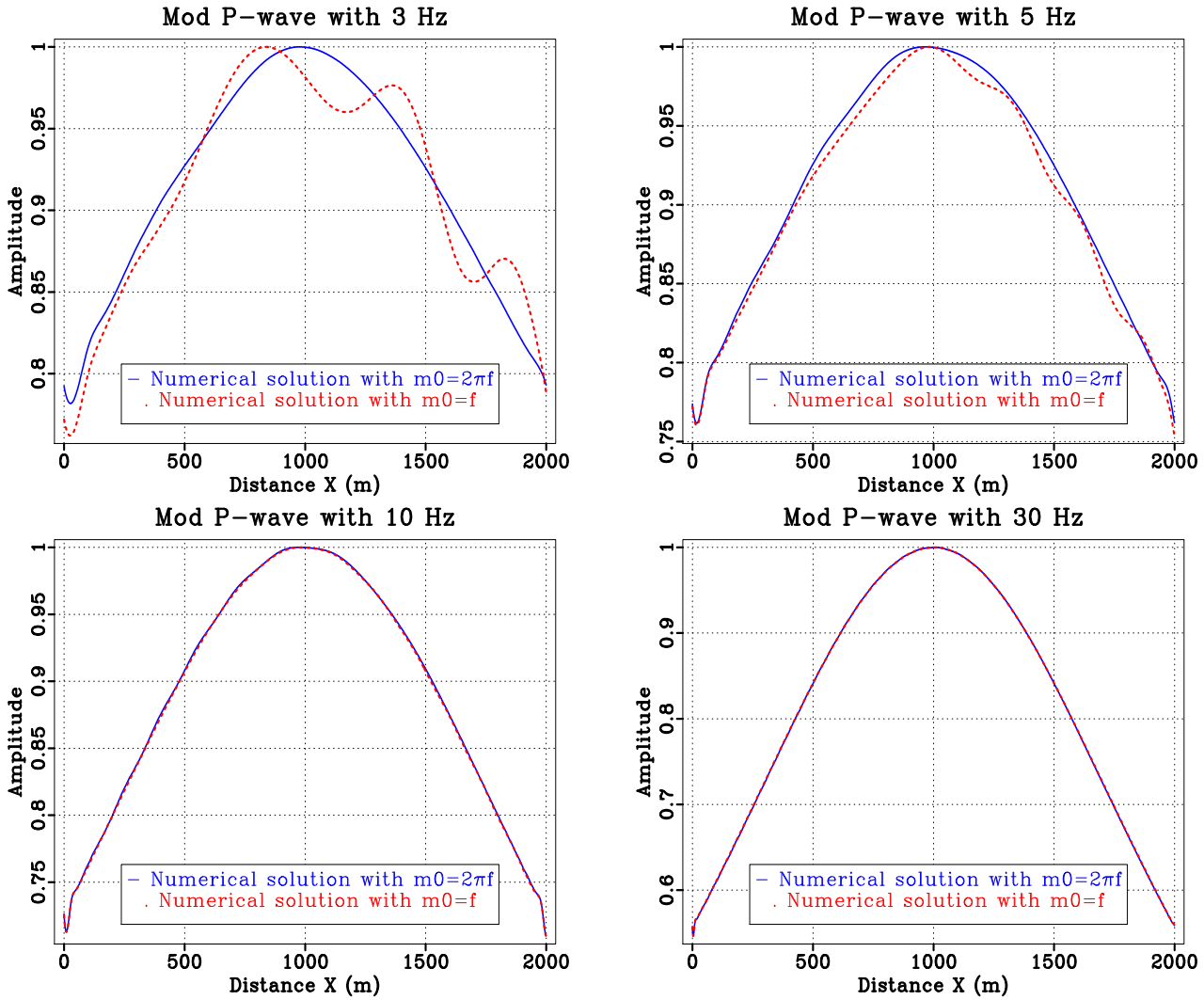


Figure 3.15: Field P-wave with $m_0 = f, \omega$ for $f = 3, 5, 10, 30$ [Hz]

3.7 Numeric solution in visco-acoustic medium and other mediums

Then, with the implementation of the PML the statement of the problem is complete and we can proceed to solve the equation numerically, for the different form of the wave equation presented in the section 2.4 we have the corresponding numerical scheme.

- Visco-acoustic medium ($\rho = \rho(\mathbf{x})$ and $\gamma \neq 0$)

So, with $m = iN_{ze} + j$, $i = 0, 1, 2, \dots, N_{ze} - 1$ and $j = 0, 1, 2, \dots, N_{ze} - 1$ and

$$\begin{aligned}
 A_{(m,n)} = & D_{(m)}\delta_{m,n} + D1_{(m)}\delta_{m,n+N_{ze}} + D2_{(m)}\delta_{m,n-N_{ze}} + D3_{(m)}\delta_{m,n+1} + D4_{(m)}\delta_{m,n-1} \\
 + & D5_{(m)}\delta_{m,n+N_{ze}-1} + D6_{(m)}\delta_{m,n-N_{ze}+1} + D7_{(m)}\delta_{m,n+N_{ze}+1} + D8_{(m)}\delta_{m,n-N_{ze}-1} \quad (3.72)
 \end{aligned}$$

For numerical solution of eq. (2.17) is the solution of $\mathbf{A}\mathbf{p} = \mathbf{s}$.

- Visco-acoustic medium ($\rho = \text{cte}$ and $\gamma \neq 0$)

In this case the numerical solution is the same, solve $\mathbf{A}\mathbf{p} = \mathbf{s}$, but the terms $b_{i\pm 1/2, j\pm 1/2}$, $b_{i\pm 1/2, j}$ and $b_{i, j\pm 1/2}$ in eq. (3.46) to eq. (3.49) disappear (they become equal to 1), and the first term in diagonals $D \frac{\omega^2}{K_{i,j}}$ is turn to be equal to $\frac{\omega^2}{c_{i,j}^2}$.

- Acoustic medium ($\rho = \rho(\mathbf{x})$ and $\gamma=0$)

In this case the numerical solution is the same, solve $\mathbf{A}\mathbf{p} = \mathbf{s}$, but he terms $\xi_{i,j}$, $\xi_{i\pm 1/2, j}$ and $\xi_{i, j\pm 1/2}$ in eq. (3.46) to eq. (3.49) disappear (they become equal to 1) into the workspace \mathcal{U} , the PML still applies in $\partial\mathcal{U}$.

- Acoustic medium ($\rho = \text{cte}$ and $\gamma=0$)

In this case the numerical solution is the same, solve $\mathbf{A}\mathbf{p} = \mathbf{s}$, but the term $b_{i\pm 1/2, j\pm 1/2}$, $b_{i\pm 1/2, j}$ and $b_{i, j\pm 1/2}$ in eq. (3.46) to eq. (3.49) disappear (they become equal to 1) and $\xi_{i\pm 1/2, j}$ and $\xi_{i, j\pm 1/2}$ in eq. (3.46) to eq. (3.49) disappear (they become equal to 1) into the workspace \mathcal{U} , the PML still applies in $\partial\mathcal{U}$.

PHYSICAL ANALYSIS OF THE PROPOSED SOLUTION

In this chapter, we will present several tests and comparisons to physically analyze the proposed solution to the forward problem presented in chapter 3. This part is important to make complete analysis and recognize, in the different models, the dispersion and attenuation effects looking to fully evaluate the proposed solution.

As a first test we model a wave propagating in a medium with constant velocity, density and attenuation. The goal of this test is to compare with the solution of the Helmholtz equation with source that for this special case can be obtained analytically. In this test we have concentrated in two points, the importance of the scale factor in the amplitude and spectrum of the model and the differences between 9-point scheme and 5-point scheme in the solution proposed compared with the analytic solution.

Then we did several tests with different velocity profiles. The density, in this case, was calculated following the relation (Mavko et al., 2009):

$$\rho(\mathbf{x}) = \begin{cases} \sum_{i=1}^5 a_i c(\mathbf{x})^i [\text{Kg}/\text{m}^3] & c(\mathbf{x}) > 1480[\text{m}/\text{s}] \\ 1050 [\text{Kg}/\text{m}^3] & c(\mathbf{x}) < 1480[\text{m}/\text{s}] \end{cases} \quad (4.1)$$

Where constants are $a_1 = 0.000106 \times 10^{-12}$, $a_2 = -0.004300 \times 10^{-9}$, $a_3 = 0.067100 \times 10^{-6}$, $a_4 = -0.472100 \times 10^{-3}$ and $a_5 = 1.6612$.

Besides, in the cases we have discussed below, the values for the quality factor associated with the different values of the velocity in the multiple layer media are modelled according to the table 4.1 (taken from (Lavergne, 1986))

Table 4.1: Relation between Quality Factor and velocity for Material

Material	Quality Factor	Velocity Range [m/s]
Clays	30-70	1100 - 2500
Marls	30-70	2000 - 3000
Sands (Welt)	70-150	1500 - 4000
Sandstones	70-150	3000 - 4500
Limestones	100 - 600	3500 - 6000
Dolomites	100 - 600	3500 - 6500
Granites	200 - 600	4500 - 6000
Basalts	200 - 600	5000 - 6000

To finish, we compare the P-wave fields obtained for all cases:

1. Visco-acoustic Medium ρ variable
2. Visco-acoustic Medium ρ constant
3. Acoustic Medium ρ variable
4. Acoustic Medium ρ constant

It is important to make a good physical analysis of the proposed solution of an attenuated medium with variable density, compared with other simpler medium to make visible the effects of attenuation and dispersion. So, once defined the optimal parameters for the discretization, we can model the propagation of a P-wave in media with different velocity profiles and verify the performance of the numerical approach we propose.

4.1 Numerical solution vs Analytic solution

In frequency domain, the Helmholtz equation with source (eq 2.15), can be written as

$$\tilde{k}^2 P(\omega, \mathbf{x}, \gamma) + \nabla^2 P(\omega, \mathbf{x}, \gamma) = S(\omega, \gamma). \quad (4.2)$$

Where $S(\omega, \gamma)$ is a source. An analytic solution to this equation is (Chen, 2004)

$$P(\omega, \mathbf{x}, \gamma) = i\pi H_0^{(2)}\left(\frac{\omega - i\gamma}{c}r\right) S(\omega, \gamma). \quad (4.3)$$

Where r accounts for the distance between the source and any point with coordinates (x, z) and is given by

$$r^2 = (x - x_s)^2 + (z - z_s)^2. \quad (4.4)$$

With x_s and z_s the position of the source.

4.1.1 9-point scheme and 5-point scheme

In order to compare the results of this analytic solution with results obtained with the 9-point and 5-point schemes, we compute the value of the P-wave amplitude in an area of $2[\text{Km}] \times 2[\text{Km}]$, by placing a line of receivers at 100 [m] and 1100[m], finding the waveform response at that point. The constant velocity of the media is 2100 [m/s], the Ricker frequency is 30 [Hz], the constant quality factor is $Q = 50$. Using the damping function eq. (2.15), the cell size Δ is $\frac{\lambda}{G_r}$, where $G_r = 7$, scale PML $m_0 = \omega$, scale factor $s = 0.75$ and the position of the source is $x_s = 1[\text{Km}]$ and $z_s = 1[\text{Km}]$. In this test we will compute the real and imaginary part of field P-wave for 9-point scheme and 5-point scheme.

In Fig. 4.1 we show the normalized amplitude of the real part P-wave as a function of the offset for shots in the receivers at 1100 [m] deep (near the source) and difference between real part P-wave found by the analytic solution and 9-point scheme and 5-point scheme, at three different frequencies. In Fig. 4.2 we show the normalized amplitude of the real part P-wave as a function of the offset for shots in the receivers at 100 [m] deep (far from the source) and difference between real part P-wave found by the analytic solution and 9-point scheme and 5-point scheme, at different frequencies.

In Fig. 4.3 we show the normalized amplitude of the imaginary part P-wave as a function of the offset for shots in the receivers at 1100 [m] deep (near the source) and difference between real part P-wave found by the analytic solution and 9-point scheme and 5-point scheme, at three different frequencies. In Fig. 4.4 we show the normalized amplitude of the imaginary part P-wave as a function of the offset for shots in the receivers at 100 [m] deep (far from the source) and difference between real part P-wave found by the analytic solution and 9-point scheme and 5-point scheme, at different frequencies.

Amplitudes are normalized dividing by its maximum value. The solid line is the analytic solution, the dashed line is the solution for 5-point scheme and the points is a solution for 9-point scheme. It is worth to note that for all frequencies the solution obtained by the 9-point scheme is the closest to the analytic solution.

One can also see the strong disagreement with the 5-point scheme, especially at P-waves away from the source, this is due mainly to numerical dispersion and grid point number, for 5-scheme point (See Fig 2.3) for $\tau_r = 0.15$ the relation between $\frac{k_r^N}{k_r^T}$ is about 0.98, when the optimal value is close to 1.0, the dispersion at P-waves away from the source is more noticeable because the effect of pollution propagates with distance, the numerical dispersion makes the P-wave to be out of phase.

In order to avoid such dispersion in the solution for the 5-point scheme, we would have to use a larger number of points (Jo, 1996) and that would mean a larger computational cost. In that sense we can conclude that the scheme 9-points provides an appropriate solution at an acceptable computational cost.

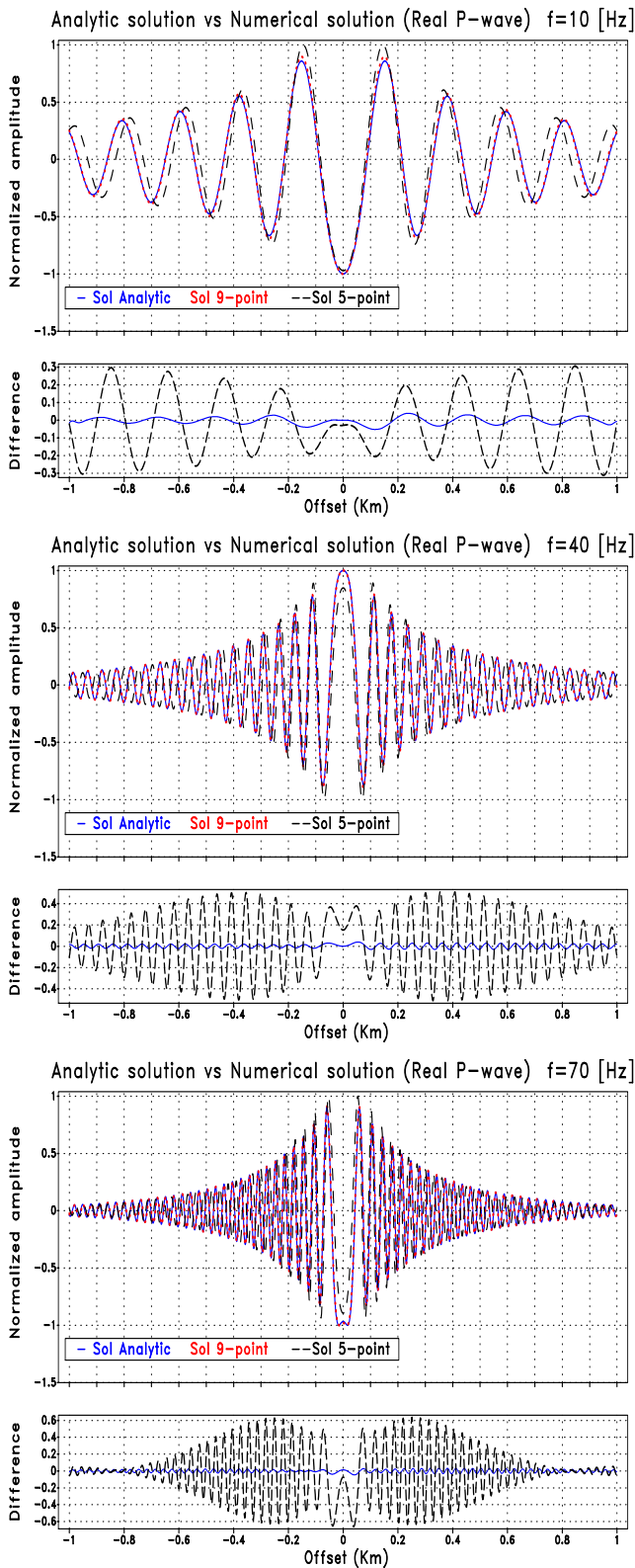


Figure 4.1: Shots (Real part) propagating in medium with constant velocity, density and attenuation for $f = 10, 40, 70$ [Hz] and receivers in $z = 1100$ [m] deep (close to the source in $z = 1000$ [m])

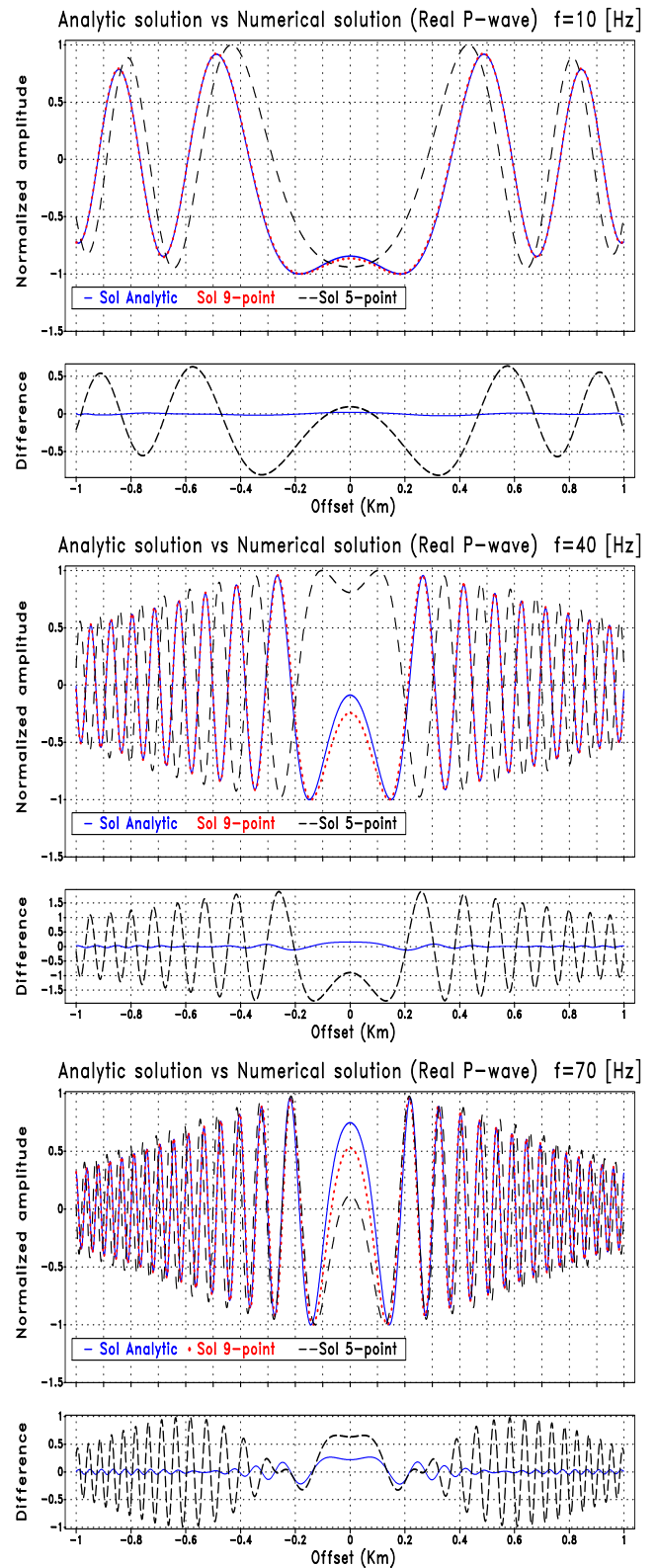


Figure 4.2: Shots (Real part) propagating in medium with constant velocity, density and attenuation for $f = 10, 40, 70$ [Hz] and receivers in $z = 100$ [m] deep (away from the source in $z = 1000$ [m])

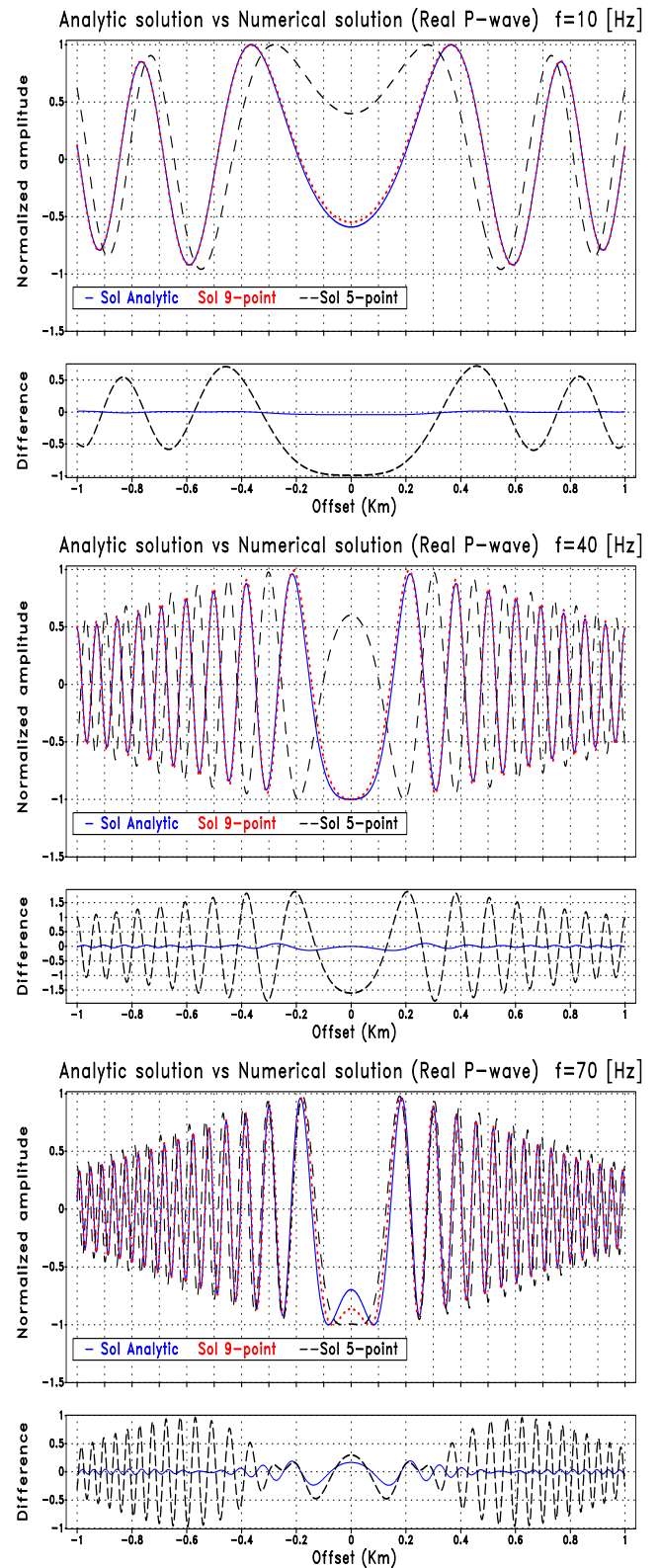
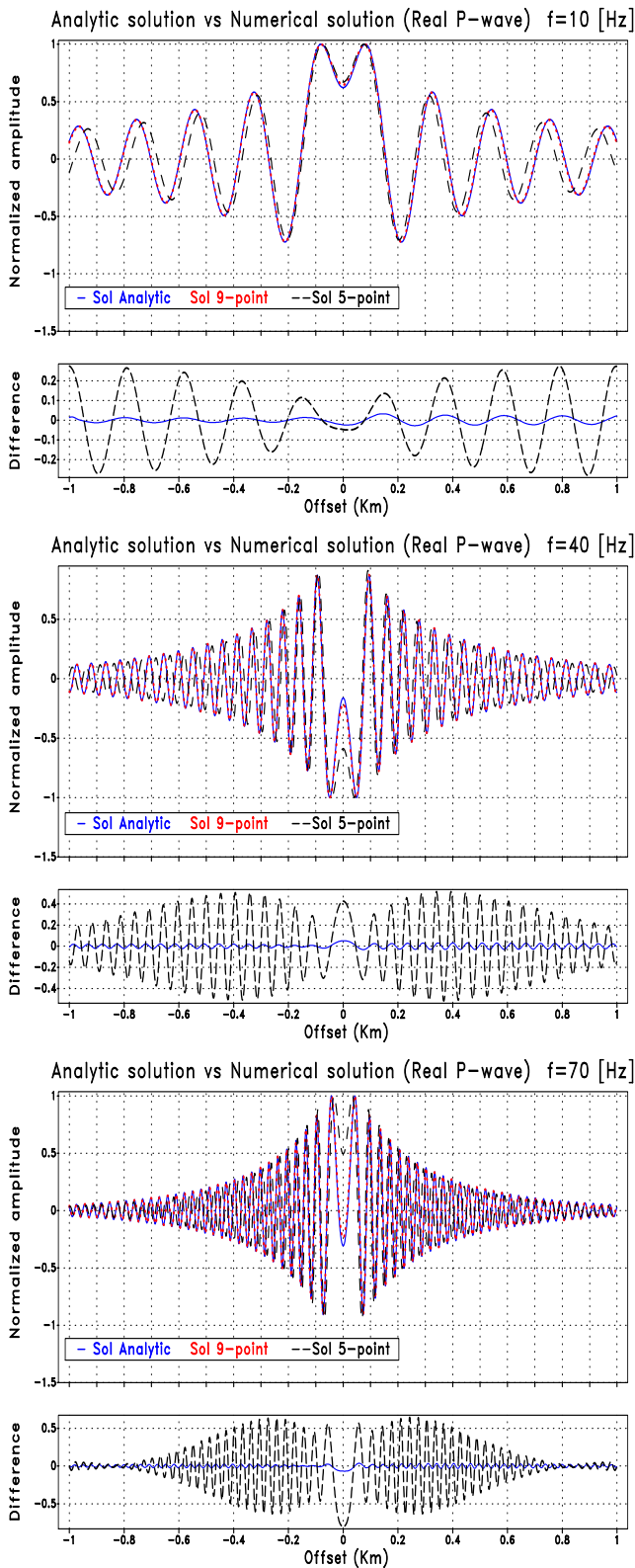


Figure 4.3: Shots (Imaginary part) propagating in medium with constant velocity, density and attenuation for $f = 10, 40, 70$ [Hz] and receivers in $z = 1100$ [m] deep (close to the source in $z = 1000$ [m])

Figure 4.4: Shots (Imaginary part) propagating in medium with constant velocity, density and attenuation for $f = 10, 40, 70$ [Hz] and receivers in $z = 100$ [m] deep (away from the source in $z = 1000$ [m])

4.1.2 The Scale factor of the source

In this test we compute the modulus of P-wave for a source, calculated with ec. 3.61 with different factor scale $s = (0.5, 0.75, 1.0, 2.0)$ for frequencies from 1 to 50 [Hz], source frequency $f_s = 30$ [Hz], the position of the source is $x_s = 1$ [Km] and $z_s = 1$ [Km] and $x_s = 1$ [Km] and $z_s = 0.015$ [Km].

In Fig. 4.5 we show the normalized amplitude of modulus P-wave as a function of the frequency for shots in the receivers at $z = 1100$ [m] and $x = 1000$ [m] (near the source) found by the analytic solution (solid line) and 9-point scheme (point line) for source frequency $f_s = 30$ [Hz] and different scale factor s , the position of the source is $x_s = 1$ [Km] and $z_s = 1$ [Km].

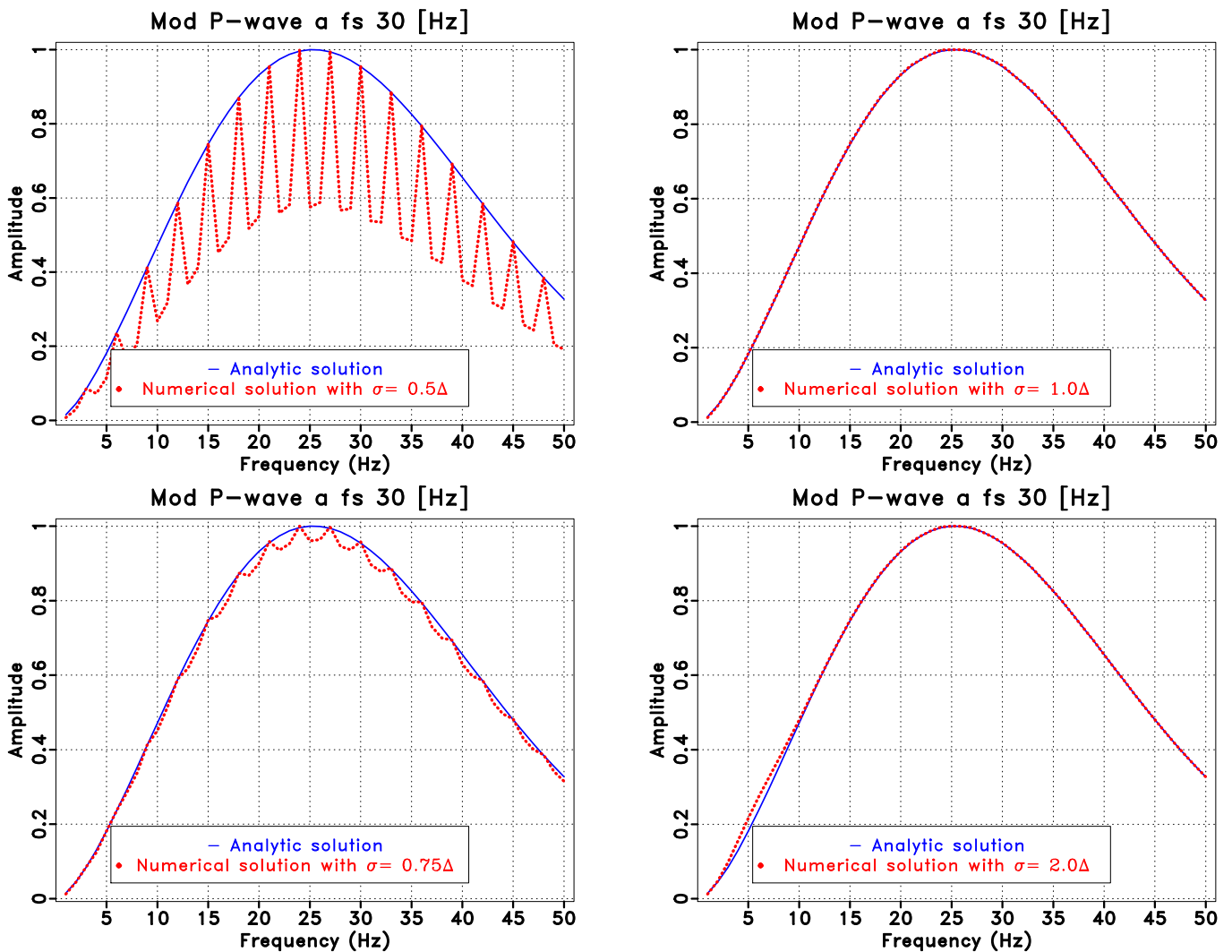


Figure 4.5: Modulus P-Wave propagating in medium with constant velocity, density and attenuation for $f = 1, 2, \dots, 50$ [Hz] in point $z = 1100$ [m] and $x = 1000$ [m] (near the source), with different σ , the position of the source is $x_s = 1$ [Km] and $z_s = 1$ [Km]

In Fig. 4.6 we show the normalized amplitude of modulus P-wave as a function of the frequency for shots in the receivers at $z = 100$ [m] and $x = 1000$ [m] (away from the source) found by the analytic solution (solid line) and 9-point scheme (point line) for source frequency $f_s = 30$ [Hz] and different scale factor s , the position of the source is $x_s = 1$ [Km] and $z_s = 1$ [Km].

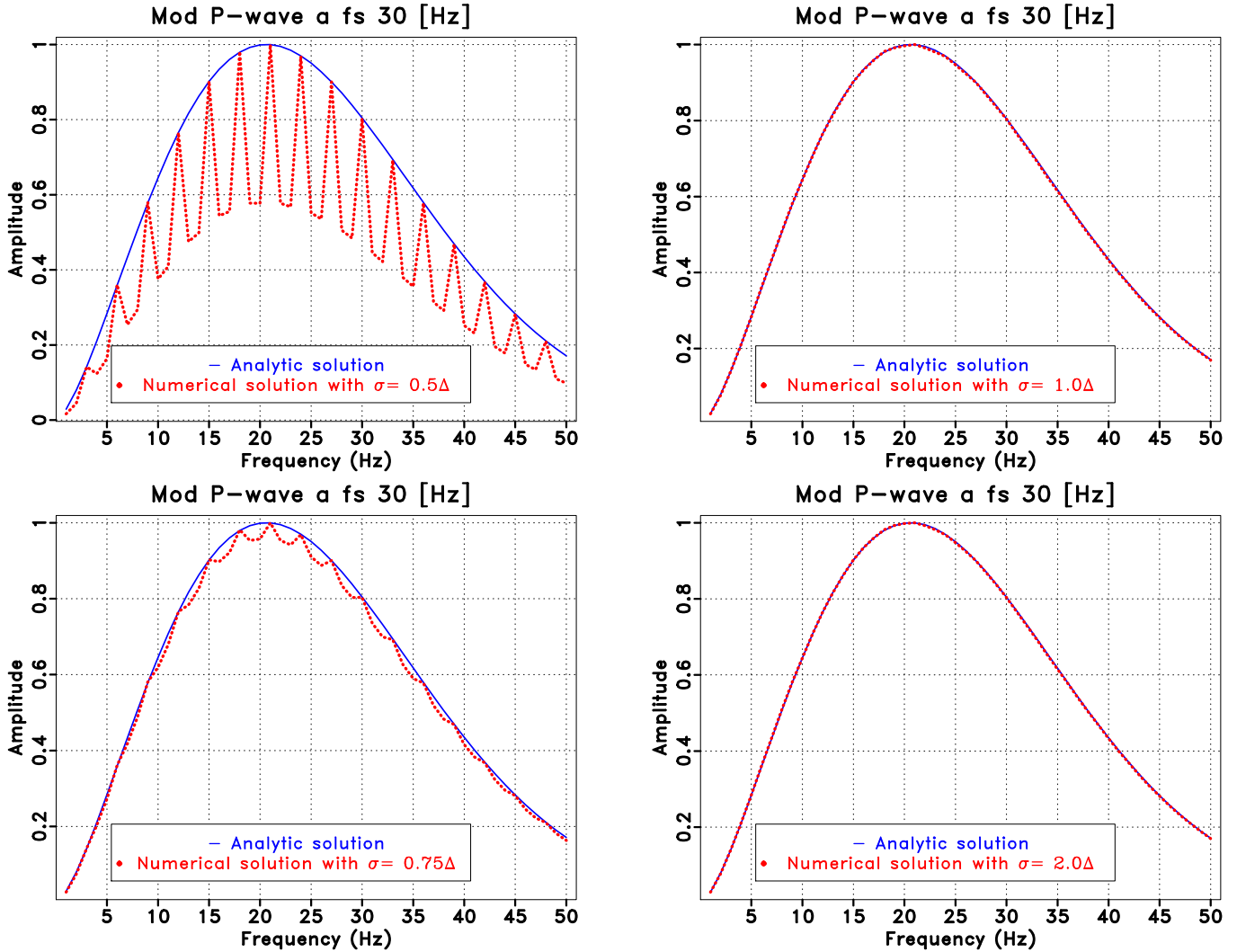


Figure 4.6: Modulus P-Wave propagating in medium with constant velocity, density and attenuation for $f = 1, 2, \dots, 50$ [Hz] in point $z = 100$ [m] and $x = 1000$ [m] (away from the source), with different σ , the position of the source is $x_s = 1$ [Km] and $z_s = 1$ [Km]

We can see that the solution using $\sigma = 0.5\Delta$ is not adequate in figures 4.5 and 4.6, the spectrum has a saw-like shape, which indicates that the discretization of the dirac delta is too unstable, as we expected according to the figure 3.5.

The other factors seem adequate for $\sigma = 0.75\Delta$ there is some instability, as discussed in section 3.5, the change in the values of the integral and the fact that the width of the Gaussian is smaller

than the cell size generates a certain discontinuity in the form of the spectrum, $\sigma = 1.0\Delta$ presents a perfect match, $\sigma = 2.0\Delta$ is adequate but near the source has a delay (see 4.5), this is due to the fact that at low frequencies the factor scale $s = 2$ did not properly discriminate the source and is something very close to it.

In Fig. 4.7 we show the normalized amplitude of modulus P-wave as a function of the frequency for shots in the receivers at $z = 100$ [m] and $x = 1000$ [m] (near the source) found by the analytic solution (solid line) and 9-point scheme (point line) for source frequency $f_s = 30$ [Hz] and different scale factor s , the position of the source is $x_s = 1$ [Km] and $z_s = 0.015$ [Km].

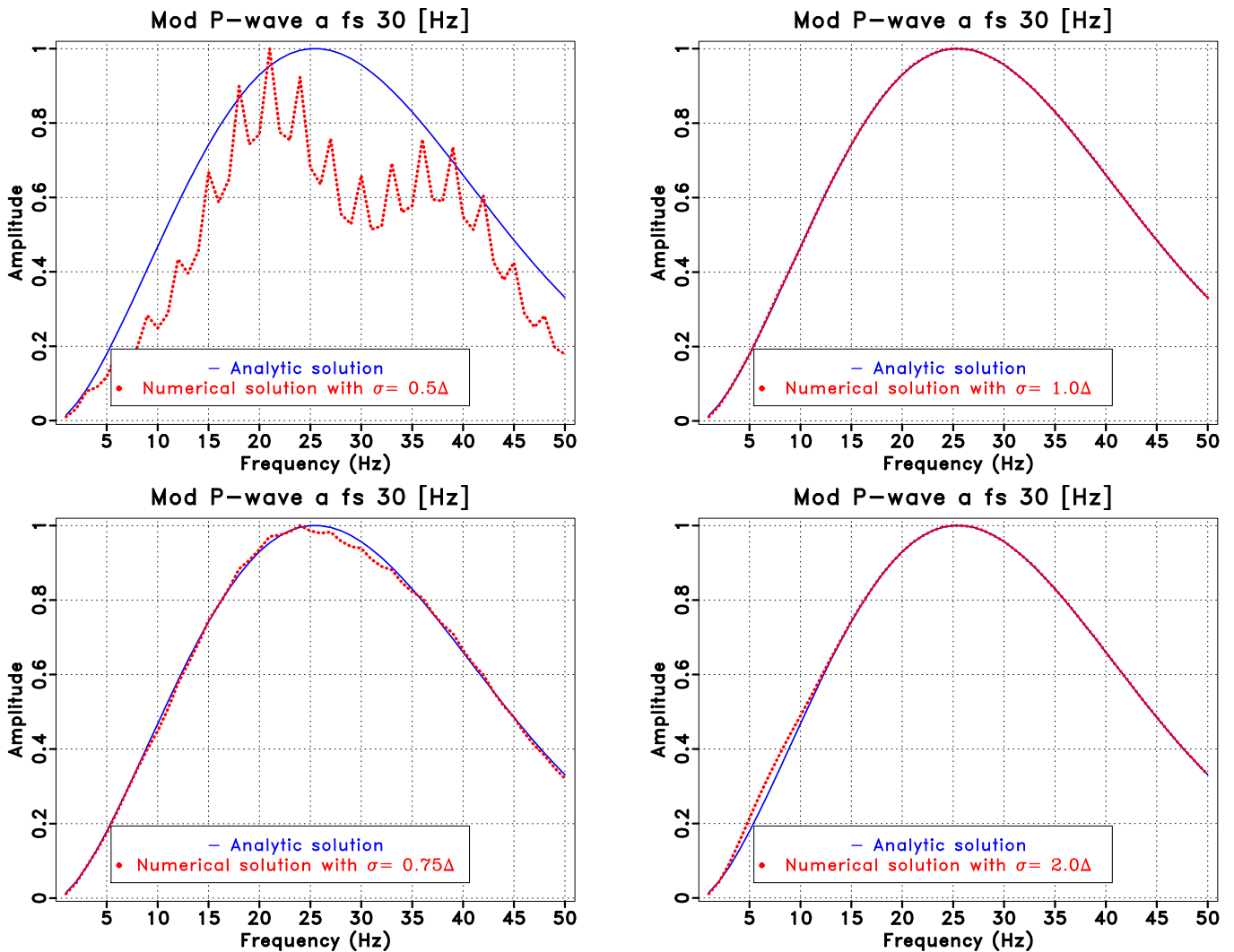


Figure 4.7: Modulus P-Wave propagating in medium with constant velocity, density and attenuation for $f = 1, 2, \dots, 50$ [Hz] in point $z = 100$ [m] and $x = 1000$ [m] (near the source), with different σ , the position of the source is $x_s = 1$ [Km] and $z_s = 0.015$ [Km]

In Fig. 4.8 we show the normalized amplitude of modulus P-wave as a function of the frequency for shots in the receivers at $z = 1100$ [m] and $x = 1000$ [m] (away from the source) found by the

analytic solution (solid line) and 9-point scheme (point line) for source frequency $f_s = 30$ [Hz] and different scale factor s , the position of the source is $x_s = 1$ [Km] and $z_s = 1$ [Km].

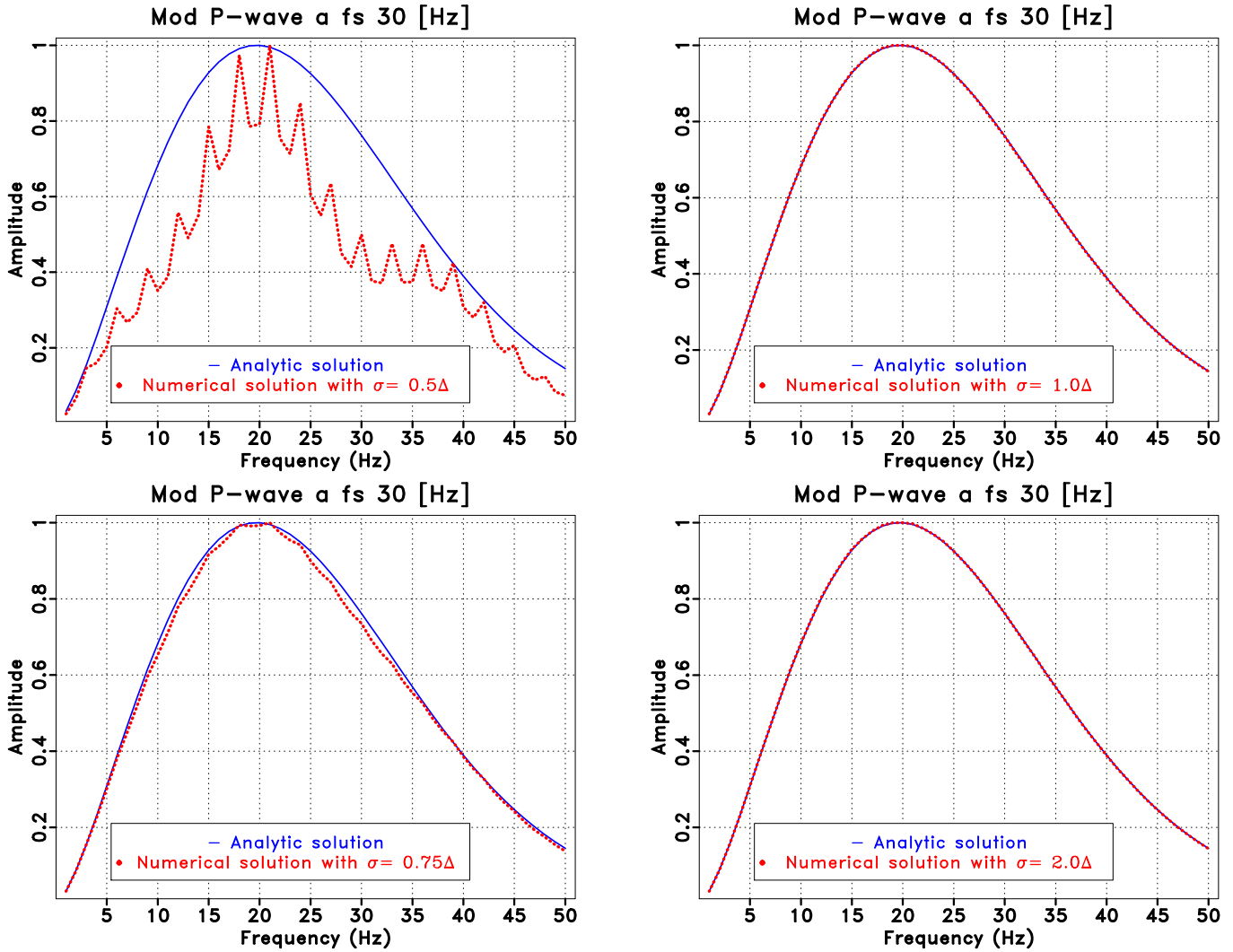


Figure 4.8: Modulus P-Wave propagating in medium with constant velocity, density and attenuation for $f = 1, 2, \dots, 50$ [Hz] in point $z = 1100$ [m] and $x = 1000$ [m] (near the source), with different σ , the position of the source is $x_s = 1$ [Km] and $z_s = 0.15$ [Km]

We can see in the figures that the solution using $\sigma = 0.5\Delta$ is not adequate again, the spectrum has a saw-like shape, which indicates that the discretization of the dirac delta is too unstable, as we expected according to the figure 3.6. The other factors seem adequate, but in figure 4.7 we can see a little difference at low frequencies for $\sigma = 2.0\Delta$ with respect to the analytic solution. This is expect according to the figures 3.6 and 3.7, because for low frequency and $\sigma = 2.0\Delta$ the integral of the discrete form of the dirac delta is less than 1.0.

The difference between the factor scale $s = 0.75$ and $s = 1.0$ is the behavior of the integral at low frequencies, for this we perform a test with source frequency $f_s = 10$ [Hz]. In this test we compute the modulus of P-wave for a source, calculated with eq. 3.61 with different factor scale

$s = (0.75, 1.0)$ for frequencies from 1 to 20 [Hz], source frequency $f_s = 10$ [Hz], the position of the source is $x_s = 1$ [Km] and $z_s = 1$ [Km] and $x_s = 1$ [Km] and $z_s = 0.015$ [Km].

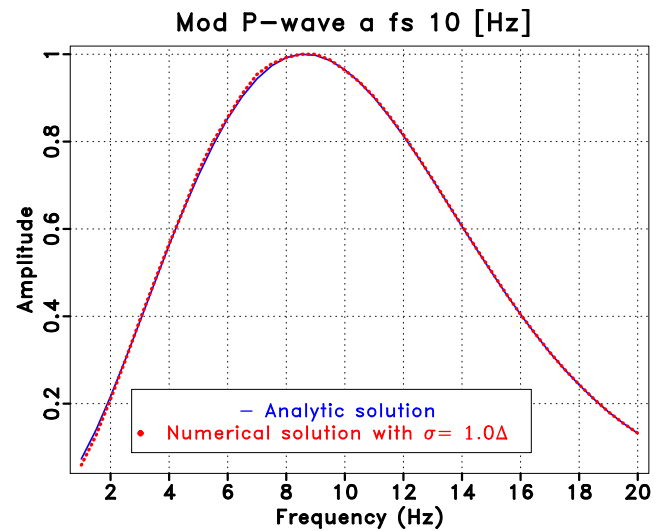
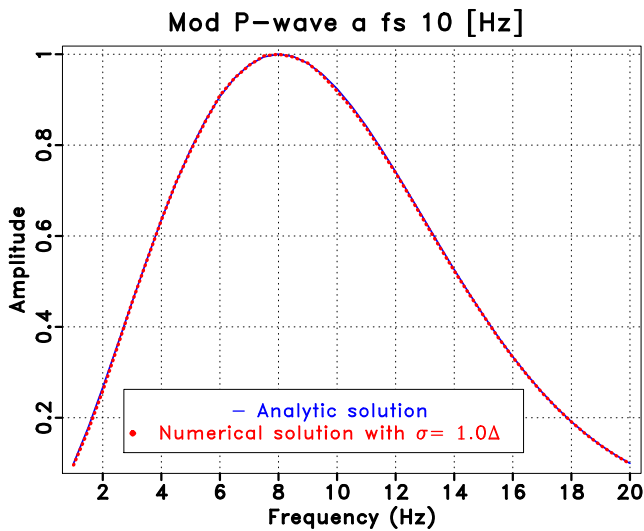
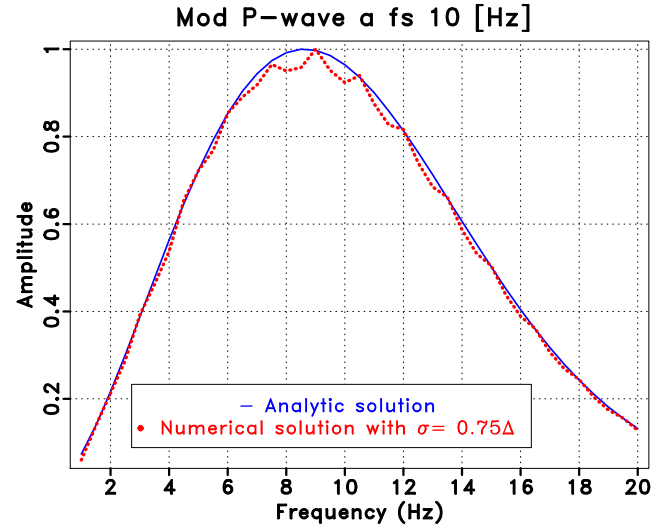
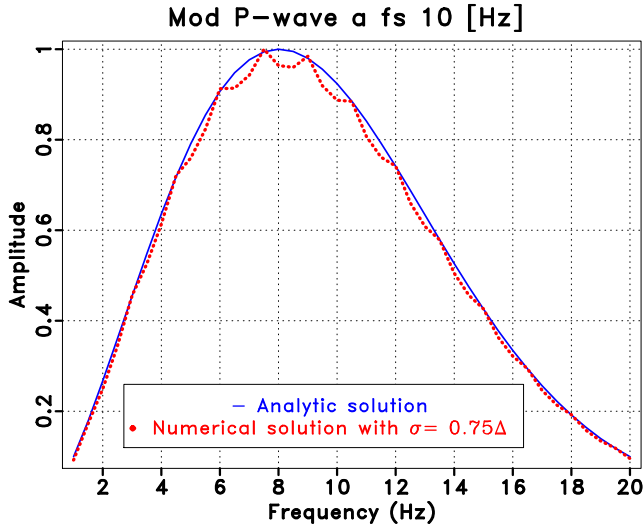


Figure 4.9: Modulus P-Wave propagating in medium with constant velocity, density and attenuation for $f = 1, 1.5, 2, \dots, 20$ [Hz] in point $z = 100$ [m] and $x = 1000$ [m] (away from the source), with different σ , the position of the source is $x_s = 1$ [Km] and $z_s = 1$ [Km]

Figure 4.10: Modulus P-Wave propagating in medium with constant velocity, density and attenuation for $f = 1, 1.5, 2, \dots, 20$ [Hz] in point $z = 1100$ [m] and $x = 1000$ [m] (near the source), with different σ , the position of the source is $x_s = 1$ [Km] and $z_s = 1$ [Km]

In Fig. 4.9 and 4.10, we show the normalized amplitude of modulus P-wave as a function of the frequency for shots in the receivers at $z = 100$ [m] and $x = 1000$ [m] (away from the source) and $z = 1100$ [m] and $x = 1000$ [m] (near the source) found by the analytic solution (solid line) and 9-point scheme (point line) for source frequency $f_s = 10$ [Hz] and different scale factor s , the position of the source is $x_s = 1$ [Km] and $z_s = 1$ [Km]. We can see in the figures that $\sigma = 0.75\Delta$ has good results but the spectrum does not have a smooth form with $\sigma = 1.0\Delta$.

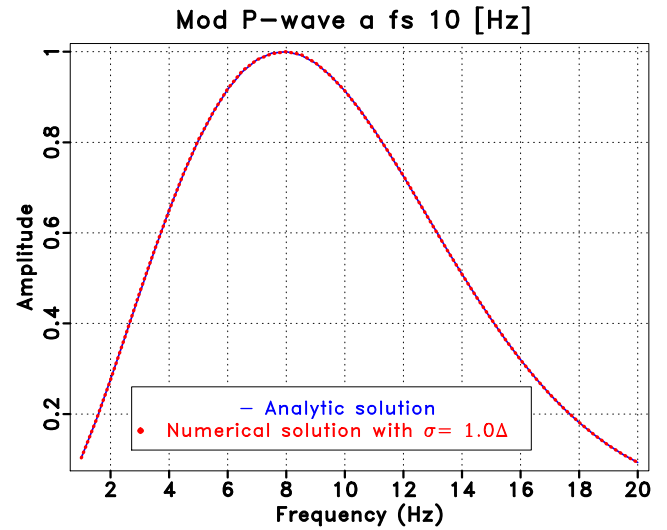
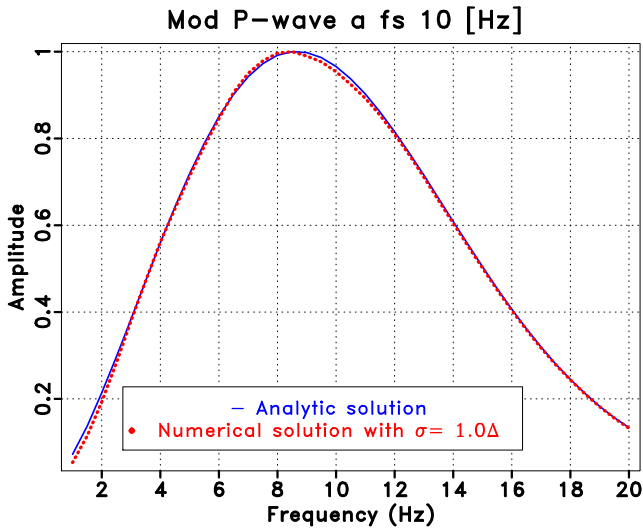
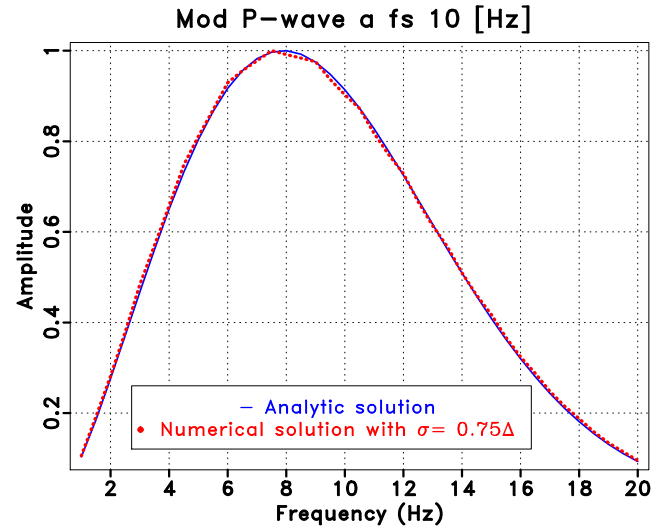
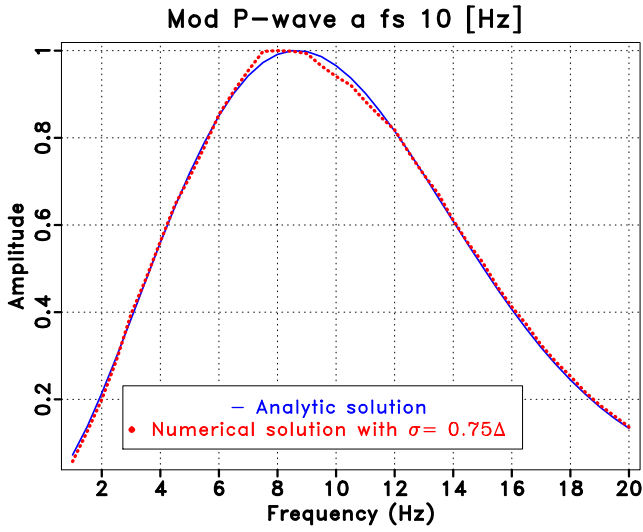


Figure 4.11: Modulus P-Wave propagating in medium with constant velocity, density and attenuation for $f = 1, 1.5, 2, \dots, 20$ [Hz] in point $z = 100$ [m] and $x = 1000$ [m] (near the source), with different σ , the position of the source is $x_s = 1$ [Km] and $z_s = 0.015$ [Km]

Figure 4.12: Modulus P-Wave propagating in medium with constant velocity, density and attenuation for $f = 1, 1.5, 2, \dots, 20$ [Hz] in point $z = 1100$ [m] and $x = 1000$ [m] (away from the source), with different σ , the position of the source is $x_s = 1$ [Km] and $z_s = 0.015$ [Km]

In Fig. 4.11 and 4.12 we show the normalized amplitude of modulus P-wave as a function of the frequency for shots in the receivers at $z = 100$ [m] and $x = 1000$ [m] (near the source) and $z = 1100$ [m] and $x = 1000$ [m] (away from the source) found by the analytic solution (solid line) and 9-point scheme (point line) for source frequency $f_s = 10$ [Hz] and different scale factor s , the position of the source is $x_s = 1$ [Km] and $z_s = 0.015$ [Km].

Now in this case, we can see how it affects the value of the integral for $s = 1.0$, which at low frequencies is greater than for $s = 0.75$ (see 3.7). The figure 4.11 with $\sigma = 1.0\Delta$ has a small delay in low frequencies, but it is not enough to consider that $\sigma = 0.75\Delta$ is a better option for the discretization of Gaussian.

In conclusion we can work with a scale factor between $s = [0.75, 1.0]$ depending on the frequencies to which we model.

4.2 Media with variable velocity, density and attenuation

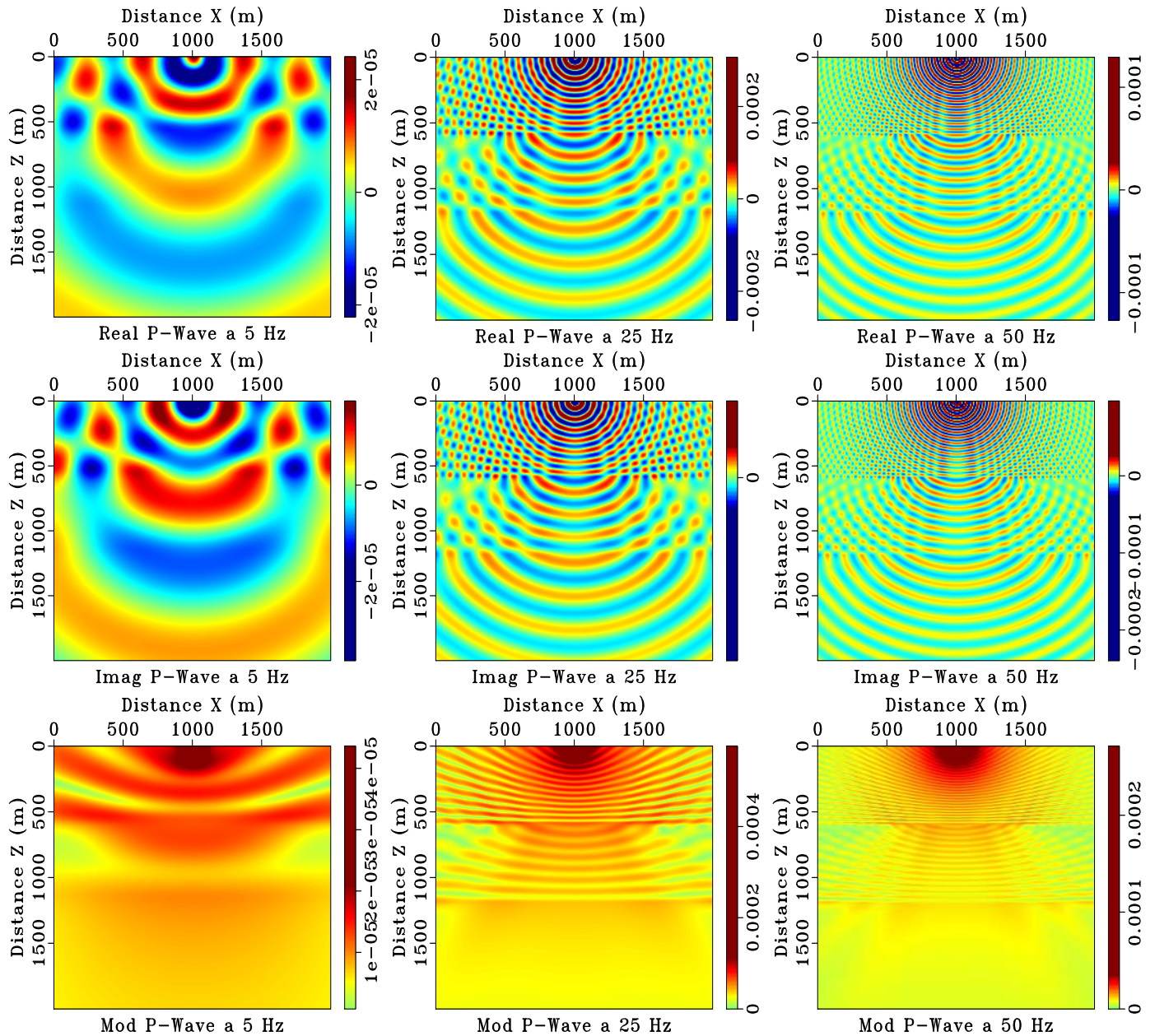


Figure 4.13: P-wave 5 [Hz].
Three Layers

Figure 4.14: P-wave 25 Hz.
Three Layers

Figure 4.15: P-wave 50 Hz.
Three Layers

4.2.1 Three Layers velocity profile

The following tests are performed with different velocity profiles. The P-wave field is computed in a configuration of three layers, with velocity $v_1 = 2100$ [m/s] at a depth of $[0, 0.6]$ [Km], $v_2 = 4300$ [m/s] at $(0.6, 1.2)$ [Km] and $v_3 = 6500$ [m/s] at $(1.2, 2.0)$ [Km] and with the source in surface at 15 [m] deep.

In figure 4.13 we show the real, imaginary and modulus of the P-wave field for frequency 5 [Hz]. At that low frequency regime, the reflectors are not well defined due to the fact that the wavelength is too large compared with the features and the scale of the discretization, and one can not define the exact position of the reflectors or anomalies at scales smaller than the wavelength of the perturbation, however the oscillation is uniform.

In figures 4.14 and 4.15 we show the same for frequencies of 25 [Hz] and 50 [Hz] respectively. Note that increasing the frequency the reflectors become more visible, but given that the gradient of the velocity is smooth there is continuity in the propagation of waves, as expected if we had relatively continuous profiles.

4.2.2 Complex velocity profile

For this test we decided to use a complex velocity profile. As it can be seen in Figure (4.16), in this case we have several wedges and important discontinuities with velocity contrast ranging from ~ 1.2 to ~ 3 [Km/s]. For this setup the source is close to the surface at 15 [m] depth.

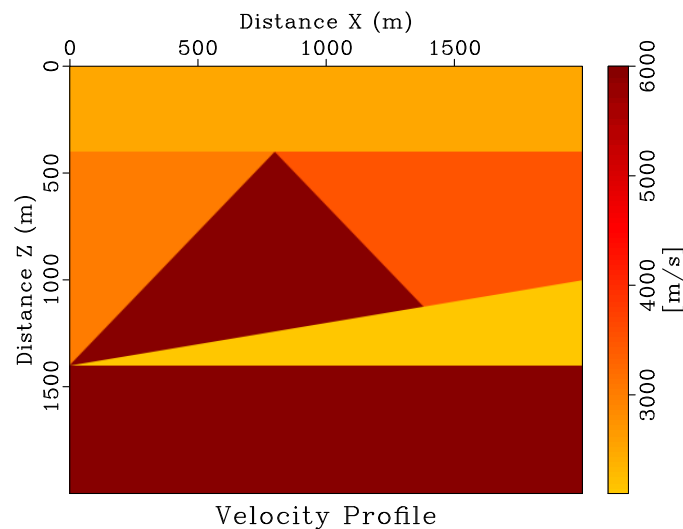


Figure 4.16: Geometric configuration of the velocity profile

In figures 4.17, 4.18 and 4.19 we show the real, imaginary part and modulus of the P-wave field for frequencies of 5, 25 and 50 [Hz]. The result is less uniform than in the previous figures, revealing a natural response to the anisotropy of the velocity field. One can see how the features of the velocity field can distort the wavefront, even at large distances. Numerical dispersion have been minimized, so most of what can be seen is real response of the wave propagating inside the complex media.

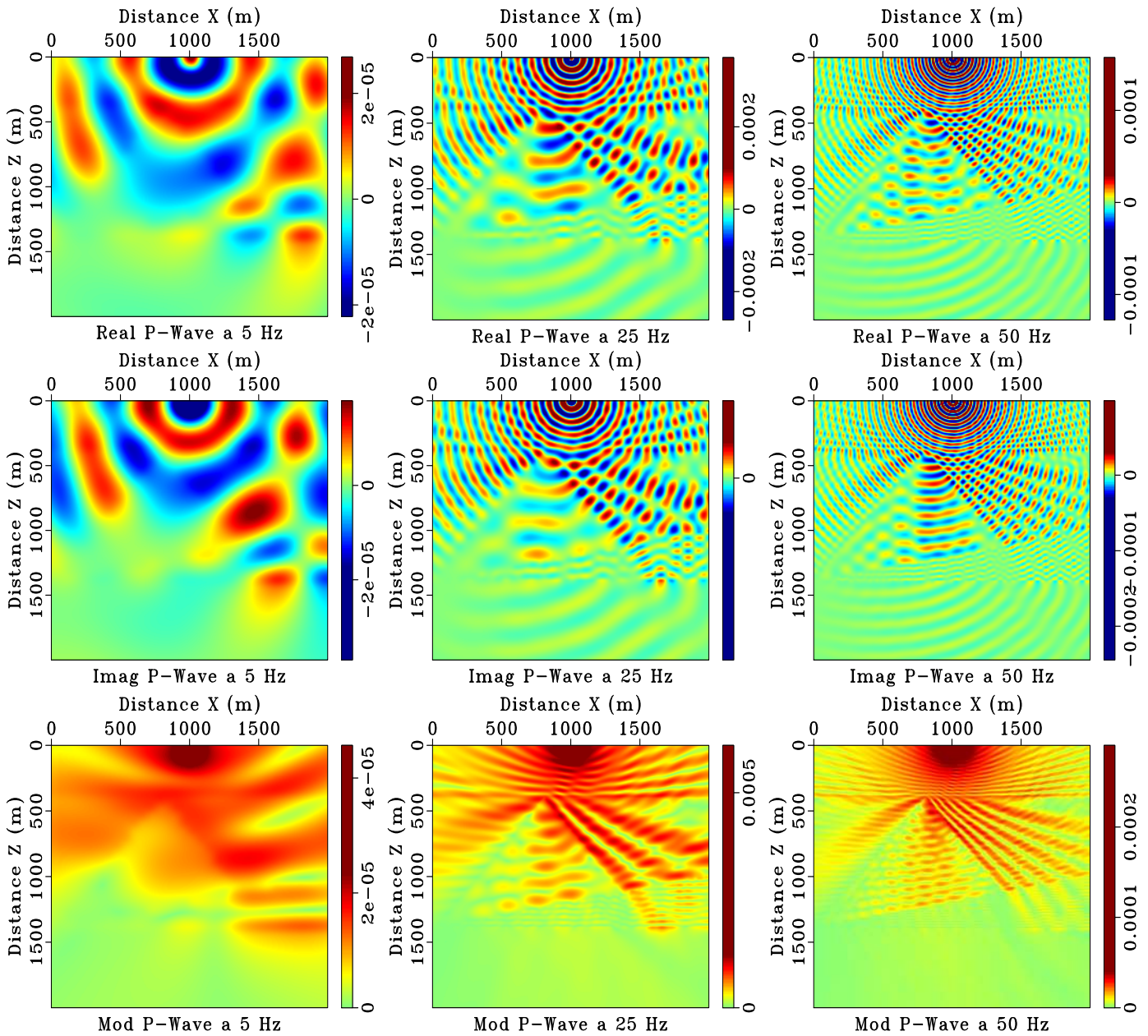


Figure 4.17: P-wave 5 [Hz].
Complex velocity profile

Figure 4.18: P-wave 25 Hz.
Complex velocity profile

Figure 4.19: P-wave 50 Hz.
Complex velocity profile

4.2.3 Marmousi velocity profile

Now, for this test we used a Marmousi velocity profile, fig (4.20). This is a popular velocity profile in the seismic literature and have several wedges and important discontinuities with velocity contrast and large lateral variation. For this setup the source is close to the surface at 15 [m] depth.

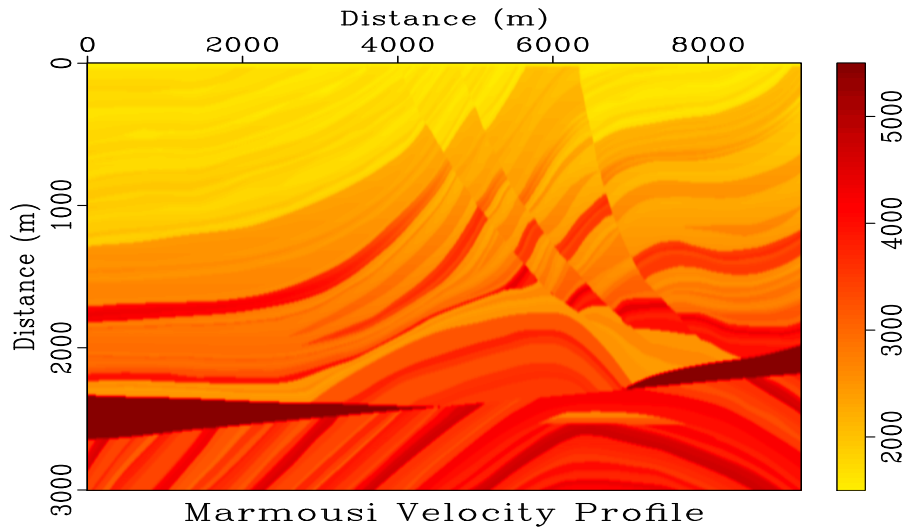


Figure 4.20: Marmousi velocity profile

In figures 4.21, 4.22 and 4.23 we show the real, imaginary part and modulus of the P-wave field for frequencies of 5, 25 and 50 [Hz]. The result is less uniform than in the previous figures, revealing a natural response to the anisotropy of the velocity field. One can see how the features of the velocity field can distort the wavefront, even at large distances. Numerical dispersion have been minimized, so most of what can be seen is real response of the wave propagating inside the complex media as in the Marmousi field velocity.

4.3 Wave propagation in other mediums

The following tests are performed with different medium: acoustic vs visco-acoustic with density variable and visco-acoustic with density constant vs visco-acoustic with density variable, such that equation 2.17 is reduced to equations 2.28 and 2.29.

Using 9-point scheme for numerical solution, in acoustic and visco-acoustic medium, we obtain P-wave field for 3 medium and P-wave amplitude for a line of receivers in x and z position, to obtain a better comparison between the solution for visco-acoustic medium with constant and variable density, and acoustic and visco-acoustic medium with variable density in order to visualize the effects of density and viscosity in the solution. It is important to add that for the comparison to be adequate, it will be used for acoustic modeling the grid -point $G = 7$, although $G = 4$ is recommended in the literature for acoustic medium (Jo, 1996). This to avoid the differences produced by the grid spacing.

In this test we show the real, imaginary part and modulus of the P-wave for frequency of $f = [5, 25, 50]$ [Hz] for this 3 medium with source in $x = 1000$ [m] and $z = 15$ [m] with Ricker frequency 30 [Hz], the domain is 2 [Km] \times 2 [Km]. with three layers velocity with $v_1 = 2100$ [m/s] at a depth of $[0, 0.6]$ [Km], $v_2 = 4100$ [m/s] at $(0.6, 1.2)$ [Km] and $v_3 = 6500$ [m/s] at $(1.2, 2.0)$ [Km] and complex velocity profile show in figure (4.16).

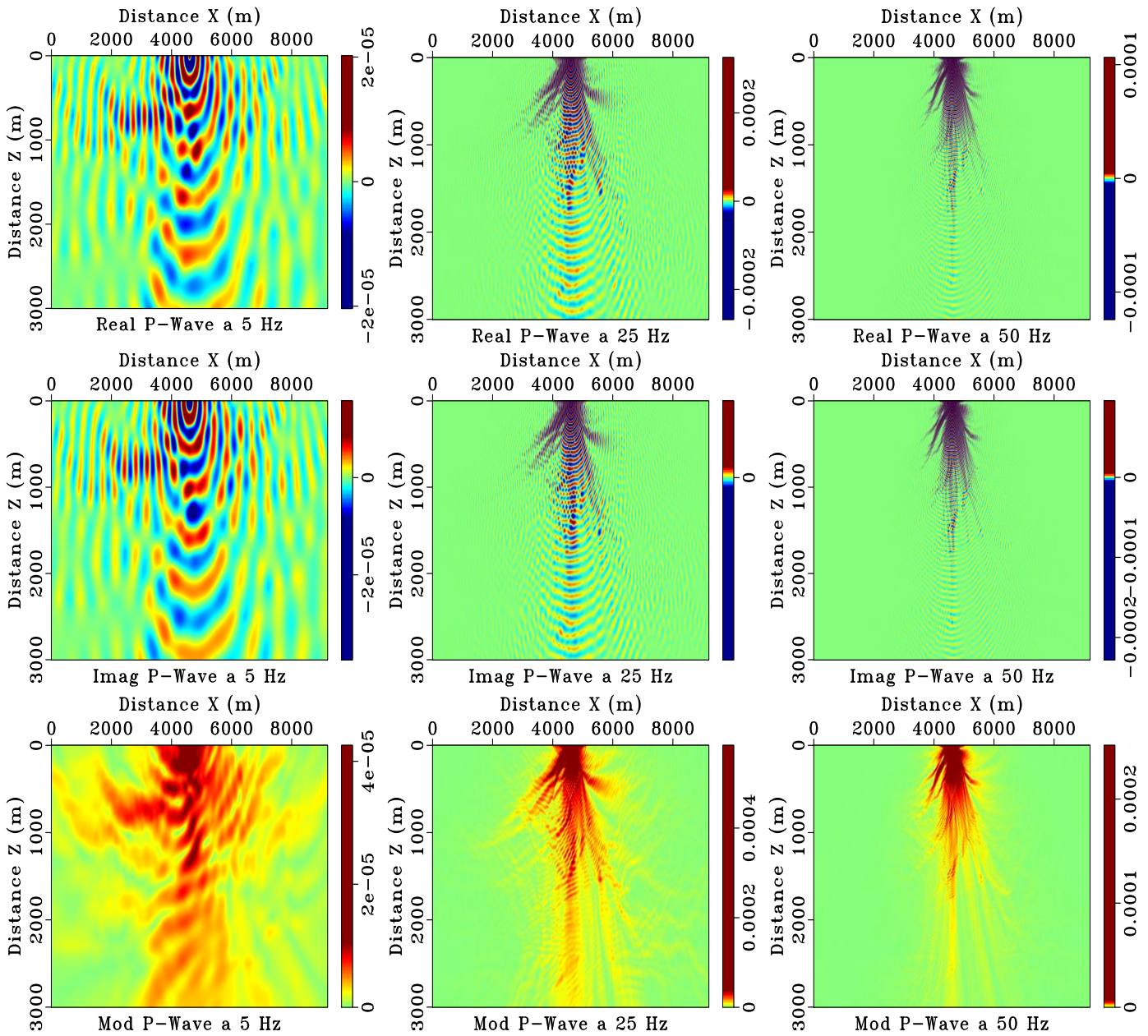


Figure 4.21: P-wave 5 [Hz].
Marmousi velocity profile

Figure 4.22: P-wave 25 Hz.
Marmousi velocity profile

Figure 4.23: P-wave 50 Hz.
Marmousi velocity profile

4.3.1 Shot comparison for density

To obtain a better comparison between the results for density effects, we compute the value of the P-wave for visco-acoustic medium with constant and variable density as a function of the distance X [m] for shots in the receivers at $z = 10$ [m] and $z = 1900$ [m] and P-wave as a function of the distance Z [m] for shots in the receivers at $x = 1000$ [m] for the three layers and complex velocity profile.

In figures, listed in the table 4.2, we show the real, imaginary part and modulus of the P-wave for three layers velocity profile and frequency 5 [Hz], 25 [Hz], 50 [Hz]. In all the figures the solid line is the solution for visco-acoustic medium with constant density and the dotted line is a solution for medium with variable density.

Table 4.2: List of figures for three layers velocity profile for shot comparison for density

Figure	Receiver position	Frequency
4.24	$z = 10$ [m]	5 [Hz]
4.25	$x = 1000$ [m]	5 [Hz]
4.26	$z = 10$ [m]	25 [Hz]
4.27	$x = 1000$ [m]	25 [Hz]
4.28	$z = 10$ [m]	50 [Hz]
4.29	$x = 1000$ [m]	50 [Hz]

We can see in the figures and as mentioned above, the difference between the medium with constant and variable density present a slight reduction in amplitude for medium with variable density, with a difference of up to 5% between the amplitudes found with the variable density with respect to the amplitudes found with constant density. The difference is calculated as:

$$\frac{[P(\rho, \gamma) - P(\rho(c), \gamma)]}{\max [P(\rho, \gamma)]}$$

The amplitudes are very symmetric for shot in $z = 10$ [m] (Fig. 4.24, 4.26 and 4.28), as expected, but there are areas where the amplitude of $P(\rho, \gamma)$ presents a slight out of phase shift and the area near the source present a lag where the difference is largest.

In the shot in $x = 1000$ [m] (Fig. 4.25, 4.27 and 4.29) we can see the interface change in the modulus of the P-wave and the difference is accentuated in the second reflector, in the real and imaginary part the change in z the amplitude of $P(\rho, \gamma)$ is phase shift in all reflectors with respect to $P(\rho(c), \gamma)$, in both we can see the interface change by the change in the wavelengths. The phase shift amplitudes are mainly due to the fact that when modeling the density as a variable, it behaves like a dipersor so that its solution presents a slight phase shift with respect to the solution with the constant density, although the differences are minimal with respect to the maximum value of the solution $P(\rho, \gamma)$ and the phase shift is very small.

It is possible that the effect of the variable density is concentrated at low frequencies, i.e. high wavelengths, where the density changes are more abrupt because the derivatives are calculated in a larger grid and in this case the change in the velocity and density profile is vertical but continuous and growing. Even so, the effect of variable density on amplitude remains small.

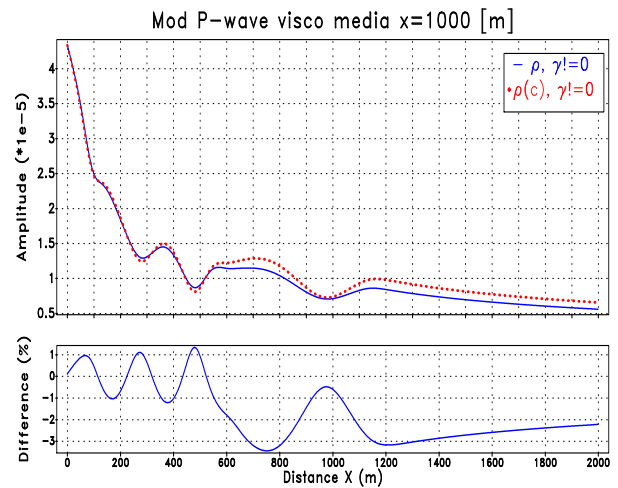
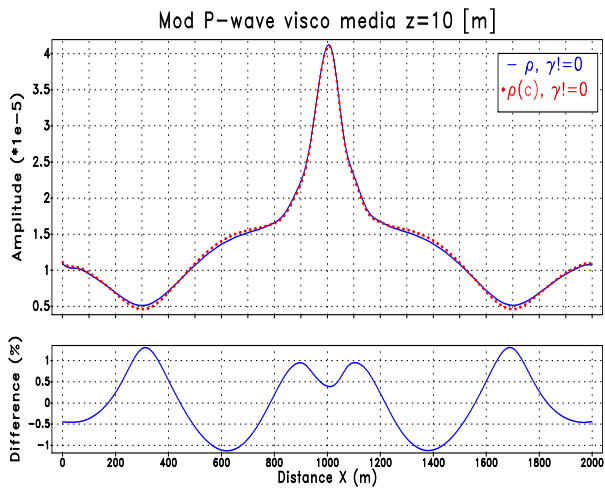
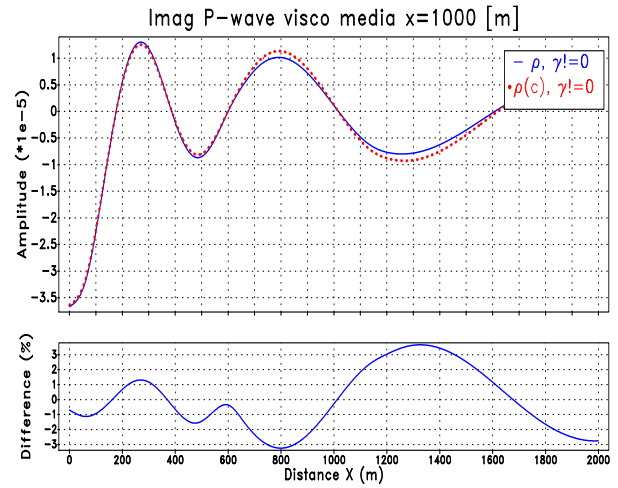
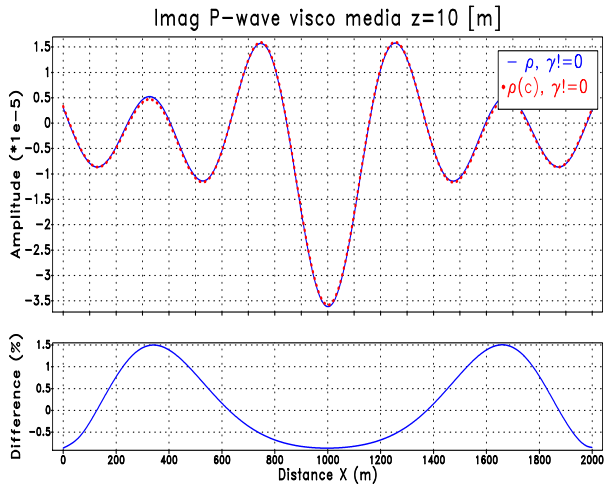
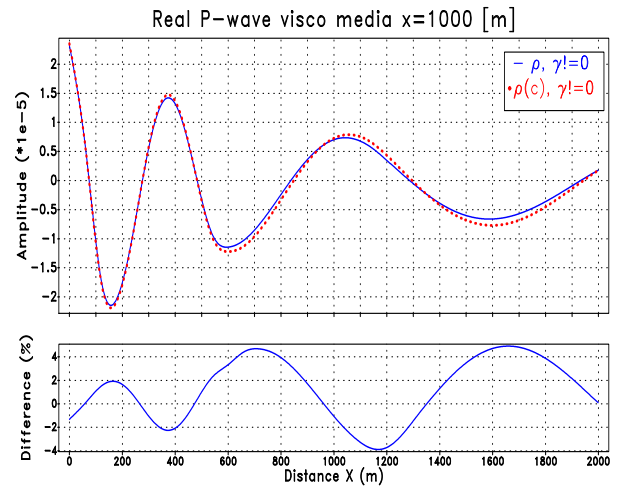
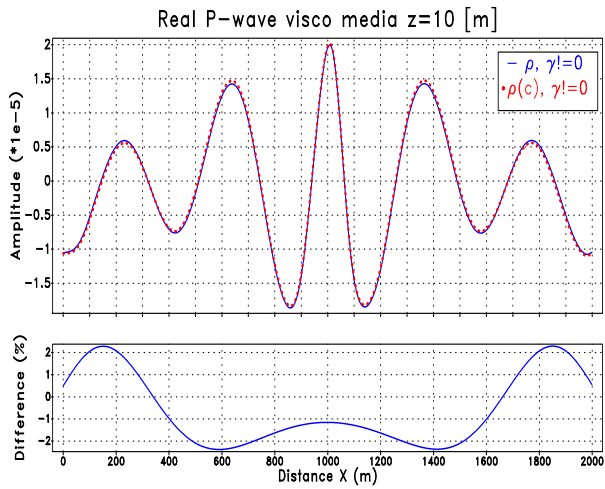


Figure 4.24: P-wave in the $z = 10$ [m] for three layers velocity profile with ρ constant and variable for $f = 5$ [Hz]

Figure 4.25: P-wave in the $x = 1000$ [m] for three layers velocity profile with ρ constant and variable for $f = 5$ [Hz]

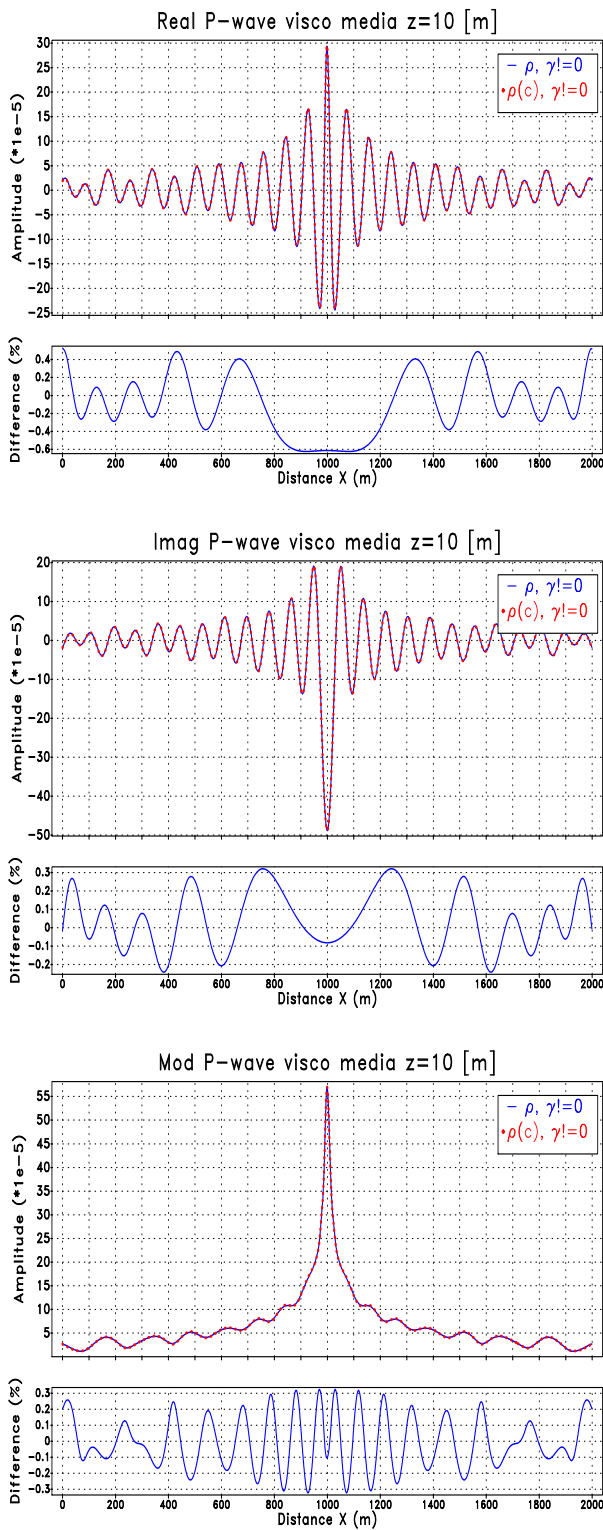


Figure 4.26: P-wave in the $z = 10$ [m] for three layers velocity profile with ρ constant and variable for 25 [Hz]

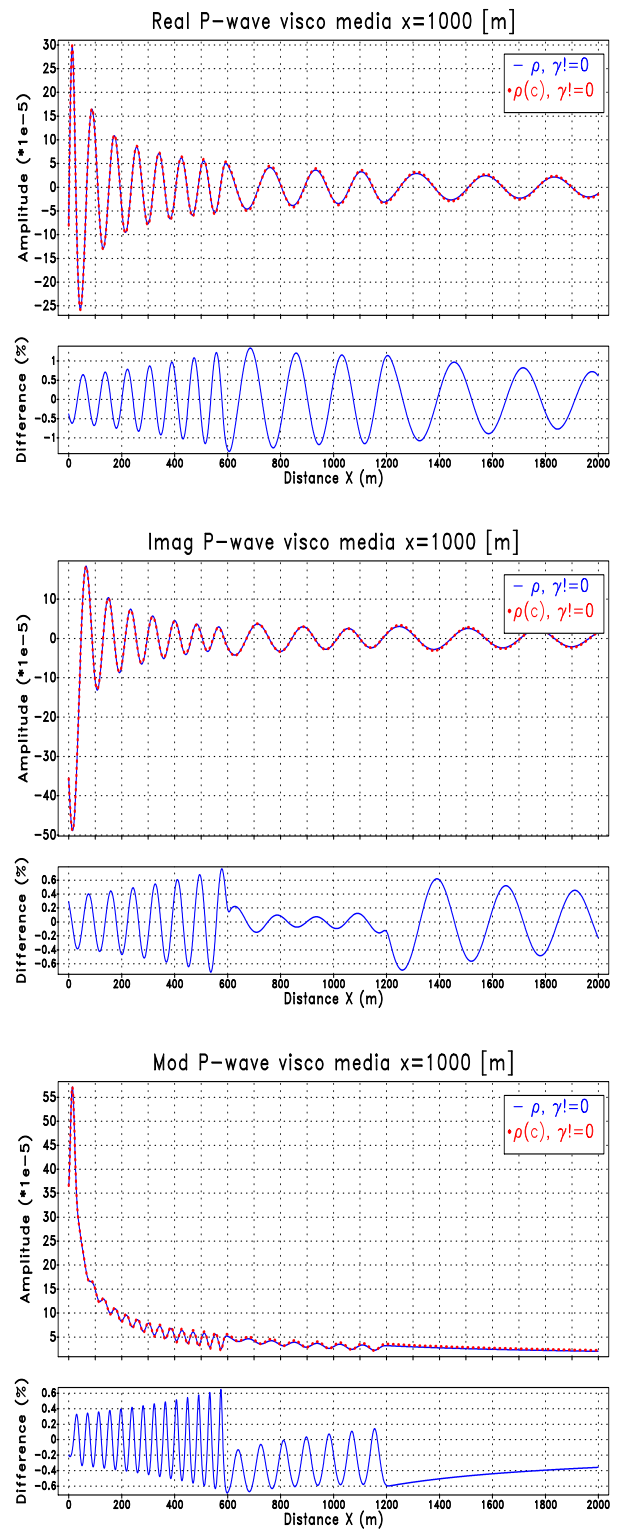


Figure 4.27: P-wave in the $x = 1000$ [m] for three layers velocity profile with ρ constant and variable for $f = 25$ [Hz]

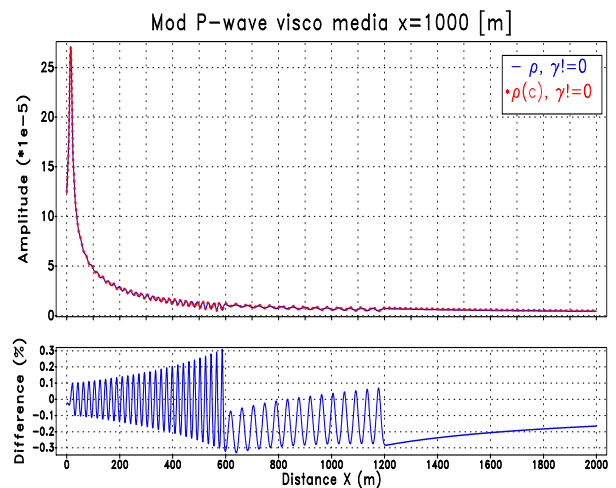
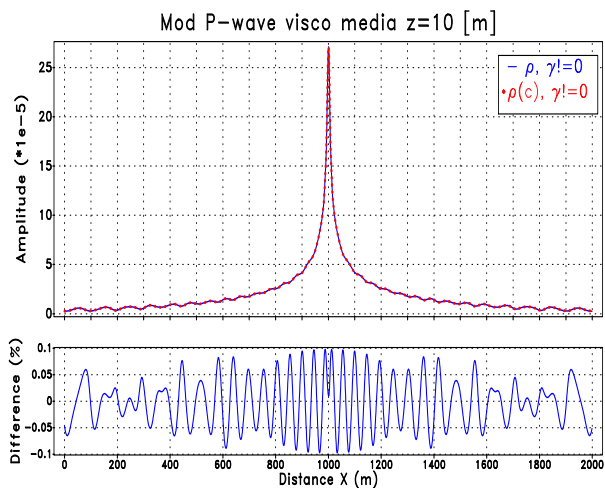
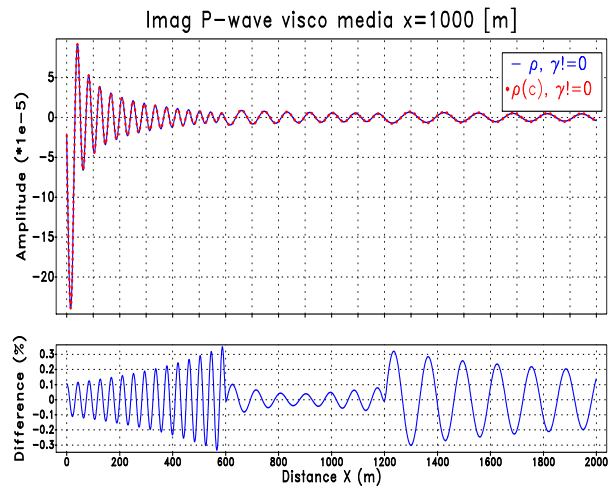
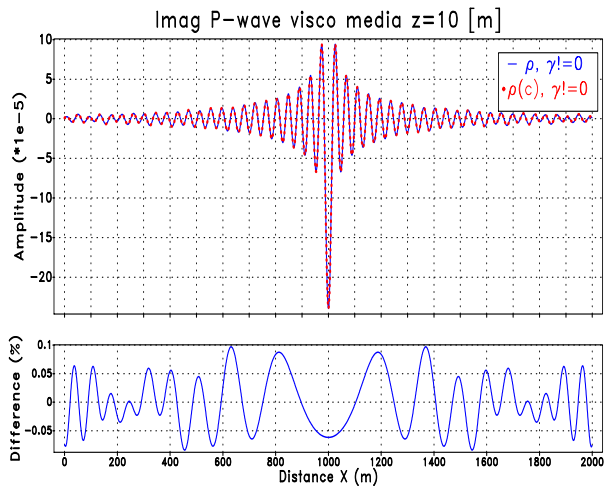
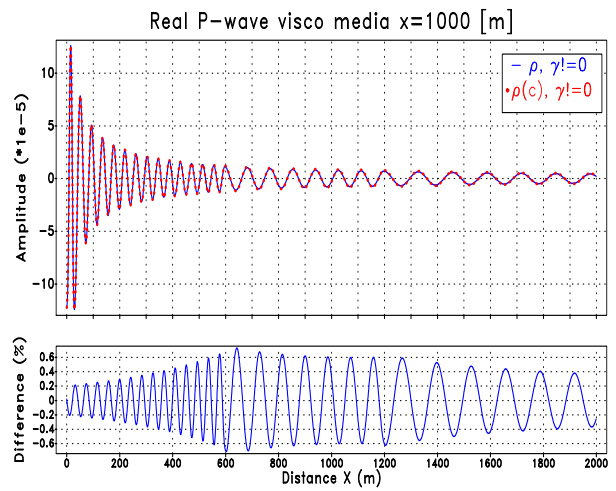
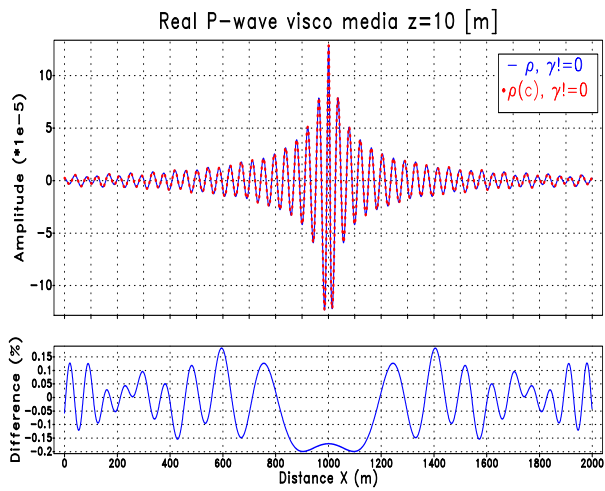


Figure 4.28: P-wave in the $z = 10$ [m] for three layers velocity profile with ρ constant and variable for 50 [Hz]

Figure 4.29: P-wave in the $x = 1000$ [m] for three layers velocity profile with ρ constant and variable for $f = 50$ [Hz]

In the same way as for three layers velocity profile, in the figures, listed in the table 4.3, we show the real, imaginary part and modulus of the P-wave for complex velocity profile and frequency 5 [Hz], 25 [Hz], 50 [Hz]. In all the figures the solid line is the solution for visco-acoustic medium with constant density and the dotted line is a solution for medium with variable density.

Table 4.3: List of figures for complex velocity profile for shot comparison for density

Figure	Receiver position	Frequency
4.30	$z = 10$ [m]	5 [Hz]
4.31	$x = 1000$ [m]	5 [Hz]
4.32	$z = 10$ [m]	25 [Hz]
4.33	$x = 1000$ [m]	25 [Hz]
4.34	$z = 10$ [m]	50 [Hz]
4.35	$x = 1000$ [m]	50 [Hz]

We can see in the figures that difference between the medium with constant and variable density present a slight reduction in amplitude for medium with variable density, with a difference of up to 5% between the amplitudes, again.

The amplitudes for shot in $z = 10$ [m] (Fig. 4.30, 4.32 and 4.34) are mostly symmetrical for all frequencies, but there are areas where the amplitude $P(\rho, \gamma)$ presents a phase shift noticeable, in the difference of modulus of the P-wave were there is a maximum where the most significant changes in the laterality of the profile are present. We could observe how the difference between amplitudes did decrease with frequency as in the case of the profile of three layers (see Fig. 4.32, Fig. 4.34), which indicates, at least in this case, that the lateral and abrupt changes of the complex velocity profile do not have an influence on the use of modeling with a variable or constant density.

In the shot in $x = 1000$ [m] (Fig. 4.31, 4.33, 4.35) we can see the interface change in the modulus of the P-wave and the difference is accentuated in the middle region, in the real and imaginary part the change in z of the amplitude of $P(\rho, \gamma)$ is phase shift in all reflectors, in both case we can see the interface change by the change in the wavelengths. The phase shift amplitudes are mainly due to the fact that when modeling the density as a variable, it behaves like a dipersor so that its solution presents a slight phase shift with respect to the solution with the constant density, although the differences are minimal with respect to the maximun value of the solution $P(\rho, \gamma)$ and the phase shift is very small.

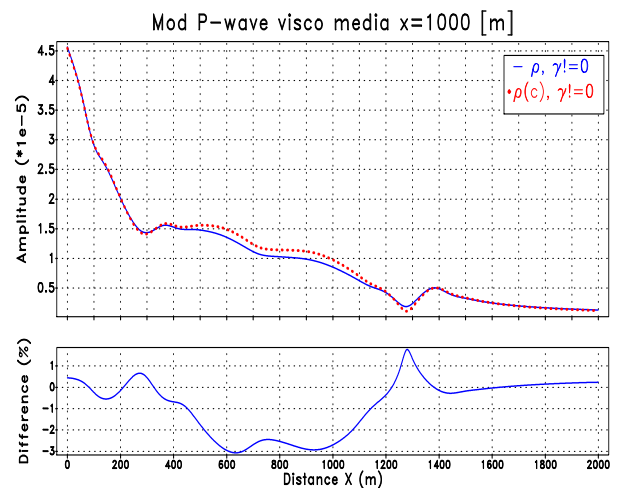
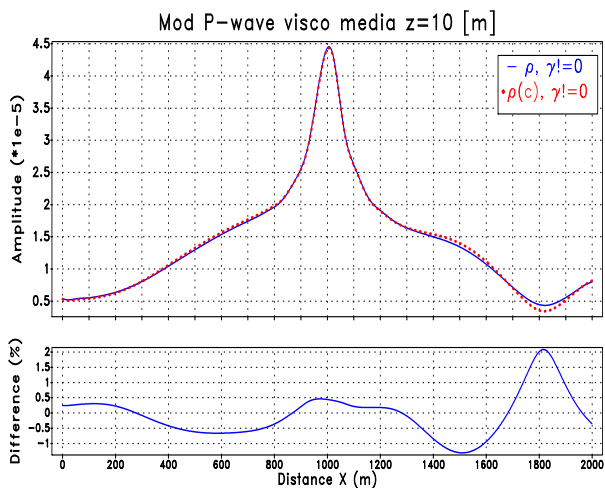
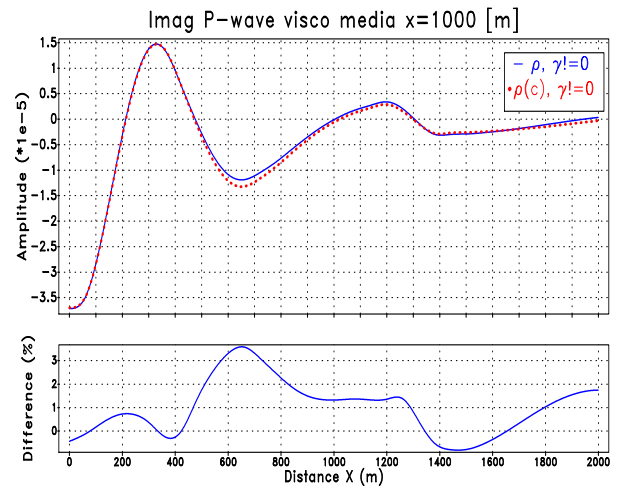
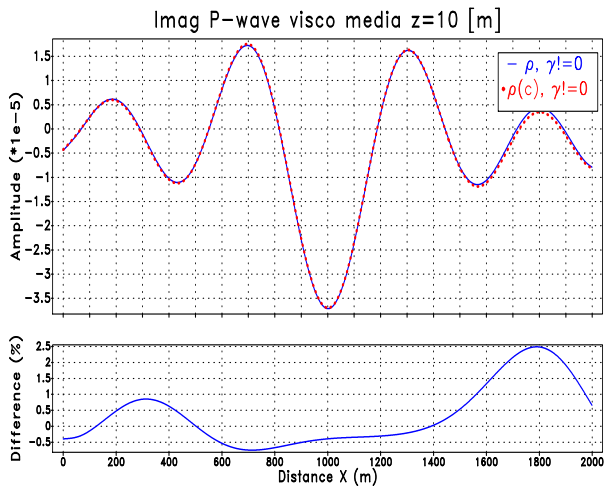
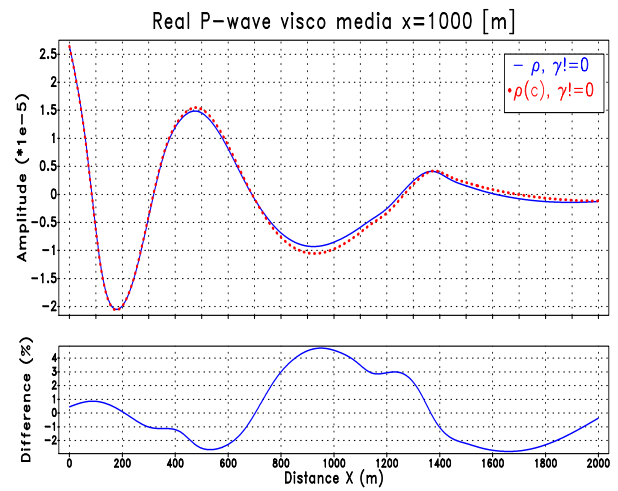
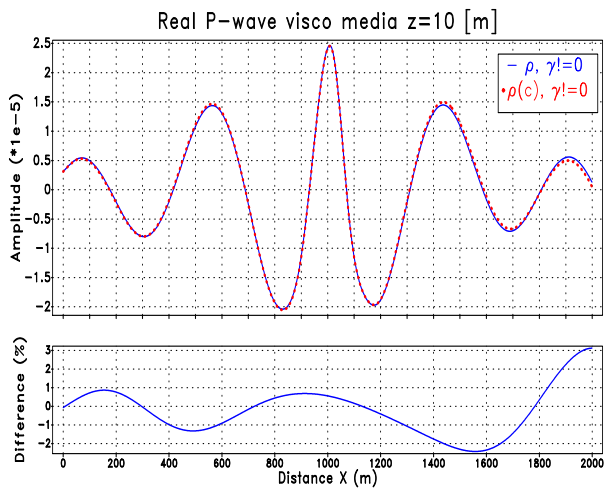


Figure 4.30: P-wave in the $z = 10$ [m] for complex velocity profile with ρ constant and variable for 5 [Hz]

Figure 4.31: P-wave in the $x = 1000$ [m] for complex velocity profile with ρ constant and variable for $f = 5$ [Hz]

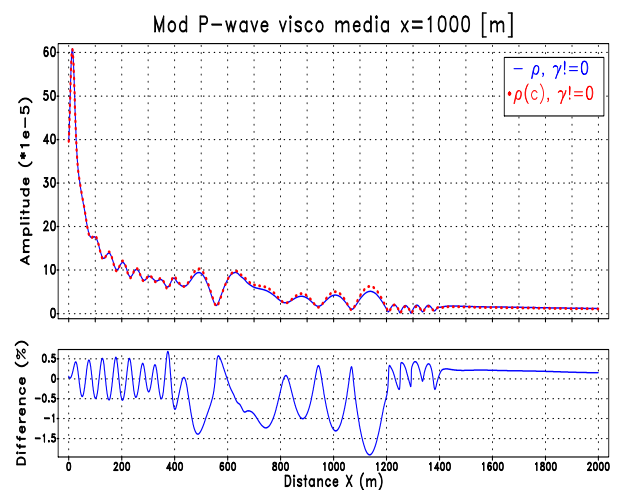
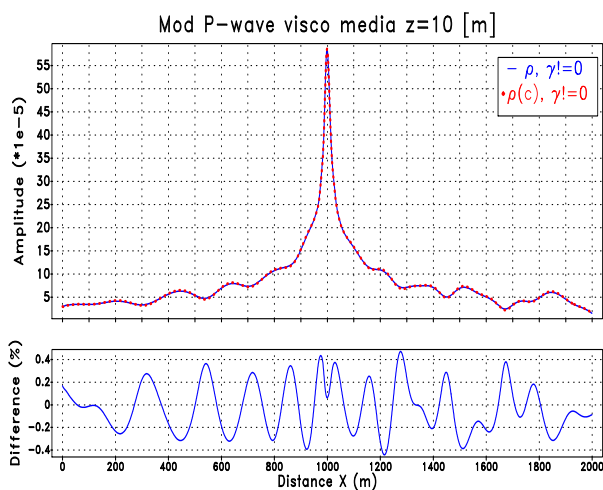
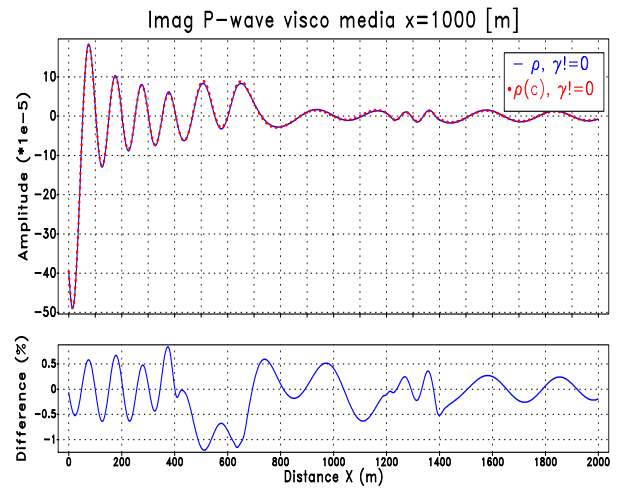
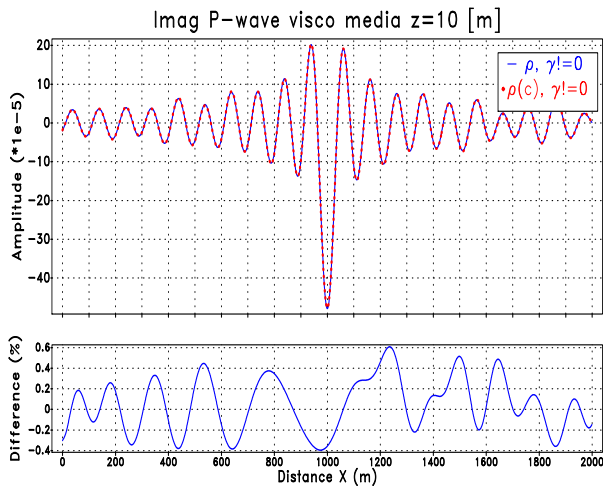
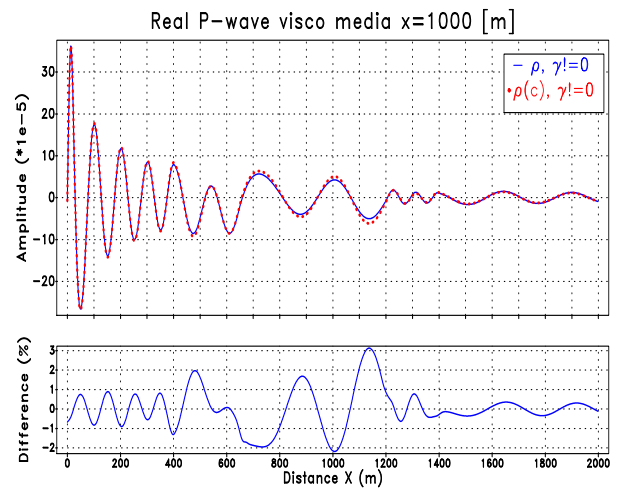
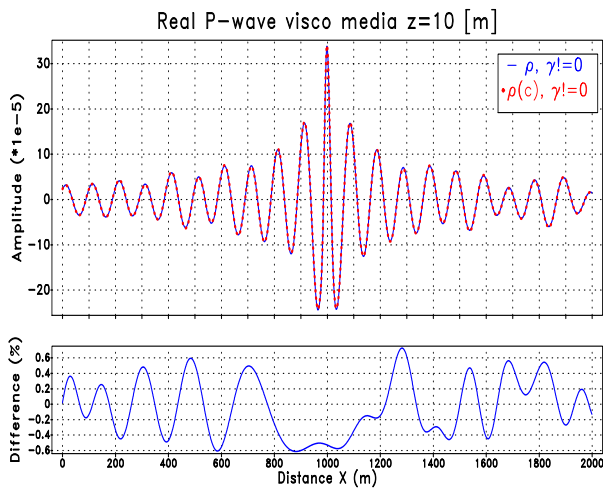


Figure 4.32: P-wave in the $z = 10$ [m] for complex velocity profile with ρ constant and variable for 25 [Hz]

Figure 4.33: P-wave in the $x = 1000$ [m] for complex velocity profile with ρ constant and variable for $f = 25$ [Hz]

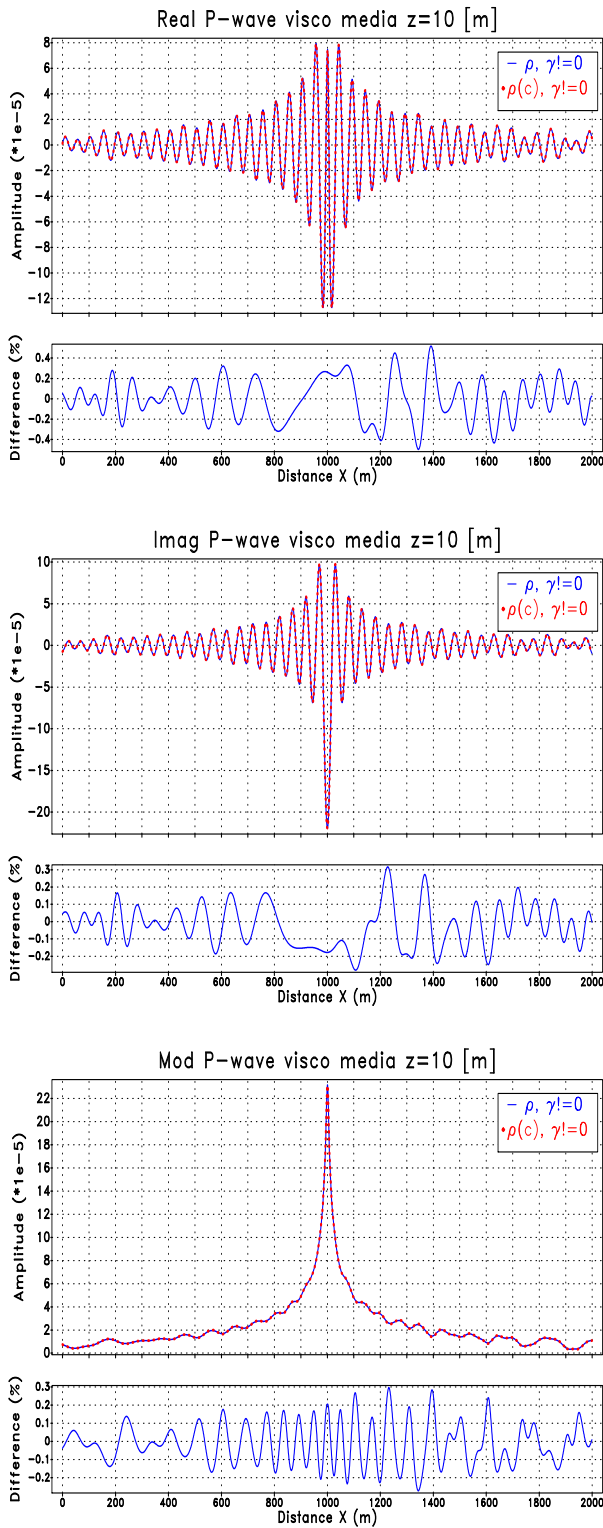


Figure 4.34: P-wave in the $z = 10$ [m] for complex velocity profile with ρ constant and variable for 50 [Hz]

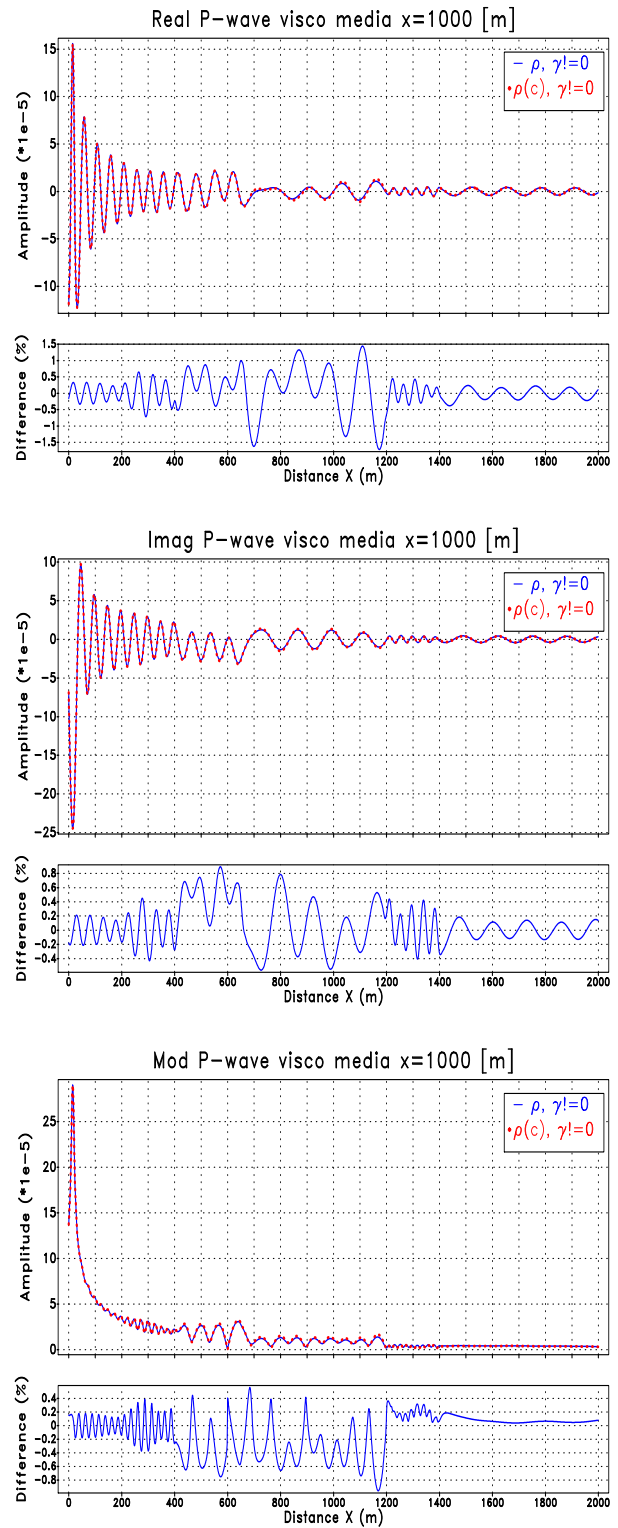


Figure 4.35: P-wave in the $x = 1000$ [m] for complex velocity profile with ρ constant and variable for $f = 50$ [Hz]

Now, to ensure the effect of density variation on amplitude, we do a final test by placing the receiver in $z = 1900$ [m], away from the source. In figures, listed in the table 4.4, we show the real, imaginary part and modulus of the P-wave for complex velocity profile and frequency 5 [Hz], 25 [Hz], 50 [Hz]. In all the figures the solid line is the solution for visco-acoustic medium with constant density and the dotted line is a solution for medium with variable density.

Table 4.4: List of figures for three layers and complex velocity profile $z = 1900$ [m] for shot comparison for density

Figure	Velocity profile	Frequency
4.36	Three layers	5 [Hz]
4.37	Complex	5 [Hz]
4.38	Three layers	25 [Hz]
4.39	Complex	25 [Hz]
4.40	Three layers	50 [Hz]
4.41	Complex	50 [Hz]

In this case the difference between the medium with constant and variable density are a larger reduction in amplitude with respect to the difference calculated at $z = 10$ [m], with a difference of up to 15% between the amplitudes found with the variable density with respect to the amplitudes found with constant density.

The amplitudes for shot in $z = 1900$ [m] (Fig. 4.36) there are areas when $P(\rho, \gamma)$ presents a phase shift noticeable, in the difference of modulus of the P-wave has a maximum where the most significant changes in the laterality of the profile are presented for Fig 4.37. We could observe how the difference between amplitudes did not decrease with frequency as in the case of the previous results with $z = 10$ [m] (see Fig. 4.38, Fig. 4.39, Fig. 4.40, Fig. 4.41), which indicates to have an influence on the use of modeling with a variable or constant density in other areas of the field P-wave.

We can conclude that considering the variable density, makes P-wave field to show a slight dispersion that is accentuated in the abrupt changes, especially those that are lateral. In addition the amplitude of the wave is also affected, and this influence depends on the frequency and its proximity to the source. At low frequencies and close to the source the difference between the amplitudes is remarkable but it is minimal at high frequencies, but far from the source the field has amplitude values that differ considerably from the wave field compared to the amplitude of the solution for the constant density case.

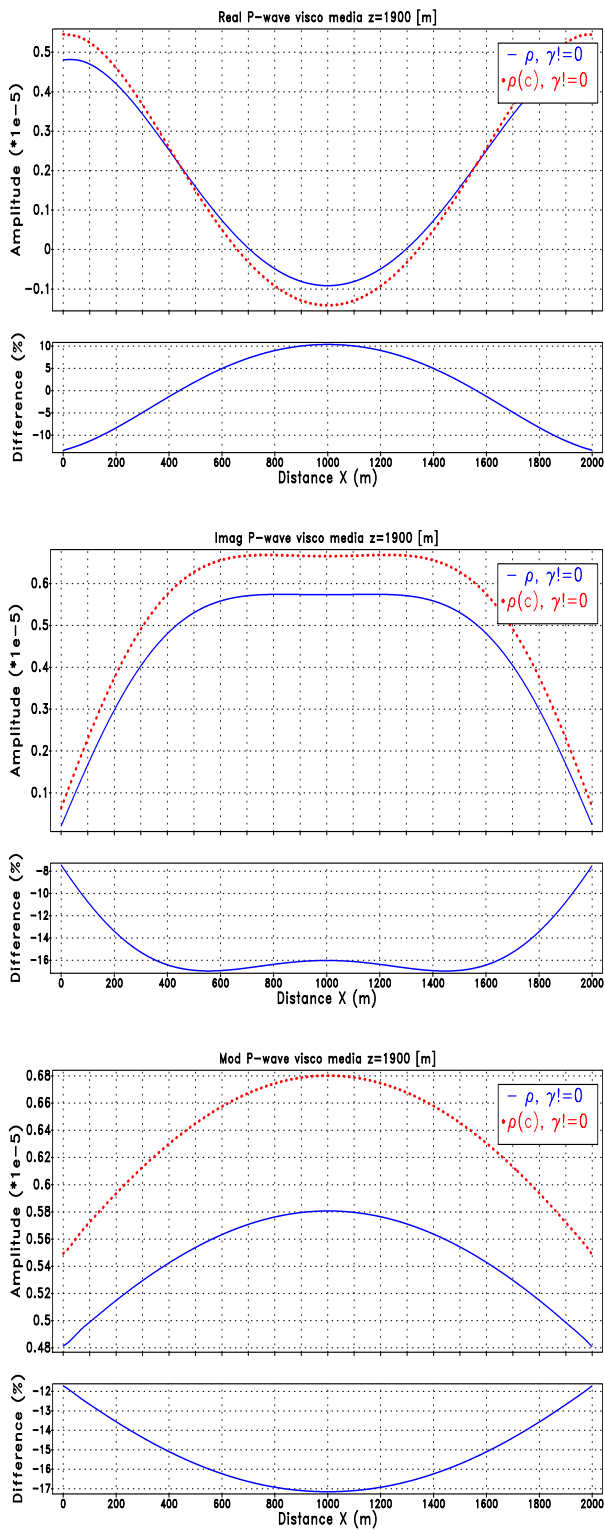


Figure 4.36: P-wave in the $z = 1900$ [m] for three layers velocity profile with ρ constant and variable for 5 [Hz]

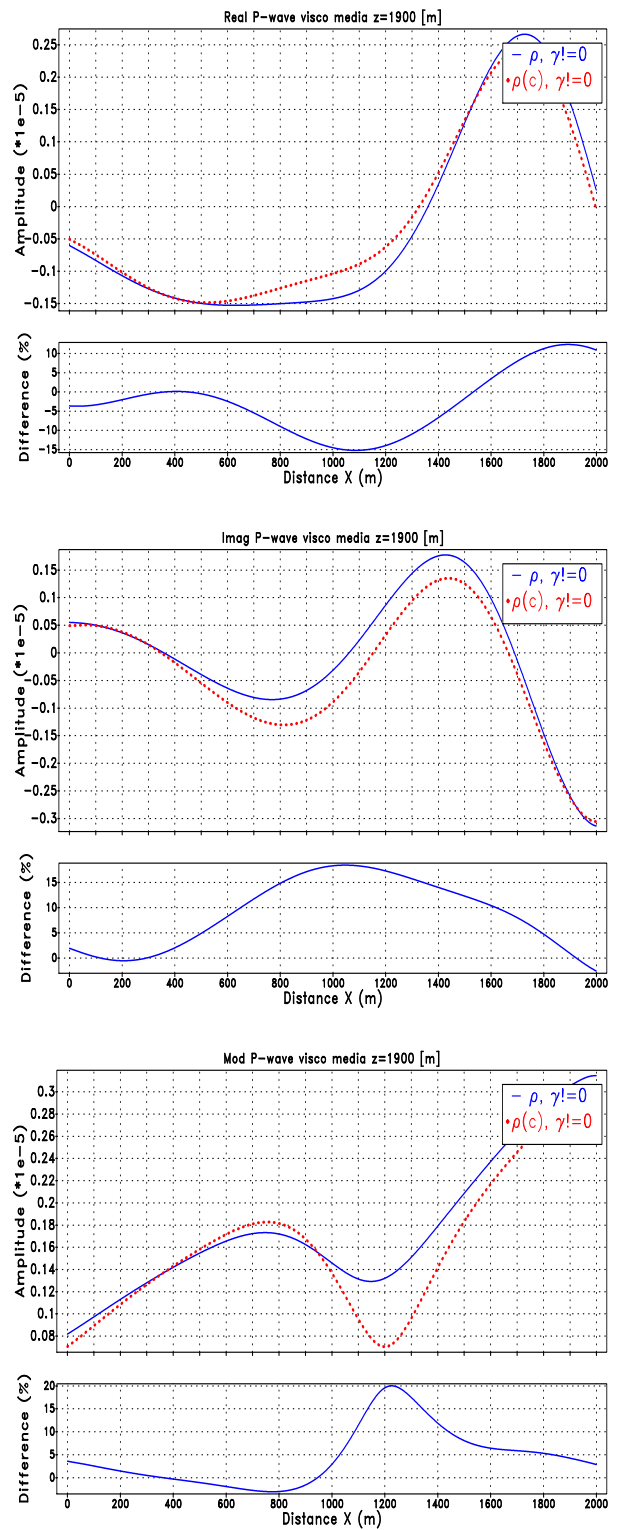


Figure 4.37: P-wave in the $z = 1900$ [m] for complex velocity profile with ρ constant and variable for $f = 5$ [Hz]

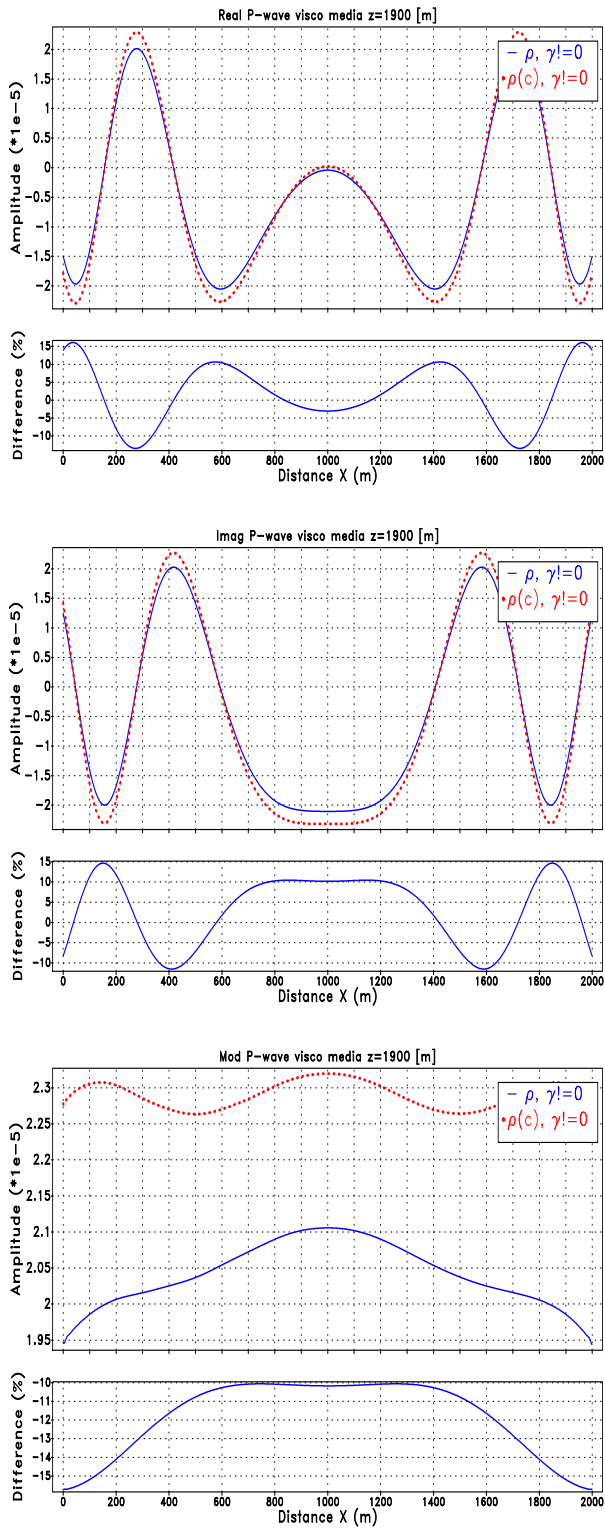


Figure 4.38: P-wave in the $z = 1900$ [m] for three layers velocity profile with ρ constant and variable for 25 [Hz]

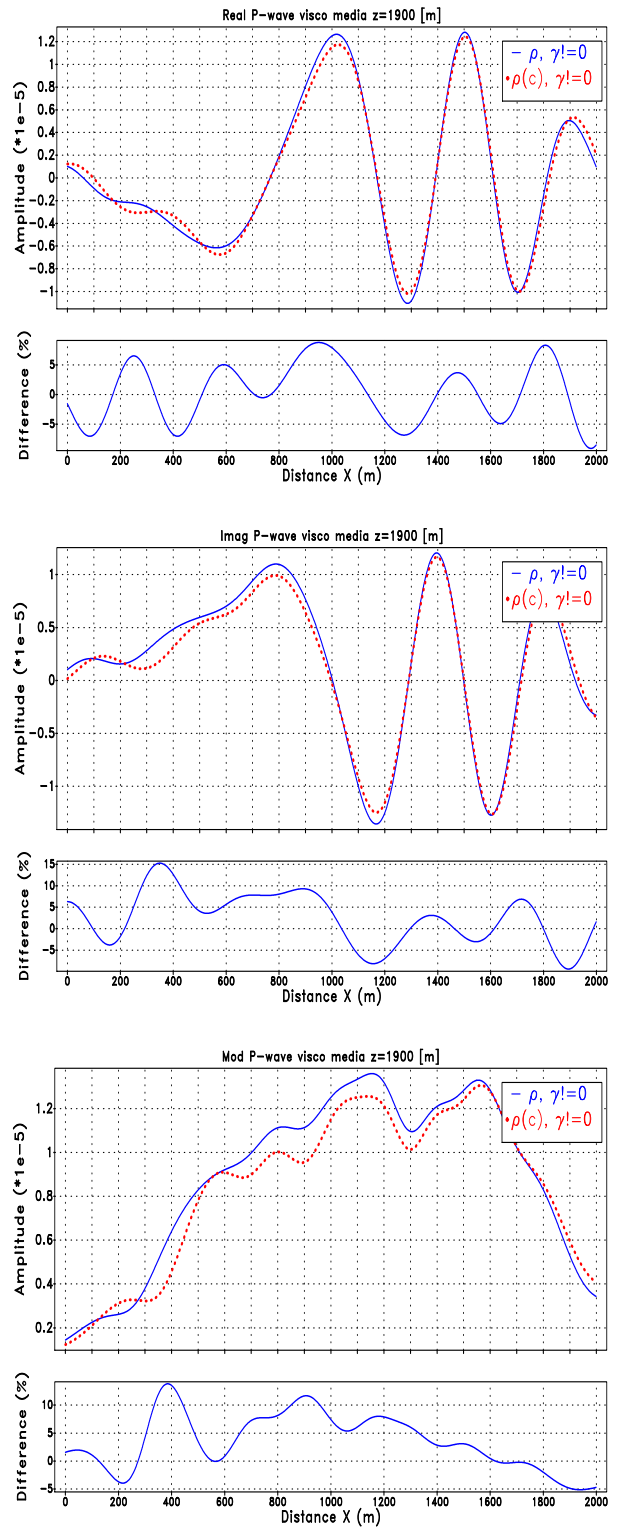


Figure 4.39: P-wave in the $z = 1900$ [m] for complex velocity profile with ρ constant and variable for $f = 25$ [Hz]

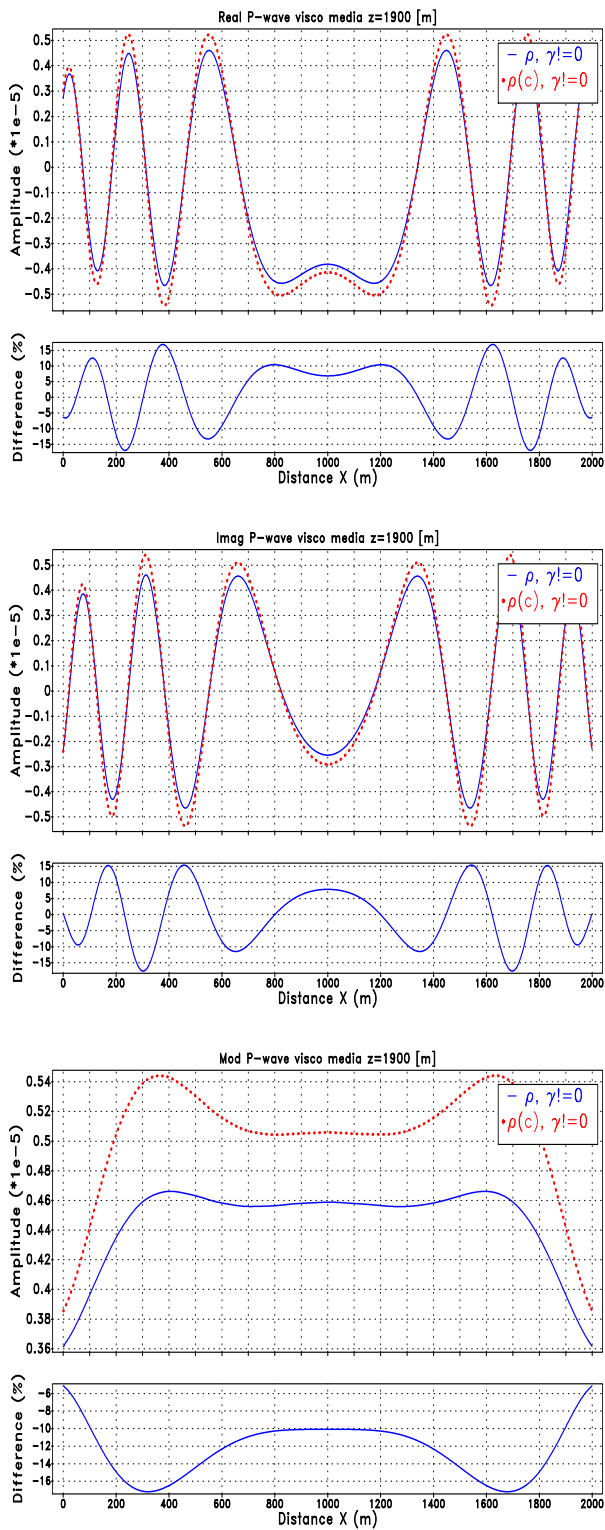


Figure 4.40: P-wave in the $z = 1900$ [m] for three layers velocity profile with ρ constant and variable for 50 [Hz]

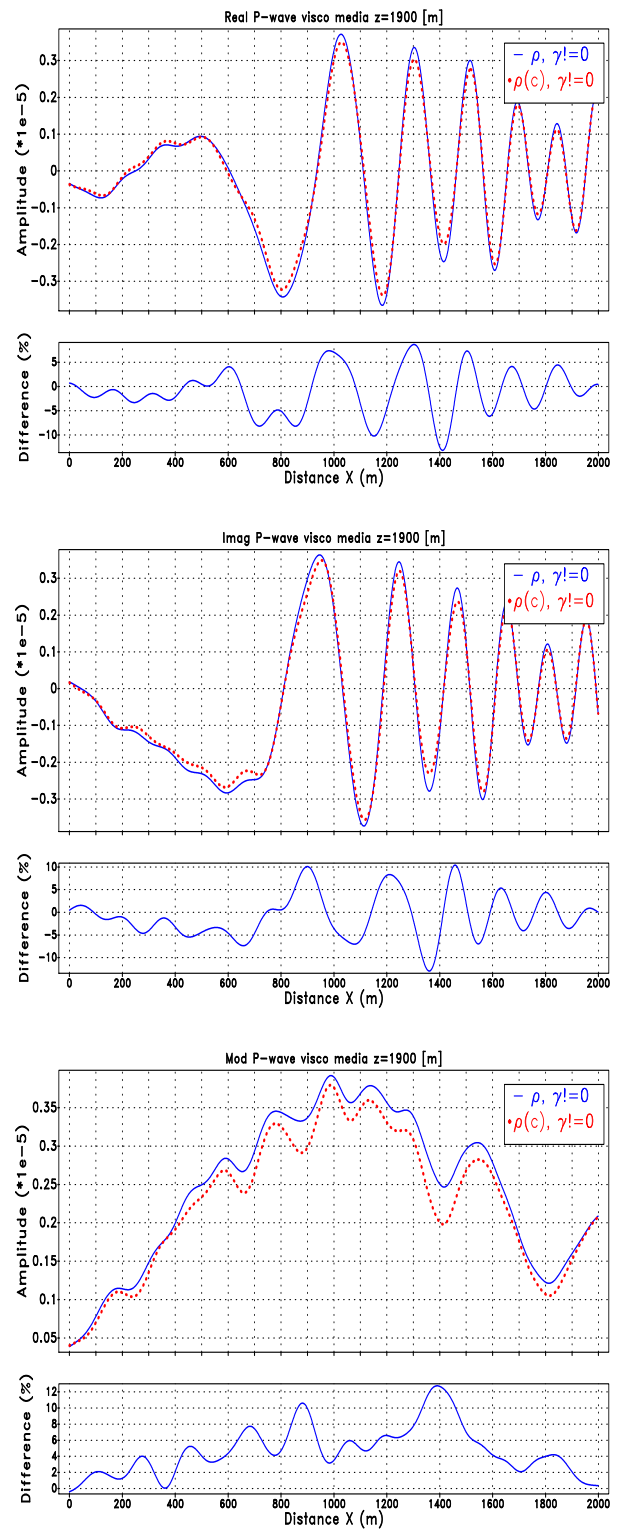


Figure 4.41: P-wave in the $z = 1900$ [m] for complex velocity profile with ρ constant and variable for $f = 50$ [Hz]

4.3.2 Shot comparison for viscosity

Now, in order to obtain a better comparison between the results for viscosity effects, we compute the value of the P-wave for visco-acoustic medium and acoustic medium with variable density as a function of the distance X [m] for shots in the receivers at $z = 10$ [m] and $z = 1900$ [m] and P-wave as a function of the distance Z [m] for shots in the receivers at $x = 1000$ [m] for the three layers and complex velocity profile.

In figures, listed in the table 4.5, we show the real, imaginary part and modulus of the P-wave for three layers velocity profile and frequency 5 [Hz], 25 [Hz], 50 [Hz]. In all the figures the solid line is the solution for acoustic medium with density variable and the dotted line is a solution for visco-acoustic medium with density variable.

Table 4.5: List of figures for three layers velocity profile for shot comparison for viscosity

Figure	Receiver position	Frequency
4.42	$z = 10$ [m]	5 [Hz]
4.43	$x = 1000$ [m]	5 [Hz]
4.44	$z = 10$ [m]	25 [Hz]
4.45	$x = 1000$ [m]	25 [Hz]
4.46	$z = 10$ [m]	50 [Hz]
4.47	$x = 1000$ [m]	50 [Hz]

We can see in the figures that the difference between the medium with and without viscosity is a reduction in amplitude for medium with viscosity, with a difference of up to 4% between the amplitudes for $f = 5$ [Hz], 15% for $f=25$ [Hz] and 20% for 50 [Hz] found with the visco-acoustic medium with respect to the amplitudes found with acoustic medium. The difference is dependent for frequency, but this is expected, since attenuation, for Kolsy's model (eq. 2.18) depends proportionally on the frequency, at low frequencies the attenuation is lower than at high frequencies as you can see in Fig 2.1, so, the attenuation increases with frequency (Wang, 2009),.

In addition, the dispersion of the wave, especially in the direction of change of velocity profile, is remarkable. The amplitudes are very symmetric for shot in $z = 10$ [m] (Fig. 4.42, 4.44 and 4.46), as expected, but there are areas where the amplitude of $P(\rho, \gamma)$ presents a phase shift which is accentuated as the wave propagates to the edges.

In the shot in $x = 1000$ [m] (see Fig. 4.43, 4.45 and 4.47) the dispersion of the wave is very remarkable in the last reflector, the phase shift in the viscous medium with respect to the acoustic medium is more noticeable in high frequency. Also, we can see the interface change in the modulus of the P-wave and the difference is accentuated in the second reflector and the imaginary part presents a slight amplitude increase at the interface between the first and second reflector.

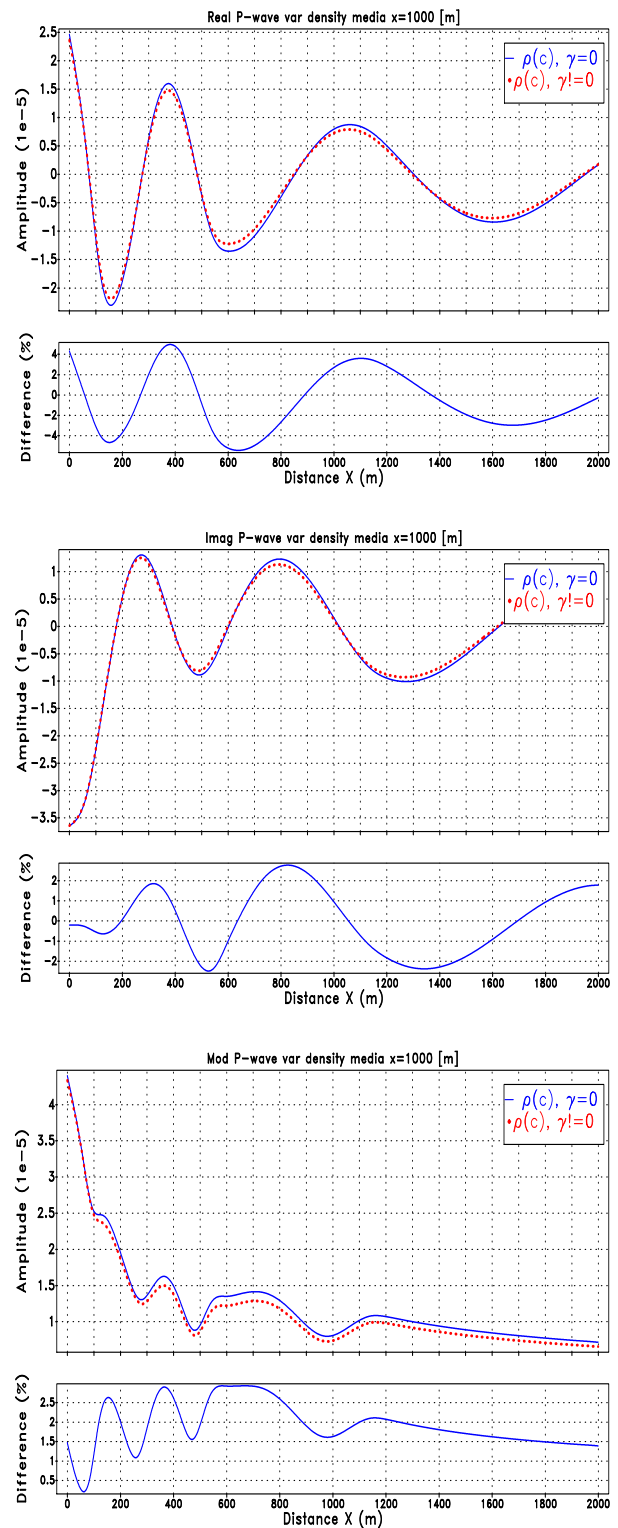
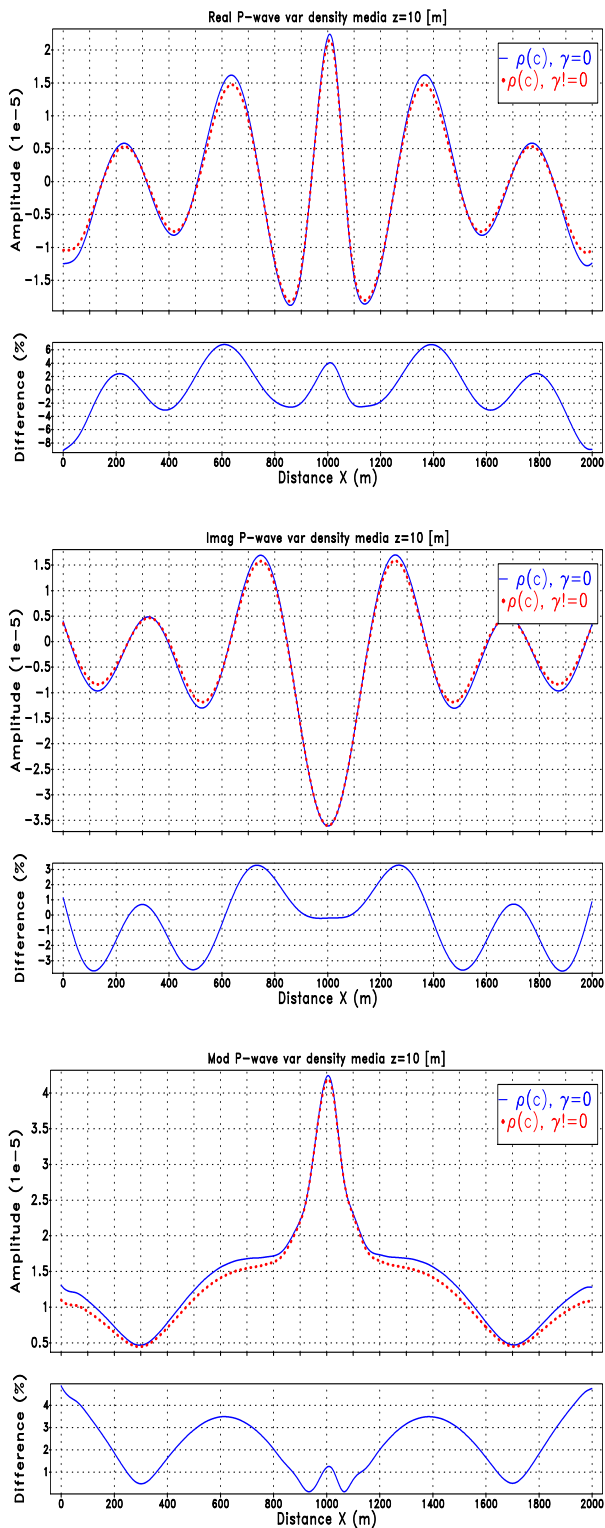


Figure 4.42: P-wave in the $z = 10$ [m] for three layers velocity profile with ρ constant and variable for 5 [Hz]

Figure 4.43: P-wave in the $x = 1000$ [m] for three layers velocity profile in acoustic and visco-acoustic medium for $f = 5$ [Hz]

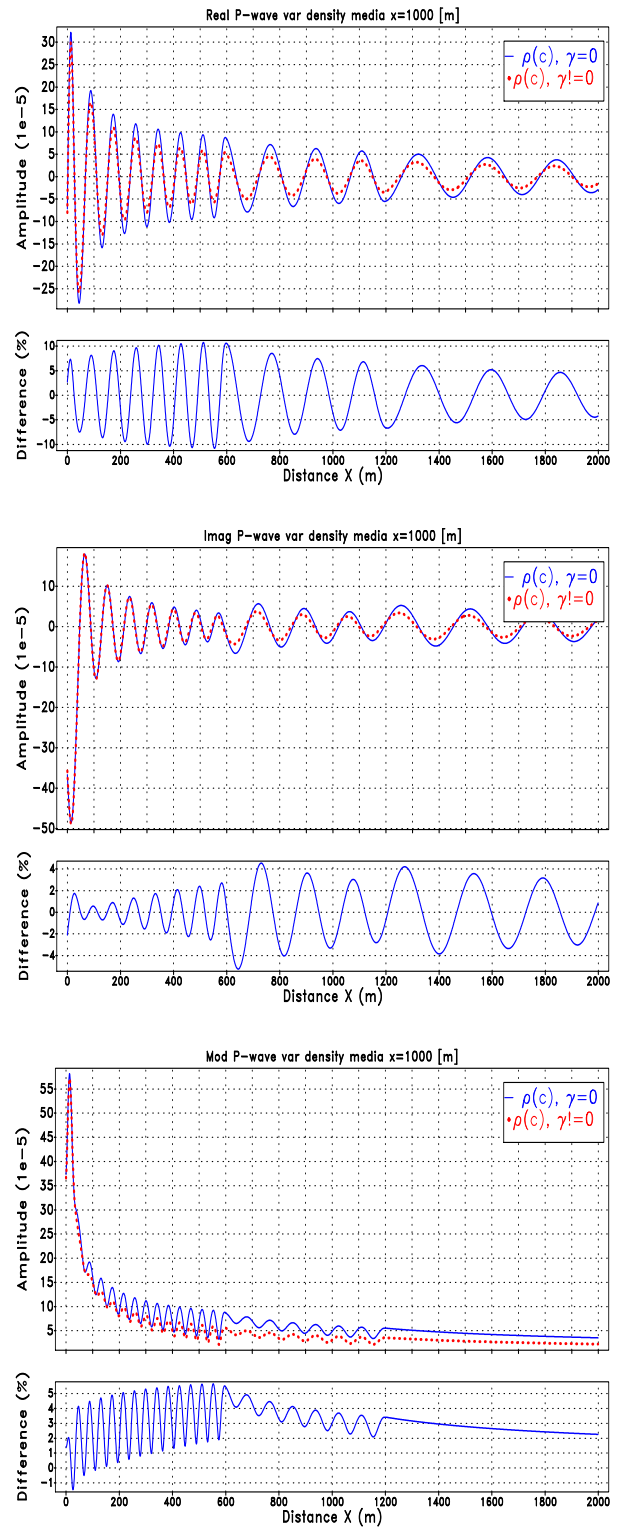
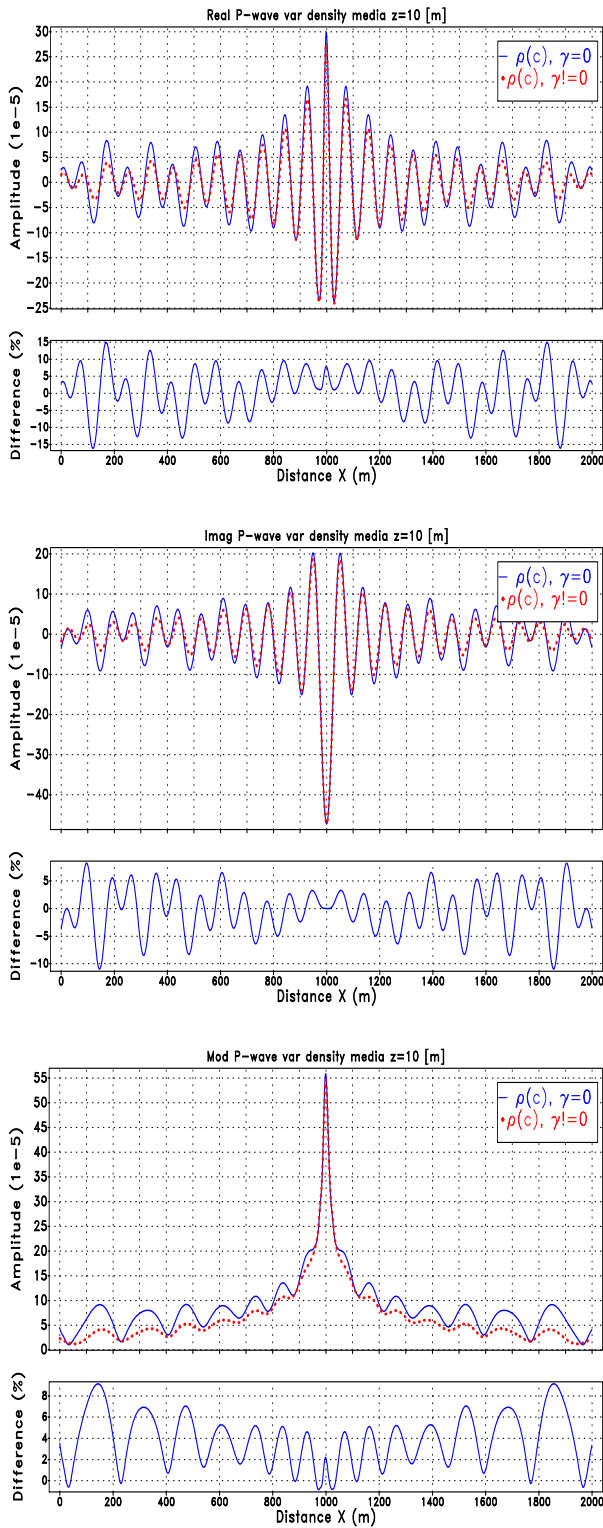


Figure 4.44: P-wave in the $z = 10$ [m] for three layers velocity profile in acoustic and visco-acoustic medium for 25 [Hz]

Figure 4.45: P-wave in the $x = 1000$ [m] for three layers velocity profile in acoustic and visco-acoustic medium for $f = 25$ [Hz]

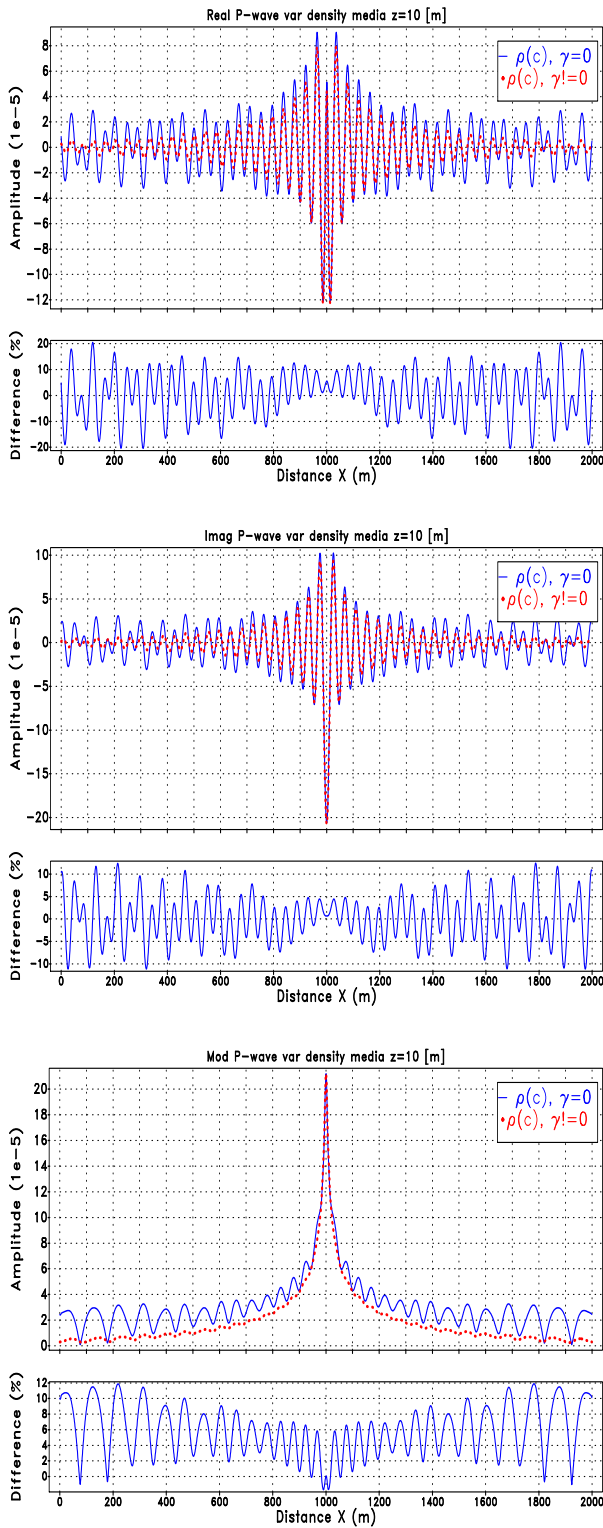


Figure 4.46: P-wave in the $z = 10$ [m] for three layers velocity profile in acoustic and visco-acoustic medium for 50 [Hz]

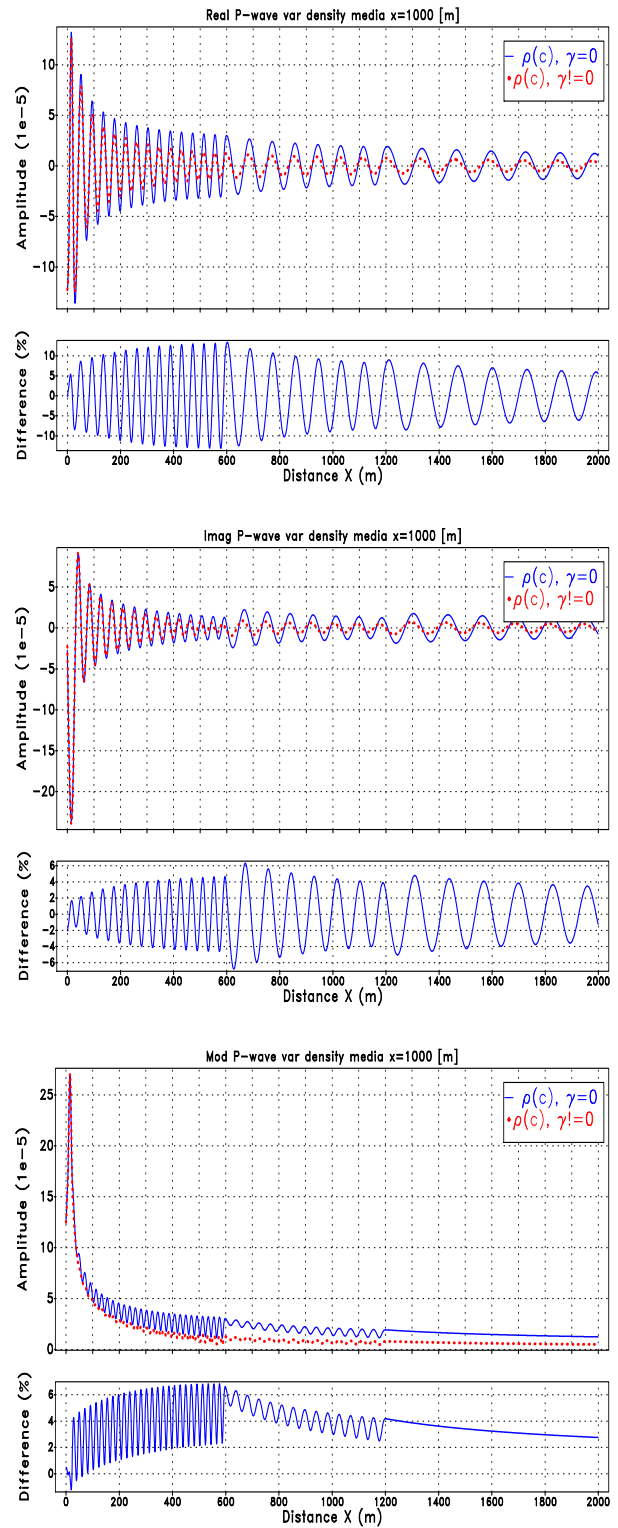


Figure 4.47: P-wave in the $x = 1000$ [m] for three layers velocity profile in acoustic and visco-acoustic medium for $f = 50$ [Hz]

In the same way as for three layers velocity profile, in the figures, listed in the table 4.6, we show the real, imaginary part and modulus of the P-wave for three layers velocity profile and frequency 5 [Hz], 25 [Hz], 50 [Hz]. In all the figures the solid line is the solution for acoustic medium with density variable and the dotted line is a solution for visco-acoustic medium with density variable.

Table 4.6: List of figures for complex velocity profile for shot comparison for viscosity

Figure	Receiver position	Frequency
4.48	$z = 10$ [m]	5 [Hz]
4.49	$x = 1000$ [m]	5 [Hz]
4.50	$z = 10$ [m]	25 [Hz]
4.51	$x = 1000$ [m]	25 [Hz]
4.52	$z = 10$ [m]	50 [Hz]
4.53	$x = 1000$ [m]	50 [Hz]

We can see in the figures that the difference between the medium with and without viscosity is a reduction in amplitude for medium with viscosity, with a difference of up to 5% for $f = 5$ [Hz], 10% for $f = 25$ [Hz] and 15% for $f = 50$ [Hz] between the amplitudes found with the visco-acoustic medium with respect to the amplitudes found with acoustic medium, as we expected the attenuation increases with frequency.

The amplitudes for shot in $z = 10$ [m] (Fig. 4.48, 4.50 and 4.52) are mostly symmetrical for all frequencies, in the shot in $x = 1000$ [m] (Fig. 4.49, 4.51, 4.52) we can see the interface change in the modulus, real and imaginary part of the P-wave and the difference is accentuated in the middle region, where the biggest changes of velocity and attenuation are found. The dispersion is a remarkable, presented the same characteristics of the previous test.

Now, to ensure the effect of viscosity on amplitude and phase, we do a final test by placing the receiver in $z = 1900$ [m], away from the source. In figures, listed in the table 4.7, we show the real, imaginary part and modulus of the P-wave for complex velocity profile and frequency 5 [Hz], 25 [Hz], 50 [Hz]. In all the figures the solid line is the solution for acoustic medium with variable density and the dotted line is a solution for visco-acoustic medium with density variable,

Table 4.7: List of figures for three layers and complex velocity profile $z = 1900$ [m] for shot comparison for viscosity

Figure	Velocity profile	Frequency
4.36	Three layers	5 [Hz]
4.37	Complex	5 [Hz]
4.38	Three layers	25 [Hz]
4.39	Complex	25 [Hz]
4.40	Three layers	50 [Hz]
4.41	Complex	50 [Hz]

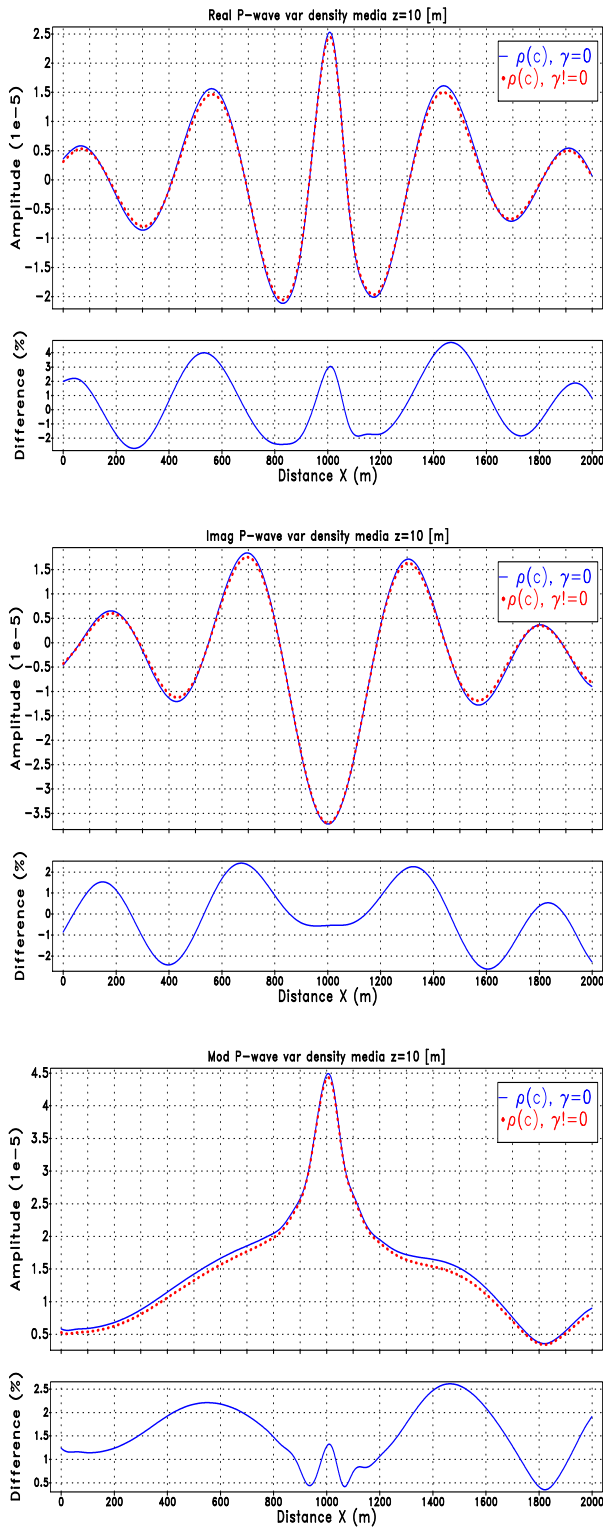


Figure 4.48: P-wave in the $z = 10$ [m] for complex velocity profile in acoustic and visco-acoustic medium for $f = 5$ [Hz]

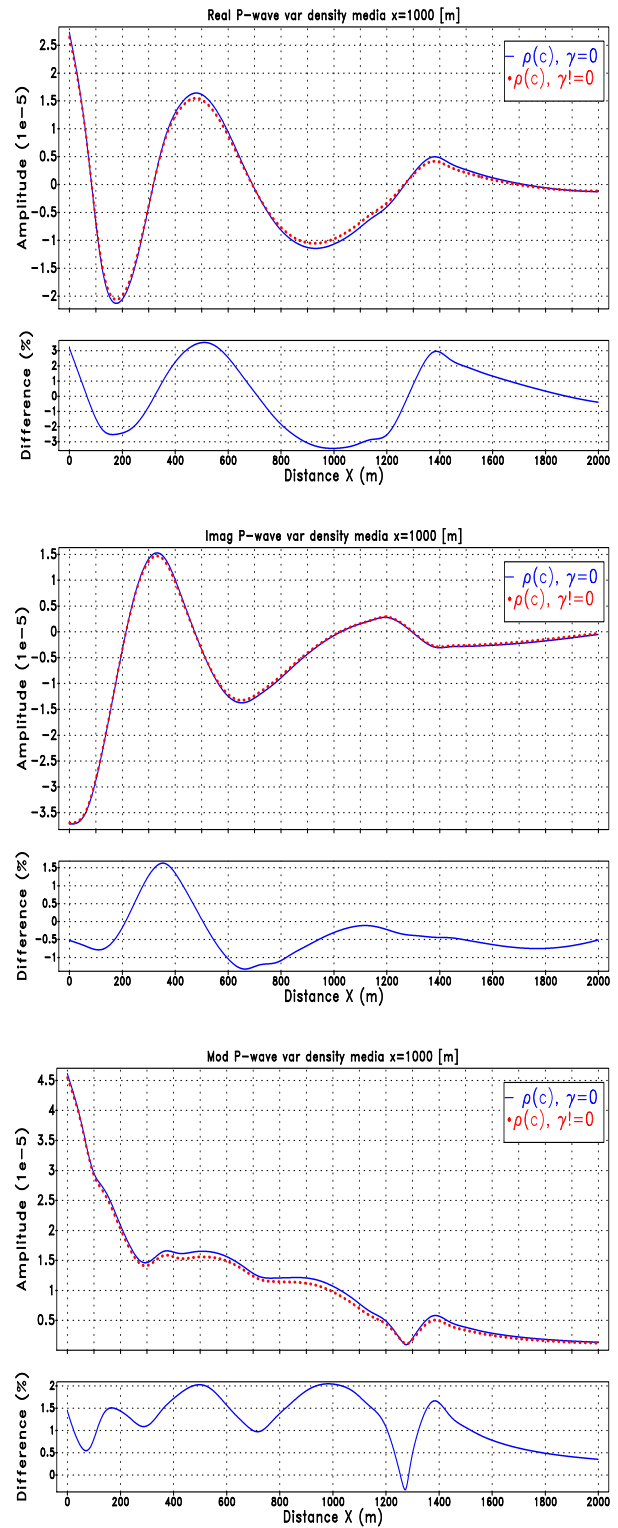


Figure 4.49: P-wave in the $x = 1000$ [m] for complex velocity profile in acoustic and visco-acoustic medium for $f = 5$ [Hz]

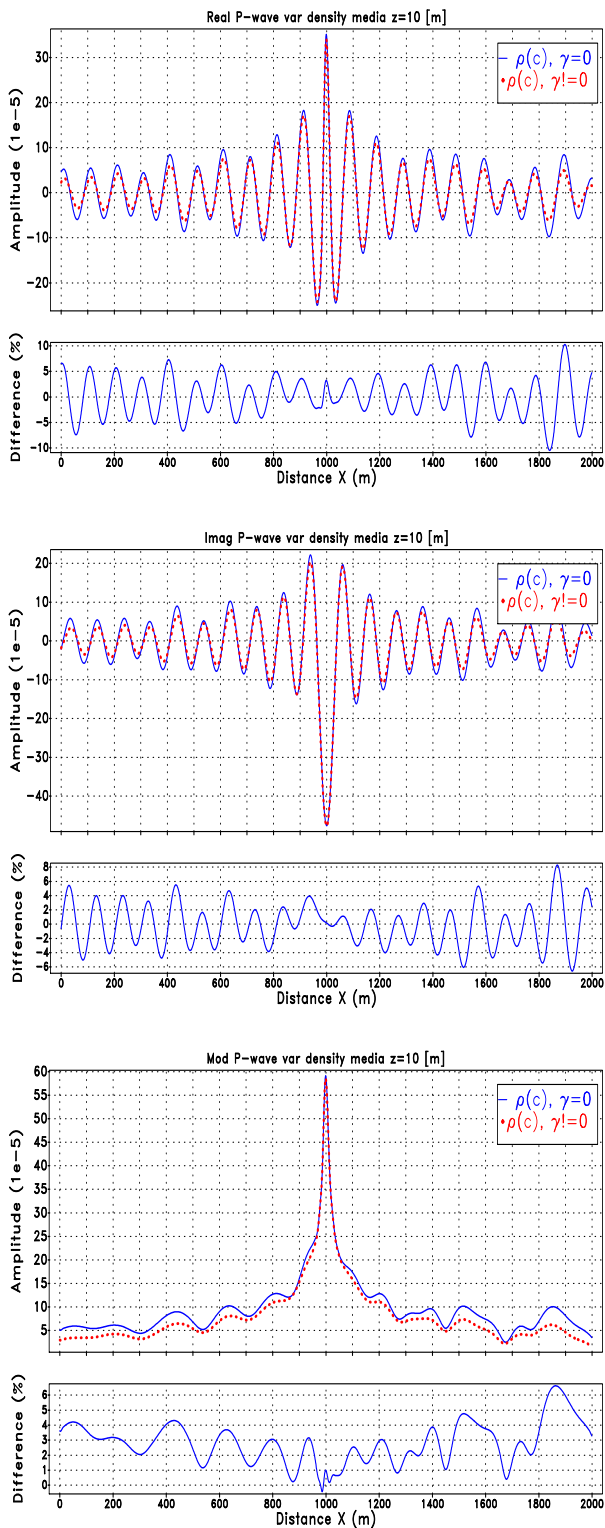


Figure 4.50: P-wave in the $z = 10$ [m] for complex velocity profile in acoustic and visco-acoustic medium for 25 [Hz]

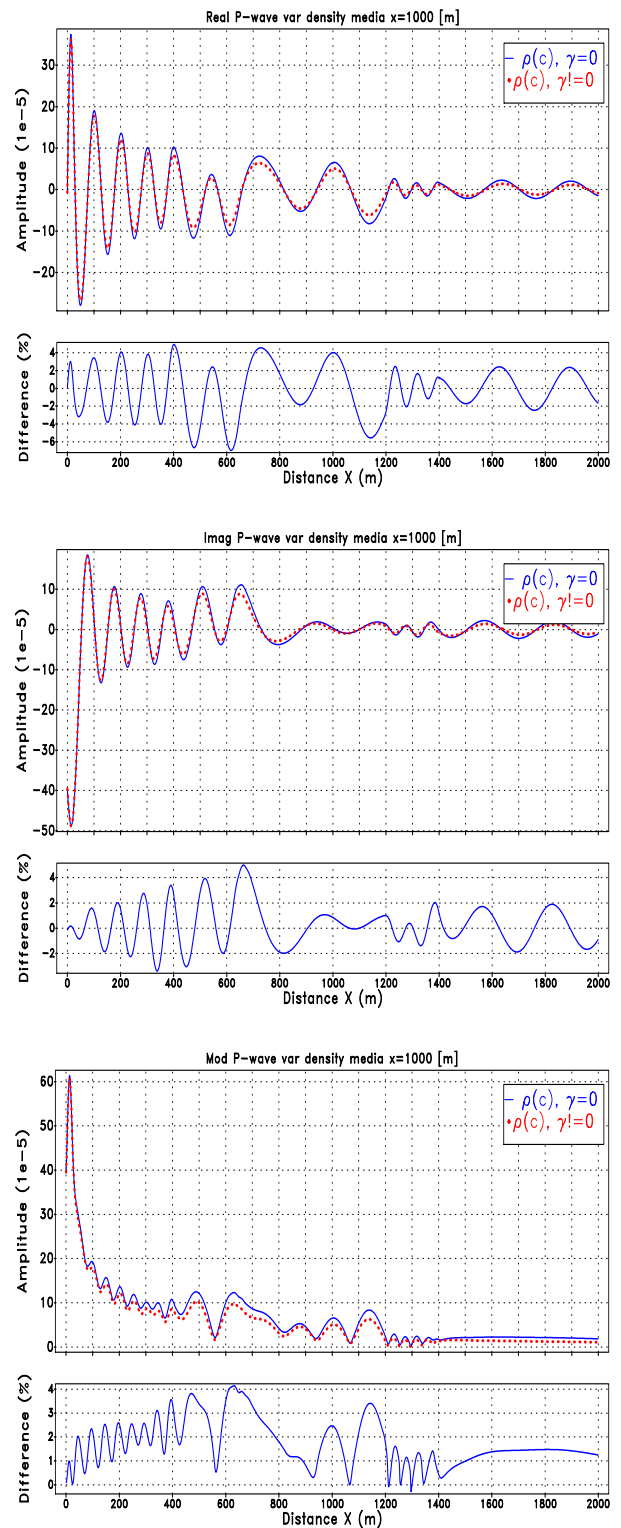


Figure 4.51: P-wave in the $x = 1000$ [m] for complex velocity profile in acoustic and visco-acoustic medium for $f = 25$ [Hz]

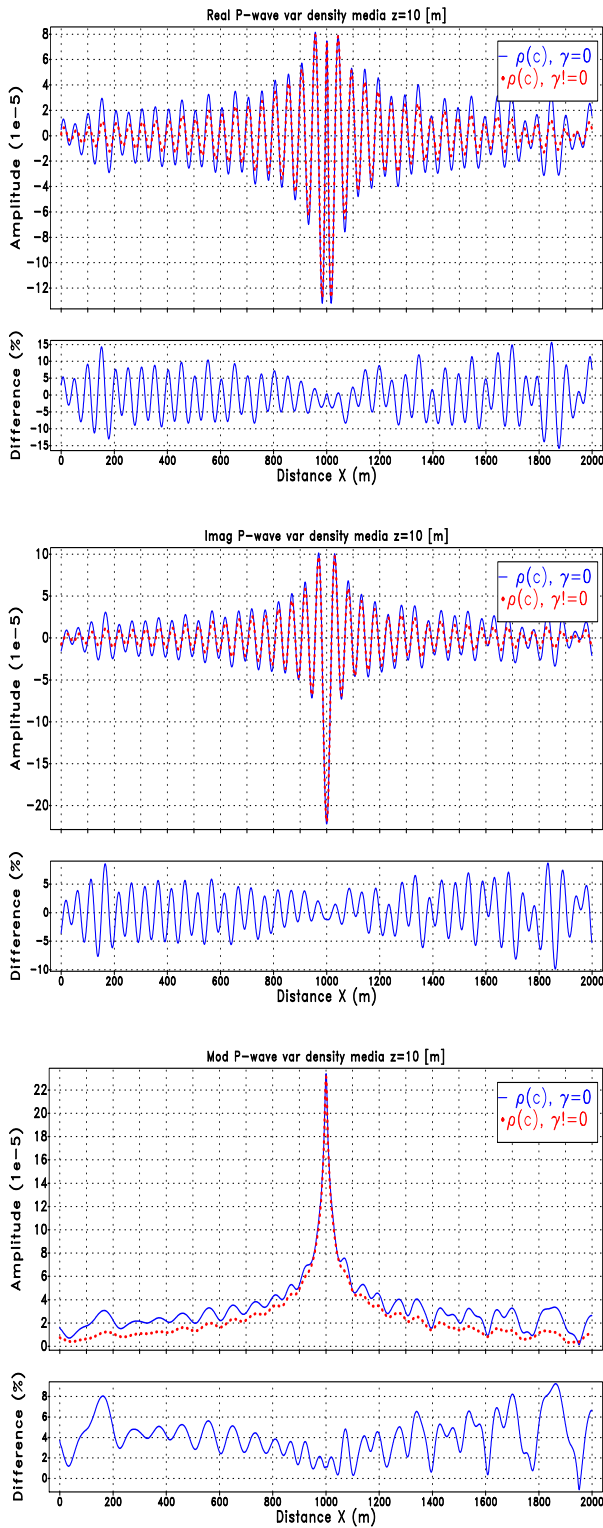


Figure 4.52: P-wave in the $z = 10$ [m] for complex velocity profile in acoustic and visco-acoustic medium for 50 [Hz]

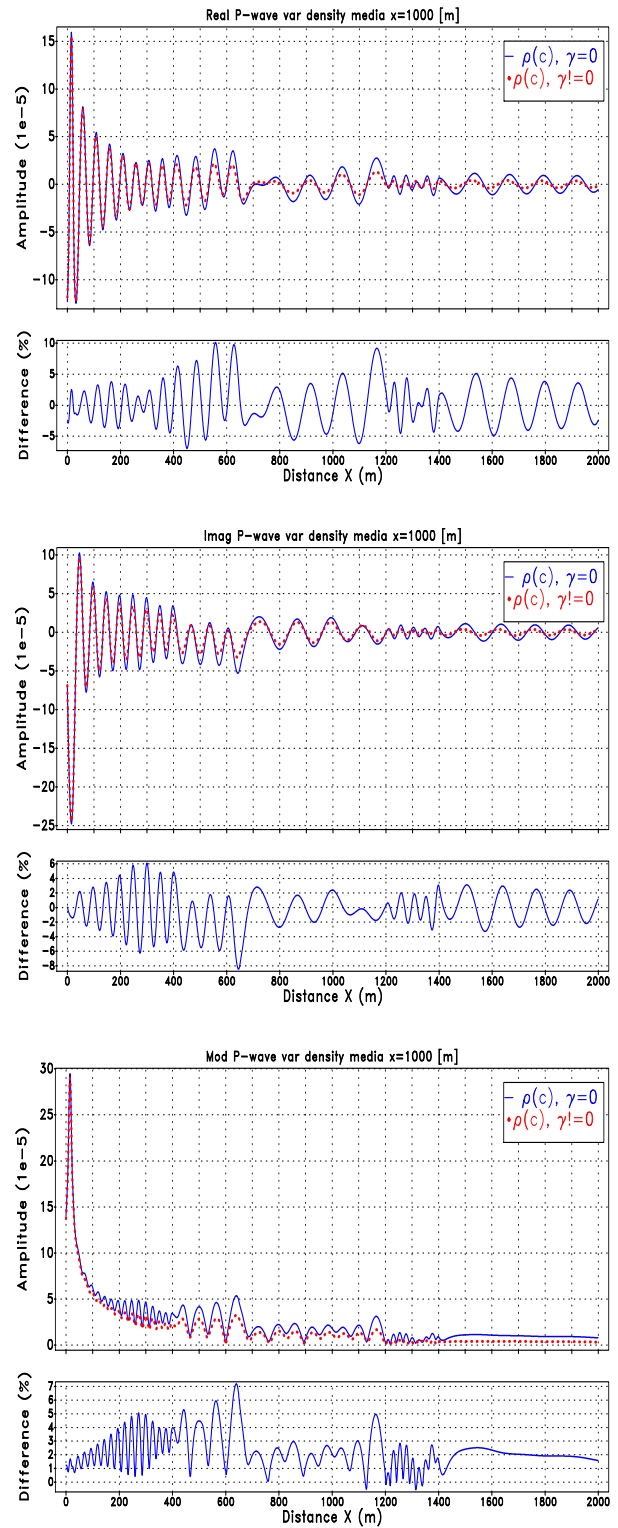


Figure 4.53: P-wave in the $x = 1000$ [m] for complex velocity profile in acoustic and visco-acoustic medium for $f = 50$ [Hz]

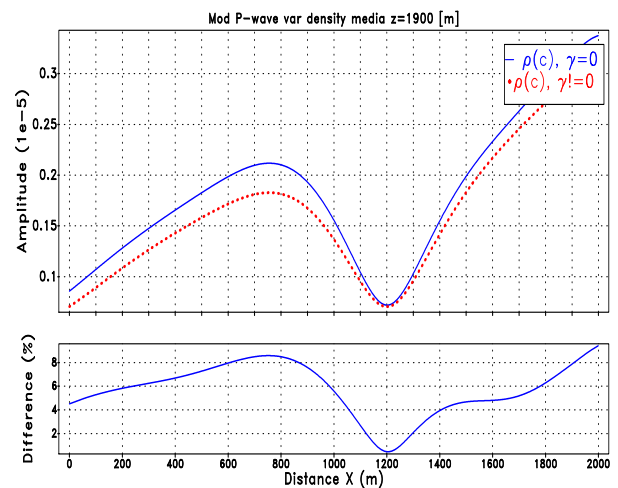
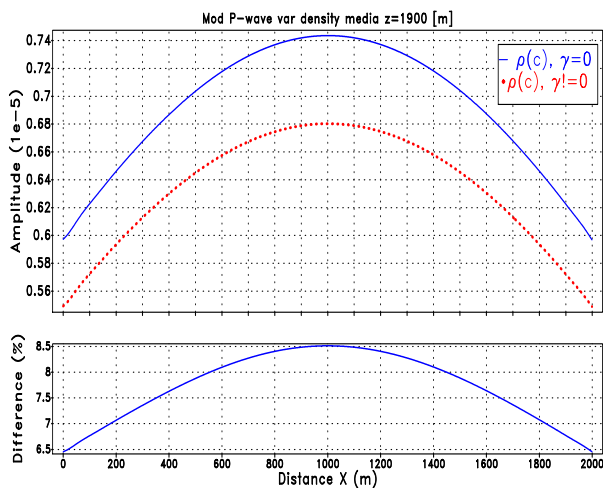
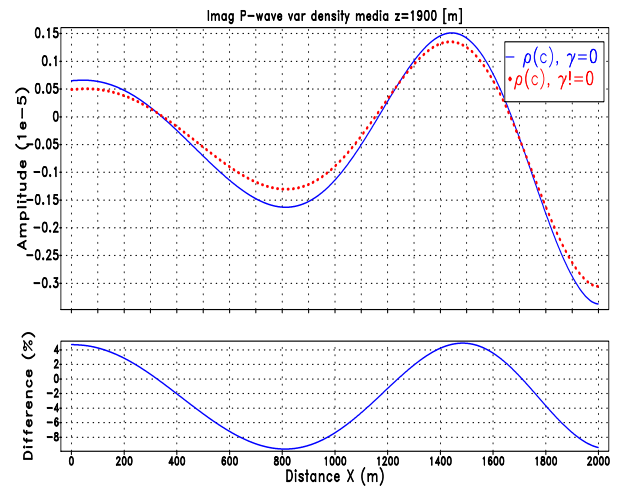
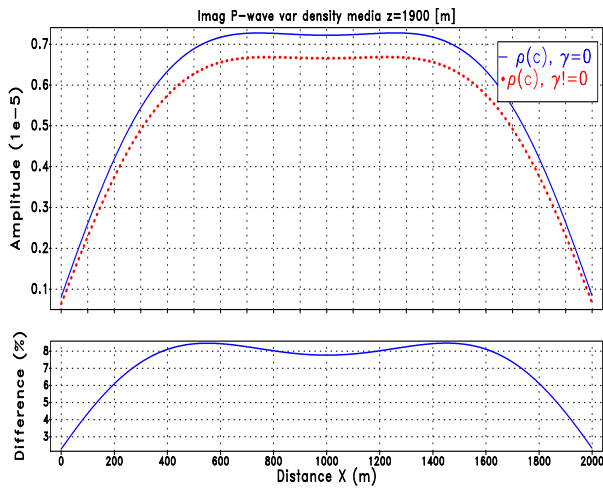
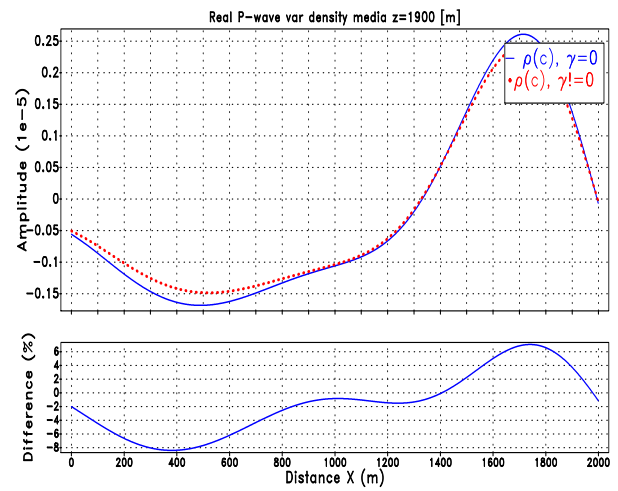
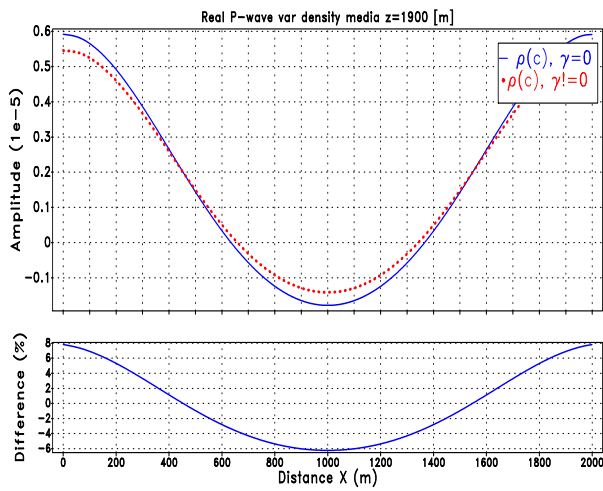


Figure 4.54: P-wave in the $z = 1900$ [m] for three layers velocity profile with ρ constant and variable for 5 [Hz]

Figure 4.55: P-wave in the $z = 1900$ [m] for complex velocity profile with ρ constant and variable for $f = 5$ [Hz]

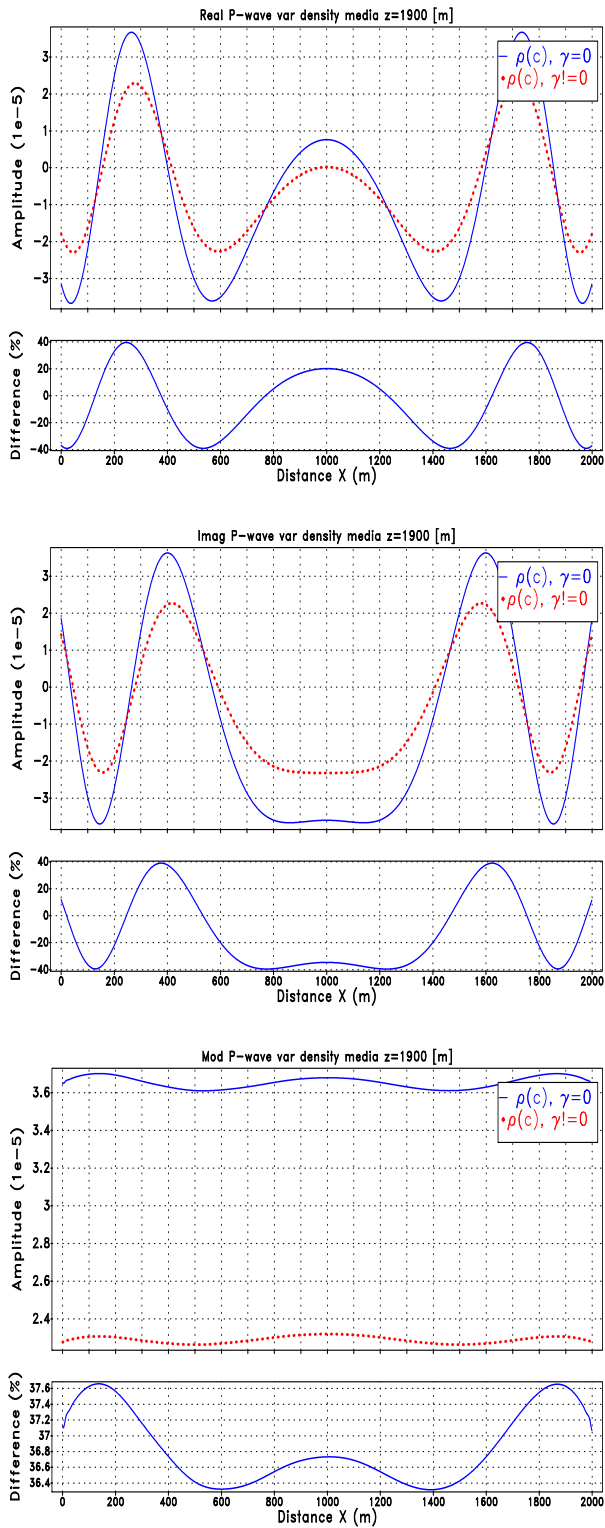


Figure 4.56: P-wave in the $z = 1900$ [m] for three layers velocity profile with ρ constant and variable for 25 [Hz]

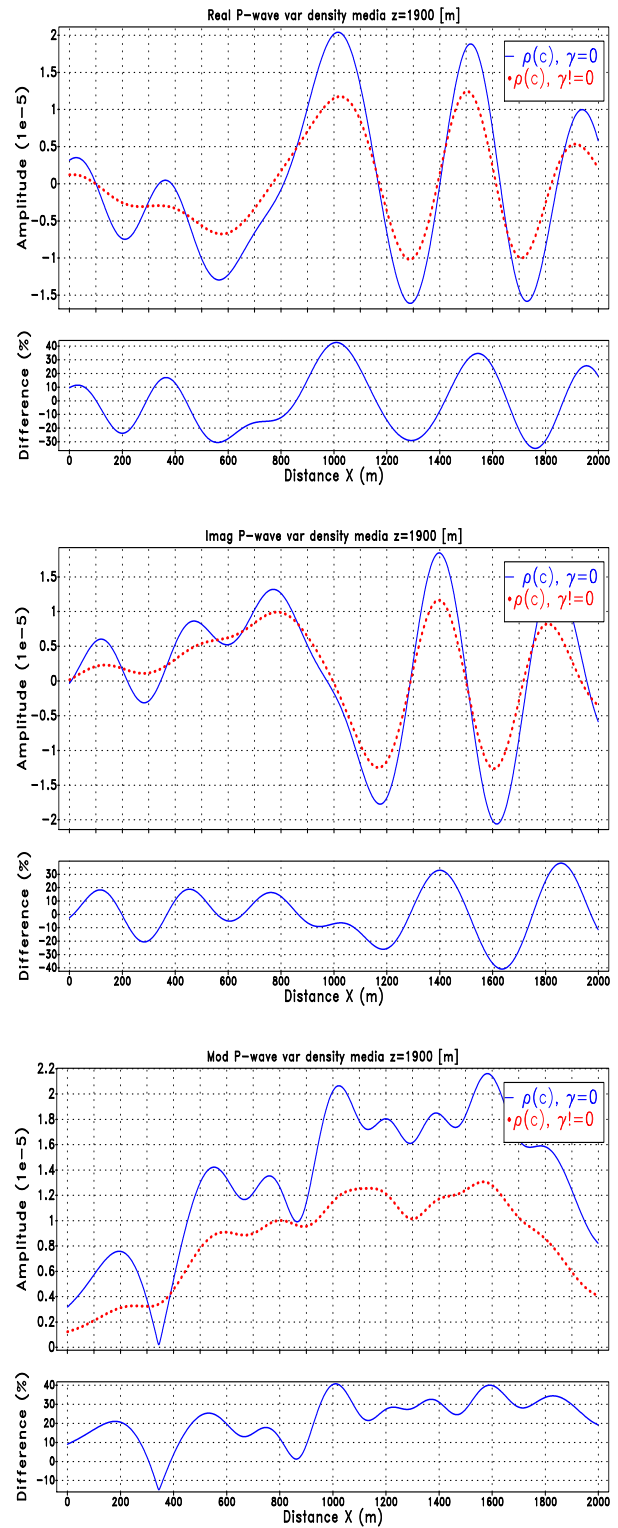


Figure 4.57: P-wave in the $z = 1900$ [m] for complex velocity profile with ρ constant and variable for $f = 25$ [Hz]

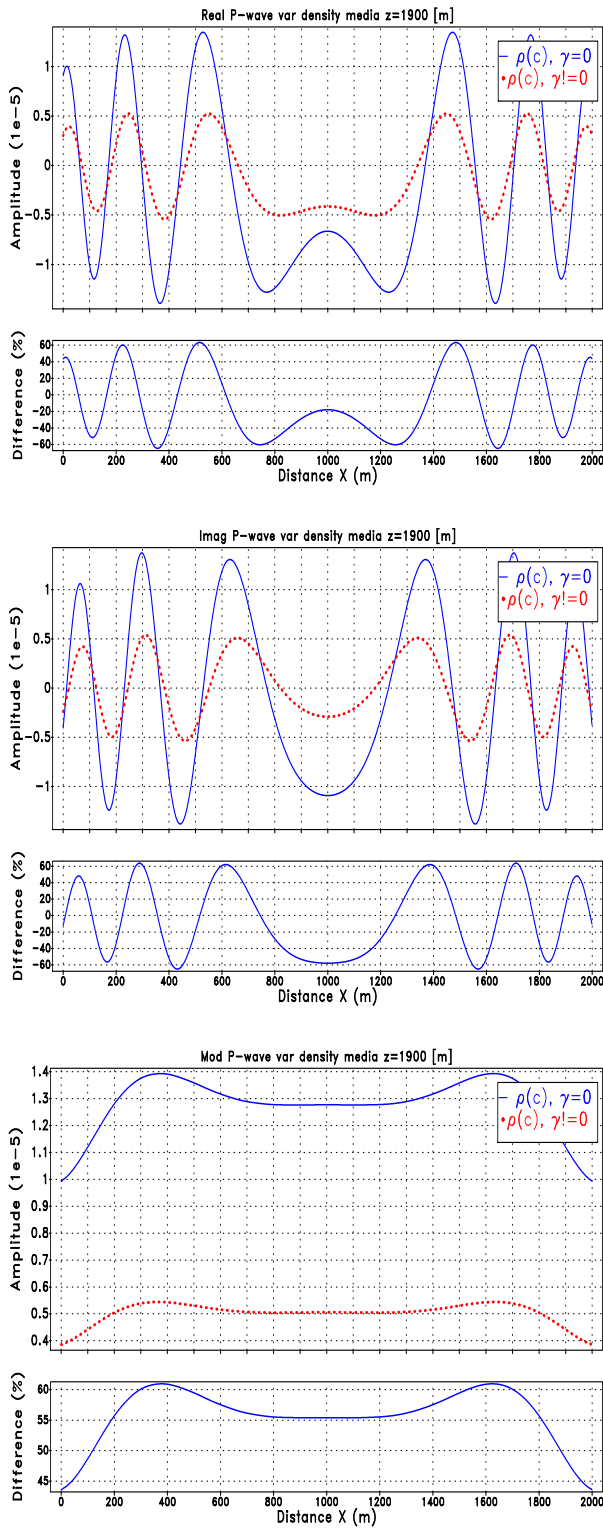


Figure 4.58: P-wave in the $z = 1900$ [m] for three layers velocity profile with ρ constant and variable for 50 [Hz]

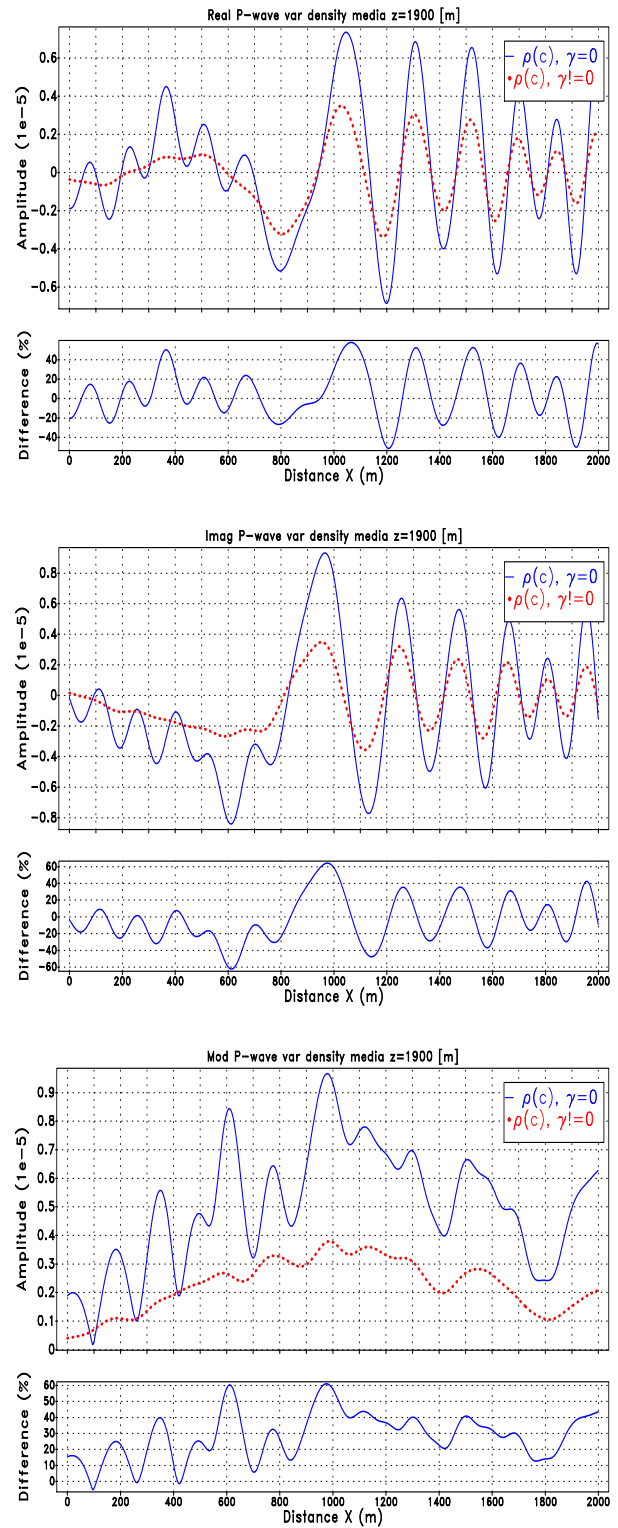


Figure 4.59: P-wave in the $z = 1900$ [m] for complex velocity profile with ρ constant and variable for $f = 50$ [Hz]

We can see in the figures that the difference between the medium with and without viscosity is a reduction in amplitude for medium with viscosity, with a difference of up to 9% for $f = 5$ [Hz], 40% for $f = 25$ [Hz] and 60% for $f = 50$ [Hz] between the amplitudes found with the visco-acoustic medium with respect to the amplitudes found with acoustic medium, as we expected the attenuation increases with frequency. The reduction is more larger in the $z = 1900$ [m] in comparison with $z = 10$ [m].

In addition, the dispersion of the wave, especially in the direction of change of velocity profile, the wave has a remarkable is phase shift in the viscous medium with respect to the acoustic medium. The dispersion is accentuated as the wave propagates to the edges, presented the same characteristics of the previous test.

We can conclude that considering the viscosity, makes P-wave field to show a dispersion that is accentuated in the change of velocity profile. The amplitude of the wave is affected, as expected, and this influence depends proportionally on the frequency and its proximity to the source. At low frequencies the difference between the amplitudes is minor and increases with frequency, but far from the source the amplitude reduces more drastically, depending on the frequency. In addition, it is important to note that the effects of viscosity and variable density on P-Waves amplitudes will definitely be more noticeable as the wave propagates through the medium.

4.3.3 Spectrum comparison for density

The following tests are performed with different frequency to obtain the spectrum the solution for visco-acoustic media with density variable in the three layers and complex velocity profile in figure (4.16), with source in $x = 1000$ [m] and $z = 10$ [m], the domain is 2 [km] \times 2 [Km].

In the figure 4.60, 4.61, 4.62 and 4.63 we show the modulus of the P-wave vs frequency at source with Ricker frequency 30 [Hz] in the points $x = [10, 1000, 1990]$ [m] and $z = [10, 1900]$ [m] in three layers and complex velocity profile. The solid line is the solution for visco-acoustic medium with constant density and the dotted line is a solution for medium with variable density, the difference between the medium with constant and variable density are a reduction in amplitude for medium with variable density, with a difference of up to 5%, for $z = 10$ [m] and 15%, for $z = 1900$ [m] in three layers velocity profile and 3%, for $z = 10$ [m] and 60%, for $z = 1900$ [m] for complex velocity profile, between the amplitudes found with the variable density with respect to the amplitudes found with constant density.

We can see that the spectrum has definite form that indicates the dependence of the amplitude of P-Wave with the source frequency beyond the range of values. Its form tells us that the maximum amplitudes of P-wave are modeled close to frequency source, this is expected in a velocity profile because the Ricker source has its maximum amplitude in the source frequency. In the point $x = 1000$ [Hz], this form is clear, but un the points $x = 10$ [m] ans $x = 1900$ [m] there is some oscillations, but this is proper of the frontiers since the farther one is from the source the more the reflections for the medium are noticed.

As we noted earlier, that considering the variable density in the modeling, makes P-wave field

presents a slight mismatch or dispersion that is accentuated in the abrupt changes for velocity profile. The amplitude of the wave in the spectrum is also affected, and this influence depends on the frequency and its proximity to the source. At low frequencies, for frequency smaller than the source frequency, and close to the source the difference between the amplitudes is remarkable but it is minimal at high frequencies, after the source frequency, but far from the source the field has amplitude values that differ considerably from the wave field considering the constant density, although they maintain the same behavior with respect to the frequencies.

4.3.4 Spectrum comparison for viscosity

The following tests are performed with different frequency to obtain the spectrum of the solution for a visco-acoustic media with density variable in the three layers and complex velocity profile in figure (4.16), with source in $x = 1000$ [m] and $z = 10$ [m], the domain is 2 [km] \times 2 [Km].

In the figure 4.64, 4.65, 4.66 and 4.63 we show the modulus of the P-wave vs frequency the source is a Ricker frequency 30 [Hz] in the point $x = [10, 1000, 1900]$ [m] and $z = [10, 1900]$ [m] in three layers and complex velocity profile. The solid line is the solution for acoustic medium with variable density and the dotted is a solution for visco-acoustic medium with density variable.

The difference into medium is a remarkable reduction in amplitude for medium with viscosity, with a difference of up to 50%, for $z = 10$ [m] and 30%, for $z = 1900$ [m] for three layers velocity profile and with a difference of up to 35%, for $z = 10$ [m] and 50%, for $z = 1900$ [m] for complex velocity profile, between the amplitudes found with the visco-acoustic medium with respect to the amplitudes found with acoustic medium, as we expected the attenuation increases with frequency.

We can see that the spectrum has a definite form that indicates the dependence of the amplitude of P-Wave with the source frequency beyond the range of values. Its form tells us that the maximum amplitudes of P-wave are modeled close to frequency source, this is expected in a velocity profile because the Ricker source has its maximum amplitude in the source frequency. In the point $x = 1000$ [Hz], this form is clear, but on the points $x = 10$ [m] and $x = 1900$ [m] there is some oscillations, but this is proper of the frontiers since the farther one is from the source the more the reflections for the medium are noticed.

As we noted earlier, considering the viscosity, makes P-wave field present a mismatch or dispersion that is accentuated in the change of velocity profile. The amplitude of the wave is affected, as expected, and this influence depends proportionally on the frequency and its proximity to the source. At low frequencies the difference between the amplitudes is minor and increases with frequency, but far from the source the amplitude reduces more drastically, depending on the frequency and the velocity profile. In the area with more attenuation (minor quality factor) the amplitude is more attenuated.

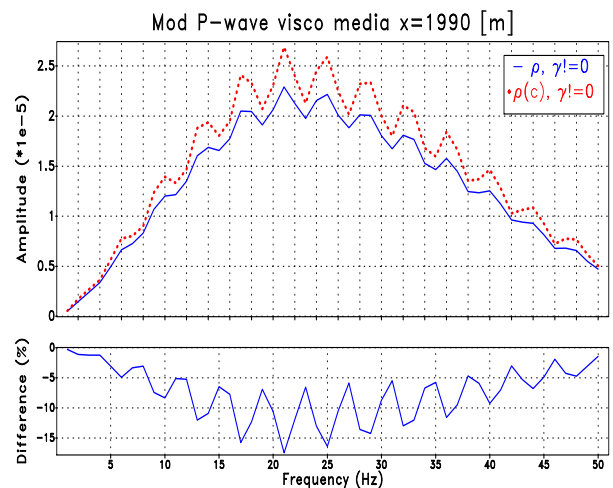
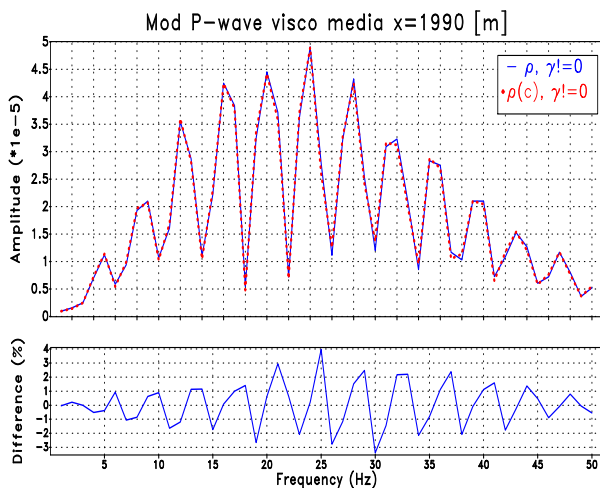
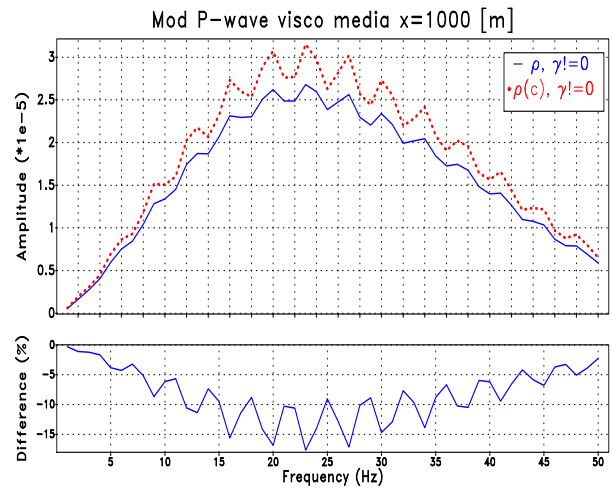
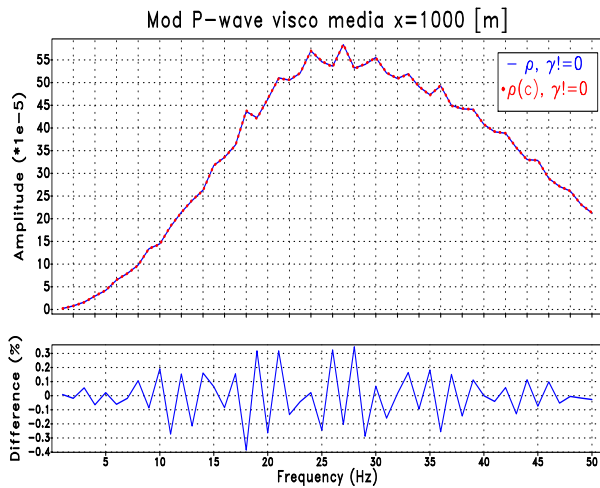
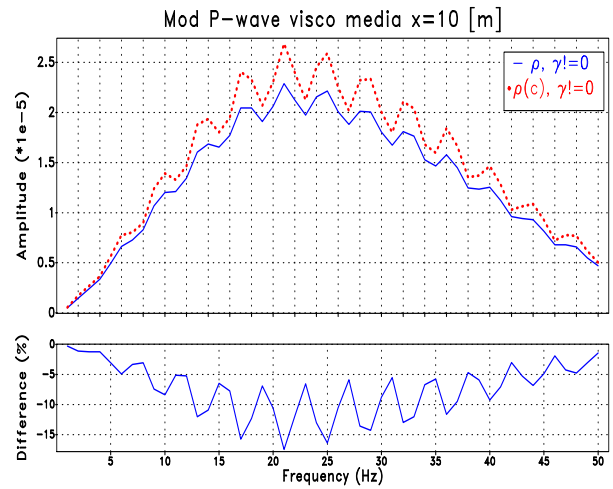
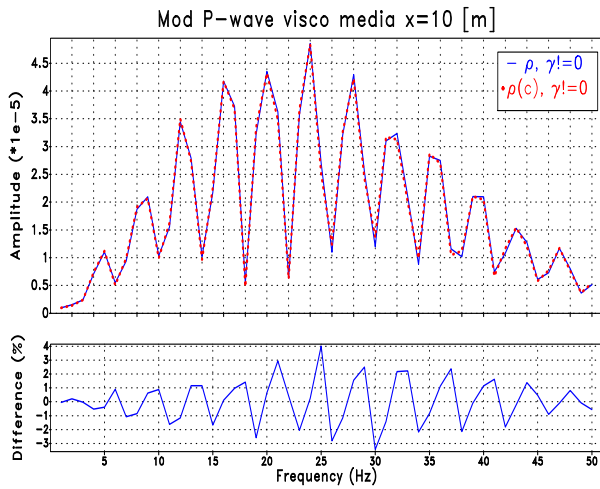


Figure 4.60: P-wave in the $z = 10$ [m] for three layers velocity profile with ρ constant and variable for $x = [10, 1000, 1990]$ [m] and source frequency $f_s = 30$ [Hz]

Figure 4.61: P-wave in the $z = 1900$ [m] for three layers velocity profile with ρ constant and variable for $x = [10, 1000, 1990]$ [m] and source frequency $f_s = 30$ [Hz]

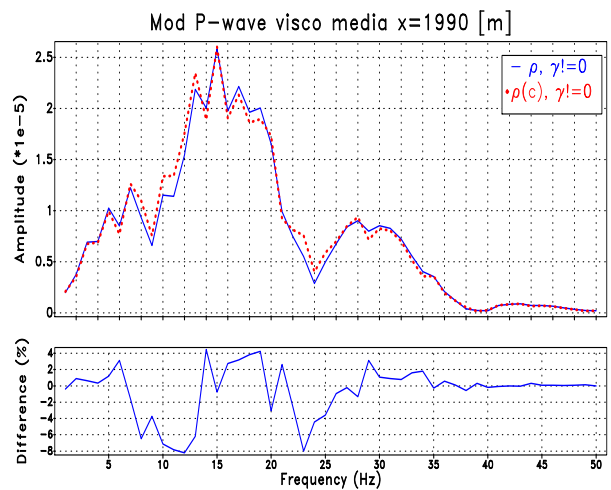
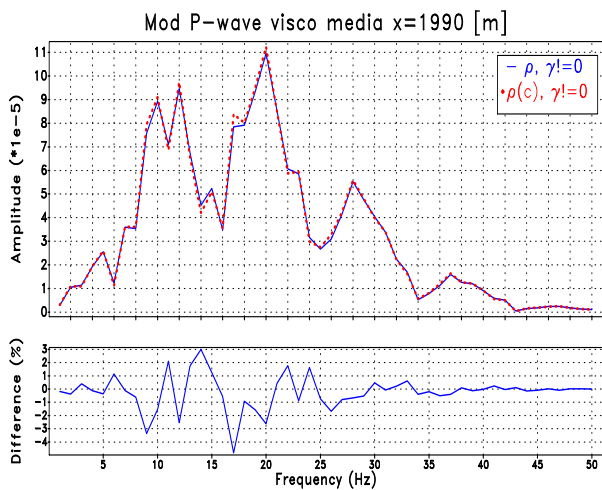
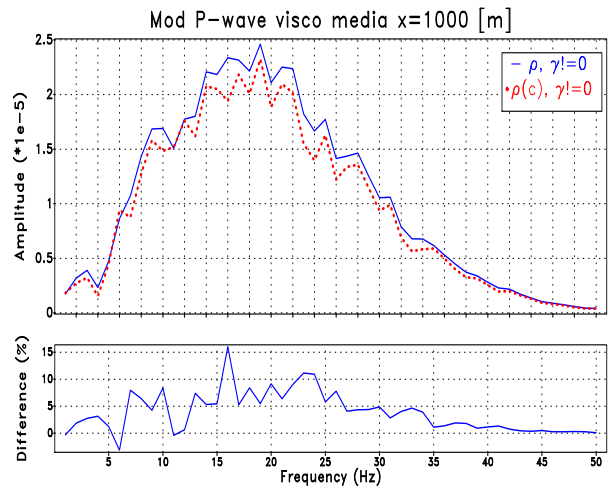
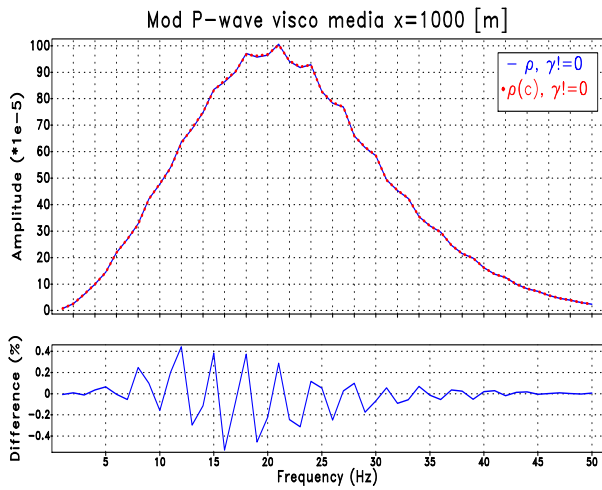
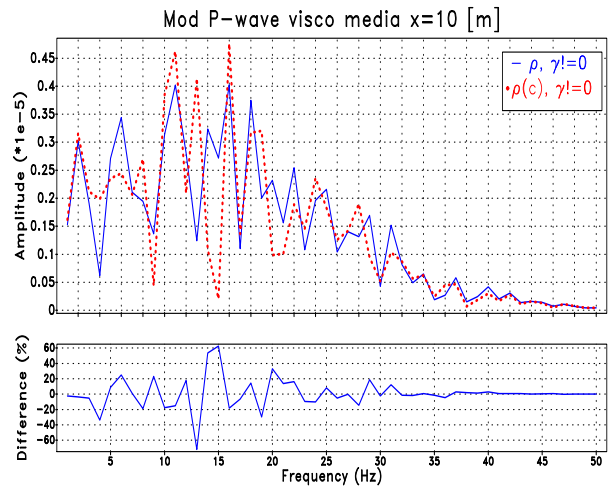
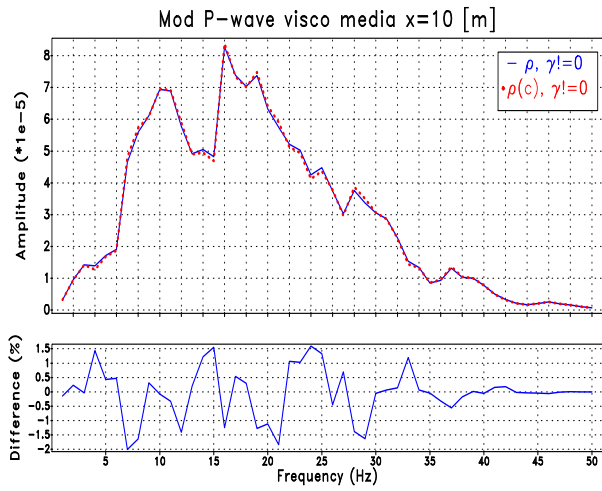


Figure 4.62: P-wave in the $z = 10$ [m] for complex velocity profile with ρ constant and variable for $x = [10, 1000, 1990]$ [m] and source frequency $f_s = 30$ [Hz]

Figure 4.63: P-wave in the $z = 1900$ [m] for complex velocity profile with ρ constant and variable for $x = [10, 1000, 1990]$ [m] and source frequency $f_s = 30$ [Hz]

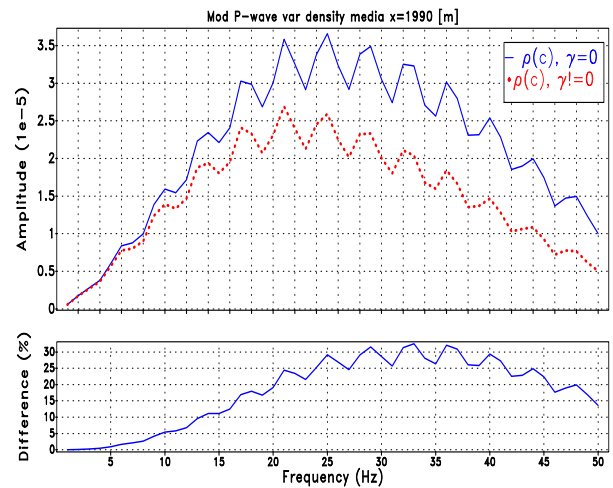
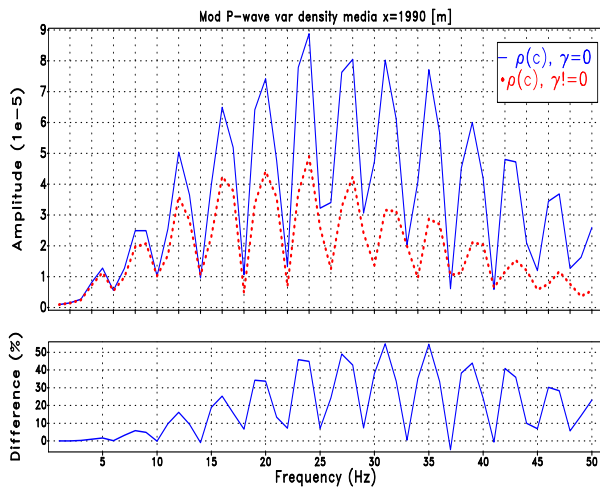
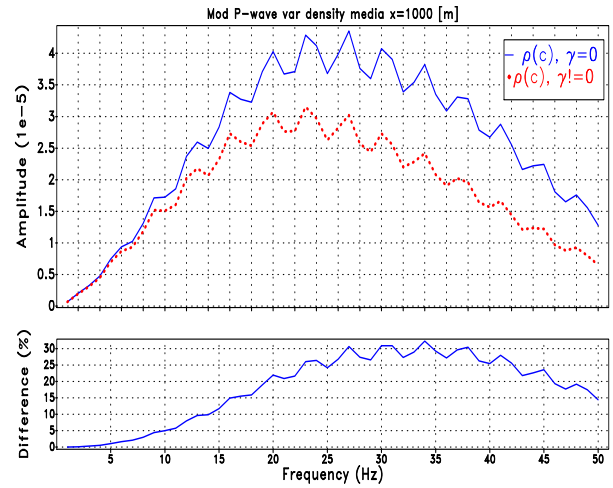
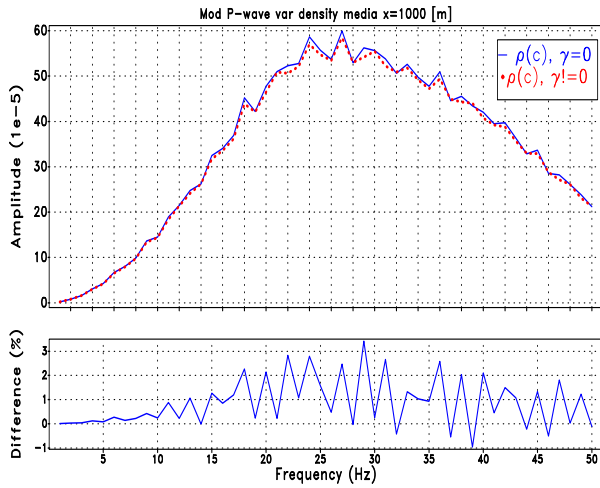
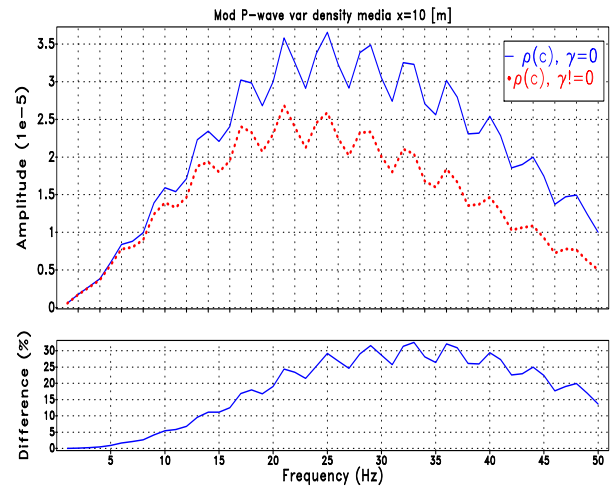
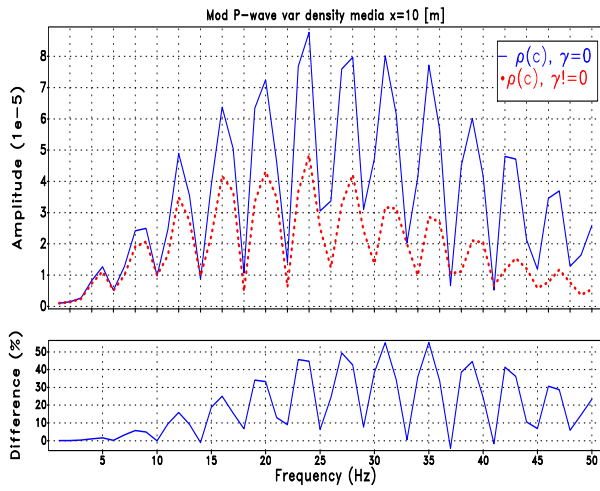


Figure 4.64: P-wave in the $z = 10$ [m] for three layers velocity profile in acoustic and visco-acoustic medium for $x = [10, 1000, 1990]$ [m] and source frequency $f_s = 30$ [Hz]

Figure 4.65: P-wave in the $z = 1900$ [m] for three layers velocity profile with in acoustic and visco-acoustic medium for $x = [10, 1000, 1990]$ [m] and source frequency $f_s = 30$ [Hz]

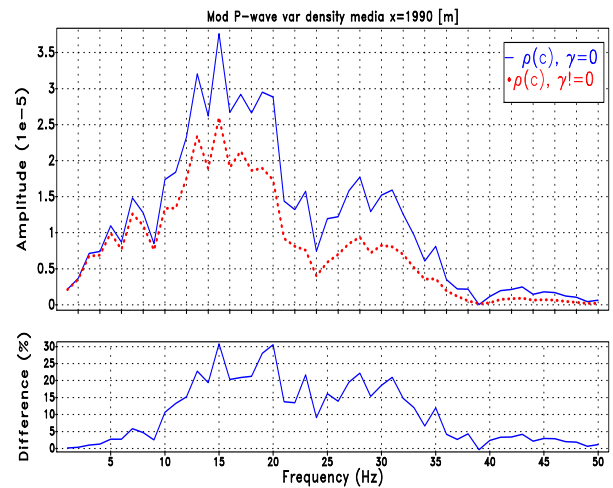
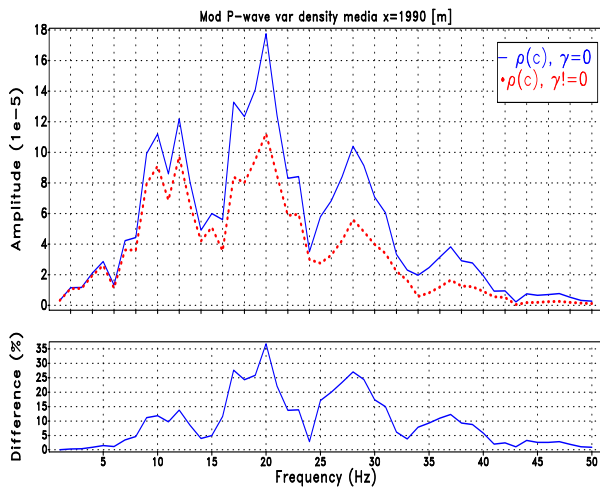
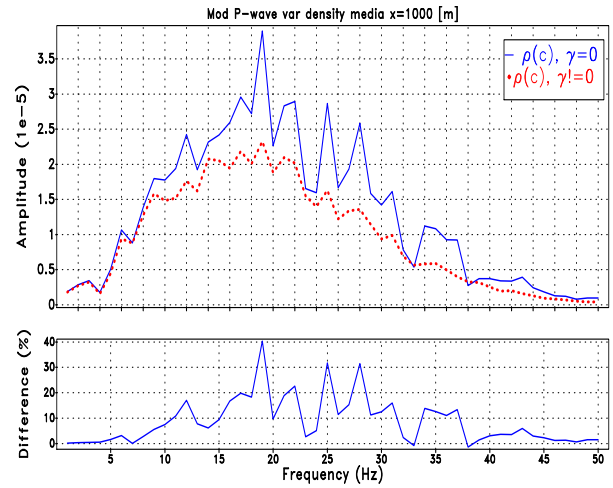
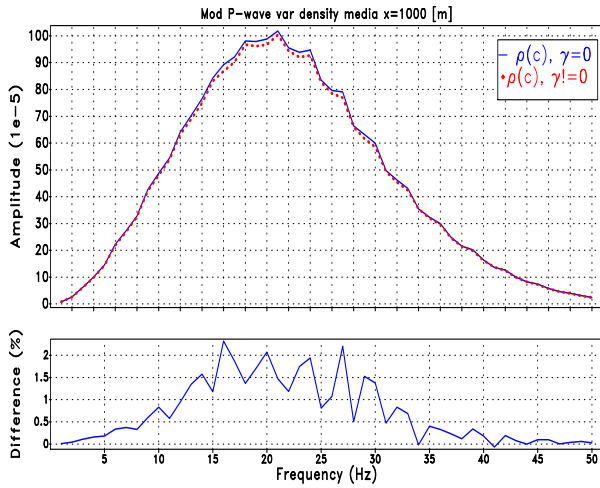
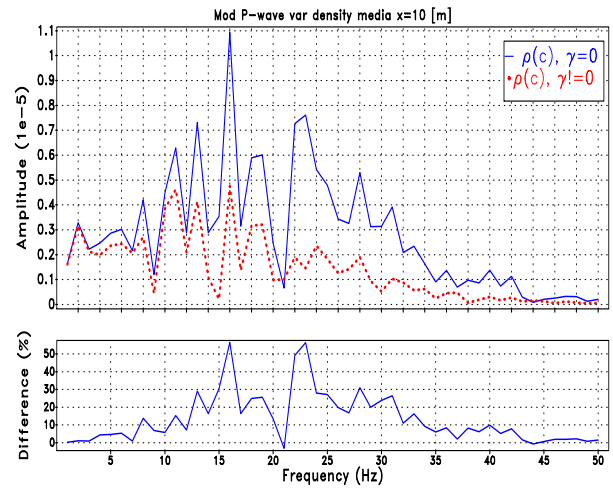
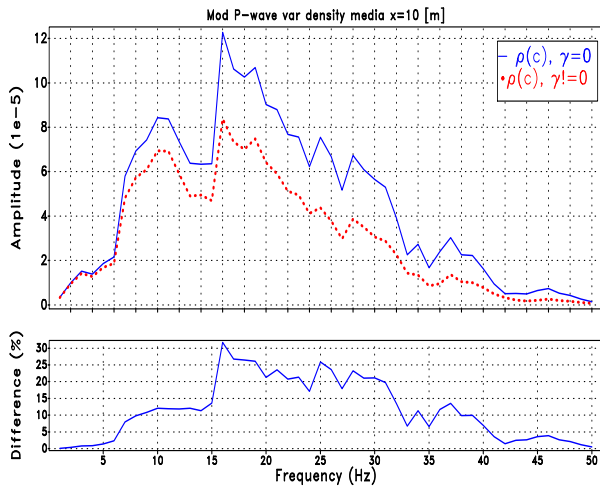


Figure 4.66: P-wave in the $z = 10$ [m] for complex velocity profile with in acoustic and visco-acoustic medium for $x = [10, 1000, 1990]$ [m] and source frequency $f_s = 30$ [Hz]

Figure 4.67: P-wave in the $z = 1900$ [m] for complex velocity profile in acoustic and visco-acoustic medium for $x = [10, 1000, 1990]$ [m] and source frequency $f_s = 30$ [Hz]

FULL WAVEFORM INVERSION IN FREQUENCY DOMAIN

As explained in the introductory section, chapter 1, seismic exploration consists in the generation of mechanical waves using an artificial source such that waves propagate through the subsurface and with this the responses are detected and recorded by a number of receiving stations for posterior processing.

So, using the seismic tomography, one of the main reconstruction techniques for processing seismic data, we one can obtain subsurface images, which are then related to the geological layers, seismic sections, velocity fields by comparing the data predicted by the direct problem solved with initial values for the parameters of the model, with the data observed, collected by receivers in some area of interest. This is a inversion problem.

Now, the inversion problem is to minimizing the function described in equation 1.2 through the variation of the parameters \mathbf{m} . In our case, the parameter we are going to invert is the propagation velocity $c(\mathbf{x})$. According to this we can define

$$\chi(\mathbf{m}) = \frac{1}{2} \delta \mathbf{d}^\dagger \delta \mathbf{d} = \frac{1}{2} (\mathbf{d}_{obs} - \mathbf{d}_{cal})^\dagger (\mathbf{d}_{obs} - \mathbf{d}_{cal}). \quad (5.1)$$

Where \mathbf{d}_{obs} and \mathbf{d}_{cal} are pressure values of observed data and calculated in the receivers, $\delta \mathbf{d}^\dagger$ is the conjugated transpose of error $\delta \mathbf{d}$ and \mathbf{d}_{cal} is estimated, according to our modeling described in chapters 2 and 3 as:

$$\mathbf{d}_{cal} = \mathbf{p}(\mathbf{x}_r, \mathbf{x}_s, c(\mathbf{x}), \omega) = [\mathbf{A}(c(\mathbf{x}), \omega, \gamma)]^{-1} \mathbf{s}(\mathbf{x}_s, \omega, \gamma) \Big|_{\mathbf{x}=\mathbf{x}_r}. \quad (5.2)$$

The matrix \mathbf{A} , although it is a square matrix, is complex, indefinite and dependent on frequency ω and rate deformation function γ , so the problem is nonlinear and the resulting values of $\mathbf{p}(\mathbf{x}_r, \mathbf{x}_s, \omega)$ are complex, because of this we use the notation \dagger for the conjugate transpose.

The model parameters for instance, the propagation velocity $c(\mathbf{x})$, is a vector of N values corresponding to the propagation velocity in a domain $N_x \times N_z = N$, with these parameters we calculate $\mathbf{p}(\mathbf{x}_r, \mathbf{x}_s, \omega)$ in the whole domain and we collect the values at \mathbf{x}_r , which have N_r values for data calculated, where N_r is the number of receivers. This procedure is performed for a defined number of frequencies N_f and of sources N_s , such that the calculated and observed data are a vectors with dimension $N_f \times N_r \times N_s$. With this, the objective function can be written

$$\chi(\mathbf{m}) = \frac{1}{2} \sum_s^{N_s} \sum_r^{N_r} \sum_f^{N_f} (d_{obs} - d_{cal})_{(s,r,f)} (d_{obs} - d_{cal})_{(s,r,f)}^*. \quad (5.3)$$

Now, the function of equation 5.1 is non-linear, so it is possible that there is more than one local minimum (Sen and Stoffa, 1995), in addition if the values of the data and values thrown by the model have different scales, it can lead to multiple solutions in the inversion or non-convergence. Therefore, for most geophysical applications generation of synthetic data is a task of higher computational demand, even for fast computers, the search for the model parameters in the space of models is usually very coarse.

For example, if each model parameter can take M possible discrete values and there are N parameter model, then there are $(N)^M$ possible configurations models to be tested. In conclusion, inversion, especially FWI where the model is a full numerical solution of the equation of wave motion, is a large problem where we must select a numerical method that minimizes the use of possible resources.

5.1 Inversion Method: Numerical considerations

The goal of Full Waveform Inversion (FWI) in the deterministic sense is to find optimal values for the parameter model, $\hat{\mathbf{m}}$, that minimizes the misfit functional, $\chi(\mathbf{m})$ such that $\forall \mathbf{m} \neq \hat{\mathbf{m}} \quad \chi(\hat{\mathbf{m}}) < \chi(\mathbf{m})$, used to quantify the discrepancies between the observed seismograms, \mathbf{d}_{obs} , and the synthetic seismograms, \mathbf{d}_{cal} .

Since the misfit function $\chi(\mathbf{m})$, is generally a complicated non-linear functional of \mathbf{m} , we approximate the optimum $\hat{\mathbf{m}}$ with the help of iterative minimization algorithms: starting from a plausible initial model \mathbf{m}_0 , iterative minimization successively updates the current model \mathbf{m}_k to a new model \mathbf{m}_{k+1} that reduce misfit the data better than its predecessor, such that \mathbf{m}_k and \mathbf{m}_{k+1} are related through:

$$\mathbf{m}_{k+1} = \mathbf{m}_k + \epsilon_k \mathbf{h}_k. \quad (5.4)$$

With conditions

$$\begin{aligned} \chi(\mathbf{m}_{k+1}) &\leq \chi(\mathbf{m}_k) + c_1 \epsilon_k \mathbf{h}_k^T \nabla_{\mathbf{m}} \chi(\mathbf{m}_k), \\ -\mathbf{h}_k^T \nabla_{\mathbf{m}} \chi(\mathbf{m}_{k+1}) &\leq -c_2 \mathbf{h}_k^T \nabla_{\mathbf{m}} \chi(\mathbf{m}_k). \end{aligned} \quad (5.5)$$

Where $0 < c_1 < c_2 < 1$. These conditions are known as Wolfe conditions.

The particular choice of the descent direction \mathbf{h}_k and the step length ϵ_k , depends on the minimization scheme used to approximate $\hat{\mathbf{m}}$. The iterative procedure is repeated until the synthetic data explain the observed data sufficiently well. For a more comprehensive discussion of both theory and methods the reader is referred to Gill et al. (1981), Fletcher (1987), Polak (1997), Kelley (1999), Quarteroni et al. (2000).

5.1.1 A brief summary of non-linear minimization methods

There are two important points in the search for the minimum of a function. The direction of descent \mathbf{h}_k and the length of the descent step ϵ_k :

Descent Directions: This consist in the election of

$$\mathbf{h}_k = -\Gamma_k \cdot \nabla_{\mathbf{m}}\chi(\mathbf{m}_k). \quad (5.6)$$

Where $\nabla_{\mathbf{m}}\chi(\mathbf{m}_k)$ is an objective function gradient. If \mathbf{m} is a vector of $i = 0, 1, 2, \dots, N$

$$\nabla_{\mathbf{m}}\chi(\mathbf{m}_k) = \sum_i^N \frac{\partial \chi}{\partial m_k^i} \mathbf{e}^i. \quad (5.7)$$

When the choice of the positive definite matrices Γ_k characterizes different descent methods and it controls the speed of convergence towards the optimum $\hat{\mathbf{m}}$. We can see that with this choice $\mathbf{h}_k^T \nabla_{\mathbf{m}}\chi(\mathbf{m}_k) < 0$ which guarantees the second Wolfe condition.

The Optimal Step Length: To complete the description of the general descent method, it remains to construct an efficient step length for each iteration. Ideally, we would like to find an optimal ϵ_k such that $\chi(\mathbf{m}_{k+1}) - \chi(\mathbf{m}_k)$ is minimal. A necessary condition for the optimal of ϵ_k is then:

$$\epsilon_k = -\frac{\mathbf{h}_k \cdot \nabla_{\mathbf{m}}\chi(\mathbf{m}_k)}{\mathbf{h}_k \cdot \mathbf{H}_{\chi}(\mathbf{m}_k) \cdot \mathbf{h}_k}. \quad (5.8)$$

Where $\mathbf{H}_{\chi}(\mathbf{m}_k)$ is the Hessian matrix for objective function.

$$[\mathbf{H}_{\chi}(\mathbf{m}_k)]_{j,i} = \frac{\partial^2 \chi}{\partial m_k^j \partial m_k^i}. \quad (5.9)$$

A brief summary is presented on the most used methods to solve inverse problems with nonlinear misfit function Fichtner (2011b):

- **Method of Steepest Descent:** This method looks for a descent direction eq. 5.5 such that update \mathbf{m}_k according to $\mathbf{m}_{k+1} = \mathbf{m}_k + \epsilon_k \mathbf{h}_k$, with a suitable step length ϵ_k that ensures $\chi(\mathbf{m}_{k+1}) < \chi(\mathbf{m}_k)$ using eq. 5.7
- **Newton's Method:** In this method determine the descent direction \mathbf{h}_k as the solution of

$$\mathbf{H}_\chi(\mathbf{m}_k) \cdot \mathbf{h}_k = -\nabla\chi(\mathbf{m}_k). \quad (5.10)$$

And update \mathbf{m}_k according to $\mathbf{m}_{k+1} = \mathbf{m}_k + \mathbf{h}_k$

- **Gauss-Newton's Method:** Is a method similar at Newton's Method. Determine the approximate Hessian:

$$\bar{\mathbf{H}}_\chi(\mathbf{m}_i) = \nabla_{\mathbf{u}} \nabla_{\mathbf{u}} \chi(\nabla_{\mathbf{m}} \mathbf{u}, \nabla_{\mathbf{m}} \mathbf{u}). \quad (5.11)$$

Where \mathbf{u} is a physical variable related with d_{cal} , and determines the descent direction \mathbf{h}_k , as the solution of

$$\bar{\mathbf{H}}_\chi(\mathbf{m}_k) \cdot \mathbf{h}_k = -\nabla\chi(\mathbf{m}_k). \quad (5.12)$$

And update \mathbf{m}_k according to $\mathbf{m}_{k+1} = \mathbf{m}_k + \mathbf{h}_k$.

5.1.2 Cycle skipping and phase difference

In addition to defining a direction \mathbf{h} and length ϵ of descent it is important to start from a set of parameters model \mathbf{m}_0 suitable to not fall into a local minimum or have convergence problems.

One of the most common problems in FWI, due to a inappropriate choice of the initial parameters, is cycle skipping. The cycle skipping is produced when predicted and observed data differ by more than half a cycle in frequency domain, and it leads the inversion to recover a local rather than the global minimum model. Overcoming cycle skipping normally requires both a good starting model and low-frequency content in the field data (Shah et al., 2012).

In our case, the field data is defined in the frequency domain and the difference phase is easy to compute:

$$[d_{comp}]_{s,r,f} = [d_{cal}]_{(s,r,f)} [d_{obs}^*]_{(s,r,f)}. \quad (5.13)$$

$$\phi_{(s,r)} = \max_f \left[\text{atan} \left(\frac{\text{Im}\{[d_{comp}]_{s,r,f}\}}{\text{Re}\{[d_{comp}]_{s,r,f}\}} \right) \right]. \quad (5.14)$$

The field $[d_{comp}]_{s,r,f}$ is the product in complex domain between the d_{cal} and d_{obs} for each receptor, source and frequency. The phase of a complex number is arctangent between its imaginary and real part, the function is defined between $[-\pi, \pi]$. The difference phase $\phi_{(s,r)}$ is the maximum value of the d_{comp} phases between all the frequencies analyzed by each receiver-source pair.

To make sure we take a suitable initial model parameter m_0 we calculate $[d_{comp}]_{s,r,f}$ in the first iteration, if data field is not cycle skipped in the frequencies analyzed, then $\phi_{(s,r)}$ will vary smoothly and consistently in space. However, if the model is cycle skipped, then $\phi_{(s,r)}$ there will be sudden, spatially consistent, 2π jumps in phase. These phase jumps are easy to observe in low-frequency and they are an immediate diagnostic of a potential problem for FWI.

5.2 An Inversion Scheme in frequency domain

(Pratt and Hicks, 1998) and (Fichtner, 2011a), compiled the most commonly used methods for working with low linearity inverse problems, Gauss-Newton and Full Newton, which propose to define the descent step by means of the gradient and the hessian of the misfit function and suggest the use of the adjoint method as an alternative to find the variations of the calculated data with respect to the parameters of the model, described in (Plessix, 2006).

The model parameters, the propagation velocity $c(\mathbf{x})$, can be iteratively update through the following formula (Pratt, 1999),(Brossier and Operto, 2009), (Taoi and Sen, 2013)

$$c_k(\mathbf{x}) = c_{k-1}(\mathbf{x}) + \epsilon_k(\mathbf{H}_{k-1} + \beta\mathbf{I})^{-1}g_{k-1}(\mathbf{x}). \quad (5.15)$$

Where $g_{k-1}(\mathbf{x}) = -\nabla_c \chi(c_{k-1}(\mathbf{x}))$, ϵ_k is a step length and is defined by line search procedure such as parabolic fitting or cubic search along the gradient direction, β is a damping factor for regularization, \mathbf{H} is the Hessian matrix. Eq. 5.15 is our choice for the inversion and minimization of the objective function, but first we must define each ingredient of the recipe.

5.2.1 Gradient of the objective function

To compute $c_k(\mathbf{x})$ it is necessary to calculate the gradient of the objective function $g_{k-1}(\mathbf{x}) = -\nabla_c \chi(c_{k-1}(\mathbf{x}))$. With Eq. 5.3 we can define the gradient as

$$\nabla_c \chi(c(\mathbf{x})) = -\frac{1}{2} \sum_f^{N_f} \sum_s^{N_s} \sum_r^{N_r} \text{Re}\{\nabla_c(d_{cal})_{(f,s,r)} \delta d_{(f,s,r)}^*\}. \quad (5.16)$$

Now, we can define \mathbf{J} , the Jacobian matrix with $N_r \times N$ elements, as

$$\mathbf{J}_{(f,s)} = \begin{pmatrix} \frac{\partial d_{cal}(f,s,1)}{\partial c(x_1)} & \frac{\partial d_{cal}(f,s,1)}{\partial c(x_2)} & \cdots & \frac{\partial d_{cal}(f,s,1)}{\partial c(x_N)} \\ \frac{\partial d_{cal}(f,s,2)}{\partial c(x_1)} & \frac{\partial d_{cal}(f,s,2)}{\partial c(x_2)} & \cdots & \frac{\partial d_{cal}(f,s,2)}{\partial c(x_N)} \\ \vdots & \ddots & \vdots & \\ \frac{\partial d_{cal}(f,s,N_r)}{\partial c(x_1)} & \frac{\partial d_{cal}(f,s,N_r)}{\partial c(x_2)} & \cdots & \frac{\partial d_{cal}(f,s,N_r)}{\partial c(x_N)} \end{pmatrix} \quad (5.17)$$

With this, we can rewrite eq. 5.16 as

$$\nabla_c \chi(c(\mathbf{x})) = -\frac{1}{2} \sum_f^{N_f} \sum_s^{N_s} \text{Re}\{\mathbf{J}_{(f,s)}^T \delta \mathbf{d}_{(f,s)}^*\}. \quad (5.18)$$

Where $\delta \mathbf{d}_{(f,s)}^*$ is a error vector in receivers with $N_r \times 1$ values, for frequency and source. Now, computing the Jacobian matrix $\mathbf{J}_{(f,s)}$ by finite difference and similar methods for each frequency and source would be computationally expensive and in (Pratt and Hicks, 1998) and (Plessix, 2006), they

propose the use of the adjoint method to re-calculate the gradient as a function of the operation between a backpropagated field and the predicted field.

The first step is to extend the matrix $\mathbf{J}_{(f,s)}$ for all points in the domain $N_x \times N_z = N$, so that we can use the equations of the direct problem to find partial derivatives, with this we would have

$$\hat{\mathbf{J}}_{(f,s)} = \begin{pmatrix} \frac{\partial d_{cal}(f,s,1)}{\partial c(x_1)} & \frac{\partial d_{cal}(f,s,1)}{\partial c(x_2)} & \cdots & \frac{\partial d_{cal}(f,s,1)}{\partial c(x_N)} \\ \vdots & \ddots & \vdots & \\ \frac{\partial d_{cal}(f,s,N_r)}{\partial c(x_1)} & \frac{\partial d_{cal}(f,s,N_r)}{\partial c(x_2)} & \cdots & \frac{\partial d_{cal}(f,s,N_r)}{\partial c(x_N)} \\ \vdots & \ddots & \vdots & \\ \frac{\partial d_{cal}(f,s,N)}{\partial c(x_1)} & \frac{\partial d_{cal}(f,s,N)}{\partial c(x_2)} & \cdots & \frac{\partial d_{cal}(f,s,N)}{\partial c(x_N)} \end{pmatrix} \quad (5.19)$$

Now, we can rewrite eq. 5.18 as

$$\nabla_c \chi(c(\mathbf{x})) = -\frac{1}{2} \sum_f^{N_f} \sum_s^{N_s} \text{Re}\{\hat{\mathbf{J}}_{(f,s)}^T \delta \hat{\mathbf{d}}_{(f,s)}^*\}. \quad (5.20)$$

Where $\delta \hat{\mathbf{d}}_{(f,s)}^* = [\delta \mathbf{d}_{(f,s)}^* \ 0 \ 0 \ \dots \ 0]$, is an error vector extended in the domain $N_x \times N_z = N$ augmented $N - N_r$ zero values to produce a new vector of length N .

To find $\hat{\mathbf{J}}_{(f,s)}$ using the equation for forward modeling $\mathbf{A}\mathbf{p} = \mathbf{s}$

$$\mathbf{A}(c(\mathbf{x}), \omega, \gamma) \mathbf{p}(\mathbf{x}, \mathbf{x}_s, c(\mathbf{x}), \omega) = \mathbf{s}(\mathbf{x}_s, \omega, \gamma). \quad (5.21)$$

If we derive eq 5.21 for each $c(x_l)$, with $l = 1, 2, \dots, N$ obtain:

$$\mathbf{A}(c(\mathbf{x}), \omega, \gamma) \frac{\partial \mathbf{p}(\mathbf{x}, \mathbf{x}_s, c(\mathbf{x}), \omega)}{\partial c(x_l)} + \frac{\partial \mathbf{A}(c(\mathbf{x}), \omega, \gamma)}{\partial c(x_l)} \mathbf{p}(\mathbf{x}, \mathbf{x}_s, c(\mathbf{x}), \omega) = \mathbf{0}. \quad (5.22)$$

Where the Jacobian matrix terms is:

$$\frac{\partial \mathbf{p}(\mathbf{x}, \mathbf{x}_s, c(\mathbf{x}), \omega)}{\partial c(x_l)} = -[\mathbf{A}(c(\mathbf{x}), \omega, \gamma)]^{-1} \mathbf{f}^{(l)}. \quad (5.23)$$

It is called the term $\mathbf{f}^{(l)}$ "virtual source"

$$\mathbf{f}^{(l)} = \frac{\partial \mathbf{A}(c(\mathbf{x}), \omega, \gamma)}{\partial c(x_l)} \mathbf{p}(\mathbf{x}, \mathbf{x}_s, c(\mathbf{x}), \omega). \quad (5.24)$$

With this, the Jacobian matrix is

$$\hat{\mathbf{J}}_{(f,s)} = \frac{\partial \mathbf{p}(\mathbf{x}, \mathbf{x}_s, c(\mathbf{x}), \omega)}{\partial c(x_l)} = -\mathbf{A}_{(f)}^{-1} \mathbf{F}_{(f,s)}. \quad (5.25)$$

Where F is an $N \times N$ matrix and $\mathbf{F} = [\mathbf{f}^{(1)} \ \mathbf{f}^{(2)} \ \dots \ \mathbf{f}^{(N)}]$, the columns of which are the virtual source terms for each of the N physical parameters. Now, it is not necessary to compute the elements of \mathbf{J} explicitly, substituting eq. 5.25 into eq. 5.20 we obtain

$$\nabla_c \chi(c(\mathbf{x})) = \frac{1}{2} \sum_f^{N_f} \sum_s^{N_s} \text{Re}\{\mathbf{F}_{(f,s)}^T \mathbf{v}_{(f,s)}\}. \quad (5.26)$$

Where $\mathbf{v}_{(f,s)}$ is the "backpropagated wavefield"

$$\mathbf{v}_{(f,s)} = (\mathbf{A}_{(f)}^{-1})^T \delta \hat{\mathbf{d}}_{(f,s)}^* = (\mathbf{A}_{(f)}^T)^{-1} \delta \hat{\mathbf{d}}_{(f,s)}^*. \quad (5.27)$$

Other form for the gradient can be obtained combining eq. 5.26 and eq. 5.24, such that the l th component of the gradient vector as

$$[\nabla_c \chi(c(\mathbf{x}))]_l = \frac{1}{2} \sum_f^{N_f} \sum_s^{N_s} \text{Re}\{\mathbf{p}_{(f,s)} \left(\frac{\partial \mathbf{A}_{(f)}}{\partial c(x_l)} \right)^T \mathbf{v}_{(f,s)}\}. \quad (5.28)$$

This form tell us that the gradient can be computed, in certain cases, by a scaled multiplication (convolution in the time domain) of forward and backpropagated wavefields. This is the description usually given for the computation of the gradient vector and imaging condition in reverse time migration algorithms.

5.2.2 Virtual Source Matrix

To compute the gradient of the objective function it is necessary calculate the Matrix \mathbf{F} or matrix of virtual source. In this case it is necessary calculate the term $\frac{\partial \mathbf{A}}{\partial c(x_l)}$. Using of eq. 3.50 we can obtain

$$\begin{aligned} \frac{\partial A_{(m,n)}}{\partial c(x_l)} &= \frac{\partial D_{(m)}}{\partial c(x_l)} \delta_{m,n} + \frac{\partial D1_{(m)}}{\partial c(x_l)} \delta_{m,n+N_z} + \frac{\partial D2_{(m)}}{\partial c(x_l)} \delta_{m,n-N_z} + \frac{\partial D3_{(m)}}{\partial c(x_l)} \delta_{m,n+1} \\ &+ \frac{\partial D4_{(m)}}{\partial c(x_l)} \delta_{m,n-1} + \frac{\partial D5_{(m)}}{\partial c(x_l)} \delta_{m,n+N_z-1} + \frac{\partial D6_{(m)}}{\partial c(x_l)} \delta_{m,n-N_z+1} \\ &+ \frac{\partial D7_{(m)}}{\partial c(x_l)} \delta_{m,n+N_z+1} + \frac{\partial D8_{(m)}}{\partial c(x_l)} \delta_{m,n-N_z-1}. \end{aligned} \quad (5.29)$$

Where $m = iN_z + j$ and is other form of represent (i, j) , where $i = 0, 1, 2, \dots, N_x - 1$ and $j = 0, 1, 2, \dots, N_z - 1$. That after simplifications can be finally written as

$$\begin{aligned} \frac{\partial A_{(m,n)}}{\partial c(x_l)} &= V_{(m,n)} \delta_{m,l} + W_{(m,l)} \delta_{m,n} + W1_{(m,l)} \delta_{m,n+N_z} + W2_{(m,l)} \delta_{m,n-N_z} + W3_{(m,l)} \delta_{m,n+1} \\ &+ W4_{(m,l)} \delta_{m,n-1} + W5_{(m,l)} \delta_{m,n+N_z-1} + W6_{(m,l)} \delta_{m,n-N_z+1} \\ &+ W7_{(m,l)} \delta_{m,n+N_z+1} + W8_{(m,l)} \delta_{m,n-N_z-1}. \end{aligned} \quad (5.30)$$

Where:

$$V_{(m,n)} = \left[\frac{-2\omega^2}{c_m^3 \rho_m} + \frac{-\omega^2}{c_m^2 \rho_m^2} \frac{\partial \rho_m}{\partial c_m} \right] [m_2 \delta_{m,n} + m_3 (\delta_{m,n+N_z} + \delta_{m,n-N_z} + \delta_{m,n+1} + \delta_{m,n-1}) + (1/4 - m_2/4 - m_3) (\delta_{m,n+N_z-1} + \delta_{m,n-N_z+1} + \delta_{m,n+N_z+1} + \delta_{m,n-N_z-1})]. \quad (5.31)$$

And from eq. 4.1 we take

$$\frac{\partial \rho_m}{\partial c_m} = \begin{cases} \sum_{i=1}^4 i a_i c_m^{i-1} & c_m > 1480 [\text{m/s}] \\ 0 & c_m < 1480 [\text{m/s}] \end{cases} \quad (5.32)$$

Each W -term is given by

$$W_{(m,l)} = - \left(\zeta_{x1(m,l)} + \zeta_{x2(m,l)} + \zeta_{z1(m,l)} + \zeta_{z2(m,l)} \right) m_1 - \left(\zeta_{rx1(m,l)}^+ + \zeta_{rx2(m,l)}^+ + \zeta_{rz1(m,l)}^+ + \zeta_{rz2(m,l)}^+ \right) (1 - m_1), \quad (5.33)$$

$$W1_{(m,l)} = \zeta_{x1(m,l)} m_1 + \left(\zeta_{rx1(m,l)}^- + \zeta_{rz1(m,l)}^- \right) (1 - m_1), \quad (5.34)$$

$$W2_{(m,l)} = \zeta_{x2(m,l)} m_1 + \left(\zeta_{rx2(m,l)}^- + \zeta_{rz2(m,l)}^- \right) (1 - m_1), \quad (5.35)$$

$$W3_{(m,l)} = \zeta_{z1(m,l)} m_1 + \left(\zeta_{rx2(m,l)}^- + \zeta_{rz1(m,l)}^- \right) (1 - m_1), \quad (5.36)$$

$$W4_{(m,l)} = \zeta_{z2(m,l)} m_1 + \left(\zeta_{rx1(m,l)}^- + \zeta_{rz2(m,l)}^- \right) (1 - m_1), \quad (5.37)$$

$$W5_{(m,l)} = \zeta_{rx1(m,l)}^+ (1 - m_1), \quad (5.38)$$

$$W6_{(m,l)} = \zeta_{rx2(m,l)}^+ (1 - m_1), \quad (5.39)$$

$$W7_{(m,l)} = \zeta_{rz1(m,l)}^+ (1 - m_1), \quad (5.40)$$

$$W8_{(m,l)} = \zeta_{rz2(m,l)}^+ (1 - m_1). \quad (5.41)$$

And where the terms ζ have the form:

$$\zeta_{x1(m,l)} = - \frac{1}{\Delta^2 \xi(m) \xi(m+N_z/2)} \left[\frac{1}{\rho_m^2} \frac{\partial \rho_m}{\partial c_l} \delta_{m,l} + \frac{1}{\rho_{m+N_z}^2} \frac{\partial \rho_{m+N_z}}{\partial c_l} \delta_{m+N_z,l} \right], \quad (5.42)$$

$$\zeta_{x2(m,l)} = -\frac{1}{\Delta^2 \xi_{(m)} \xi_{(m-N_z/2)}} \left[\frac{1}{\rho_m^2} \frac{\partial \rho_m}{\partial c_l} \delta_{m,l} + \frac{1}{\rho_{m-N_z}^2} \frac{\partial \rho_{m-N_z}}{\partial c_l} \delta_{m-N_z,l} \right], \quad (5.43)$$

$$\zeta_{z1(m,l)} = -\frac{1}{\Delta^2 \xi_{(m)} \xi_{(m+1/2)}} \left[\frac{1}{\rho_m^2} \frac{\partial \rho_m}{\partial c_l} \delta_{m,l} + \frac{1}{\rho_{m+1}^2} \frac{\partial \rho_{m+1}}{\partial c_l} \delta_{m+1,l} \right], \quad (5.44)$$

$$\zeta_{z2(m,l)} = -\frac{1}{\Delta^2 \xi_{(m)} \xi_{(m-1/2)}} \left[\frac{1}{\rho_m^2} \frac{\partial \rho_m}{\partial c_l} \delta_{m,l} + \frac{1}{\rho_{m-1}^2} \frac{\partial \rho_{m-1}}{\partial c_l} \delta_{m-1,l} \right], \quad (5.45)$$

$$\begin{aligned} \zeta_{rx1(m,l)}^\pm &= -\frac{1}{4\Delta^2 \xi_{(m)}} \left(\frac{1}{\xi_{(m+N_z/2)}} \pm \frac{1}{\xi_{(m-1/2)}} \right) \left[\frac{1}{\rho_m^2} \frac{\partial \rho_m}{\partial c_l} \delta_{m,l} + \frac{1}{\rho_{m-1}^2} \frac{\partial \rho_{m-1}}{\partial c_l} \delta_{m-1,l} \right. \\ &+ \left. \frac{1}{\rho_{m+N_z}^2} \frac{\partial \rho_{m+N_z}}{\partial c_l} \delta_{m+N_z,l} + \frac{1}{\rho_{m+N_z-1}^2} \frac{\partial \rho_{m+N_z-1}}{\partial c_l} \delta_{m+N_z-1,l} \right], \end{aligned} \quad (5.46)$$

$$\begin{aligned} \zeta_{rx2(m,l)}^\pm &= -\frac{1}{4\Delta^2 \xi_{(m)}} \left(\frac{1}{\xi_{(m-N_z/2)}} \pm \frac{1}{\xi_{(m+1/2)}} \right) \left[\frac{1}{\rho_m^2} \frac{\partial \rho_m}{\partial c_l} \delta_{m,l} + \frac{1}{\rho_{m+1}^2} \frac{\partial \rho_{m+1}}{\partial c_l} \delta_{m+1,l} \right. \\ &+ \left. \frac{1}{\rho_{m-N_z}^2} \frac{\partial \rho_{m-N_z}}{\partial c_l} \delta_{m-N_z,l} + \frac{1}{\rho_{m-N_z+1}^2} \frac{\partial \rho_{m-N_z+1}}{\partial c_l} \delta_{m-N_z+1,l} \right], \end{aligned} \quad (5.47)$$

$$\begin{aligned} \zeta_{rz1(m,l)}^\pm &= -\frac{1}{4\Delta^2 \xi_{(m)}} \left(\frac{1}{\xi_{(m+N_z/2)}} \pm \frac{1}{\xi_{(m-1/2)}} \right) \left[\frac{1}{\rho_m^2} \frac{\partial \rho_m}{\partial c_l} \delta_{m,l} + \frac{1}{\rho_{m+1}^2} \frac{\partial \rho_{m+1}}{\partial c_l} \delta_{m+1,l} \right. \\ &+ \left. \frac{1}{\rho_{m+N_z}^2} \frac{\partial \rho_{m+N_z}}{\partial c_l} \delta_{m+N_z,l} + \frac{1}{\rho_{m+N_z+1}^2} \frac{\partial \rho_{m+N_z+1}}{\partial c_l} \delta_{m+N_z+1,l} \right], \end{aligned} \quad (5.48)$$

$$\begin{aligned} \zeta_{rz2(m,l)}^\pm &= -\frac{1}{4\Delta^2 \xi_{(m)}} \left(\frac{1}{\xi_{(m-N_z/2)}} \pm \frac{1}{\xi_{(m-1/2)}} \right) \left[\frac{1}{\rho_m^2} \frac{\partial \rho_m}{\partial c_l} \delta_{m,l} + \frac{1}{\rho_{m-1}^2} \frac{\partial \rho_{m-1}}{\partial c_l} \delta_{m-1,l} \right. \\ &+ \left. \frac{1}{\rho_{m-N_z}^2} \frac{\partial \rho_{m-N_z}}{\partial c_l} \delta_{m-N_z,l} + \frac{1}{\rho_{m-N_z-1}^2} \frac{\partial \rho_{m-N_z-1}}{\partial c_l} \delta_{m-N_z-1,l} \right]. \end{aligned} \quad (5.49)$$

The term $f^{(l)}$ is computed using eq 5.24 and 5.30.

For the other medium, we have

- Visco-acoustic medium ($\rho=\text{cte}$ and $\gamma \neq 0$) and Acoustic medium ($\rho=\text{cte}$ and $\gamma=0$)

In these cases the eq. 5.30 is the same, but the term $\frac{\partial \rho_m}{\partial c_m}$ in eq. (5.31) to eq. (5.49) disappear (they become equal to 0), the eq. 5.30 reduces to:

$$\begin{aligned} \frac{\partial A_{(m,n)}}{\partial c(x_l)} &= \left[\frac{-2\omega^2}{c_m^3 \rho_m} \right] [m_2 \delta_{m,n} + m_3 (\delta_{m,n+N_z} + \delta_{m,n-N_z} + \delta_{m,n+1} + \delta_{m,n-1}) + \\ &+ (1/4 - m_2/4 - m_3) (\delta_{m,n+N_z-1} + \delta_{m,n-N_z+1} + \delta_{m,n+N_z+1} + \delta_{m,n-N_z-1})] \delta_{m,l}. \end{aligned} \quad (5.50)$$

When ρ is constant the matrix $\frac{\partial \mathbf{A}}{\partial c(x_l)}$ is a matrix full of zeros except for the points where $m = l$.

- Acoustic medium ($\rho = \rho(\mathbf{x})$ and $\gamma=0$)

In these cases the eq. 5.30 is the same, but the term $\xi_{(m)}$, $\xi_{m \pm Nz/2}$ and $\xi_{m \pm 1/2}$ in eq. (5.42) to eq. (5.49) disappear (they become equal to 1) into the workspace \mathcal{U} , the PML still applies in $\partial\mathcal{U}$.

5.2.3 Hessian of the objective function

Now, to calculate the Hessian matrix we have

$$[\mathbf{H}_\chi(\mathbf{c}(\mathbf{x}))]_{q,l} = \frac{\partial^2 \chi}{\partial c(x_q) \partial c(x_l)} = \frac{\partial}{\partial c(x_q)} \left[-\frac{1}{2} \sum_f^{N_f} \sum_s^{N_s} \text{Re}\{\hat{\mathbf{J}}_{(f,s)}^T \delta \hat{\mathbf{d}}_{(f,s)}^*\} \right]_l,$$

$$\mathbf{H}_\chi = \frac{1}{2} \sum_f^{N_f} \sum_s^{N_s} \text{Re}\{\hat{\mathbf{J}}_{(f,s)}^T \hat{\mathbf{J}}_{(f,s)}^* + \frac{\partial \hat{\mathbf{J}}_{(f,s)}^T}{\partial \mathbf{c}(\mathbf{x})} \delta \hat{\mathbf{d}}_{(f,s)}^*\}. \quad (5.51)$$

It is common to define $\mathbf{H} = \mathbf{H}_a + \mathbf{H}_r$. Where \mathbf{H}_a is the "approximate Hessian".

In the Gauss-Newton method of inversion using the approximate hessian \mathbf{H}_a , this term is a straightforward to compute, whereas the second term, \mathbf{H}_r , is often difficult to compute. Further \mathbf{H}_r is small if the residual $\delta \mathbf{d}$ is small o the forward equation is quasi linear. If we neglect the term \mathbf{H}_r assuming that the changes in the parameters do not cause a change in Jaccobian matrix, we could to define our formula for updating the model parameters as

$$c_k(\mathbf{x}) = c_{k-1}(\mathbf{x}) + \epsilon_k (\mathbf{H}_{\mathbf{a}k-1} + \beta \mathbf{I})^{-1} g_{k-1}(\mathbf{x}). \quad (5.52)$$

Now, the matrix \mathbf{H}_a is diagonally dominated, due to the autocorrelations occurring on the main diagonal. Due to this characteristic is possible to facilitate the inversion of the Hessian matrix, to approximate \mathbf{H}_a it to a diagonal matrix \mathbf{H}_a^d , so

$$c_k(\mathbf{x}) = c_{k-1}(\mathbf{x}) + \epsilon_k (\mathbf{H}_{\mathbf{a}k-1}^d + \beta \mathbf{I})^{-1} g_{k-1}(\mathbf{x}). \quad (5.53)$$

5.2.4 The Optimal Step Length

Finally, we use to find the step length ϵ of line search procedure such as parabolic fitting. The line search as parabolic fitting is a simple method where we calculate two or more values for the objective function in each iteration, moving in the direction of descent and calculate parabolic fitting.

If we assume in each iteration k that $\chi(c(\mathbf{x}) + \epsilon \mathbf{h})$ as quadratic function of ϵ , $\chi(\epsilon) = a\epsilon^2 + b\epsilon + c$, if $a > 0$ the minimum of the function $\chi(\epsilon)$ would be $\hat{\epsilon} = -b/(2a)$, being more strict, $b < 0$ for that minimum of the function is $\hat{\epsilon} > 0$.

Using hessian matrix and line search as parabolic fitting, in (Gomes dos Santos, 2013) suggests the following algorithm for each iteration k

1. Calculate $\chi(c(\mathbf{x}))$

2. Calculate $\mathbf{h} = (\mathbf{H}_a^d + \beta \mathbf{I})^{-1} g(\mathbf{x})$
3. Solve $\max(\epsilon_1 |c(\mathbf{x})|) \leq \frac{\max(|\mathbf{h}|)}{100\psi}$
4. Calculate $\chi(c(\mathbf{x}) + \epsilon_1 \mathbf{h})$
5. Assign a random value of $[0, 1]$ for Ψ_ϵ and Ψ_ψ
6. If $\chi(c(\mathbf{x}) + \epsilon_1 \mathbf{h}) < \chi(c(\mathbf{x}))$ then $\epsilon_2 = 10\Psi_\epsilon \epsilon_1$ and $\psi_{k+1} = \psi_k$
7. If $\chi(c(\mathbf{x}) + \epsilon_1 \mathbf{h}) \geq \chi(c(\mathbf{x}))$ then $\epsilon_2 = \Psi_\epsilon \epsilon_1$ and $\psi_{k+1} = \Psi_\psi \psi_k$
8. Calculate $\chi(c(\mathbf{x}) + \epsilon_2 \mathbf{h})$
9. With points $x = [0, \epsilon_1, \epsilon_2]$ and $y = [0, \chi(\epsilon_1), \chi(\epsilon_2)]$, find a parabolic fitting $\chi(\epsilon) = a\epsilon^2 + b\epsilon + c$.
10. Calculate $\epsilon_{k+1} = \frac{-b}{(2a)}$

5.2.5 Other considerations

Finally, there are several considerations described in (Pratt, 1999), (Brossier and Operto, 2009) and (Gomes dos Santos, 2013) to avoid problems with differences between scales between observed and predicted data amplitudes. It is recommended to make some adjustment or normalization between the scales so that the objective function is smoother. In our case we use the following normalization

$$\chi(\mathbf{m}) = \frac{1}{2} \sum_s^{N_s} \sum_r^{N_r} \sum_f^{N_f} (d_{obs} - \mu d_{cal})_{(s,r,f)} (d_{obs} - \mu d_{cal})_{(s,r,f)}^* \quad (5.54)$$

$$\mu = \frac{\mathbf{d}_{obs}^T \mathbf{d}_{cal}^*}{\mathbf{d}_{cal}^T \mathbf{d}_{cal}^*} \quad (5.55)$$

Where μ is a complex number, this number is used for the adjustment of the amplitudes and is not explicitly taken into account in the calculation of the gradient or the hessian since it is taken as a scaling of the predicted data, such that the backpropagation field is found with the error between the observed data and the scaled calculated data. That is to say our $\mathbf{d}_{cal} \equiv \mu \mathbf{d}_{cal}$.

5.3 First results

In order to obtain a better understanding of the iterative minimization process as inversion scheme in frequency domain, we perform tests using data modeled on a velocity profile (\mathbf{d}_{obs}) starting from a similar velocity profile. The propagation is modeled in a acoustic and visco-acoustic medium with constant density.

The reason to perform these tests in a medium with constant density is the that the estimation of the matrix \mathbf{F} , in the case of a medium with variable density is of size $N \times N$ and has 9 diagonals

of non-zero values as \mathbf{A} , while in a medium with constant density \mathbf{F} is a diagonal matrix, which facilitates many calculations and operations.

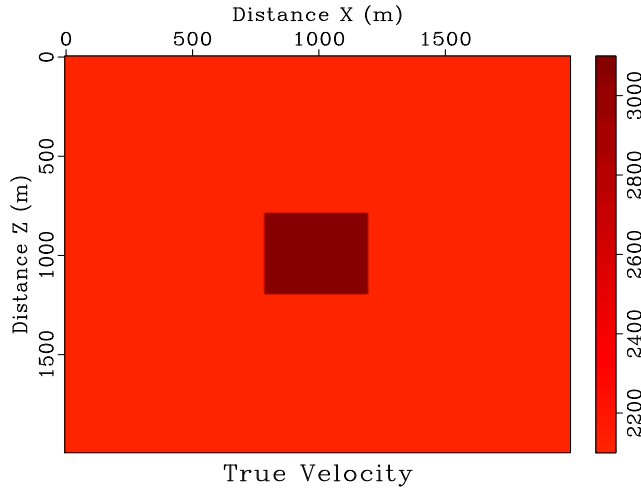


Figure 5.1: Geometric configuration of the velocity profile

In this inversion test the observed data \mathbf{d}_{obs} were produced computing the value of the P-wave amplitude in an area of $2[\text{Km}] \times 2[\text{Km}]$, by placing a line of receivers at 15 [m] and 1990 [m], finding the waveform response at that point. The velocity profile of the media is show in figure 5.1, with velocity of 2100 [m/s] and quality factor $Q = 50$ of background and contrast region in the middle with velocity of 3100 [m/s] and $Q = 70$, for the damping function using eq. (2.15), the Ricker frequency is 10 [Hz], $R_0 = 1000$, the cell size Δ is $\frac{\lambda}{G_r}$, where $G_r = 7$, scale PML $m_0 = \omega$ and scale factor $s = 1.0$. The test were made with one or several sources and for one or more frequencies and the initial velocity profile is a constant velocity profile with $c = 2100$ [m/s].

To determine the frequencies to be used in the inversion, we use the proprieties of the discrete Fourier transform. Given that the observed data would be data in the time domain, we must apply the Fourier transform to this data to work with them in the frequency domain. According to the properties of the transform, the delta frequency is determined by the size of the window in time, so we must work on those same frequencies.

The frequency δf is determined from the inverse of the maximum time t_{max} , in our tests we will take it as twice the time that would take the wave with minor propagation velocity, travel the domain in Z .

$$t_{max} = \frac{2L_z}{c_{min}} \quad \delta f = \frac{1}{t_{max}} \quad f_{min} = \delta f \quad f_{max} = \frac{c_{min}}{G_r \Delta_1}. \quad (5.56)$$

The frequency range with which we work would go from the delta of frequency δf (closest to 0 within our frequencies) and the maximum frequency would be determined by the grid delta of the velocity profile that we wish to recover. The Δ_1 is different from the Δ (that is calculated with the eq. 3.58), for our modeling the grid delta Δ varies with the frequency, with those points we find our data and interpolate to work everything to the same scale. According to this for the following tests we have $f = [0.525 : 0.525 : 29.500]$.

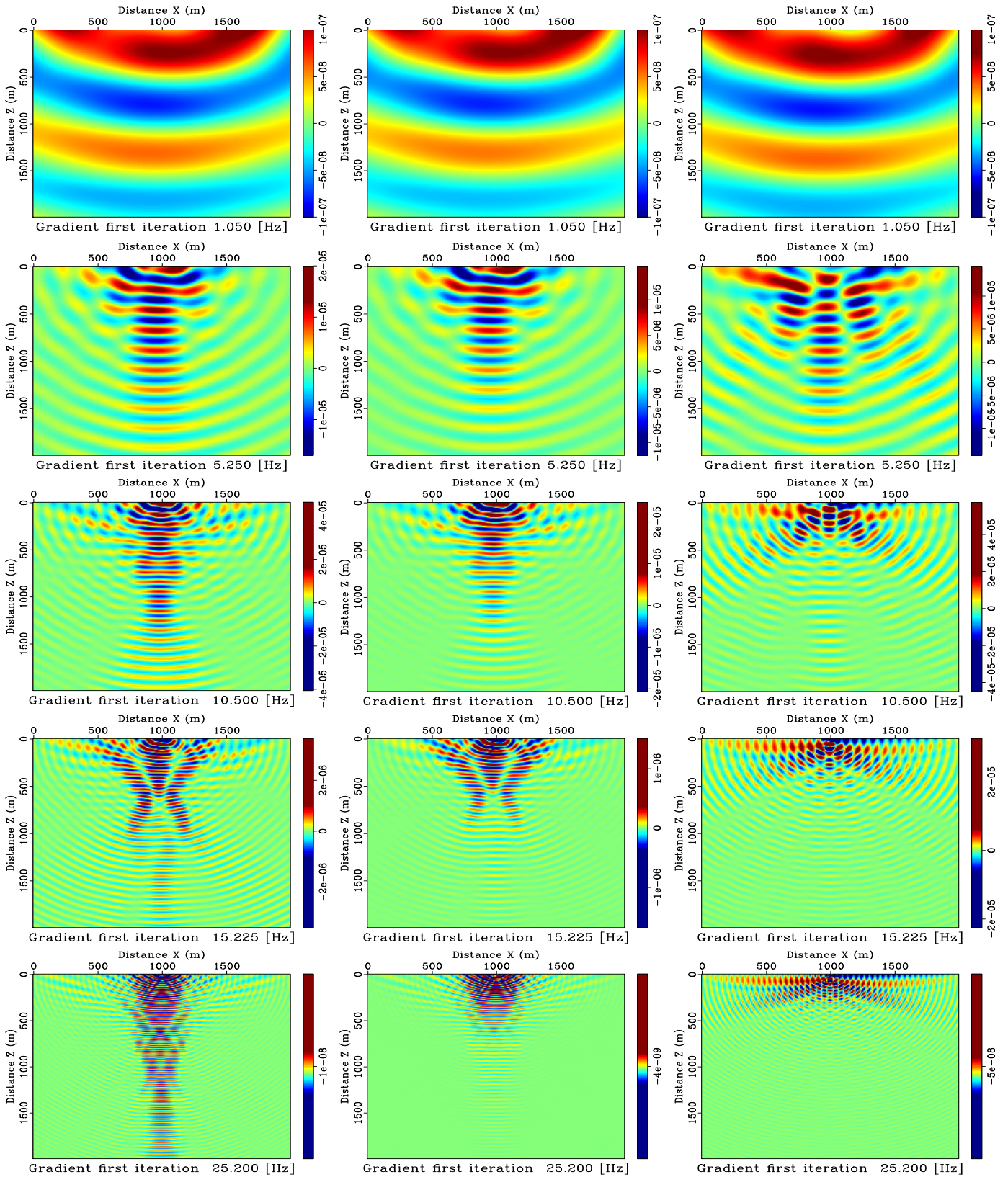


Figure 5.2: Gradient for acoustic modeling and acoustic inversion for receivers line in $z = 15$ [m]

Figure 5.3: Gradient for viscoacoustic modeling and viscoacoustic inversion for receivers line in $z = 15$ [m]

Figure 5.4: Gradient for viscoacoustic modeling and acoustic inversion for receivers line in $z = 15$ [m]

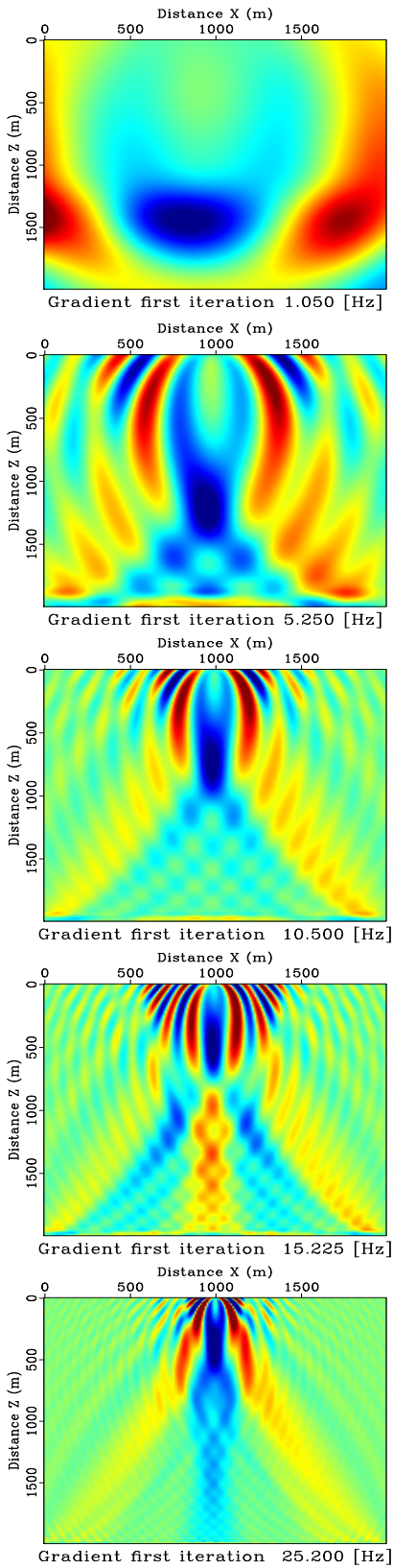


Figure 5.5: Gradient for acoustic modeling and acoustic inversion for receivers line in $z = 1990$ [m]

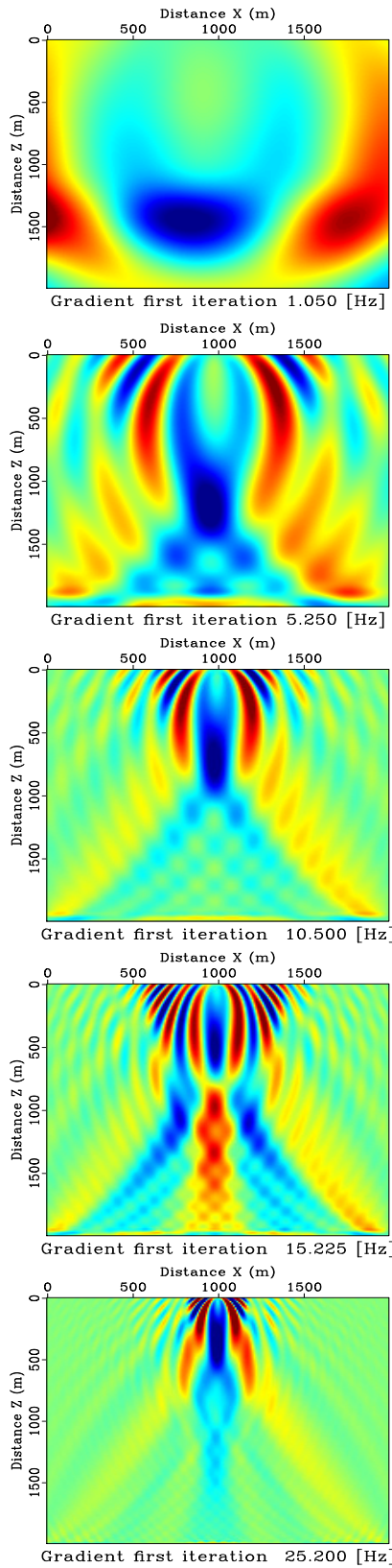


Figure 5.6: Gradient for viscoacoustic modeling and viscoacoustic inversion for receivers line in $z = 1990$ [m]

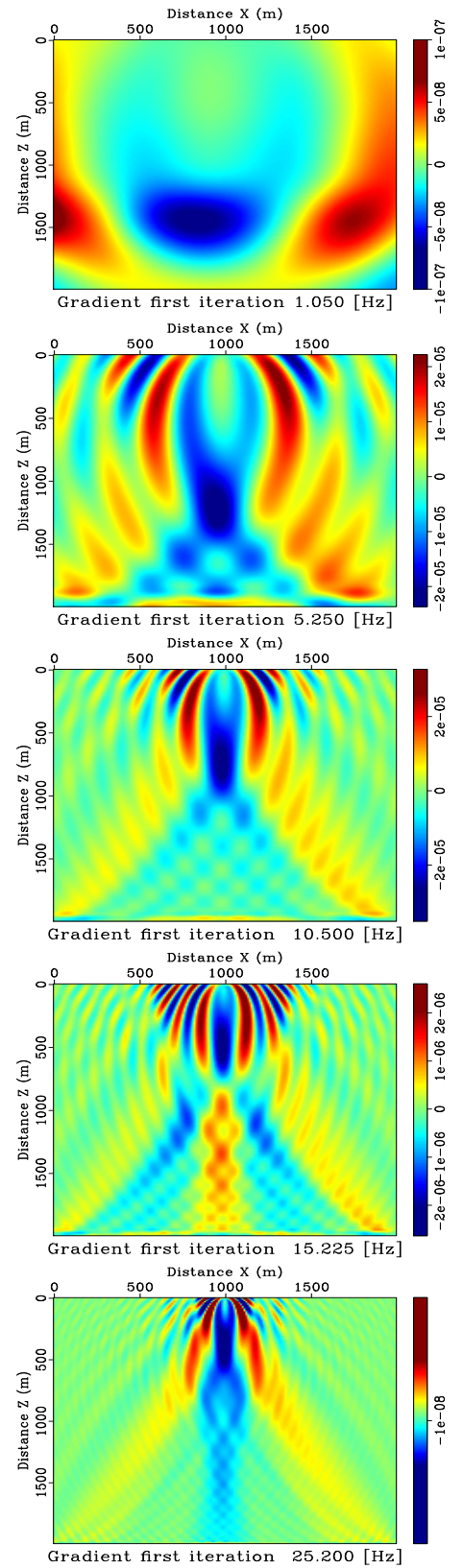


Figure 5.7: Gradient for viscoacoustic modeling and acoustic inversion for receivers line in $z = 1990$ [m]

5.3.1 Gradients for single source by frequency

In this test we work with only one source placed at $x_s = 1[\text{Km}]$ and $z_s = 0.010[\text{Km}]$. The gradients were calculated individually for each frequency in $f = [1.050, 5.250, 10.500, 15.225, 25.200]$ [Hz].

In figures 5.2, 5.3 and 5.4 we show the gradient of objective function $= \nabla_c \chi(c_0(\mathbf{x}))$ for the first iteration for frequencies $f = [1.050, 5.250, 10.500, 15.225, 25.200]$ [Hz], the data is collected in receivers line $z = 15$ [m]. In figure 5.2 the observed data d_{obs} is modeled as solution in acoustic media and predicted data d_{cal} is modeling as solution in acoustic media. In figure 5.3 the observed data d_{obs} is modeling as solution in visco-acoustic media and predicted data d_{cal} is modeled as solution in visco-acoustic media. In figure 5.4 the observed data d_{obs} is modeling as solution in visco-acoustic media and predicted data d_{cal} is modeled as solution in acoustic media.

Although the gradient is found for a single source, it can be seen how the contrast area is detected. The higher the frequency, the clearer the detection of contrast area. The gradient value is quite small compared to the velocity used, between the background velocity and the velocity of the contrast area there is 1000 [m/s] difference, but the gradient in all cases is not larger than 10^{-5} [m/s].

As it is expected there are higher values and the area of contrast is better localized is at the frequency close to the source frequency, since the amplitude of the P-wave has a maximum at the frequency of the source. The gradient values are lower for the visco-acoustic inversion/modeling than for the acoustic inversion/modeling, as expected, the differences become larger with increasing frequency.

The most interesting thing of this test is the inversion of the data obtained with a viscous model with a inversion acoustic. This inversion was made assuming, erroneously, that the medium was acoustic and the results in the gradient are inferior to those found in previous cases, since it does not locate well the contrast area and, as the frequency increases, this area disappears completely.

In figures 5.5, 5.6 and 5.7 we show the gradient of the objective function $= \nabla_c \chi(c_0(\mathbf{x}))$ for first iteration for frequencies $f = [1.050, 5.250, 10.500, 15.225, 25.200]$ [Hz], the data is collected in a line of receivers at $z = 1990$ [m]. They have the same organization as the previous experiment, the first column for inversion/model acoustic, the second column for visco-acoustic inversion/modeling and the third column for visco acoustic modeling with acoustic inversion.

In this case the results are very similar among each other, except for the values of the gradient, even for the acoustic inversion with the visco-acoustic modeling. The main difference found with data collected in the upper part of the domain (seismic surface) in the previous test, is that the gradient locates the area of contrast from low frequencies but does not locate them at the proper depth, the best results are still at the frequencies close to the source.

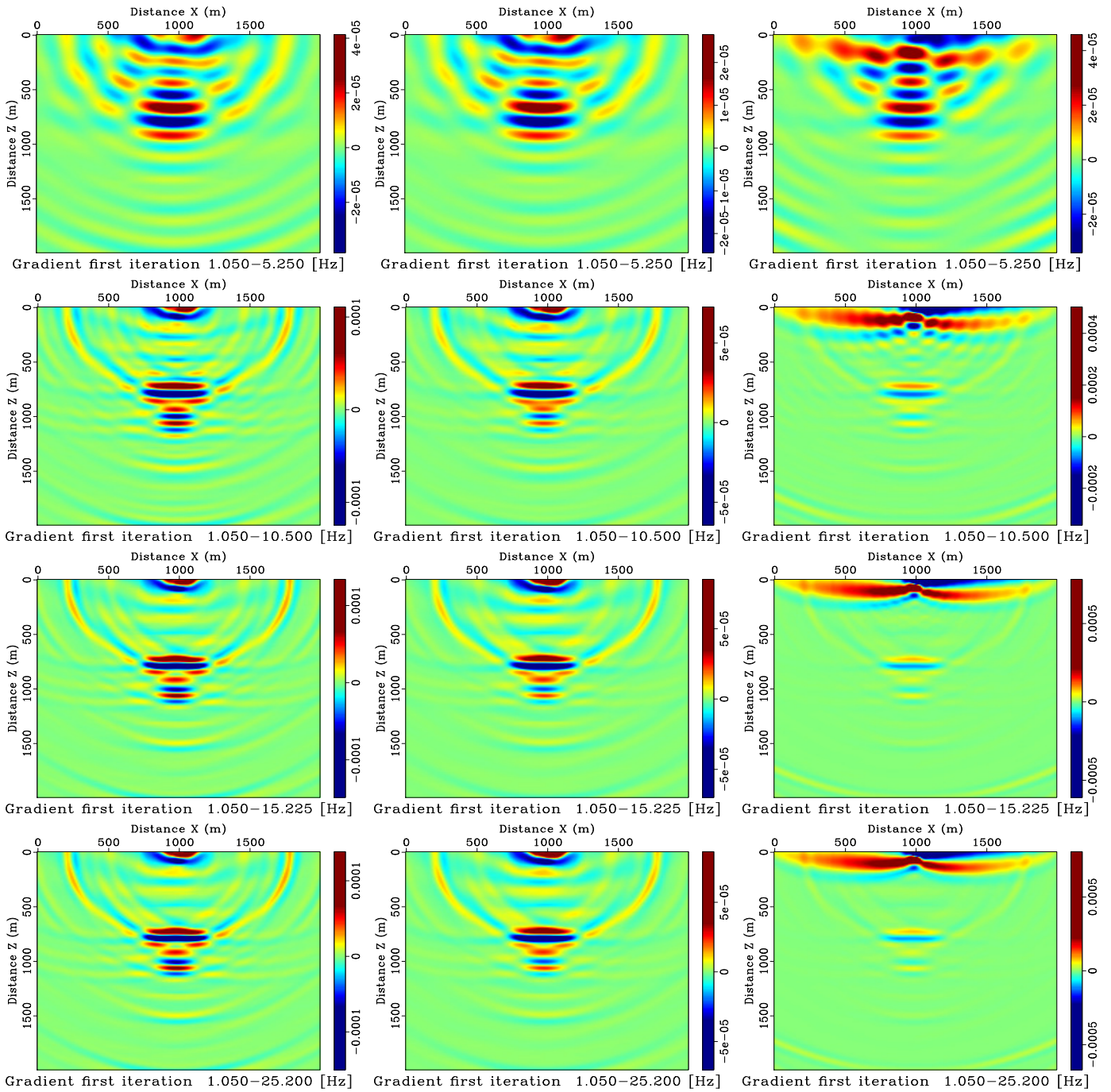


Figure 5.8: Gradient for acoustic modeling and acoustic inversion for receivers line in $z = 15$ [m]

Figure 5.9: Gradient for viscoacoustic modeling and viscoacoustic inversion for receivers line in $z = 15$ [m]

Figure 5.10: Gradient for viscoacoustic modeling and acoustic inversion for receivers line in $z = 15$ [m]

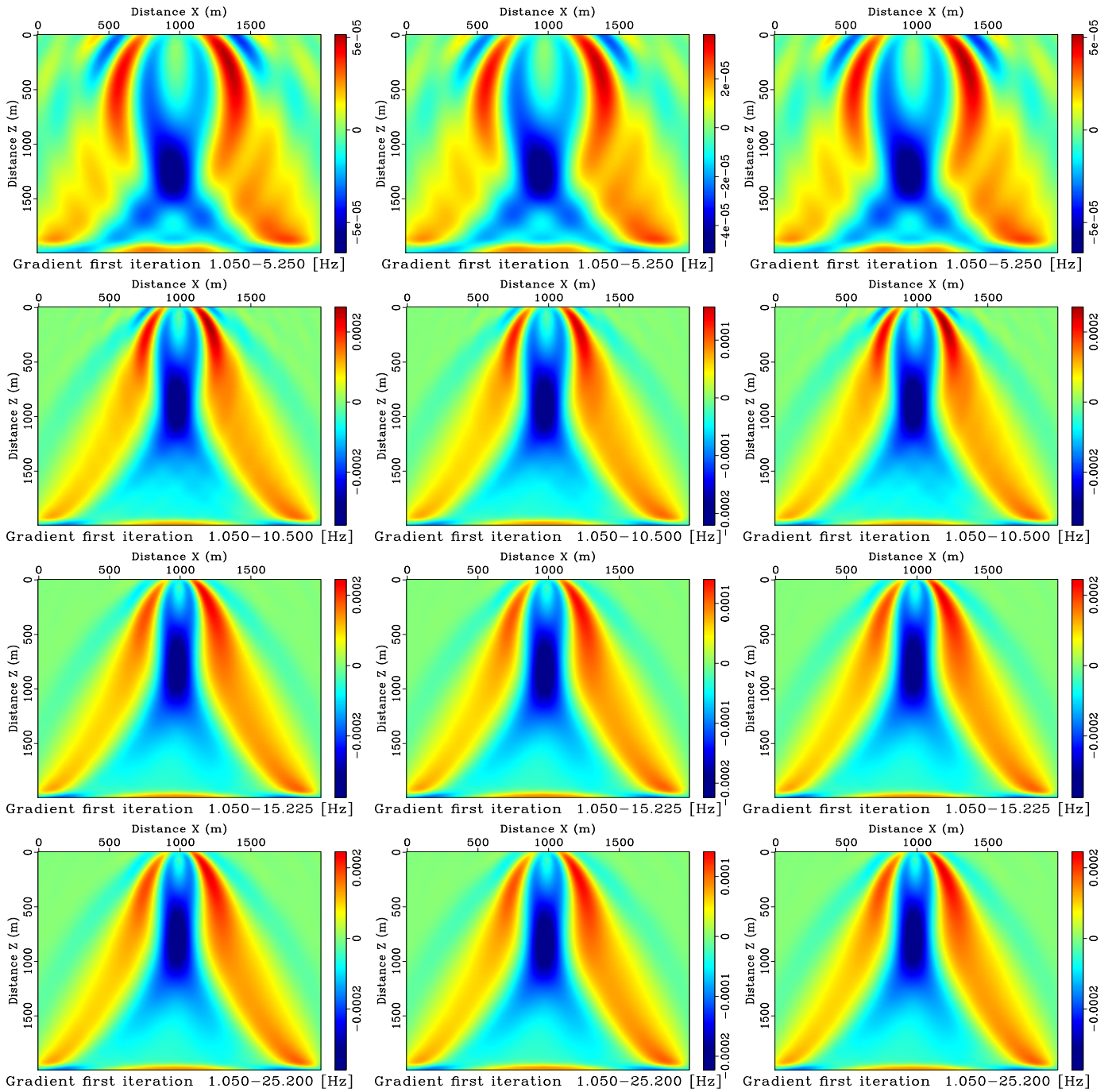


Figure 5.11: Gradient for acoustic modeling and acoustic inversion for receivers line in $z = 1990$ [m]

Figure 5.12: Gradient for visco-acoustic modeling and visco-acoustic inversion for receivers line in $z = 1990$ [m]

Figure 5.13: Gradient for visco-acoustic modeling and acoustic inversion for receivers line in $z = 1990$ [m]

5.3.2 Gradients for single source for an interval of frequencies

In this test the position of the source is at $x_s = 1$ [Km] and $z_s = 0.010$ [Km] and there is only source. The gradients were calculated at intervals of frequencies $f = [1.050, 5.250]$, $f = [1.050, 10.500]$,

$f = [1.050, 15.225]$ and $f = [1.050, 25.200]$ [Hz].

In figures 5.8, 5.9 and 5.10 we show the gradient of the objective function $= \nabla_c \chi(c_0(\mathbf{x}))$ for the first iteration for intervals of frequencies. The data is collected in the receivers line $z = 15$ [m]. They have the same organization as the previous experiment, the first column for acoustic inversion/modeling, the second column for visco-acoustic inversion/modeling and the third column for visco-acoustic modeling and acoustic inversion.

We can see a better located the area for the contrast region than in the case of a single frequency. Again the gradient value is quite small compared to the velocity used, in all cases with values not larger than 10^{-4} [m/s]. The differences between the acoustic inversion/modeling and visco-acoustic inversion/modeling remain in the amplitudes of the gradient. The shape varies a little as a function of the frequency but nothing as remarkable as the behavior found for a single frequency. For the visco-acoustic modeling and acoustic inversion we continue to see a smaller gradient, where the contrast area is not well located.

In figures 5.11, 5.12 and 5.13 we show the gradient $= \nabla_c \chi(c_0(\mathbf{x}))$ for the first iteration for intervals of frequencies, the data is collected in receivers line $z = 1990$ [m]. They have the same organization as the previous experiment. In this case the contrast area is very well with respect to the horizontal, but remains variable with respect to the vertical depending on the frequencies involved. The values of the gradient remain small, but there is no large difference between one gradient and another, beyond the value of the amplitude between the acoustic and visco-acoustic case.

5.3.3 Gradients for multiples source by frequency

In this test we have multiple sources in a line of sources at $z_s = 0.010$ [Km]. The gradients were compute by a single frequency $f = [1.050, 5.250, 10.500, 15.225, 25.200]$ [Hz].

In figures 5.14 to 5.19 we show the gradient $= \nabla_c \chi(c_0(\mathbf{x}))$ for first iteration for single frequency, the data 5.14 to 5.16 is collected in receivers line $z = 15$ [m] and the data 5.17 to 5.19 is collected in receivers line $z = 1990$ [m]. They have the same organization as the previous experiment, the first column for acoustic inversion/modeling, the second column for visco-acoustic inversion/modeling and the third column for visco-acoustic modeling and acoustic inversion.

The results are similar to the previous experiments, except that the contrast area is better located horizontally and in depth, as is to be expected from data found by several sources, the gradient values remain small, with a maximum value of 10^{-3} , between visco-acoustic inversion/modeling and acoustic inversion/modeling there is mainly a difference of amplitudes and few differences between the greater the frequency. The acoustic inversion/ visco-acoustic modeling continues to find the worst gradients when the data are calculated on the surface, disappearing the area of interest the larger the frequency. For the data computed at $z = 1990$ [m] the gradients do not vary too much.

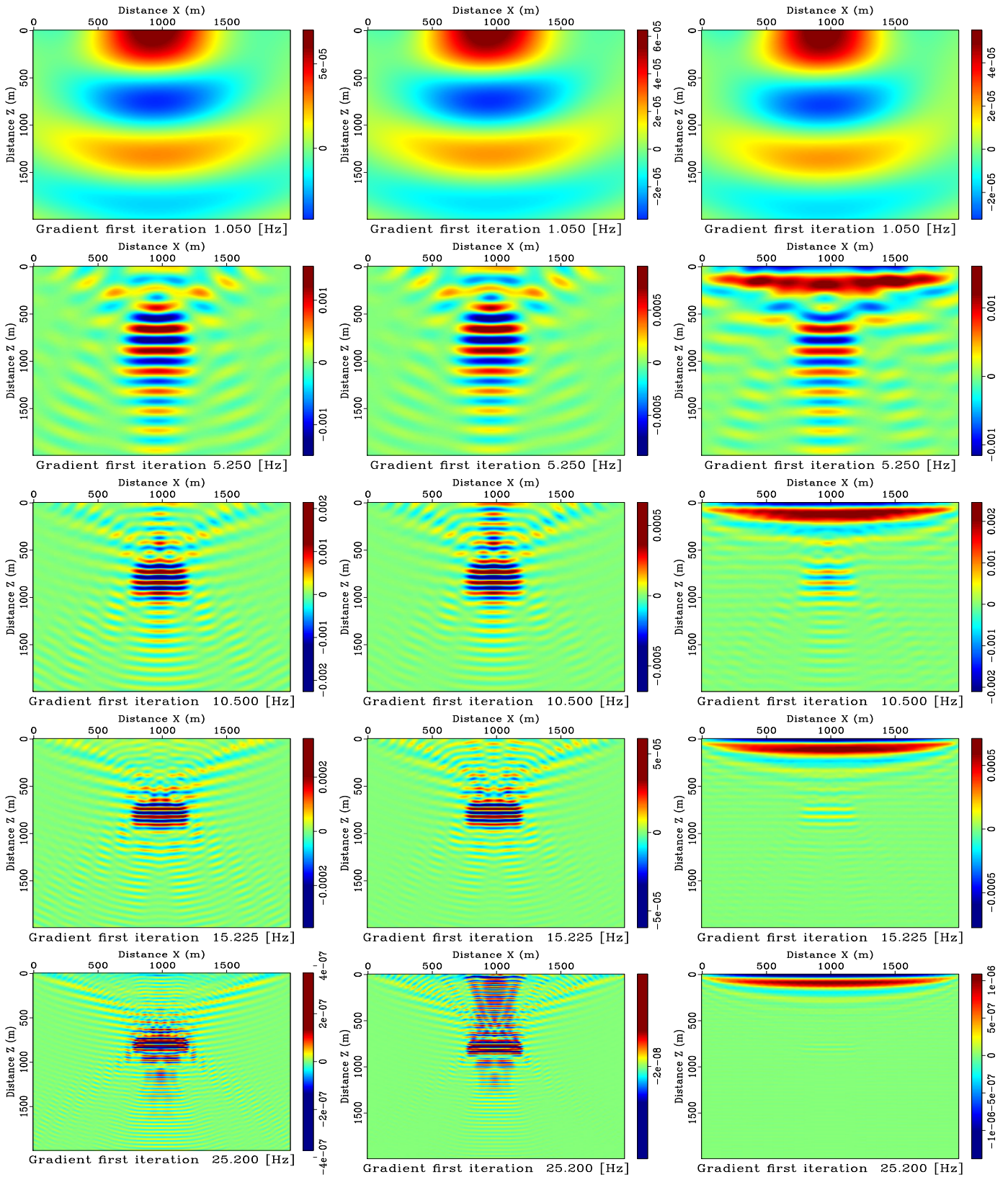


Figure 5.14: Gradient for acoustic modeling and acoustic inversion for receivers line in $z = 15$ [m]

Figure 5.15: Gradient for viscoacoustic modeling and viscoacoustic inversion for receivers line in $z = 15$ [m]

Figure 5.16: Gradient for viscoacoustic modeling and acoustic inversion for receivers line in $z = 15$ [m]

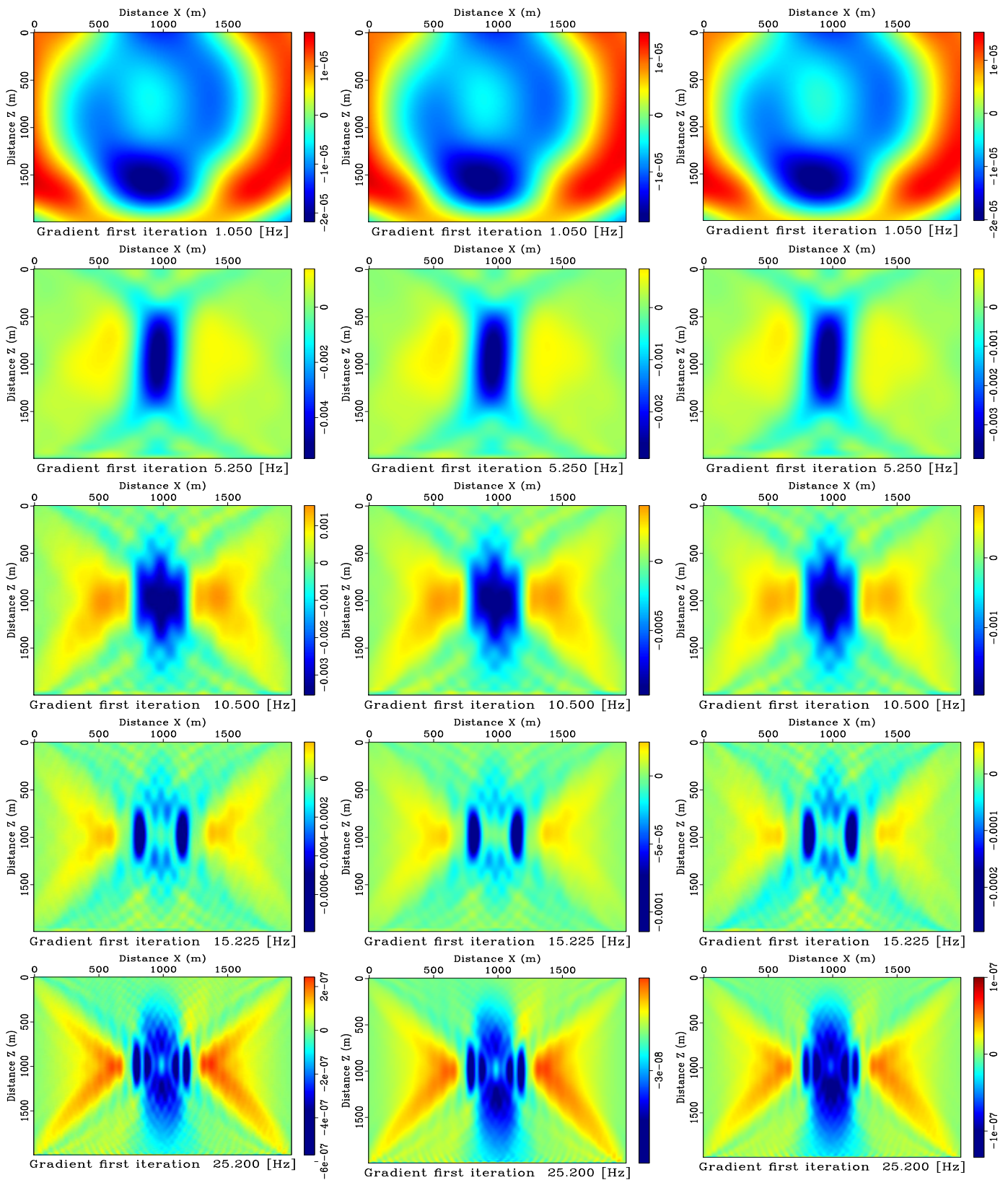
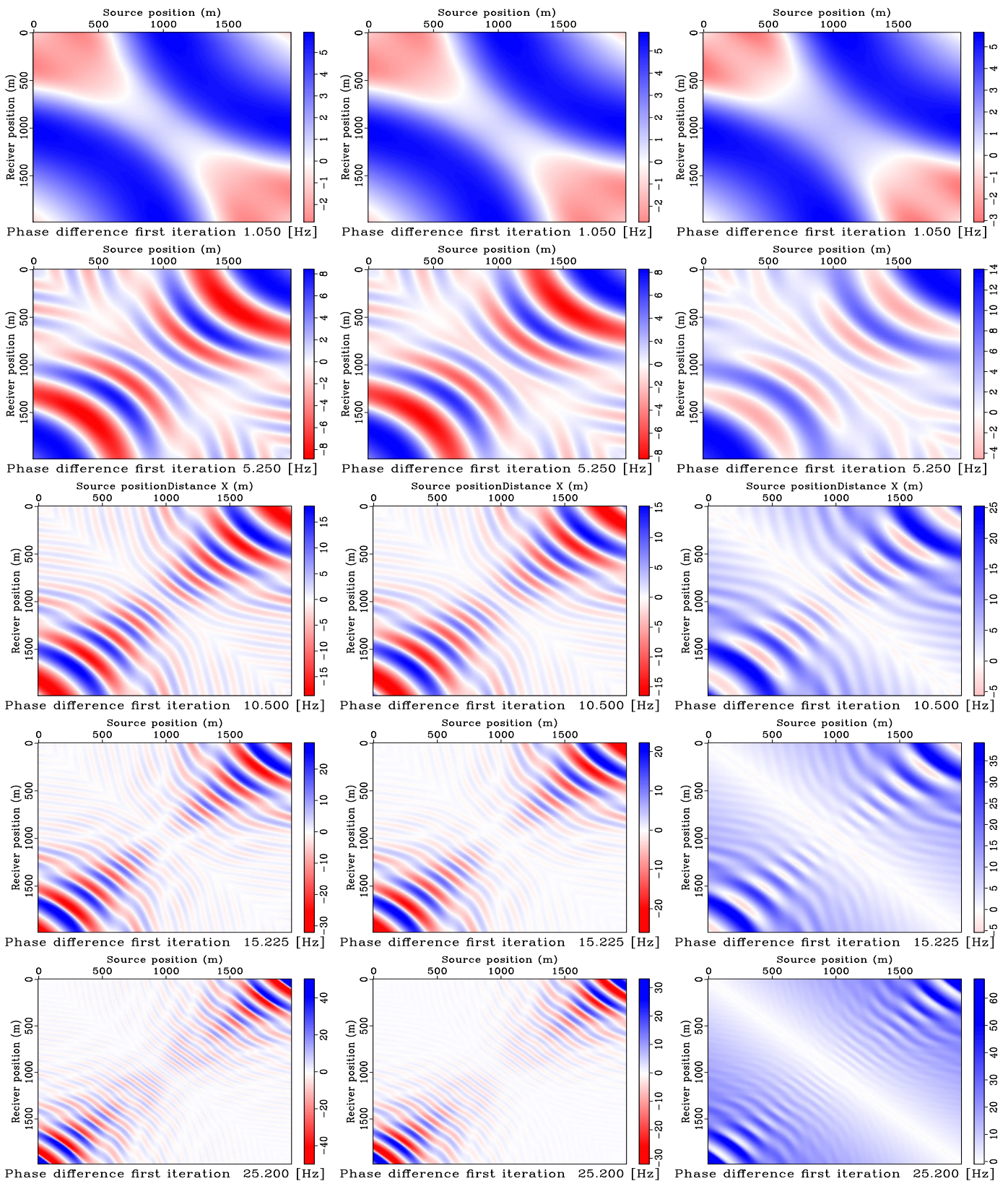


Figure 5.17: Gradient for acoustic modeling and acoustic inversion for receivers line in $z = 1990$ [m]

Figure 5.18: Gradient for viscoacoustic modeling and viscoacoustic inversion for receivers line in $z = 1990$ [m]

Figure 5.19: Gradient for viscoacoustic modeling and viscoacoustic inversion for receivers line in $z = 1990$ [m]



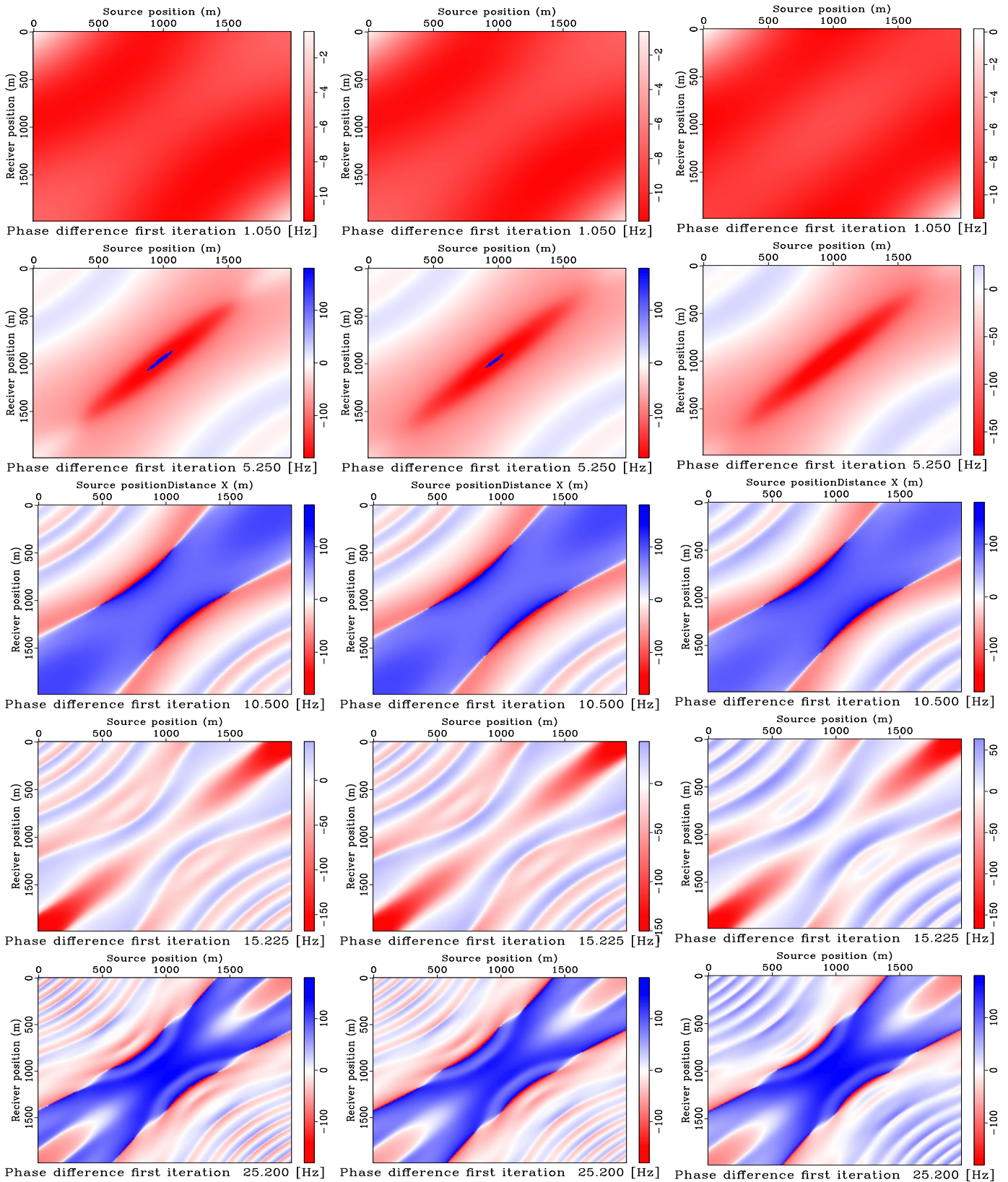


Figure 5.23: Phase difference for acoustic modeling and acoustic inversion for receivers line in $z = 1990$ [m]

Figure 5.24: Phase difference for visco-acoustic modeling and visco-acoustic inversion for receivers line in $z = 1990$ [m]

Figure 5.25: Phase difference for visco-acoustic modeling and acoustic inversion for receivers line in $z = 1990$ [m]

Now, in figures 5.20 to 5.25 we show the phase difference of d_{cal} and d_{obs} for first iteration for single frequency, and the data 5.20 to 5.22 is collected in receivers line $z = 15$ [m] and the data 5.23 to 5.25 is collected in receivers line $z = 1990$ [m]. They have the same organization as the previous experiment.

The phase difference is an important indicator of the presence of Cycle Skipping (CS), it is desired that the phase change smoothly and no sudden jumps between negative and positive angles are present. We can see that for the data collected in surface this is fulfilled, increasing the phase differences between the greater the frequency. The phase difference for the visco-acoustic modeling and acoustic inversion is the highest at all frequencies. In the cases of the data collected in $z = 1990$ [m] there is presence of Cycle Skipping in certain areas, although in small areas, however this could be an indication that the investment could fall to a local minimum, in addition the gradients of these frequencies have a strong area around the area of contrast that could lead to inversion in the wrong way.

5.3.4 Gradients for multiple sources by a interval of frequencies

In this test we have multiple source in a line of source in $z_s = 0.010$ [Km]. The gradients were calculated by a intervals frequencies $f = [1.050, 5.250]$, $f = [1.050, 10.500]$, $f = [1.050, 15.225]$ and $f = [1.050, 25.200]$ [Hz].

In figures 5.26 to 5.31 we show the gradient $= \nabla_c \chi(c_0(\mathbf{x}))$ for first iteration for intervals of frequencies, the data is collected in receivers line $z = 15$ [m] and receivers line $z = 1990$ [m]. They have the same organization as the previous experiment.

This would be the expected gradient a real inversion, where we must take into account both a number of sources and frequencies to get the best gradient. We can observe similarities with the previous experiments, the contrast area is better located horizontally and in depth, the gradient values are small with a maximum value of 10^{-2} . Between visco-acoustic inversion/modeling and acoustic inversion/modeling there is mainly a difference of amplitudes, the acoustic inversion/visco-acoustic modeling continues to find the worst gradients when the data are calculated on the surface and for the data computed at $z = 1990$ [m] the gradients do not vary too much.

In figures 5.32 to 5.37 we show the phase difference of d_{cal} and d_{obs} the for first iteration for single frequency. The data is collected in receivers line $z = 15$ [m] and receivers line $z = 1990$ [m]. They have the same organization as the previous experiment. inversion.

In this test we can observe similarities with the previous experiments, for the data collected in surface the phase difference is smooth and increasing the values by phase differences between the greater the intervals frequencies. In the cases of the data collected in $z = 1990$ there is presence of Cycle Skipping in all intervals, the gradients of these frequencies have a strong area around the area of contrast that could lead to inversion in the wrong way.

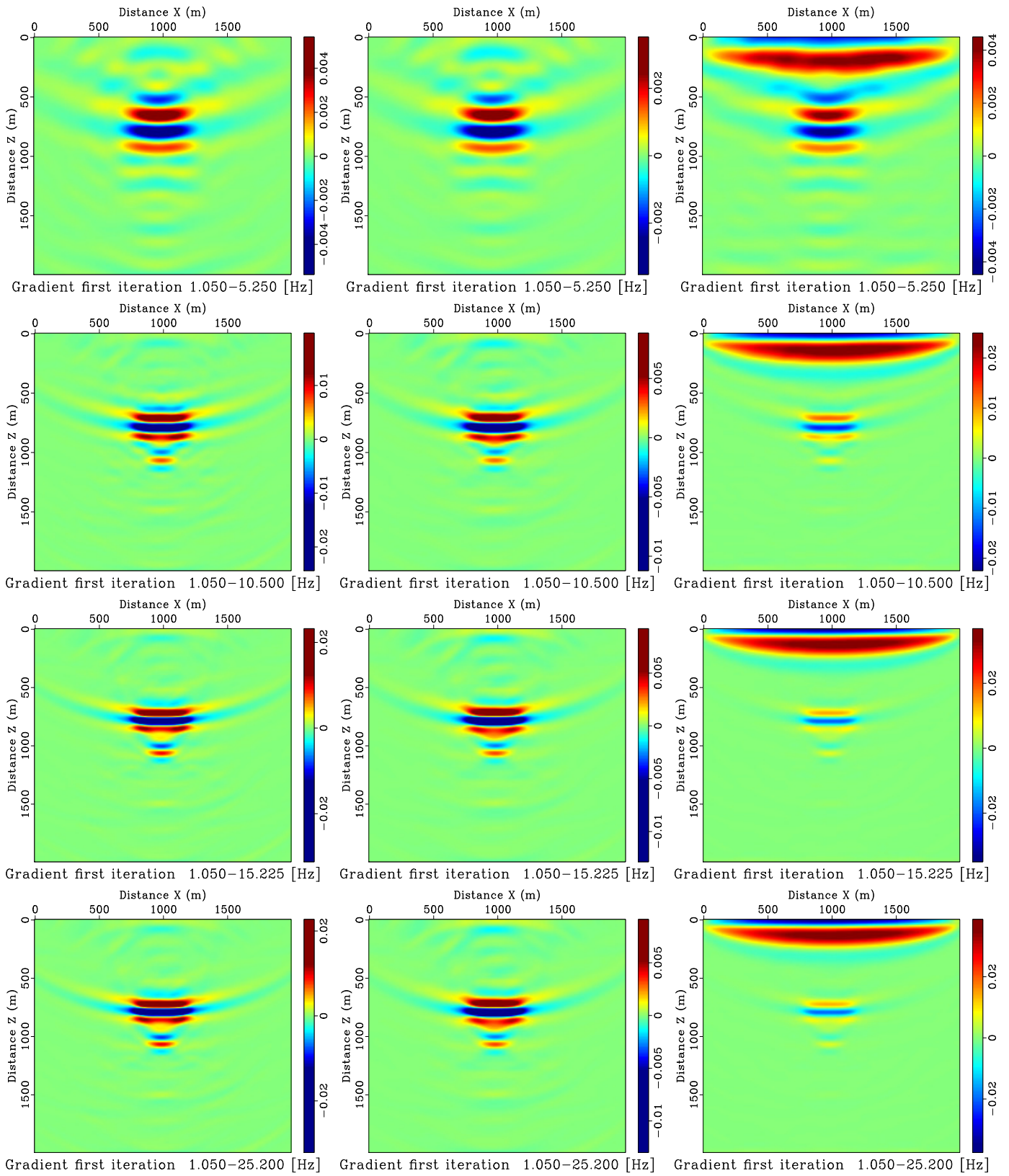


Figure 5.26: Gradient for acoustic modeling and acoustic inversion for receivers line in $z = 15$ [m]

Figure 5.27: Gradient for viscoacoustic modeling and viscoacoustic inversion for receivers line in $z = 15$ [m]

Figure 5.28: Gradient for viscoacoustic modeling and acoustic inversion for receivers line in $z = 15$ [m]

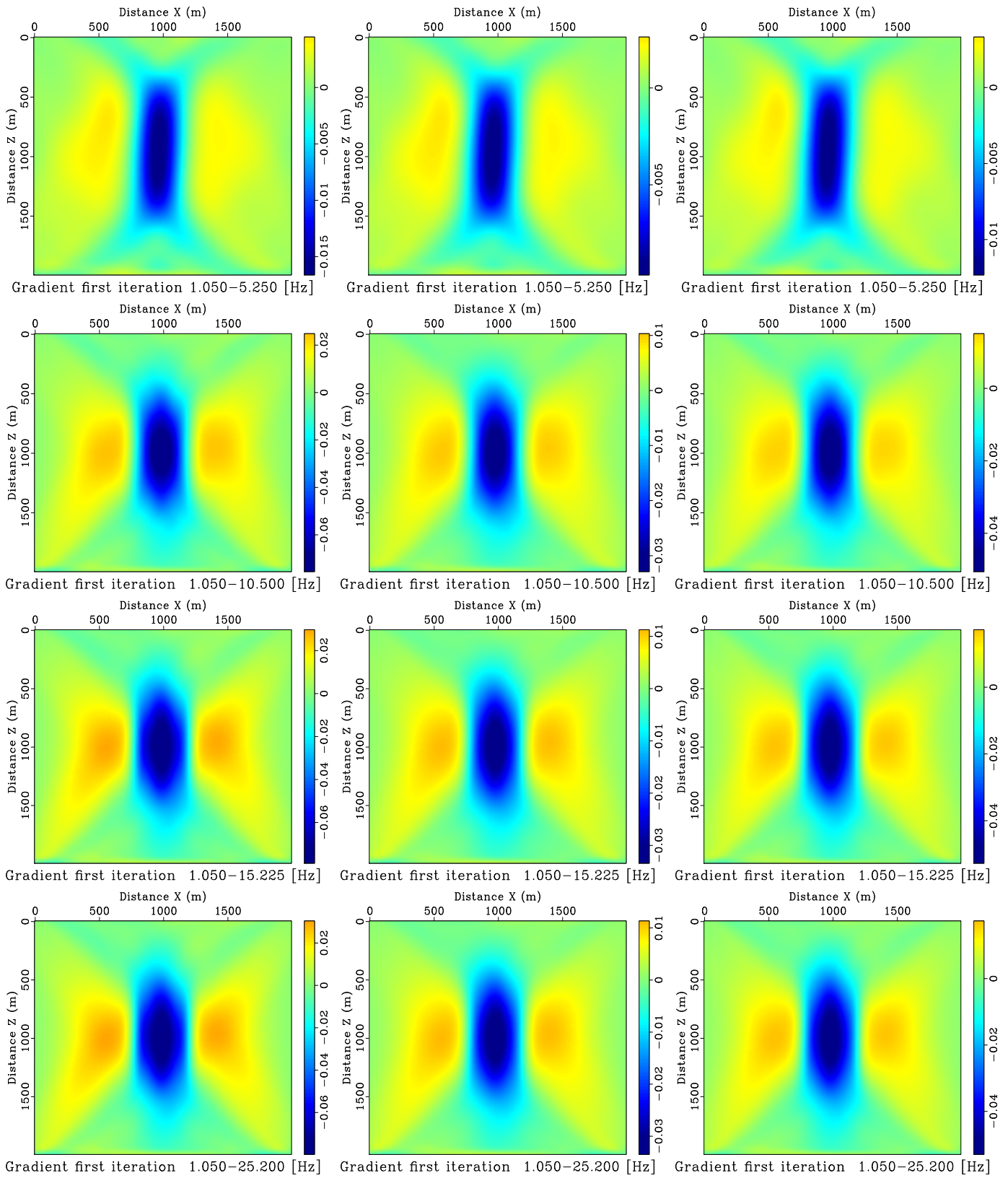


Figure 5.29: Gradient for acoustic modeling and acoustic inversion for receivers line in $z = 1990$ [m]

Figure 5.30: Gradient for viscoacoustic modeling and viscoacoustic inversion for receivers line in $z = 1990$ [m]

Figure 5.31: Gradient for viscoacoustic modeling and acoustic inversion for receivers line in $z = 1990$ [m]

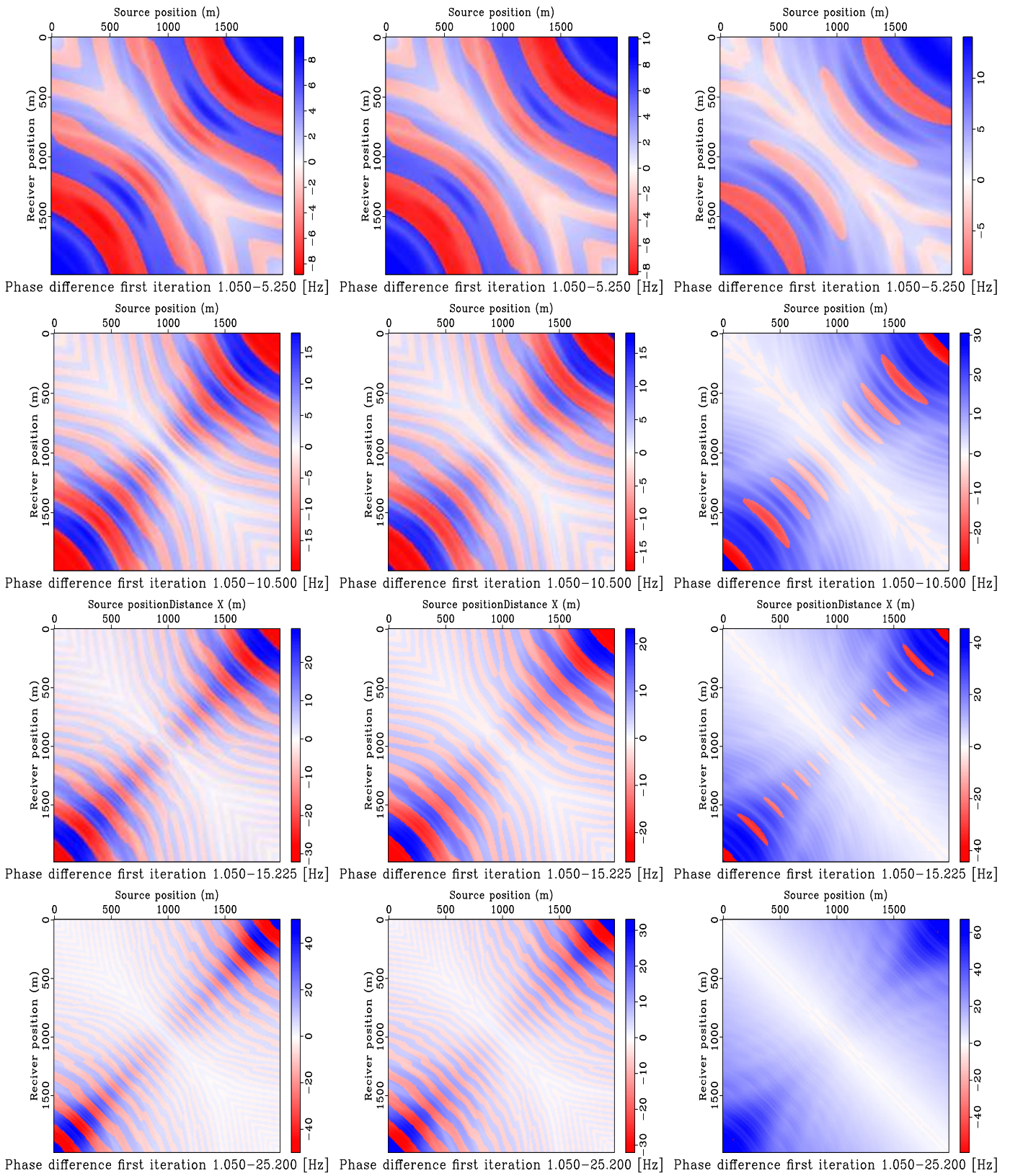
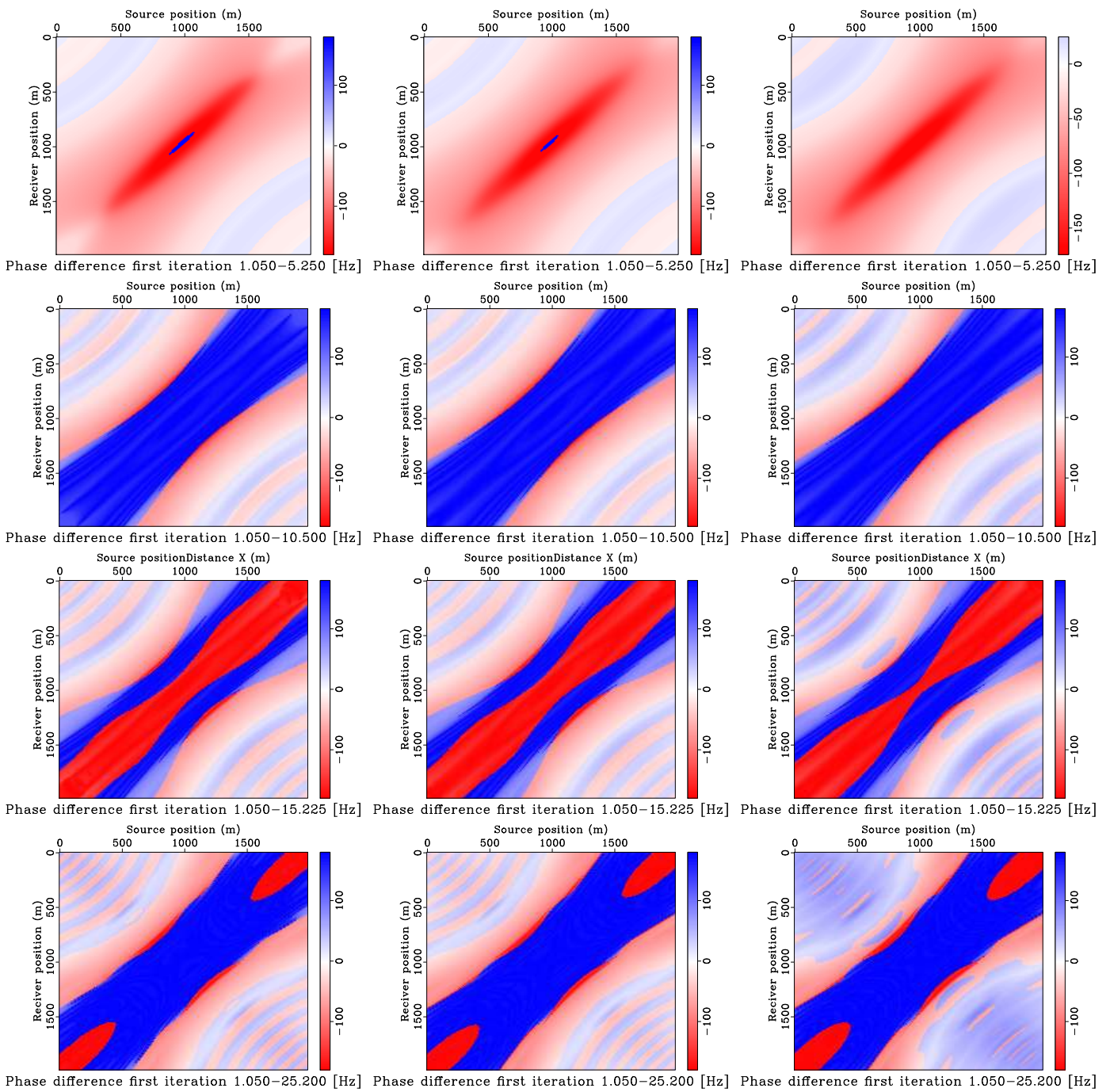


Figure 5.32: Phase difference for acoustic modeling and acoustic inversion for receivers line in $z = 1990$ [m]

Figure 5.33: Phase difference for visco-acoustic modeling and visco-acoustic inversion for receivers line in $z = 1990$ [m]

Figure 5.34: Phase difference for visco-acoustic modeling and acoustic inversion for receivers line in $z = 1990$ [m]



5.3.5 Filtering gradients with Hessian

The last test is to calculate the gradients in the frequency intervals $f = [1.050, 5.250]$ and $f = [1.050, 10.500]$ [Hz] multiplied by the inverse Hessian for a single source, the position of the source is $x_s = 1$ [Km] and $z_s = 0.010$ [Km] and the data collected in $z = 15$ [m], in order to see the improvement in the gradients when using this approximation of the hessian.

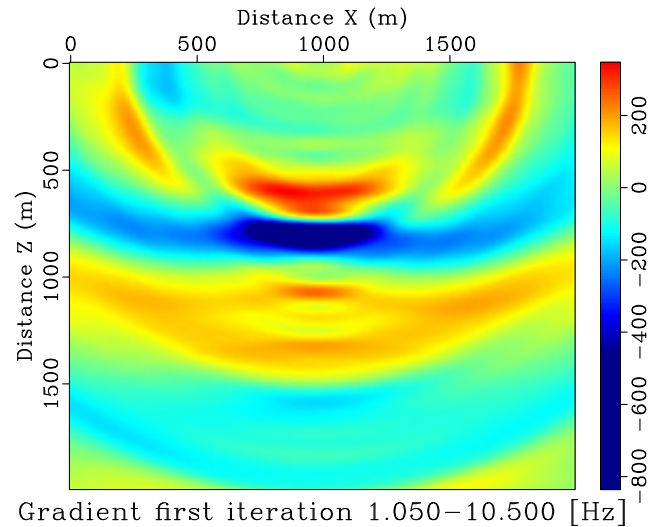
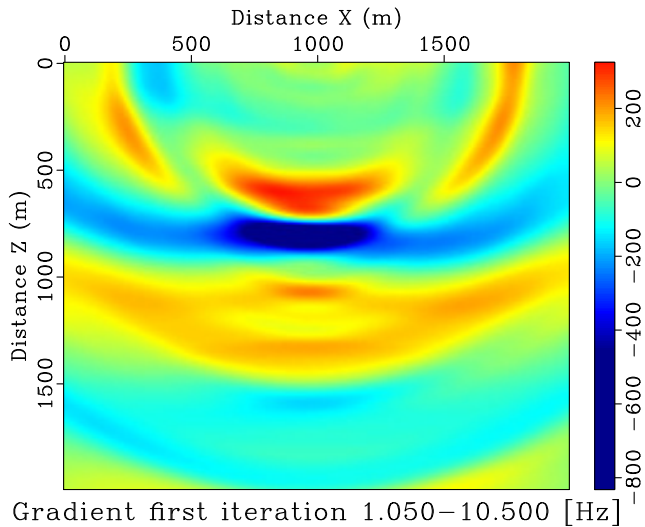
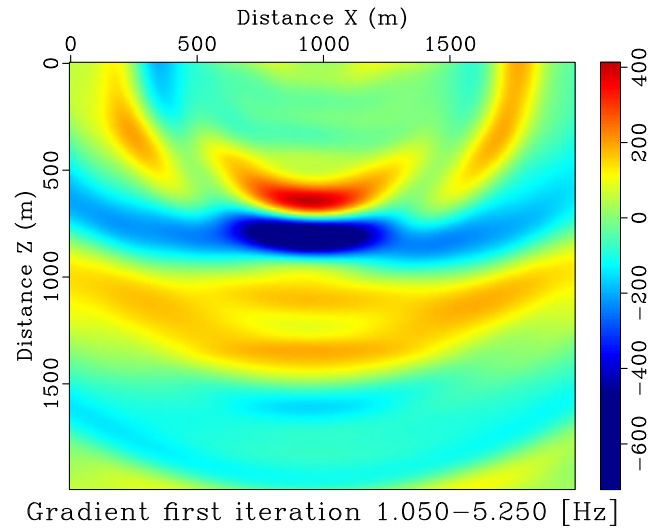
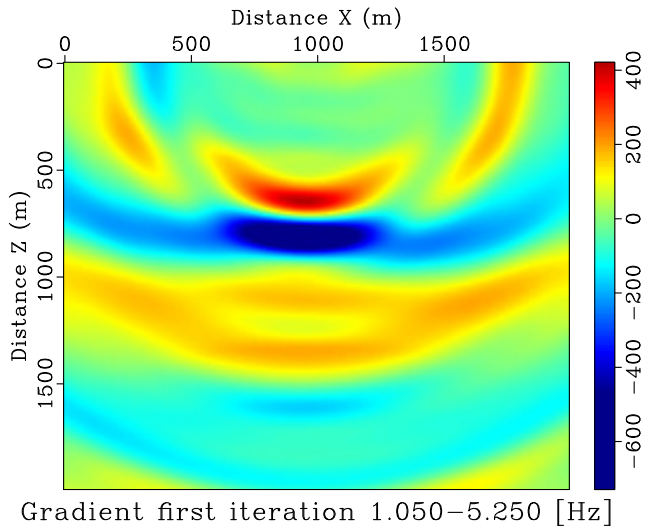


Figure 5.38: Gradient for acoustic modeling and acoustic inversion

Figure 5.39: Gradient for visco-acoustic modeling and visco-acoustic inversion

In figures 5.38 and 5.39 we show the gradient $= \nabla_{c\chi}(c_0(\mathbf{x}))$ for the first iteration for intervals of frequencies. The first column is gradient for acoustic inversion/modeling, the second column for visco-acoustic inversion/modeling.

We can see the differences with respect to the figures 5.8 and 5.9, for the first two intervals of frequencies. In both cases the contrast area is located horizontally but not in depth but there is an improvement with respect to the non-Hessian gradient, given that only one source is expected.

One should note that the amplitude is much larger and more in line with the difference between background and contrast velocities, that both results are similar despite being made with data from different models and that the result found at lower frequencies (or its shape) is maintained with respect to that found at higher frequencies.

5.4 FWI applying in three layers velocity profile

Now, using the inversion scheme described above eq. 5.15, we decided to apply it on data modeled with the three layers velocity profile with velocity $v_1 = 2100$ [m/s] at a depth of $[0, 0.6]$ [Km], $v_2 = 4300$ [m/s] at $(0.6, 1.2)$ [Km] and $v_3 = 6500$ [m/s] at $(1.2, 2.0)$ [Km], starting from a constant velocity profile. This is quite far from the final solution but will give us an idea of the scheme's applicability.

The test has been done with a line of 49 sources in $z = 10$ [m] and a line of 49 receivers in $z = 15$ [m] each 40 [m] from 0 [m] in domain of 2 [Km] $\times 2$ [Km] and the frequency intervals have been used $f = [0.525, 2.675]$, $f = [0, 525, 5.250]$, $f = [0.525, 10.500]$, $f = [0.525, 15.225]$ [Hz] to avoid cycling skipping (CS) using.

In figure 5.40 and 5.41 we can see the final velocity for inversion scheme for different intervals frequencies and in figure 5.42 and 5.43 the phase difference for last iteration. The figures is the result after 30 iterations.

There are several important things to note in these results, first the obtained final model locates the second reflector but not the third, somewhat compressible given that the amplitudes in the visco-acoustic model gradually attenuate such that the anomaly located in the parts lower values of the domain are not visible the larger the frequency.

Second, although the second reflector is located, the velocity is not fully recovered, possibly because of the presence of CS. In this test we calculated the phase differences for each frequency and found that at low frequencies the CS was not present but since $[7-8]$ [Hz] these abrupt changes were beginning to be noticed.

It is possible that for this test, the success of the inversion will be concentrated in the low frequencies, but given that these wavelengths are very long the details of the gradient would not be strong enough to recover the entire domain. We tried to get into higher frequencies but the CS grew, making the result lower than those shown.

Despite the result, we consider the experiment interesting, since it allows us to see the scope of inversion scheme and the use of the designed modeler. The execution times were also adequate, producing results in 7-10 iterations with a reduction of the objective function between 60 – 80% in less than 4 hour at the most set of frequencies. Note that the scheme works with Hessian is an encouraging result, although the cost of saving the entire array remains the biggest problem in developing the scheme.

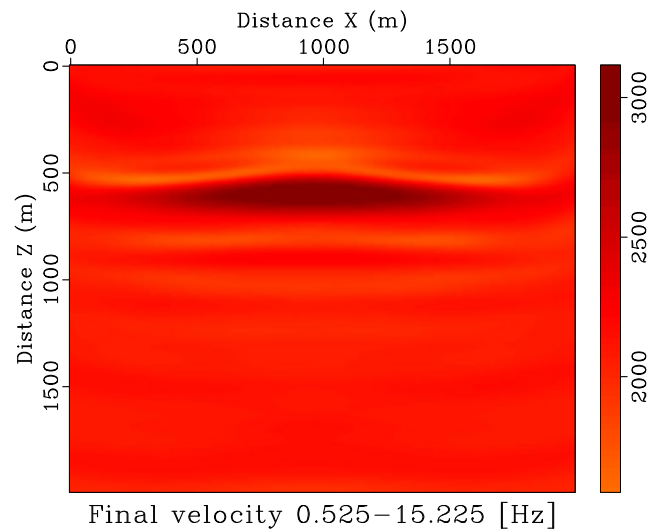
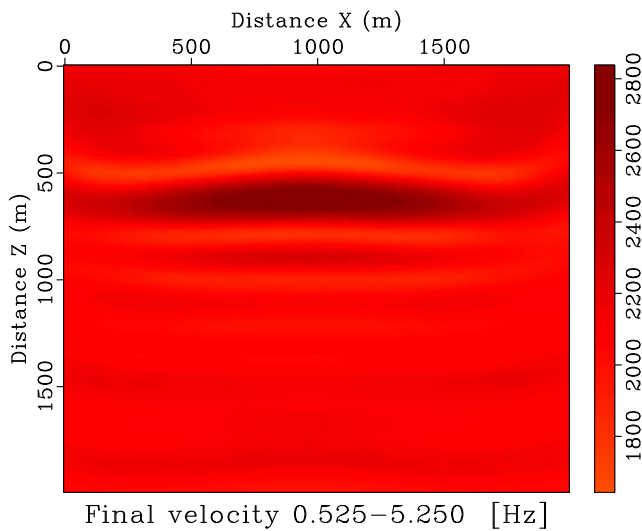
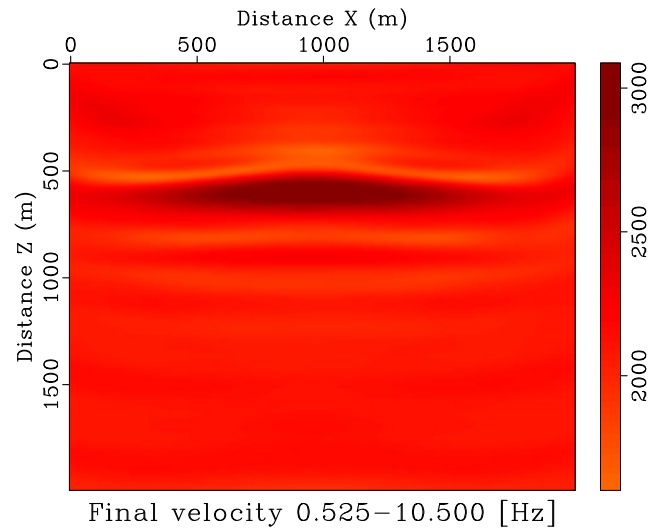
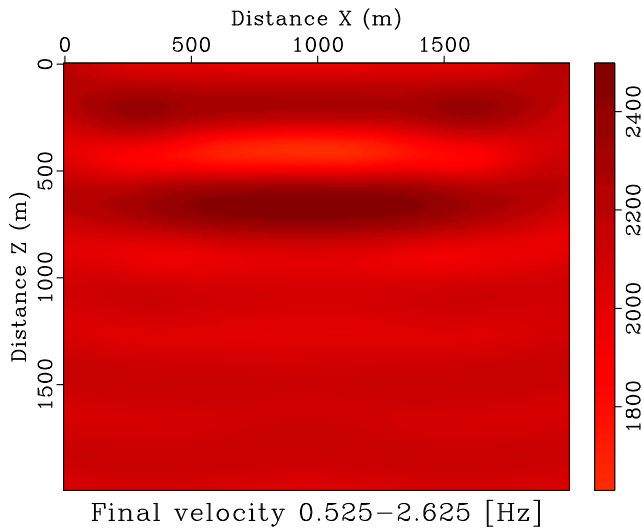


Figure 5.40: Final velocity for visco-acoustic modeling and visco-acoustic inversion.

Figure 5.41: Final velocity for visco-acoustic modeling and visco-acoustic inversion.

It is also possible to notice the importance of choosing the frequencies or set of frequencies, since the CS and the grid size depend on them. It is possible that a review of the methodology used and the way we interpolate the results at each frequency can give us better results. Another important thing in this subject is the application of the conditions of Wolfe, we take care of putting conditions of stop as soon as we have a violation to the conditions such that the objective function always goes in descending mode, but for this we to choose a good set of parameters so that the search step length is adequate.

Although there is a lot of work to be done on the inversion scheme, something that is natural since each type of modeling has tricks that must be found after a long analysis of many experiments and configurations, it is remarkable that the result has been obtained with requirements Computational less than the usual ones in this type of numerical processes thanks to the design of the modeling and the exploitation of the qualities of the same.

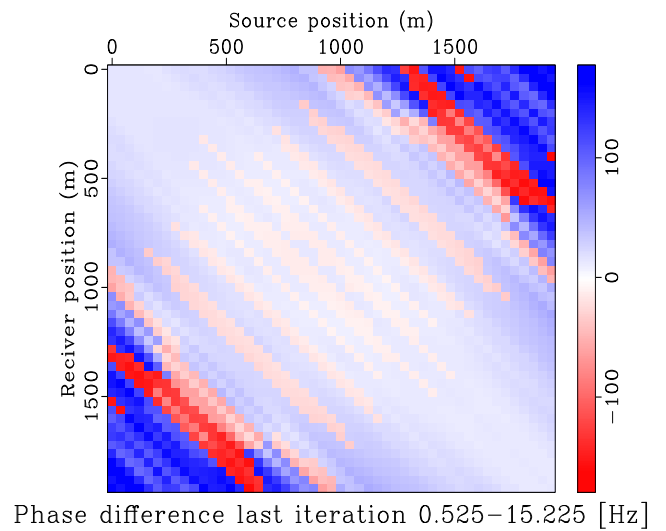
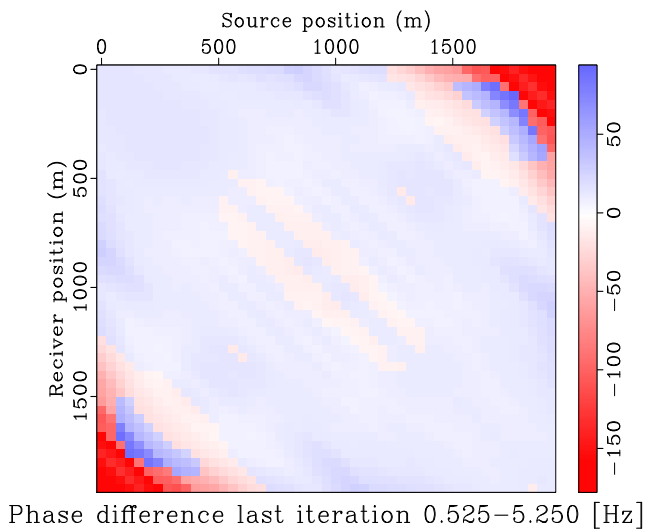
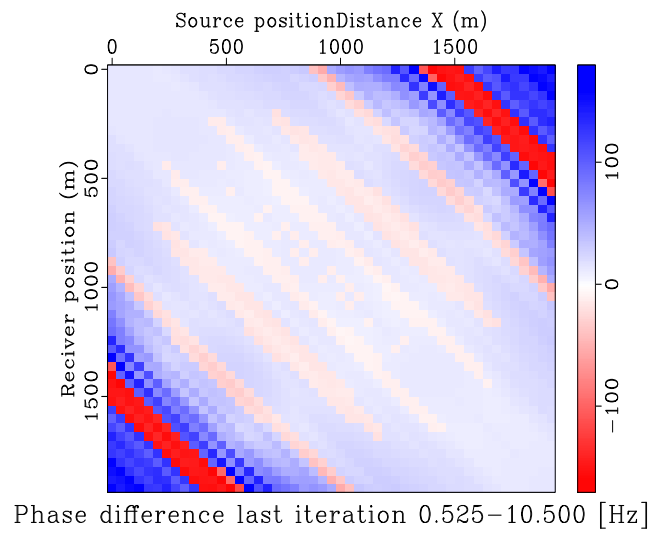
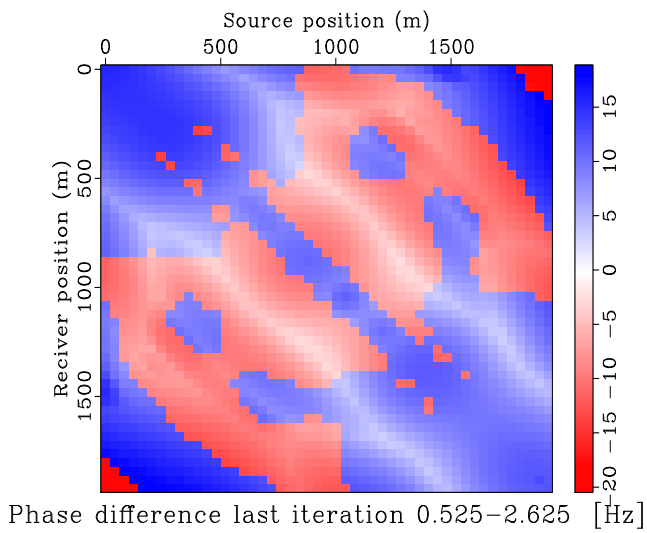


Figure 5.42: Phase difference for visco-acoustic modeling and visco-acoustic inversion

Figure 5.43: Phase difference for visco-acoustic modeling and visco-acoustic inversion

CONCLUSIONS

In this work we have studied the propagation of waves in a visco-acoustic medium through explicit modelling of the attenuation making use of damping functions that allow for dispersion that depends on the quality factor Q . We have implemented a finite difference scheme to solve the problem in frequency domain. Special care have been taken on the pollutive numerical dispersion issues of the modelling, for which we have used a mixed grid technique and optimal setup of the intercalated grids to minimize numeric dispersion.

We have shown the ability of the optimization scheme to minimize the numerical dispersion for the visco-acoustic case, and show that indeed the mixed grid scheme (9-point) with the optimization scheme provides solutions that are very much close to the real solution than the solutions obtained for the classic 5-point scheme.

Comparison of the numeric scheme with the analytic solution obtained for the case of wave propagation in a homogeneous medium has shown the advantages of the optimized mixed grid scheme. As it was shown in figures 4.1 and 4.2 the optimized 9-point mixed grid scheme provides solutions that are in general a few percent away from the analytic solution, while the standard 5-point scheme deviates notoriously from the analytic solution even for this simplistic case.

We have also shown that this modelling works quite well in models of high velocity/density contrast, commonly found in the field. We have shown that the explicit modelling of attenuation allows to model easily the superposition of complex velocity fields and to resolve properly the behaviour of waves in such scenarios.

We have verified the behaviour of the method for different well known attenuation-dispersion model Kolsky (Wang, 2009), and in particular noticed the clear difference between the attenuation of the amplitude of the wavefront due to the distribution of energy in the wavefront and the extra attenuation introduced by the damping functions and its dependence on frequency. Also we verify the effects of the density in the solution and its dispersion effect on the model.

In addition, it was verified that the obtained spectrum has a suitable form with respect to the Ricker source used, using the proposed grid delta, found with the dispersion analysis for the model, which allows us to compare the result with a solution in the time domain, which have spectrum with a maximum related to the frequency of the source. This allows us to verify that the proposed solution yields results that show the physical effects of the attenuation and the dispersion, effects expected by the variables that are defined in the problem.

This kind of behaviour has a notorious importance for methods like FWI. In the case of field exploration, sub-surface information can be obtained through the use of Full Waveform Inversion. The quality of the information acquired through the inversion is of course dependent of the ability of the model to approach the physical properties of the medium.

Visco-acoustic modeling represents a compromise between simplicity and realism that offers good results in the FWI technique, so, this kind of modeling has very promising impact in such procedures. In particular, given the iterative nature of FWI, the use of optimized mixed grid technique ensures the quality of the solution at reasonable computational cost. Another potential use is that an appropriated modeling of the attenuation may lead to better compensation for correct processing in e.g. RTM migration.

Finally we can conclude on the tests carried out using the inversion scheme denoted in chapter 5, that the scheme, which is summarized to a minimization process of a target function, has an expected behavior and reported in references (Pratt and Hicks, 1998) and (Gomes dos Santos, 2013), where the gradient is able to locate the anomaly between the greater the configuration of frequency-source-receiver, besides of them improvements that allows the application of the inverse of the hessian. The final result, in the small test we did on the three-layer profile, indicates the applicability of the modeling in this type of high performance techniques, since a result was obtained with the characteristics expected for a visco-acoustic medium using a Number of computational resources adequate.

Of course there is much that can be improved in the face of inversion (FWI), present other schemes, increase the challenge and use the complete Hessian to determine a better gradient, make analysis of the influence of the amplitude on the inversion and the nonlinearity of the objective function, to propose a adequate methodology so that with the help of the calculation of the phase difference we can avoid the Cycle Spiking (CS), review several configurations source-receiver to do an analysis between the modeling and the inversion for the same, all that within suitable time limits and computational resources, thanks to the properties of the proposed modeling.

BIBLIOGRAPHY

- Angeles, E. and Coss, M. D. L. M. (2005). *Los Métodos de Tomografía en la Enseñanza de la Interpretación Geofísica*. Memoria de ponencia, Universidad Nacional Autónoma de México, Departamento de Geofísica, Facultad de Ingeniería UNAM.
- B., U. and T., T. (2002). Comparison of seismic dispersion and attenuation models. *Studia Geophysica et Geodaetica*, 46:293–320.
- Berenger, J. P. (1994). A perfectly matched layer for absorption of electromagnetic waves. *Journal of Computational Physics*, 114:185–200.
- Brossier, R., Etienne, V., and Operto, S. & Virieux, J. (2010). *Frequency-Domain Numerical Modelling of Visco-Acoustic Waves with Finite-Difference and Finite-Element Discontinuous Galerkin Methods*. Don Dissanayake.
- Brossier, R. and Operto, S. & Virieux, J. (2009). Seismic imaging of complex structures by 2d elastic frequency-domain. *Geophysics*, 74:WCC105–18.
- C., C., D., K., and R., K. (1985). A nonreflecting boundary condition for discrete acoustic and elastic wave equations. *Geophysics*, 50:2117–2131.
- Carcione, J. M., Herman, G. C., and Kroode, A. T. (2002). Seismic modeling. *Geophysics*, 67:1304–1325.
- Chen, J.-B. (2004). Laplace-fourier-domain dispersion analysis of an average derivative optimal scheme for scalar-wave equation. *Geophys. J. Int.*, 197:1681–1692.
- Deraemaeker, A., Babuska, I., and Bouillard, P. (1999). Dispersion and pollution of the fem solution for helmholtz equation in one, two and three dimensions. *International Journal for Numerical Methods in Engineering*, 46:471–499.
- Dutta, G., Lu, K., and Wang, X. & Schuster, G. (2013). Attenuation compensation in least-squares reverse time migration using the visco-acoustic wave equation. In *SEG Houston 2013 Annual Meeting*.
- Fichtner, A. (2011a). *Full Seismic Waveform Modelling and Inversion*. Springer, Berlin.
- Fichtner, A. (2011b). *Full Seismic Waveform Modelling and Inversion*. Springer, New York.
- Fletcher, R. (1987). *Practical methods of optimization*. Wiley, New York.

- Florez, G. (2004). *Procesado de Sísmica de Reflexión Superficial en el Complejo Turbidítico de Ainsa (Huesca)*. Master thesis (pre-bologna period), Universitat Politècnica de Catalunya, Departament d'Enginyeria del Terreny, Cartogràfica i Geofísica. Barcelona, España.
- Gill, P. E., Murray, W., and Wright, M. H. (1981). *Practical optimization*. Academic Press, London.
- Gomes dos Santos, A. W. (2013). *Inversão de forma de onda aplicada à Análise de velocidades sísmicas utilizando uma abordagem multiescala*. Dissertação de mestrado, Universidade Federal da Bahia.
- Hicks, G. J. and Pratt, R. G. (2001). Reflection waveform inversion using local descent methods: Estimating attenuation and velocity over a gas-sand deposit. *Geophysics*, 66:598–612.
- Huazhong, W. and Libin, Z. & Zaitian, M. (2003). Seismic wave imaging in visco-acoustic media. *Science in China Ser. A Mathematics.*, 47:146–154.
- Ihlenburg, F. and Babuška, I. (1995). Finite element solution of the helmholtz equation with high wave number part i: The h-version of the fem. *Computers and Mathematics with Applications*, 30:9–37.
- Ihlenburg, F. and I. Babuška (1997). Finite element solution of the helmholtz equation with high wave number part i: The h-version of the fem. *SIAM Journal on Numerical Analysis*, 34:315–358.
- Jackson, D. D. (1979). The use of priority data to resolve non-uniqueness in linear inversion. *Geophysical journal of the Royal Astronomical Society*, 57:137–157.
- Jo, C.-H. (1996). An optimal 9-point, finite-difference, frequency-space, 2-d scalar wave extrapolator. *Geophysical Journal*, 61:529–537.
- Kelley, C. T. (1999). *Iterative methods for optimization*. SIAM, Philadelphia.
- Kim, M. H., Choi, Y., Cha, Y. H., and Shin, C. (2009). 2-d frequency-domain waveform inversion of coupled acoustic-elastic media with an irregular interface. *Pure and Applied Geophysics*, 166:1967–1985.
- Lailly, P. (1983). The seismic inverse problem as a sequence of before stack migrations: . *Conference on Inverse Scattering, Theory and Application*, Expanded Abstracts:206–220.
- Lavergne, M. (1986). *Seismic Methods*. Editions Technip.
- Marfurt, K. (1984). Accuracy of finite-difference and finite-element modelling of the scalar and elastic wave equations. *Geophysics*, 49:553–559.
- Mase, G. T. and Mase, G. E. (1999). *Continuum Mechanics for Engineers*. CRC Press, Boca Raton, Florida.
- Mavko, G., Mukerji, T., and Dvorkin, J. (2009). *The Rock Physics Handbook*. Cambridge University Press, California.
- Mayo, A. (1984). The fast solution of poisson's and the biharmonic equations on irregular regions. *SIAM J. Sci.*, 21:285–299.

- Operto, S. and Virieux, J. (2006). *Practical aspects of Frequency-domain finite-difference modelling of Seismic wave propagation*. Ecole thématique SEISCOPE.
- Operto, S., Virieux, J., Amestoy, P., L'Excellent, J., and Giraud, L. & Ben Hadj, H. (2007a). 3d finite-difference frequency-domain modeling of visco-acoustic wave propagation using a massively parallel direct solver: A feasibility study. *Geophysics*, 72:SM195–SM211.
- Operto, S., Virieux, J., Amestoy, P., L'Excellent, J., and Giraud, L. & Ben Hadj, H. (2007b). Finite-difference frequency-domain modeling of viscoacoustic wave propagation in 2d tilted transversely isotropic (tti) media. *Geophysics*, 74:T75–T95.
- Ospina, M. A. (2016). *Dispersión y Estabilidad en el procesos de modelado en Full Wave Inversion para un medio visco-acustico en el dominio de la frecuencia en dos dimensiones*. Trabajo presentado como requisito parcial para optar al título de magíster en matemáticas, Universidad de Antioquia.
- Plessix, R.-E. (2006). A review of the adjoint-state method for computing the gradient of a functional with geophysical applications. *Geophys. J. Int*, 167:495–503.
- Polak, E. (1997). *Optimization*. Springer, New York.
- Pratt, R. G. (1990). Inverse theory applied to multi-source cross-hole tomography, part ii: Elastic waveequation method. *Geophysical Prospecting*, 38:311–330.
- Pratt, R. G. (1999). Seismic waveform inversion in the frequency domain, part i: Theory and verification in a physical scale model. *Geophysics*, 64:888–901.
- Pratt, R. G. and Hicks, C. S. . G. J. (1998). Gauss-newton and full newton methods in frequency-space seismic waveform inversion. *Geophys, J. Int*, 133:341–362.
- Pratt, R. G. and Worthington, M. H. (1990). Inverse theory applied to multi-source cross-hole tomography, part i: Acoustic wave-equation method. *Geophysical Prospecting*, 38:287–310.
- Quarteroni, A., Sacco, R., and Saleri, F. (2000). *Numerical Mathematics*. Springer, New York.
- Sen, M. K. and Stoffa, P. L. (1995). *Advances In Exploration Geophysics 4, Global Optimization Methods In Geophysical Inversion*. Elsevier, 1000 AE Amsterdam, The Netherlands.
- Shah, N., Warner, M., Nangoo, T., Umpleby, A., Stekl, I., Morgan, J., and Guasch, L. (2012). *Quality assured full-waveform inversion: Ensuring starting model adequacy*, pages 1–5.
- Shin, C. and Cha, Y. H. (2008). Waveform inversion in the laplace domain. *Geophysics*, 173:992–931.
- Strikwerda, J. (2007). *Finite Difference Schemes and Partial Differential Equations*. Society for Industrial and Applied Mathematics.
- Suh, S., Yoon, K., and Cai, J. & Wang, B. (2012). Compensating visco-acoustic effects in anisotropic resverse-time migration. In *SEG Las Vegas 2012 Annual Meeting*.

- Taoi, Y. and Sen, M. K. (2013). Frequency-domain full waveform inversion with a scattering-integral approach and its sensitivity analysis. *Geophysics and Engineering*, 10:065008.
- Tarantola, A. (1984). Inversion of seismic reflection data in the acoustic approximation. *Geophysics*, 49:1259–1266.
- Thurber, C. and Ritsema, J. (2007). *Seismic Tomography and Inverse Methods*, chapter Theory and Observations – Seismic Tomography and Inverse Methods, pages 323 – 354. Elsevier B.V.
- Tornberg, A. and Engquist, B. (2004). Numerical approximations of singular source terms in differential equations.
- Wang, Y. (2009). *Seismic Inverse Q Filtering*. Wiley.
- Yang, Z. and Liu, Y. & Ren, Z. (2014). Comparisons of visco-acoustic wave equations. *Journal of Geophysics and Engineering*, 11:025004.